Studies of a series of Benzene-1,3,5-derivatives and some other supramolecular building blocks and their self-assembly properties

Emanuele Cappello, M.Sc

January 2021

University of Dublin
Trinity College

Based on research carried out under the direction of Prof. Thorfinnur Gunnlaugsson

A thesis submitted to the School of Chemistry, Trinity College Dublin, The University of Dublin, for the degree of Doctor of Philosophy

I declare that this thesis has not been submitted as an exercise for a degree at this or any other university and is my own work. Parts of the work described herein are the product of collaboration and are acknowledged at the beginning of each chapter. I agree to deposit this thesis in the University's open access institutional repository or allow the library to so on my behalf, subject to Irish Copyright legislation and Trinity College Library conditions of use and acknowledgements.

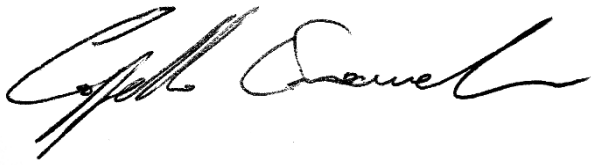

Emanuele Cappello

Abstract

This thesis, titled "Studies of a series of Benzene-1,3,5-derivatives and some other supramolecular building blocks and their self-assembly properties", describes the synthesis and characterisation of novel tripodal systems based on the benzene-1,3,5-tricarboxamide (BTA) motif. As will be outlined in the introduction, the ability to design, tune and control supramolecular materials formed through self-assembly processes is an area of great importance and increasing interest. The introduction will provide the reader with an overview of functional supramolecular materials, the various interactions that drive their formation and their properties. Some of the most relevant advances in the literature are reviewed, with a particular focus on soft materials showing gelation. While gelation is a behaviour very well known for high molecular weight systems, such as covalent polymers, the field of low-molecular weight gelators (LMWGs), *i.e.* systems able to achieve gelation through networks of supramolecular interactions has gained increased attention in the last few decades and will be hereby discussed. Several tripodal systems based on the BTA motif possessing these properties will be outlined. Furthermore, the introduction will present an overview of the lanthanide metal ions, detailing their photophysical properties, their role in the formation of the metal-directed self-assemblies, supramolecular polymers *etc*, and finally the chapter will close describing some of the most relevant advancement to supramolecular chemistry achieved by the Gunnlaugsson group in the recent years.

Chapter 2 will describe the design rationale and the synthesis of the tripodal BTA systems presented in the thesis, their purification procedures and the chemical characterisation. An alternative synthetic pathway will also be presented, and a second family of supramolecular building blocks will be shown.

Chapter 3 will focus on the spectroscopic and morphologic investigations of the systems presented in the previous chapter. The interactions of the BTA ligand with the Eu(III) ions is investigated by performing titration at two different ligand concentrations; ultraviolet-visible spectroscopy as well as fluorescence is recorded and used to gain some insight on the ground and excited states of the ligands, while metal-centred emission studied through phosphorescence spectroscopy. The data obtained from these titrations is processed using non-linear regression analysis to determine speciation and stability constants, while proposing a mode for the formation of the self-assembled species. The formation of such aggregates in solutions is then investigated including their morphology

using scanning electron microscopy (SEM) of their dried solutions; furthermore, the formation of various gels is investigated using the same technique.

Chapter 4 will describe a collaboration work performed with a fellow Gunnlaugsson group member in which one of the BTA systems will be used in conjunction with a Tb(III) cyclen-based complex to form a ternary system able to self-assemble into a higher order aggregates. The synthesis of the ternary system, as well as the spectroscopic and morphologic characterisation is presented.

Chapter 5 will present a series of aggregating systems based on two well-known motifs, squaramide and 1,8-naphthalimide. The studies highlight the processes leading to their self-assembly properties and how the appropriate design influences the forces that lead to the aggregation, correlating the structures with the morphologies observed through SEM imaging.

Chapter 6 contains the experimental details and will be followed by references in Chapter 7. The additional information, such as data for the work described, characterisation *etc*, can be found in the Appendix.

Acknowledgements

First and foremost, I would like to thank my supervisor, prof. Thorri Gunnlaugsson, for giving me a chance to take on the incredible journey that this PhD has been for me, for constantly supporting me and guiding me in the last four and a half year.

Secondly, I would like to thank Dr Chris Hawes and Dr Robert Elmes, as well as their research teams from Keele an Maynooth University for the collaboration works shown in Chapter 5, wishing the best for your academic careers.

An enormous and most sincere thanks to the Experimental and Technical staff from the School of Chemistry, particularly Dr John O'Brien who helped me solve my NMRs conundrums (no matter how "evil" my samples were!), Dr Manuel Ruether for his patient help in getting set up with all the instruments and Dr Gary Hessman for his help with mass spectrometry.

To all the people I've met in the Gunnlaugsson group, past and present, thanks a million: you all were amazing to be around. Oxana, you are an absolutely incredible person to be around and I would have learned half the things I did without you, and I will always be grateful to you. Big thanks Sachi for helping me set off on this tripodal trip and showing me the ropes of SEM. Gearóid staying late in the lab was no trouble if you were around, since a good laugh or an Irish History class was always involved! Eoin, Bjorn, I hope you're keeping well! Dermot, you are an incredibly brilliant person and scientist, so always remember to have fun! Thank you for all the funny movie talks Han and sorry for scaring you (and Oxana, too) that one time! And big thanks to you and Isabel for welcoming in your fumehood when I had just arrived! Sam and Anna, I hope life is treating you good! Helena and Sandra, thanks for the laughs and the random Spanish chats. Thanks for the science chats and helping me out with a thesis English corrections, Adam and Helen! Best of luck to you and Tumpa for your research in Dublin. Thanks a million for solving my crystal structures, June! It's going to be up to you soon. Thanks a lot, Deirdre! For the corrections and for inviting me to join the 10k run (and for bringing me home afterwards, when I could barely stand)! Also, thank your sister from me, I think she's fed me a few kilos of pastries over the last two years (and I enjoyed shamelessly every gram of it)! Best of luck for your PhDs Shauna, Tomas, Patrick, Laura and Connie! The group has a bright future with you. Jason, you are a good lad and it was thrilling sharing the way with you (although we are still not sure who's going to be number 50)!

Well, it's now your turn Bruno: I owe you. Thanks for giving my name to Thorri, for hosting me when I arrived and for, simply, being a great friend.

Ruth, while the whole world was going crazy out there in the last year and a half you still made my life amazing (and fluffier!). You have been a constant and loving support for me, helping me with everything and giving me your love. Is breá liom tú, lacha bheag.

To Peppe and the "Trinity Italians gang", you were the best family I could find, a million miles away from home. In the hardest days, coffee breaks and lunches were little oases to take a breath. Paolo, Marco, you truly are elder brothers to me, thanks for always giving me advices and your most honest opinions, you were my safety net and my "mainframe".

To Marie, Keith and all the other amazing friends I was lucky enough to meet, thanks for gifting me with your friendship.

A chiudere, ultimi ma non per importanza, non posso che ringraziare la mia famiglia. Le parole non possono spiegare l'amore che provo per voi. Grazie per gli infiniti sacrifici, grazie per tutto l'amore che mi avete dato, grazie per il supporto incondizionato, grazie per essere stati semplicemente meravigliosi. Vi voglio bene.

This thesis is dedicated to two people with the same name. My grandfather, whose memory will always remind me how a man is supposed to be like, and to me, in the hope that I could follow his example and make him proud wherever he is.

Abbreviations

3D	Three dimensional
°C	Celsius degree
Å	Angstrom
a.u.	Arbitrary units
ACQ	Aggregation-caused quenching
AFM	Atomic Force Microscope
AIE	Aggregation-induced emission
Ala	Alanine
atm	Atmospheres
BTA	Benzene-1,3,5-tricarboxamide
CD	Circular Dichroism
cm	Centimetre
cryo-TEM	Cryoscopic temperatures
DCC	Dicyclohexylcarbodiimide
DCM	Dichloromethane
DIC	Diisopropylcarbodiimide
DIPEA	Diisopropyl ethylamine
DMA	Dimethylacetamide or dimethylaniline (as relevant)
DMAP	Dimethylamino pyridine (4-(Dimethylamino)pyridine)
DMF	Dimethyl formamide
DMSO	Dimethyl sulphoxide
DNA	Deoxyribonucleic Acid
EDCI	N-ethyl-N'-(3-dimethylamino-propyl)carbodiimide hydrochloride
eq	Equivalents
ET	Energy transfer
EtOH	Ethanol
FTIR	Fourier transform infrared
GδL	Glucono-d-lactone
Gly	Glycine
HBC	Hexa-peri-hexabenzocoronene
HBTU	N,N,N′,N′-tetramethyl-O-(1H-benzotriazol-1-yl)uronium hexafluorophosphate
HNMR	spelled differently in different chapters NB find and replace
HOBt	1-hydroxybenzotriazole
HRMS	High Resolution Mass spectrometry
ICT	Internal Charge Transfer
ISC	Intersystem crossing
L:M	Ligand to Metal ratio
LMCT	Ligand to Metal charge transfer
LMWG	Low molecular weight gelators
Ln	Lanthanide
M	Molar concentration
m/z	Mass to charge ratio
MALDI-MS	Matrix-assisted laser desorption/ionisation Mass spectrometry

MCH	Methylcyclohexane
MeCN	Acetonitrile, methyl cyanide
MeOH	Methanol
MLCT	Metal to ligand Charge transfer
mM	Millimolar
MOFs	Metal-organic frameworks
MRI	Magnetic resonance imaging
ms	Millisecond
MW	Microwave
NDI	Naphtalenediimide
NIR	Near-infrared
nm	Nanometre
NMR	Nuclear Magnetic resonance
OF	Oligofluorence
OLEDs	Organic light emitting diodes
OPV	Oligo(phenlene vinylene)
Pery	Perylene bismide
pH	-log[H+]
Phe	Phenylalanine or Phenyl group (as relevant)
ppm	Parts per million
Py	Pyrene
q	Numver of metal-bound water molecules
q value	Hydration state
RT	Room temperature
SANS	Small-Angle Neutron Scattering
SEM	Scanning Electron Microscopy or microscope (as relevant)
SOVP	S-oligo-(p-phenylene vinylene,
StD	Standard deviation
T	Temperature
TCD	Trinity College Dublin
TCE	1,1,2,2-tetrachloroethane
TEA	Triethyl amine
TEM	Transmission Electron Microscopy
TFA	Trifluoroacetic acid
T_{gel}	Thermal stability of the gel
THF	Tetrahydrofuran
ToF	Time of flight
tpy	2,2’,6’,2’’-terpyridine
Tris	Tris(hydroxymethyl)aminomethane
UnU	Bisurea bolaamphiphiles p8 intro
UPy	2–ureido-4-pyrimidone moiety
UV	Ultraviolet
UV-Vis	Ultraviolet-visible
wt	Weight
XRD	X-ray Diffraction
Δ/Λ	Delta or lambda helicity

ε	Molar absorption coefficient
λ_{em}	Emission wavelength
λ_{ex}	Excitation wavelength
λ_{max}	Maximum absorbance or intensity at corresponding wavelength
µL	Microlitre
µM	Micromolar
µm	Micrometre
τ	Variable time

Table of Contents

Chapter 1

Introduction

1.0 Introduction

Since Jean Marie Lehn defined it as 'chemistry beyond the molecule,' supramolecular chemistry has become an increasingly researched area within chemistry that encompasses the study of systems forming networks of reversible, non-covalent interactions, like hydrogen bonds and metal ion coordination.[1-4] These networks result in structures of high complexity through autonomous processes of self-assembly between small, and structurally simple units. Examples of supramolecular systems are extremely common in nature and form the basis of many biological processes such as protein folding mechanisms, enzymatic activities and self-replication processes. The most common biological example is the structure of deoxyribonucleic acid (DNA); but DNA is composed of two strands of covalently bound monomers that interact through hydrogen bonds to form the eminent double helical structure on which life relies, though complementary supramolecular interactions, consisting of dominantly hydrogen bonding and $\pi-\pi$ stacking. Both these features will be central to the work described in this PhD Thesis.

The self-assembly interactions, through the balance of the repulsive and attractive forces lead to a thermodynamic minimum for the final structure,[5] resulting in a stable macrosystem. The novel class of materials formed through these interaction are commonly referred to as 'soft' or 'responsive,' and have found applications in many fields, including sensors,[6-7] next-generation LEDs,[8-9] probes to study biological matrices[10-13] and gels.[14-18] Such a vast range of applications for these materials is due to unique properties, such as the ability to respond to external stimuli.[19] Furthermore, the materials display various morphologies like nanoarchitectonics,[20] gels[9, 16, 18] and porous structures.[8, 11] These properties are consequently dependant on the nature of the units forming the networks. Therefore, an understanding of how small structural changes (e.g. different functional groups, physical properties, and structure) in the 'starting blocks' (also refereed to herein as supramolecular building blocks) will correlate to the final aggregate becomes the challenge researchers face in order to design systems aimed at specific tasks. Being able to correlate structure with the morphological outcome is a challenge that has not been easily achieved to date. However, the establishment of such correlation, and understanding of such effects, can help in achieving control over self-assembly pathways, which ultimately, should allow for the formation of building blocks that have predictable hierarchical (or higher order) structure, and hence, properties. The

aim of this PhD thesis is to address this with the formation, characterisation and analysis of several novel structures possessing building blocks that can partake in various supramolecular binding interactions and self-assemble in solution. In more detail, the main focus of the PhD project described in this Thesis is the development of novel tripodal systems based on the benzene-1,3,5-tricarboxamide (**BTA**) framework using aromatic and chiral spacers connected to a 2,2',6',2''-terpyridine (**tpy**) unit. These systems showed the ability to form supramolecular aggregates through self-assembly processes, and metal ion coordination chemistry. The effect of the nature of the spacers was observed in order to achieve a deeper understanding of such systems, their effect upon new materials formation; to do so the properties of these resulting materials, were investigated both, as free ligands and complexes with metal ions. Other systems will also be featured in this Thesis.

This Introduction chapter will briefly cover topics related to the current state-of-the-art, beginning with a general introduction on the formation of what has been defined as supramolecular polymers, which are systems related to conventional polymers (see below), consisting of repeatable units, formed through weak and non-covalent bonding interactions. This is then followed by a more detailed description of how the target **BTA** scaffolds form part of this context, both on a molecular level and as macroscopic materials. A short description of the general characteristics of the lanthanide metal ions to contextualize their use in the formation of complexes, and as bridging or crosslinking ions, is then provided before finishing with a brief description of the content of this Thesis.

1.1 Supramolecular polymers

Polymers are defined by the IUPAC as substances composed of macromolecules.[21] Macromolecules are generated by the formation of covalent bonds between smaller molecules in a repetitive pattern, and possess a larger relative molecular mass than the individual repeating units. These systems present a vast range of properties that make them ubiquitous in life.[22] Systems in which the units forming the final substance are not bonded covalently, but by networks of reversible, directional, weak interactions, such as π-π stacking, hydrogen bonds, metal-ligand interactions, *etc*. are defined as supramolecular polymers. The aggregate formed is not defined a macromolecule in this case, but instead, as a **supramolecule** or supramolecular assembly, and by tuning the conditions, the properties displayed are analogous to polymeric materials.[23]

Analogous to 'traditional' polymeric materials, supramolecular polymers are commonly classified depending on their formation mechanism in three macrocategories: isodesmic, chain-ring and cooperative supramolecular polymerization. In the first case, the aggregation is a linear process, where all the steps involve the same interaction. It can be compared with the polycondensation of esters, leading to a polydispersed final result, and in coil-like structures lacking interactions strong enough to establish a long range order. In the second case, chain-ring supramolecular polymerization, the use of ditopic monomers leads to the formation of cyclic aggregates *via* the interaction of the end groups. Contrary to the covalent case, where the control of these processes is kinetic in nature, the supramolecular ring polymers are formed under thermodynamic control and the resulting systems are composed of both rigid rings and coil-like systems in equilibrium. Finally, the cooperative mechanism can be compared to the 'live' chain polymerization. The key-concept to highlight, is the fact that this processes happens in two steps, nucleation and elongation, with the latter being the more thermodynamically favourable. This translates into linear chains that possess a higher degree of order and results in fibrous aggregates.[23]

Lehn and co-workers obtained the first synthetic supramolecular polymer through the use of molecular recognition between tartaric acid derivatives with complementary pyridinc units, which assembled into monodimensional arrays with liquid crystal-like behaviour, Figure 1.1.[24] The use of tartaric acid derivatives found that the three different isomers (D-, L- and meso-forms) influenced the chirality of the final helical aggregate (**Figure 1.1**).[24]

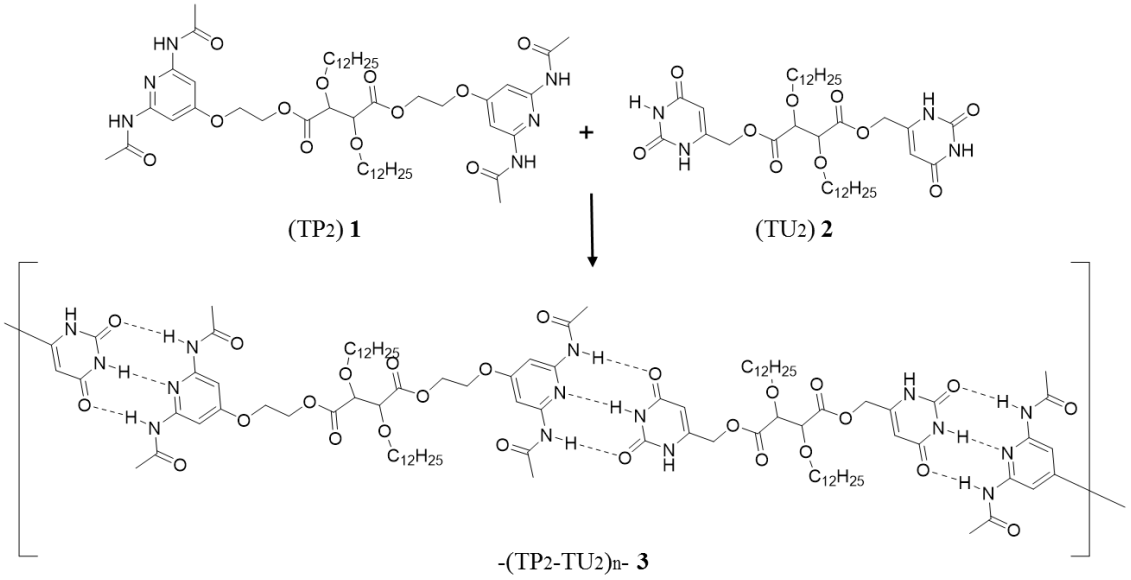

Figure 1.1 Molecular structure of **1** (TP_2) and **2** (TU_2) and schematic representation of their interaction to form a supramolecular liquid crystalline polymer **3**, reproduced from ref.[24]

Following this 'all organic' work, the focus of this area of research widened, with an aim of designing compounds capable of assembling into more complex structures, ranging from bidimensional arrays to extremely complex nanoarchitectonics, often with the help of classical coordination chemistry.[25] Within this field, the underlying principal is the understanding that an appropriate design of the building block will be cardinal in the assembly processes it is involved in, and therefore, in the properties of the resulting aggregate including; which functionalities it contains, its structure, and aromaticity, *etc*. The problem remains, as was eluded to above, that normally, minor structural changes can have detrimental effect on the material outcome, and controlling these can be difficult to achieve, particularly for systems of high structural complexity.

Expanding upon Lehn's work, Meijer *et al.* increased the complexity of the pyridinic unit and designed a self-complementary unit capable of forming four hydrogen bonds, 2–ureido-4-pyrimidone (**UPy, 4)**.[26-27] In this case, **UPy**, **4**, was used as the terminal moiety at each end of an alkyl chain (**5**, **Figure 1.2**, B), which resulted in a monodimensional aggregate forming fibres. Adding to the solution molecules containing three **UPy** moieties induces a reticulation that connects the single strands into a network with completely polymer-like behaviour (**Figure 1.2**, E). On the macroscale, this allows the resulting materials to display good mechanical properties, akin to covalent polymer ones, while still maintaining the ability to reverse to their monomeric form due to their supramolecular nature.

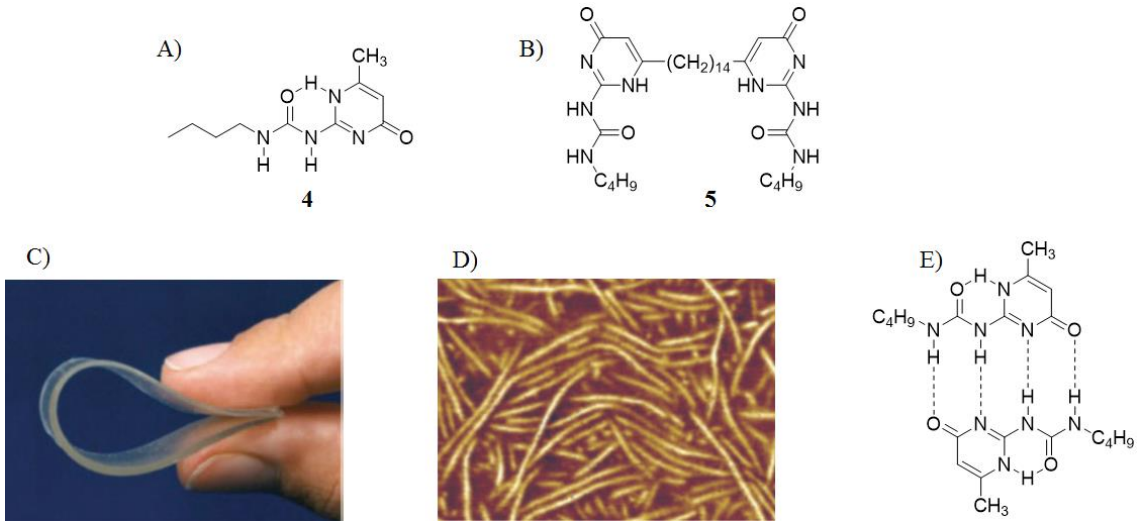

Figure 1.2: A) Schematic representation of the **UPy** unit **4**; B) linear system **5**, with **UPy** units at both ends; C) picture and D) AFM imaging supramolecular material derived from **5**; E) schematic representation of the four-fold interaction between **UPy** units. Reproduced from ref.[26-27]

As previously mentioned, analogous to the covalent macromolecules, assemblies can also be formed between different partners leading to supramolecular co-polymers. Schenning

et al. obtained materials suitable for the production of OLEDs with tuneable emissions.[28] To do so, they designed three π-conjugated oligomers able to emit under UV irradiation, a blue-emitting oligofluorene (**OF**, **6**), a green-emitting oligo(phenlene vinylene) (**OPV**, **7**) and a red-emitting perylene bismide (**Pery**, **8**), all of which were functionalised with two **UPy** moieties.

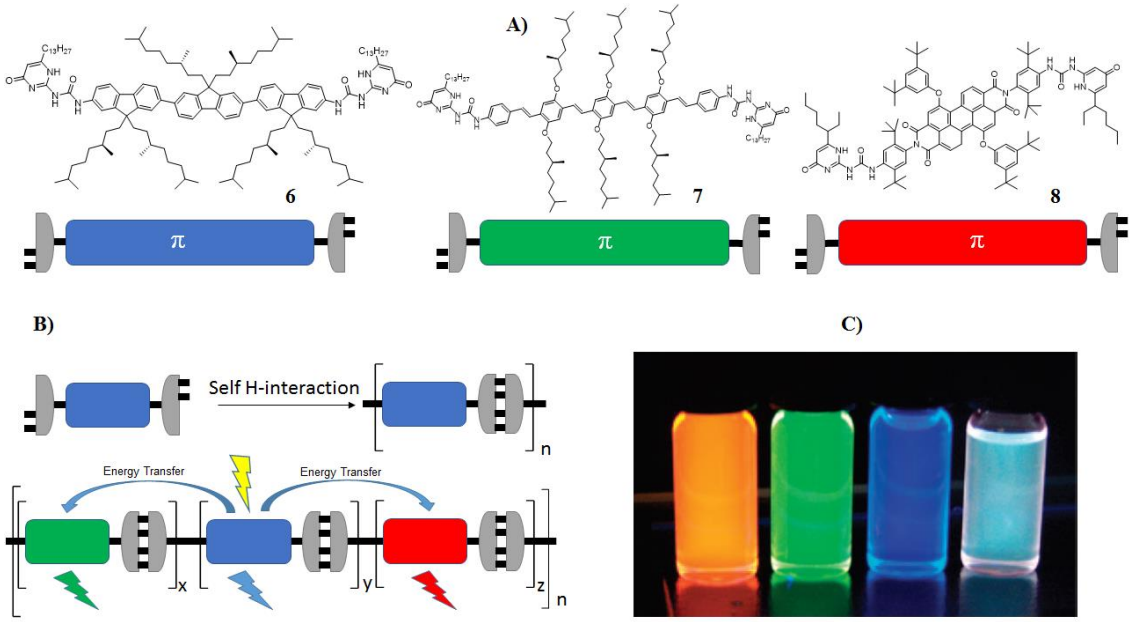

Figure 1.3 A) Chemical structures of the **UPy** di-functionalised chromophores **OF** (**6**), **OPV** (**7**) and **Pery** (**8**); B) Representation of the aggregation mechanism for pure **5** (top) and after mixing with **5** and **7** (bottom); C) $CHCl_3$ solutions of pure **7**, **6**, **5** and mixture upon irradiation at 365 nm. Images reproduced from ref.[28]

These systems showed the ability to aggregate into supramolecular polymers both in $CHCl_3$ solution and in bulk. The electronic configuration of the oligomers leads to an energy transfer from the **OF** unit to **OPV** and **Pery**, causing all three oligomers to emit light; the final emission being dependant on the composition of the aggregates involved. In fact the authors showed that a white light could be achieved through a fine tuning between the three components.[28]

Following this, work from Meijer *et al.* expanded on the assembly properties of the **OPV** systems.[29-30] To do so, the **OPV** core was functionalised with long alkyl chains on one end and a ureidotriazine moiety the other; this was coupled with the presence of a chiral centre on the side chains connected to the core, to obtain a *S*-oligo-(*p*-phenylene vinylene, **SOVP**) (**Figure 1.4: A**). The presence of the ureido functionality on one end directs these systems to assemble into dimers. Such dimeric units were observed to undergo a π-π stacking process with a small dihedral angle, which upon elongation, led to a chiral helical

aggregate of length and properties tuneable for modifying the environmental conditions it was exposed to, such as temperature or solvent polarity.

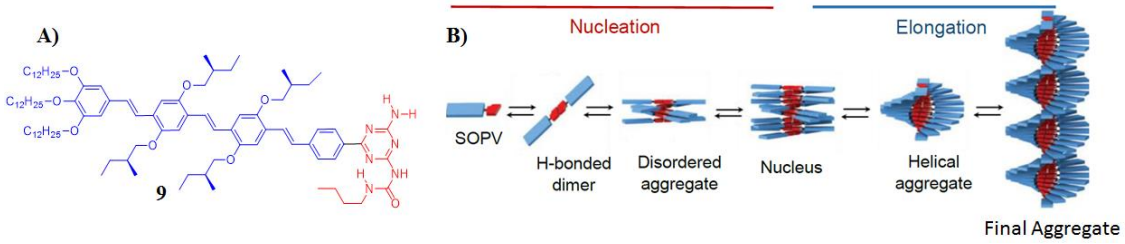

Figure 1.4: A) Molecular structure of **9** and B) schematic representation of the assembly process with the nucleation driven by quadruple hydrogen bond to form the dimeric seeds, followed by the stacking into nuclei that then elongate into helical aggregates. Images reproduced from ref.[30]

The co-assembly approach was used by Aida *et al.* in order to obtain a nanostructured material with optoelectronic properties employable as a platform to study the behaviour of charge carriers.[31] In particular, they were able to obtain an organic heterojunction using two gemini-shaped hexa-*peri*-hexabenzocoronene (HBC) derivatives, HBC 1 and HBC 2 (**10** and **11**), respectively. A solution of **10** in THF showed the formation of bundles of nanotubular aggregates upon CH_3OH diffusion, with the geminal arms on the outer surface of the single nanotubes. Upon treatment with a Cu^{2+} salt solution, and sonication, these bundles separated into discrete nanotubes with a charged surface due to the ions bound to the bypiridinic arms.

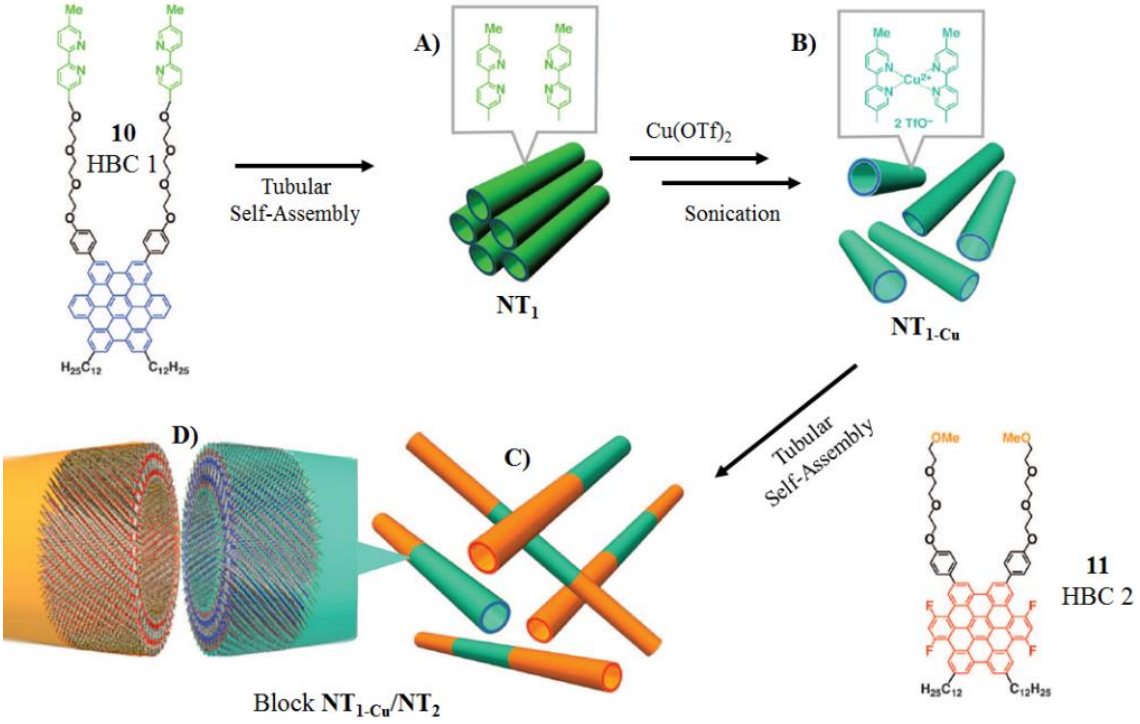

Figure 1.5 A) Schematic illustration of **10** self-assembling into bundled nanotubes NT_1; B) formation of the $NT_{1\text{-}Cu}$ dispersed nanotubes; C) formation of the block $NT_{1\text{-}Cu}/NT_2$ nanotubes and D) cross-section at the supramolecular heterojunction. Images reproduces from ref.[31]

The resulting charged nanotubes $NT_{1\text{-}Cu}$ were treated with **11**, which would stack on the already formed nanotubular scaffolds of $NT_{1\text{-}Cu}$, forming the heterojunction (**Figure *1.5***). This elongation process was observed to be preferential to the formation of nanotube bundles of **11**, which would normally occur in the absence of $NT_{1\text{-}Cu}$. Furthermore, the presence of multi-block nanotubes was not found, hinting to the lack of post-connection of the two different families of nanotubes.

The $NT_{1\text{-}Cu}/NT_2$ was studied through the use of high-resolution microscopy and optical spectroscopy, with the first confirming the (morphological) block nature of the nanotubular aggregates, and the second confirming that these systems behave exactly as a π-n junction, displaying fluorescent properties, not present in the singularly assembled of $NT_{1\text{-}Cu}$ and NT_2, derived from the efficient communication between the segments over the heterojunction interface.[31]

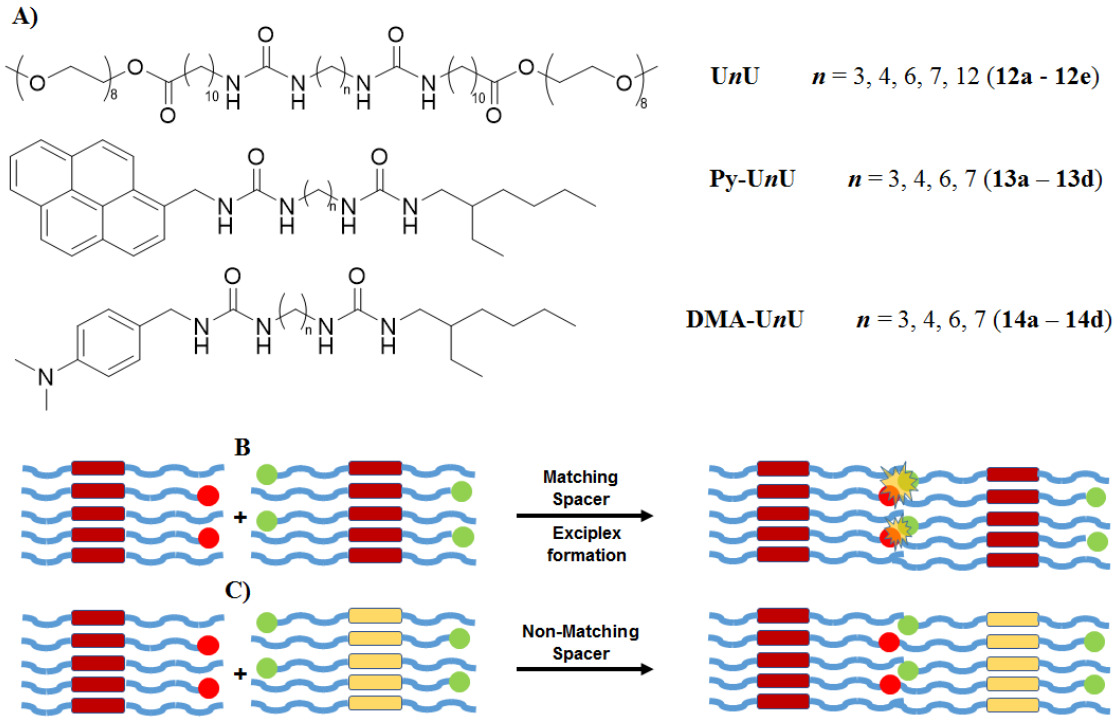

Figure 1.6 A) General chemical structures of compounds **12(a - e)**, **13(a - d)** and **14(a - d)**; B) schematic representation of the formation of the fluorescent exciplex in case of matching spacer (top) and the formation of a non-emissive aggregate in case of non-matching spacer (bottom). Images reproduced from ref.[32]

Following upon the idea of exploiting the high directionality of hydrogen bonds, Sijbesma *et al.* used a bisurea motif in conjunction with covalent oligomers to obtain micellar aggregates with highly hydrophobic compartments.[32] In their work, the use of a series of bisurea bolaamphiphiles (**U*n*U**, **12a-11e**) demonstrated that the micellar aggregates are formed in a very selective way and have a dynamic nature. Adding a small percentage of

two bisurea functionalised with luminescent probes (pyrene, **Py-U4U**, **13b** and dimethylaniline, **DMA-U4U**, **14b**) to different bolaamphiphiles in aqueous solution, they observed that the probes were easily integrated into the micelles. The assembling would lead to luminescent emission only when the main bisurea system has the same length, with a solution of **12b** resulting into an excimer, while **12c** would not (**Figure 1.6**).

Another interesting series of supramolecular polymers based on a bisurea system were prepared and studied by Boué *et al*.[33] In their work, they prepared a series systems, **15(a-d)** with a bisurea core, connected *via* nonpolar alkylene chains (used to drive and stabilise association through hydrophobic effect), to ethylene oxide moieties, which would allow better solubility both in aqueous and organic media (**Figure 1.7**: **A**). The formation of assemblies was studied and observed through Small-Angle Neutron Scattering (SANS) measurements in three reference solvents; water, acetonitrile and toluene, respectively.

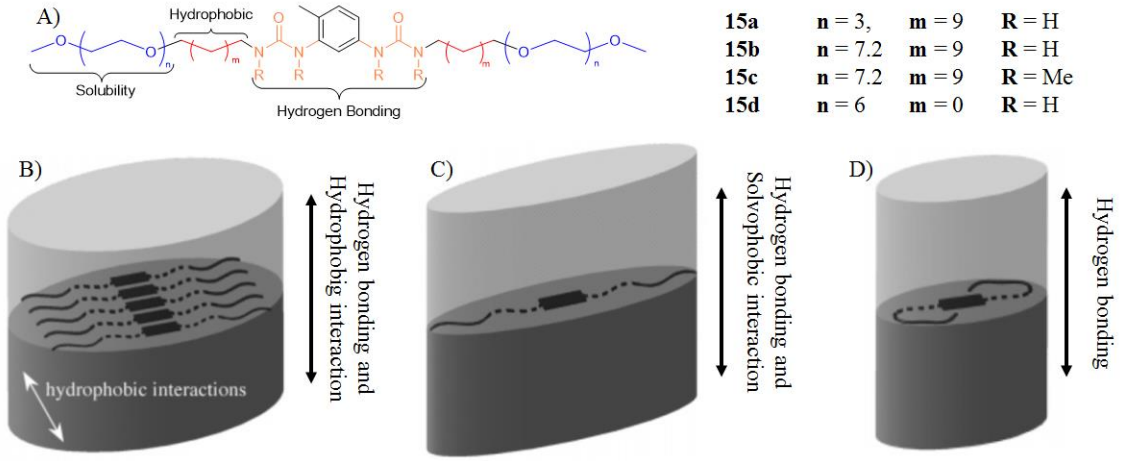

Figure 1.7 A) General structure of compounds **15 (a - d)**; schematic structure for the cross-section of the aggregated compound **15b** in water (B), acetonitrile (C) and toluene (D). Images reproduced from ref.[33]

The results show that in water and dilute acetonitrile solutions; the aggregates assemble into long filaments, with the ones formed in water showing a relatively large cross-section diameter. In contrast, the filaments formed in acetonitrile, were basically shown to be monomolecular. Considering this, the authors speculated that hydrogen bonding is responsible or directing the stacking interactions between the layers, while the cross-section packing interactions are based on a solvophobic effect. This provides a reasonable explanation as to why the system is more strongly packed in water compared to the acetonitrile solution, as the alkylene chains will interact with the organic solvent in a more efficient way compared to that in water. The measurements in toluene show a much shorter length of the filaments, due to the fact that the akylene chains present no solvophobic effect, therefore they behave in a more flexible way. Hence, the authors

assumed that here a different conformation (in this solvent) occurred, which was dictated by the formation of intra-molecular hydrogen bonding between the oxygen atoms of the ethylenoxy moieties and the bisurea cores. In this case, the accurate design of the target molecules allowed for the development of systems that assemble differently as a function of the solvent.

In a series of work starting in the early 2000s, Stupp *et al.* designed the (large) peptide amphiphile **16**, capable of forming an aggregate similar to a collagen derivative,[34] with the goal of obtaining a supramolecular polymer able to mimic biological systems. To achieve such a result, the molecule was designed with a hydrophobic chain, an amino acid sequence and a highly polar unit, with a phosphate group bound to a serine molecule. This design ensured an aggregation driven initially by the hydrophobic interaction between the alkyl chains. The amino acid segment chosen has a tendency to form β-sheets and this would lead the system, together with the polar component, to twist itself into a helical structure. The single conical units then assemble into higher-order cylindrical micelles, with the hydrophobic chains shielded in the inner area and the polar component on the outer surface. The phosphate functionality allows for the mineralisation into a filament of the micellar aggregate by surface diffusion of $CaCl_2$ and Na_2HPO_4.

The resulting system was found to interact with cells and had the advantage, over a covalent collagen-like structure, of being reversible and therefore more able to fit into the cell, assemblying itself *in situ* to accommodate the preferred orientation in the cellular environment.[35] These early studies led to more complex systems that Stupp and co-workers proved to be bioactive *in vivo*, thus paving the way for a possible new class of prosthetic bones and cartilage.[36-37] Furthermore, Stupp *et al.* demonstrated that systems designed, following the same rationale, were able to interact with a linear negatively charged biopolymer, consisting of a macromolecule containing a disaccharide repeat unit of *N*-acetylglucosamine and glucuronic acid.[38-39] Such interaction would result in highly packed fibrous bundles that formed microsacs. This was of high interest, as they managed to prove that such capsules were able to entrap and encompass proteins that had been structurally modified by conjugation of a fluorescent emitting functionality.[38-39]

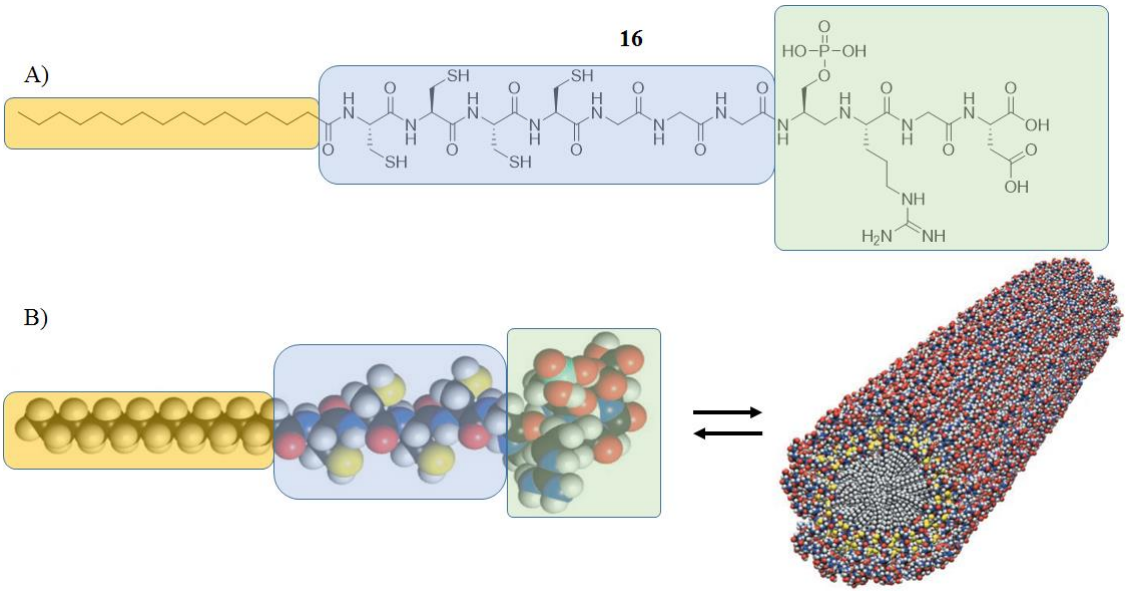

Figure 1.8 A) Schematic representation of **16**. The hydrophobic moiety is highlighted in yellow; the amino acid segment that allows for the secondary interactions is shown in blue and in green: the highly polar head group. B) Molecular model of **15** and self-assembly into cylindrical micelles. Images reproduced from ref.[34]

As outlined above, the systems featured have all consisted of organic molecules that capitalise on the use of weak non-covalent binding interactions. However, the use of metal ions together with hierarchical assembling to obtain complex systems was explored in a recent study by Hua and co-workers.[40] A linear supramolecular polymer was initially obtained through the assembly of two homoditopic monomers, a 2,2′-bipyridine-bridged pillar[5]arene dimer **17**, and a symmetric chain containing two triazole rings and cyano terminations **18 (Figure 1.9: A)**. The aggregate was formed through the host-guest interactions between the arene aromatic pockets and the triazole rings, and it was observed and studied in $CHCl_3$ using NMR techniques.

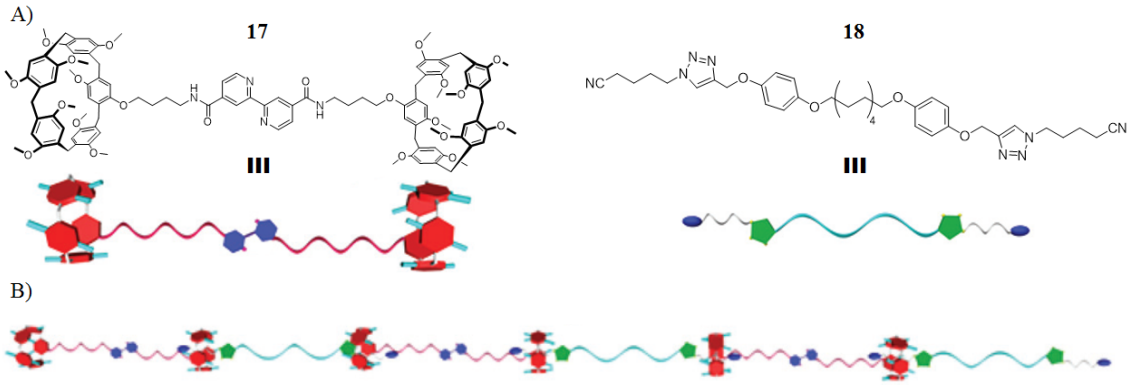

Figure 1.9 A) schematic structures and representation of the pillar[5]arene dimer **17** and symmetric host **18**; B) linear supramolecular polymer formed *via* host-guest interactions. Images reproduced from ref.[40]

The linear polymer was then treated with a Zn(II) salt solution, which led to an exponential increase in the relative viscosity of the system. Electron microscopy investigation confirmed a change in the morphology, with a 3D network formed through

a reticulation induced by the Zn(II) ions (**Figure 1.10**: **A**). The reticulated systems formed stable and thermo-reversible organogels in $CHCl_3$ which were characterised using rheological measurements. It is clear that the use of metal ions has a major impact, or influence, on the formation, stability, morphology, and the properties of the resulting self-assembly. Hence, it is of no surprise that the use of metal ions in the constructions of robust self-assembly structures has become an active area of research. The next sections deals with some examples of such structures.

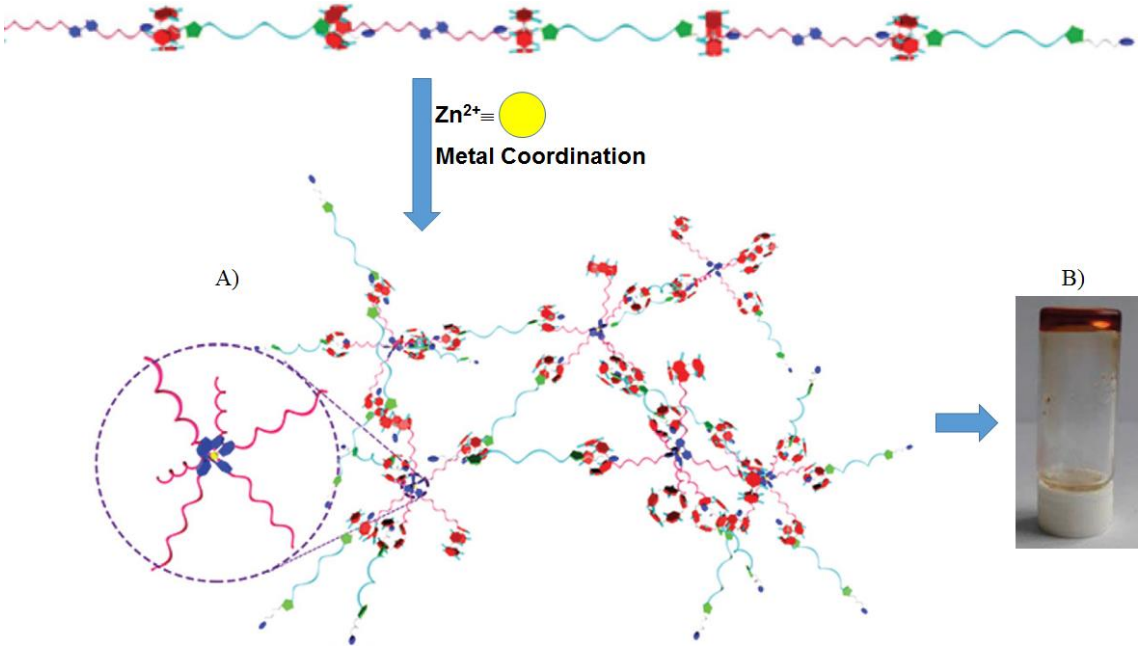

Figure 1.10: A) Schematic representation of the crosslinking between linear chains of **17**-**18** induced by the coordination of Zn^{2+} ions and B) picture of the resulting gel. Images reproduced from ref.[40]

1.2 Metal-organic frameworks (MOFs)

One of the approaches that supramolecular chemistry has been widely exploited is the use of metal ions as template to guide the formation complex mono-, bis and three-dimensional structures. These ordered structures, formed through extended metal-ligand interactions, potentially extending infinitely, are generally referred as coordination polymers, or porous coordination polymers. Metal-organic frameworks, or MOFs,[41] is the term, which is commonly used to refer to microcrystalline, porous materials containing polynuclear clusters, has been extended to include and describe any extended array composed of metal nodes.[41] The materials that arise from MOFs are of particular interest because of their large internal surface area and high porosity. Indeed, such properties have allowed MOFs to find applications in various fields, such as energy storage, chemical purification, heavy metal removal from water, catalysis, as well as biomedical application and sensing.[41-45]

In a recent work, Schmitt and co-workers[46] presented a photoactive MOF with a large tubular aperture. The system used two *d*-metal ions, Cu(II) and Ru(II), in conjunction with a carboxylate derivative of 1*H*-imidazo [4,5-*f*][1,10]-phenanthroline, **19** (**Figure 1.11**). The system was designed in order to possess a main binding unit, the carboxylate, and a secondary binding unity, a polypyridyl phenanthroline group. The phenanthroline moiety bound the Ru(II) ions that act as photosensitizers, allowing for the population of the excited states of the ligand through Metal-to-Ligand Charge Transfer (MLCT). This consequently activated the ligand-centred emission, while the carboxylate group allowed for the binding of the Cu(II) ions.

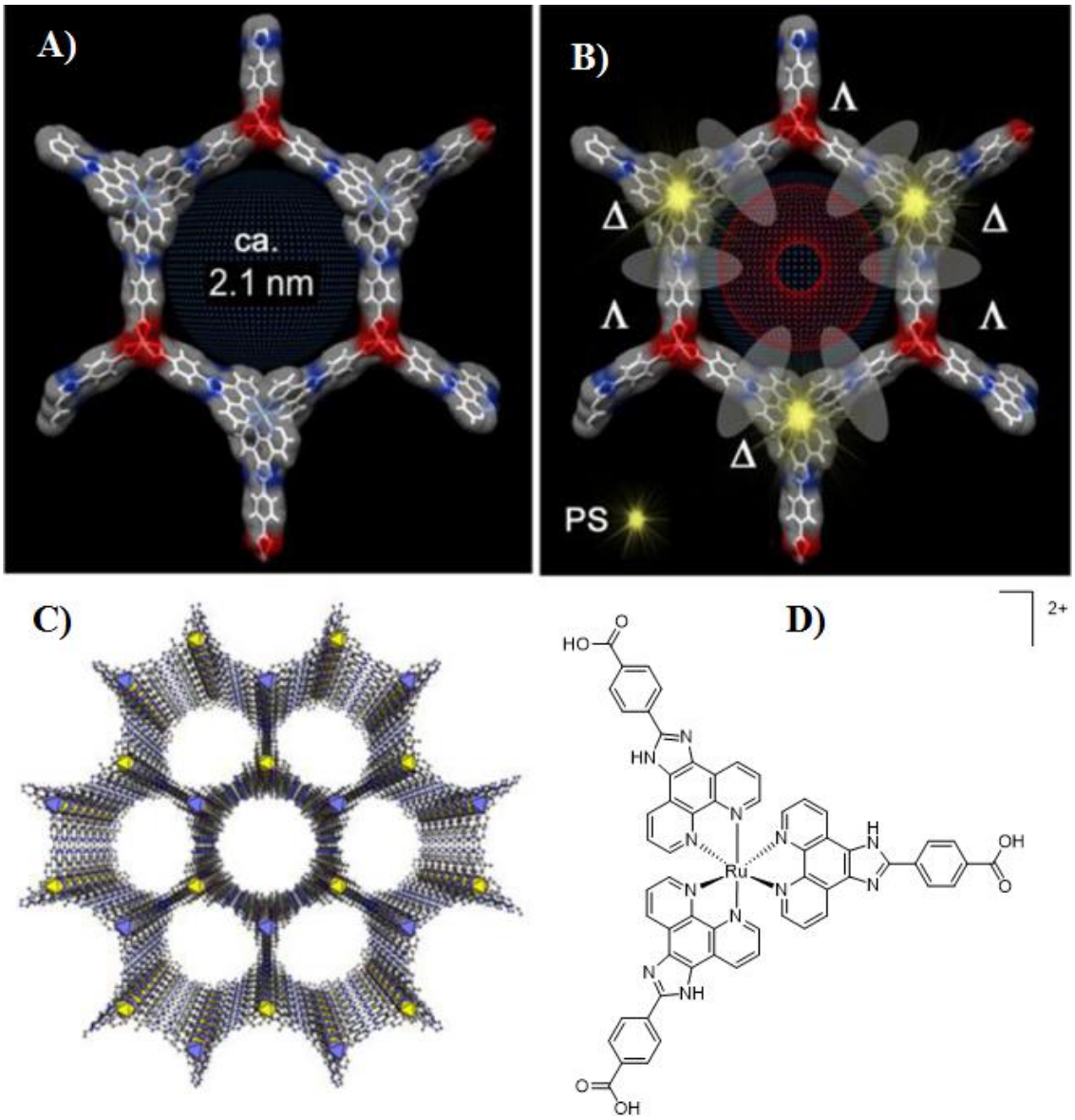

Figure 1.11 A) Crystal structure of Photo-MOF, hexagonal channel along the [001] direction, highlighting the diameter of the channel of ca. 2.1 Å. B) Key attributes of Photo-MOF, including RuII/phenanthroline-based photosensitisers (in yellow); nodes with opposite helicity and imidazole-based binding sites. C) Extended structure of Photo-MOF along the crystallographic c-axis. D) Structure of metallo-ligand $[H_3\mathbf{19}Ru]^{2+}$ that directs the assembly into a hexagonal topology. Image reproduced from ref.[46]

The system, starting from $[H_3\mathbf{19}^{Ru}]^{2+}$ assembles into honeycomb structures with the metal centres of Cu(II)/Ru(II) possessing alternate Δ/Λ helicity while maintaining the spectroscopic properties of the single molecule. The cavities showed a regular diameter of *ca.* 2.1 Å through which the system proved itself able to adsorb reversibly gas such as CO_2 and N_2, with a higher selectivity towards the first, making **19** an interesting material for catalytic purposes upon further development.

1.3 Benzene tricarboxamide (BTA) systems

Amidst the frameworks able to form supramolecular aggregates, benzene-tricarboxamide (BTA) has received significant interest in the last decades. The three amide moieties are connected to the benzene core in alternate positions, 1, 3 and 5, and are able to form networks of intermolecular hydrogen bonds, often consisting of high symmetry, which can translate, under appropriate conditions, to supramolecular polymers that have found several applications.[47]

It is possible to divide BTA molecules into two families according to which atom (-C or -N) of the amide group is connected directly to the benzene core, resulting in C-/N-centred BTA molecules as shown in **Figure 1.12**. The work described in this Thesis focuses on the latter of these molecules, and in particular on the ones bearing the same substituents on all three the amide groups, thus displaying C_3 symmetry.

After a facile synthetic protocol was established by Königstein *et al*,[48] a wide range of BTA scaffolds with different properties have been prepared over the years.[47] This has made them a useful and versatile tool to study how functional groups, solvent and structures will affect the assembly processes in supramolecular aggregates. These studies have become reference points to design and obtain defined and complex nanostructures with a large range of possible applications.[47]

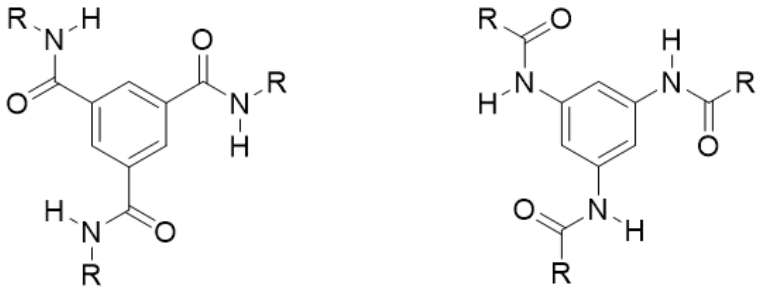

Figure 1.12 General structures for C=O and N centred BTA molecules

Following these studies, it became possible to predict some general properties of the resulting materials, depending on the nature of the R group. Functionalising the amide

moiety with non-polar aromatic groups display a tendency to form organogels,[49] and linear alkyl chain functionalisation leads to liquid crystalline behaviour.[50-52] When the R group is a polar, water soluble group, the resulting BTA molecules have been shown to form hydrogels, often through modulation in either or both pH or ionic strength.[53-55] By employing sterically hindered, or bulky groups, has been shown to induce the formation of aggregates with less compact packing, introducing voids that translate into organic materials with higher degrees of porosity.[56-57] Substituent groups of particular interest include those that can be used to form specific secondary interactions. Metal-binding groups have been shown to form metallogels (as was eluded to above),[58-59] while systems containing structures capable of forming ternary interactions can lead to complex final higher order structures such as microspheres.[60]

Although as a class of compounds, BTAs are known since Curtius reported their synthesis at the beginning of the 20th century,[61] studies that focused on their assembly processes came much later. Banerjee *et al.* reported one of the earliest cases and employed the use of simple chains with a carboxylic group.[62] In their work, the use of an enantiomeric pair (D- and L-valine) bound to the BTA core showed the formation of fibrous aggregates with higher order structures. In particular, the two different enantiomers led to the formation of two chiral helical secondary structures; the resulting handedness of which depends on the enantiomer bound to the BTA core, showing that the point chirality can be transferred to the bulk (supramolecular) material. These systems (**20 *R/S***) were of particular interest due to the packing arrangement of the resulting helices, which were found to pack into a hexagonal cell observed using single crystal X-ray diffraction (XRD). This particular arrangement then led to a quaternary structure, observed by Transmission Electron Microscopy (TEM) imaging, made up of a triple helix of such ternary hexagonal tertiary structures. These higher order aggregates are formed not only through the hydrogen bonding of the amide groups, but also through different non-covalent interactions such as π-π stacking between the aromatic cores.[62]

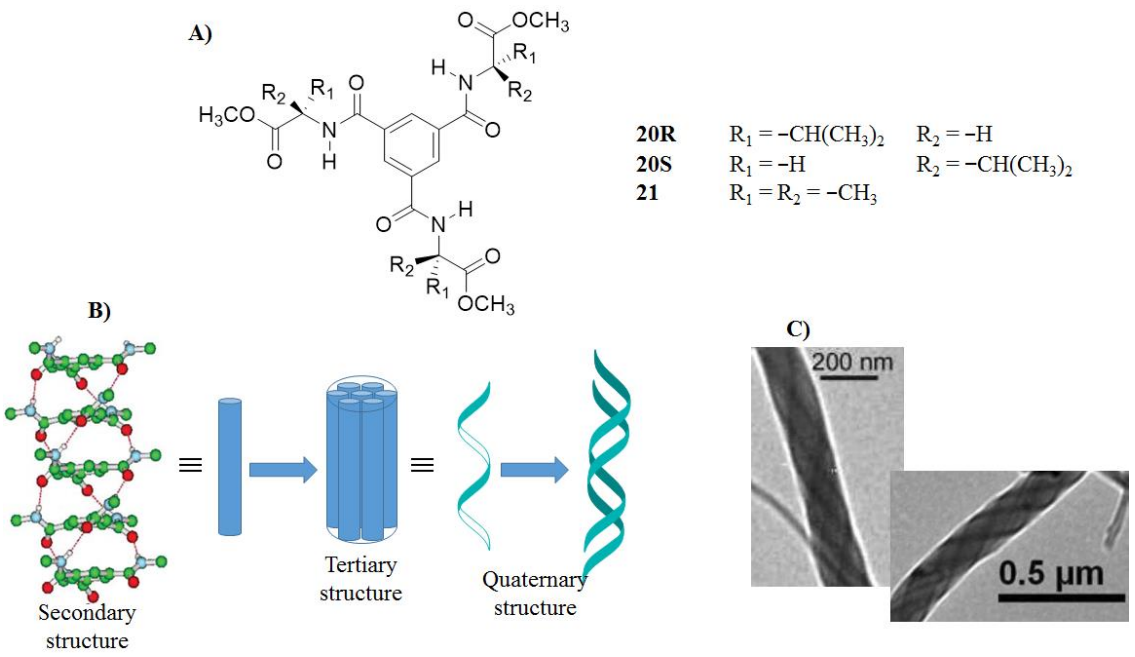

Figure 1.13 A) Molecular structures of compounds **20 R/S** and **21**. B) Schematic representation of the aggregations into fibres. C) TEM images from ref.[62]

A large contribution to the BTA material research has been provided by Meijer and co-workers. In one of their earliest reports,[63] they investigated the effect induced on the aggregation when the alkyl chain bound to the BTA core, lacked or contained a chiral center, in a similar manner to that described above They found that the resulting aggregates showed a remarkable "Cotton effect" when a chiral centre was present within the alkyl chain of the structure, while no such phenomena in the case of achiral group was observed, indicating a preferential aggregation into one helical structure (**Figure 1.14**), again, being dictated by a point chirality on the three arms.

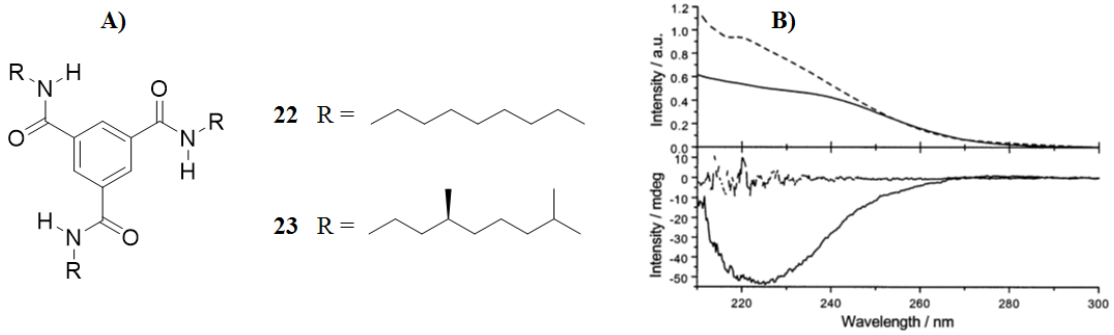

Figure 1.14 A) Structures of compounds **20** and **21**. B) Absorption (top) and CD (bottom) spectra for **20** (dotted line) and **21** (solid line). Images reproduced from ref.[63]

This work was expanded on[64-65] to show that the chirality of the centre in the side chain would direct the aggregation towards one helical orientation preferentially. Furthermore, subsequent work,[66] showed that the use of mixtures of chiral and achiral derivatives would lead to a chiral aggregate; this is due to the so-called 'sergeants-and-soldiers'

principle, where a much smaller quantity of the chiral BTA (in this case, down to 4% in concentration) directed the self-assembly process towards the formation of a chiral aggregate. The reversibility of all these supramolecular processes was also proved in the studies, as the use of solvents that would compete with the self-association of BTAs (*i.e.* in the formation of hydrogen bonds) such as acetonitrile, induced a depolymerisation, with the system returning from the 'gel state' to the 'sol state'.

This early work showed how these moieties can significantly affect the assembly processes of BTA structures, and therefore, why these systems are such a versatile tool in the study of assembly processes, at the same time as they can lead to the formation of unexpected products, but that area has been investigated by the Gunnlagusson group over the last few years and will be discussed in some details later on in this chapter.[47] A breakthrough was made in this field of research when amino acids were studied in conjuction with BTA molecules. Their well known chemistry, variety and large availability as enantiomers all aided in the understanding of the effect of the introduction of a chiral centre on the aggregation processes of BTAs.

In a following study by Palmans and co-workers,[67] the effect of the chirality on the aggregation in conjunction with a sterically hindered system was examined. This was achieved by designing and comparing the behaviours of BTAs with a C_3 symmetry to asymmetric ones. In their study, two families of enantiomeric couples were synthesized. Long alkyl chains were used in conjunction with phenylalanine (Phe) to examine the effect of chirality and steric encumbrance on the aggregation.

Compounds **24R** and **24S** were prepared by functionalising one of the arms of the BTA with the Phe spacer, while compounds **25R** and **25S** were prepared with all of the arms containing it. In both cases, CD spectra highlighted a chiral behaviour of the helical aggregates, but most importantly that the two systems undergo aggregation *via* different mechanisms: in methylcyclohexane (MCH) **24** showed a positive (for **24S**) and negative (for **24R**) CD effect between 205 and 275 nm, indicating the formation of a chiral aggregate. Compound **25** showed mirrored CD spectra typical of entantiomeric systems. However, in this case the intensity was higher (with a $\Delta\varepsilon$ of 76 L $mol^{-1}cm^{-1}$ versus 30 L $mol^{-1}cm^{-1}$ for **24**) in the range 200-270 nm. To gain a deeper understanding of these aggregation processes, the systems were investigated spectroscopically at variable (90 - 20 °C) temperature. In these conditions, a linear dependence in CD intensity variation was observed for **25**, paired with minor changes in the absorption spectra.

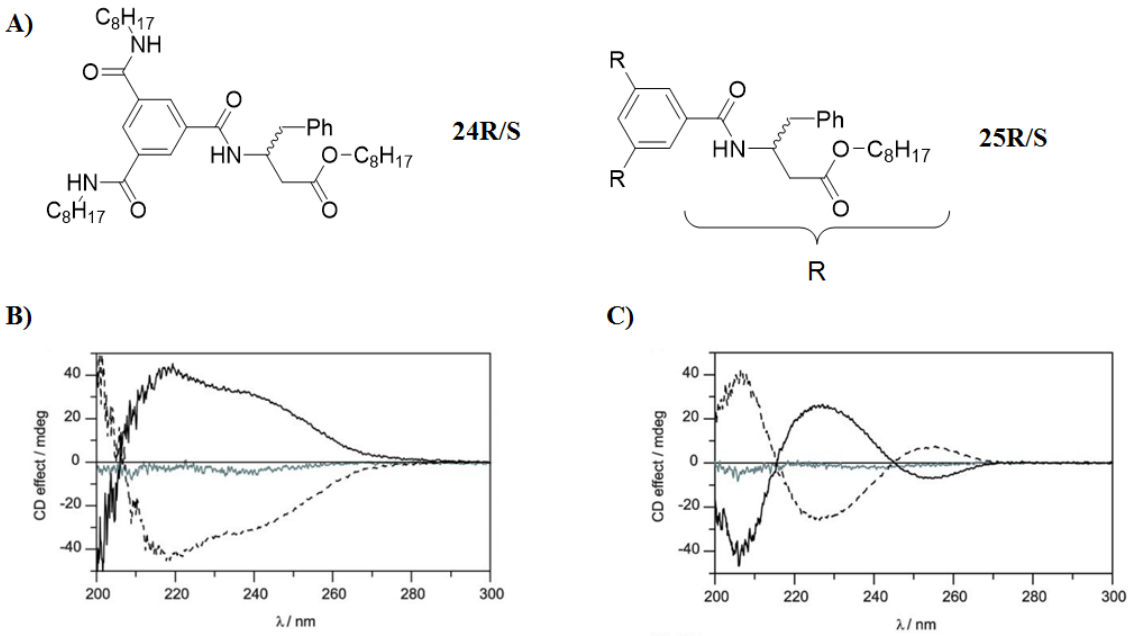

Figure 1.15 A) Chemical structures of asymmetrical and symmetrical BTA molecules with chiral side chains. B) CD spectra of **24R** (dashed black line) and **24S** (solid black line). C) CD spectra of **25R** (dashed black line) and **25S** (solid black line). Images reproduced from ref.[67]

In contrast, the signal from **24** showed a sigmoidal behaviour both in the CD and in the UV-Vis absorption spectrum. These results proved that the presence of a single sterically hindered group affects the aggregational behaviour of **24**, that switches from the cooperative procedure previously observed for linear chains[68] to an isodesmic mechanism of aggregation. Furthermore, the spectra of **25** suggests that in this case, the aggregation is ill-defined and shows no evidence

Following this, Mejer, Palmans *et al.*[69] attempted to translate their previous studies in aqueous environment. To do so, they designed and studied the properties of BTAs functionalised with a glycol chain, both in absence and presence of chiral centres. These systems were found to be soluble in water at higher temperature (**26**, achiral) or *via* methanol injection (**27**, chiral). At room temperature, the systems were described as being highly viscous solutions, which is typical for the formation of large aggregates, which were then studied using transmission electron microscopy at cryoscopic temperatures (by using cryo-TEM). of cooperative behaviour.

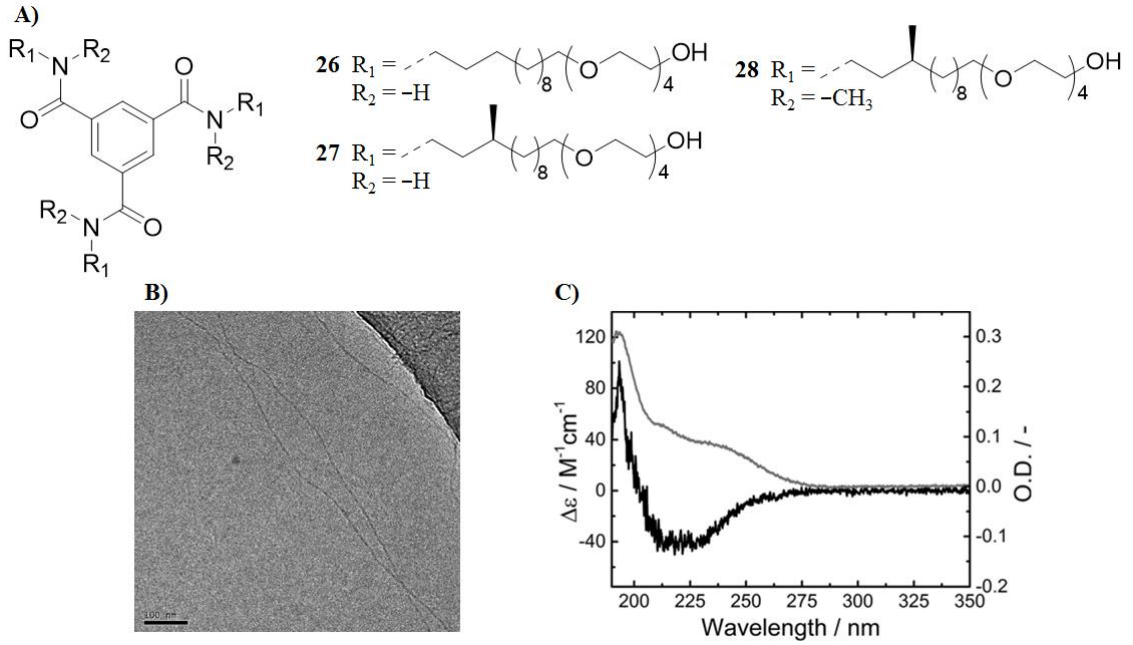

Figure 1.16 A) Structures of compounds **26**, **27** and **28**. B) Cryo TEM showing the formation of aggregates of **26** in water. C) CD (black) and UV-vis absorption (grey) spectra of **27**. Images reproduced from ref.[69]

In both cases, fibrous aggregates with high aspect ratios were observed. This result was unusual when compared to other BTA-based hydrogelators previously reported,[54, 70] where the aggregates were thicker fibrils. Of even greater interest was the difference in the nature of the two aggregates, as while the two fibers looked initially analogous, with a cross-section diameter around 5 nm, then at higher resolution it was possible to discern that the diameter for **26** was slightly larger, and a subtle and periodic variation in the contrast and diameter was observed. This is a behaviour typical of systems that form helical bundles or ribbons, which is not observed for **27**. Both the use of UV-Vis absorption and CD spectroscopy confirmed that **27** formed helical aggregates similar to those formed in organic solutions. However, it was not possible to identify the exact type of packing that aggregates of **26** formed; showing once more that the presence of a single enantiogenic methyl group deeply affects the aggregation process. In the same study, the amidic nitrogen atom was methylated (**28**), to observe the differences that such a change would induce. The lack of the NH group from the amidic core prevented the system from aggregating, confirming that the process is driven by the formation of H-bonds.

Haldar *et al.*[71] investigated the effects of the interactions between side chains using two BTAs functionalised with a β-alanine (**29**) and a ɣ-aminobutyric acid (**30**), both containing a chiral centre, a carboxylic group and differing only by a methylene group. The experiments showed that in aromatic solvents, like toluene and xylene, **30** self-assembles yielding thermoreversible and opaque organogels, while compound **29** did not

show any significant assembling property. An explanation to these behaviours was found through electron microscopy and crystallographic analysis. After drop casting solutions of both **29** and **30** in 1,2-dichlorobenzene, it was possible to observe that while the shorter chain derivative **29** displays a more prominent rigidity, **30** displays an entangled network that extends from the core of the aggregate analogously to what happens to it in its xerogel form. Through crystallography, it was noted that while both the derivatives form columnar aggregates through the triple H-bonding interactions, the longer chain and higher flexibility of **30** led to secondary interactions, hydrophobic in nature, that support the formation of supramolecular networks, while **29** self assembled into bundle-like structures.

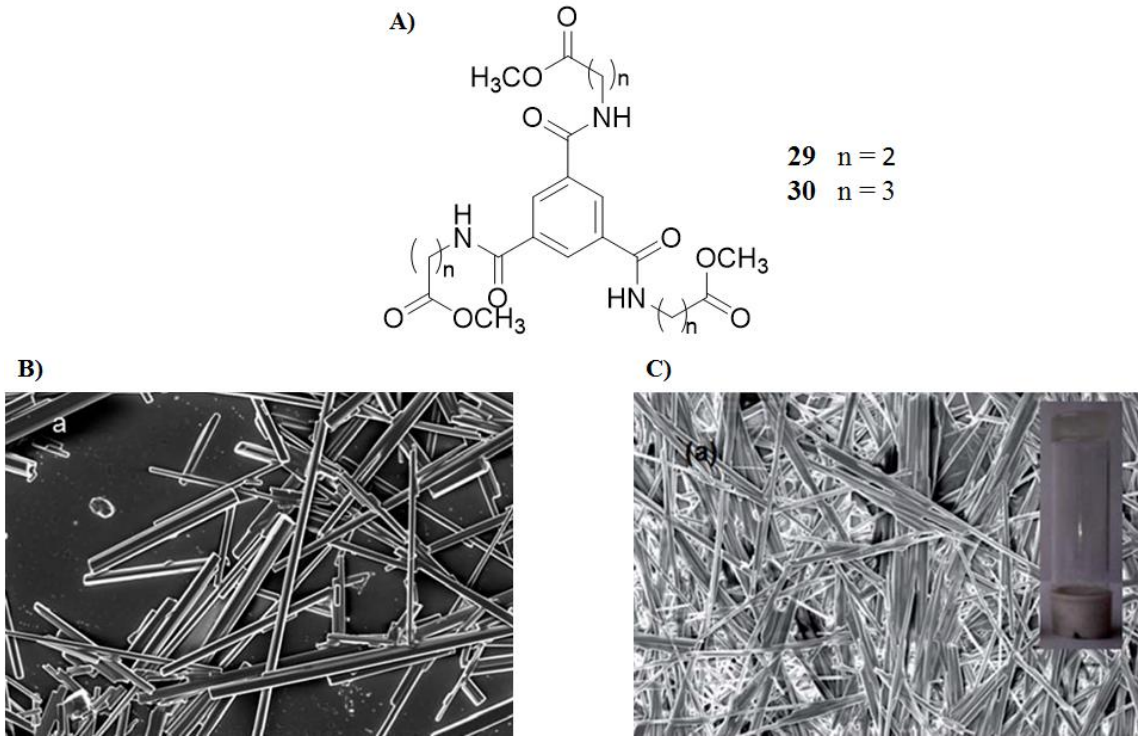

Figure 1.17 Structures of BTA with alkyl chains **29** and **30**. B) SEM of crystalline rods from a drop casted solution of **29** in 1,2-dicholorobenzene. C) SEM of the xerogel of **30** from toluene. Images reproduced from ref.[71]

Kumar *et al*,[72] in their 2004 work, used pyridil amides with BTA. In their work, the use of two different isomers bound to the BTA core, **31** and **32** enabled them to observe, for the first time, the presence of N-H···N hydrogen bond networks, which lead to the formation of bidimensional networks. In such networks, the presence of a strongly hydrophobic cavity was observed in the crystal structures for the two BTA derivatives, obtained solving X-ray diffraction data. The balance between the hydrophobicity of the system and the hydrogen interactions, allowed them to assume that both **31** and **32** could behave as aggregators in appropriate conditions. Such conditions were found and met

using solvent mixtures of water and several polar organic solvents such as DMSO, DMF, MeOH and EtOH.

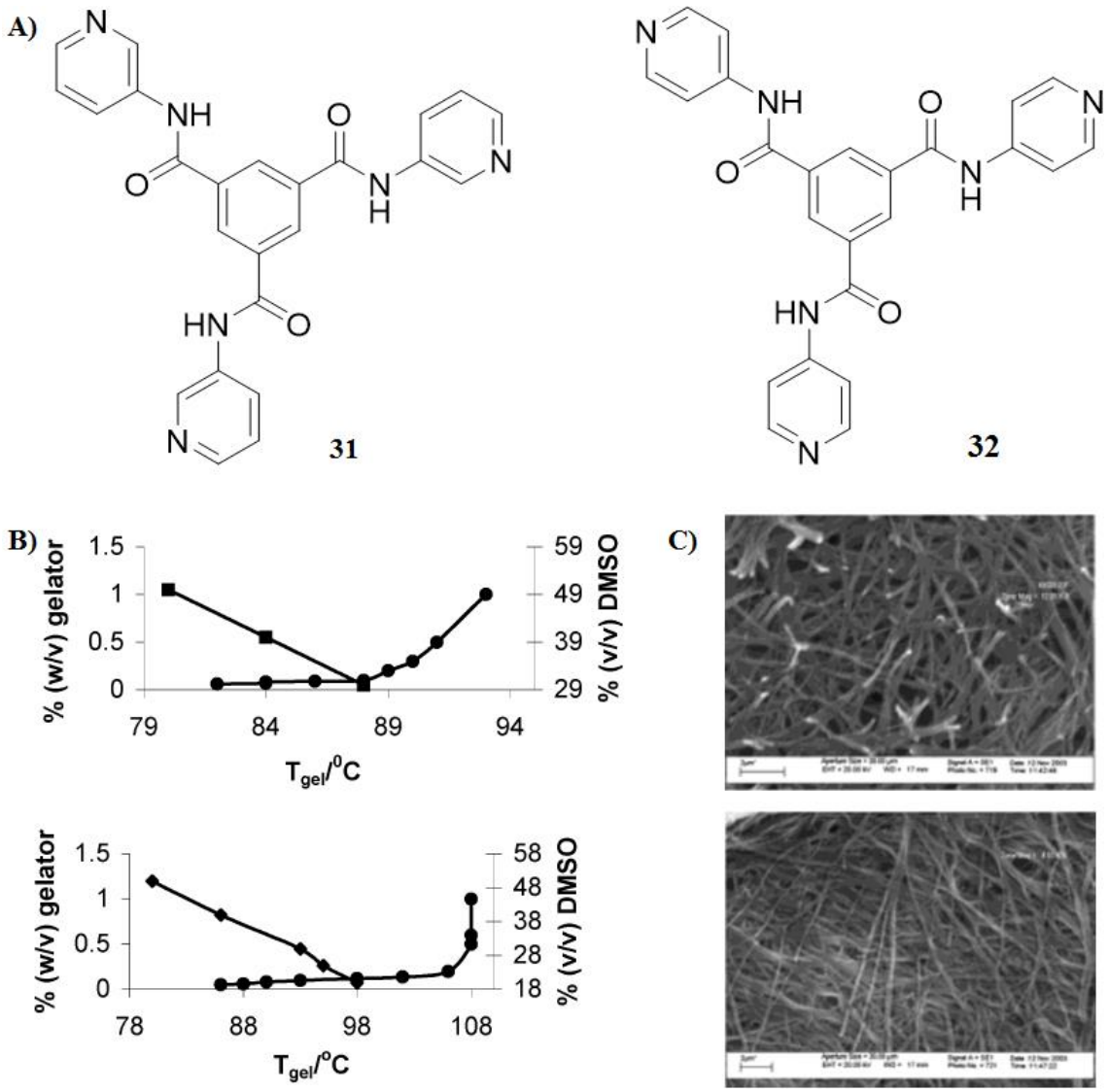

Figure 1.18 A) Structure for LMWG **31** and **32**, B) T_{gel} plots in different conditions for gels of **31** (top) and **32** (bottom); ♦ T_{gel} at 0.1 wt % varying the DMSO fraction, • T_{gel} at 7:3 DMSO: H_2O varying the wt %. C) SEM images for gels of **31** (top) and **32** (bottom). Image reproduced from ref.[72]

The gels were studied both thermally and morphologically; the SEM imaging showing the formation of networks of fibres, with cross section diameters of *ca.* 160 - 400 nm for **31**, and 110 - 280 nm for **32**, that could trap the solvents and therefore lead to the gelation. The thermal stability of the H_2O/DMSO gels was studied as a function of both the quantity of the gelators (normally reported in mol %) as well as the fraction of organic solvent used. It was found that for both systems, that a sharp increase in the T_{gel} could be observed upon increasing the quantity of the gelator, indicating that a greater amount of interactions would stabilize the gels further. On the other hand, fixing the amount of gelator and increasing the fraction of DSMO, resulted in a decrease in the T_{gel}. This was to be

expected, as DMSO, was considered by the authors to be a very good solvent for both **31** and **32**, as well as a competitive solvent for hydrogen bonds, would break down the intermolecular interactions.

An interesting behaviour for a BTA system was observed by Wang, Liu and co-workers.[73] In their work, they observed that in a 60% DMF/H_2O mixture, a BTA functionalised with ethyl cinnamate, **33** (BTAC, **Figure 1.19 A**) formed gels with a concentration of 1.5%, due to the formation of twisted aggregates *via* hydrogen bond and π-π interactions. Such aggregates were expected to form following a stochastic distribution, but instead a non-null Cotton effect was observed, as both left and right (*M* and *P* respectively) handed twisted aggregates formed, but in an uneven amount. This is due to the formation, during the early gelation phases, of preorganised columnar aggregates. This could be considered the slow step of the aggregation process and the handedness of such 'chiral seeds' will lead to a predominant *M* or *P* conformation.

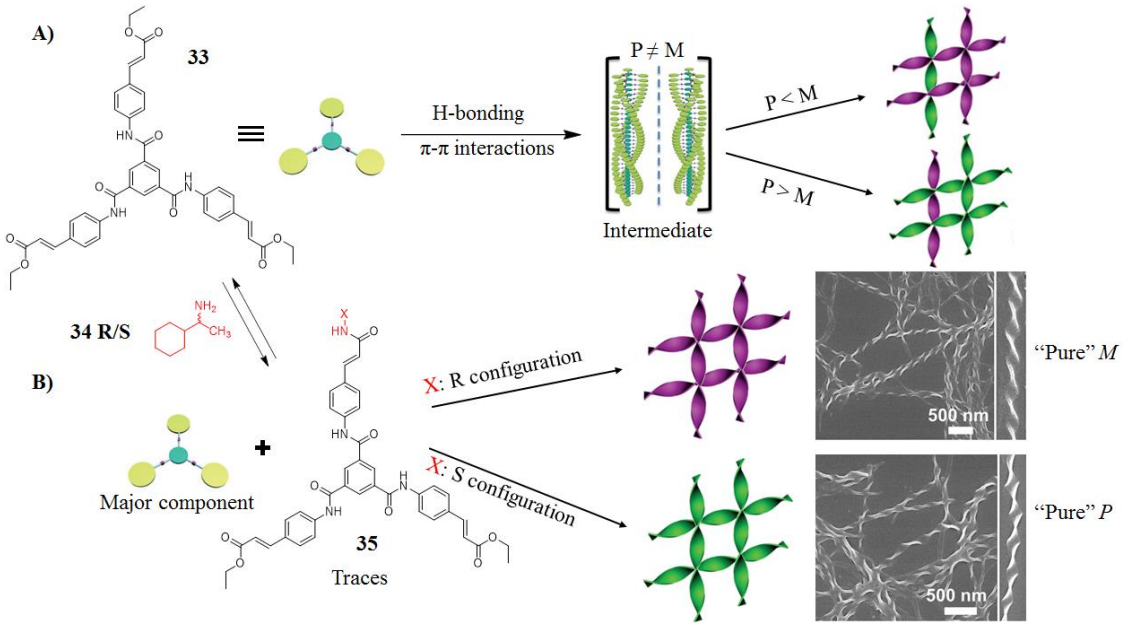

Figure 1.19 A) Structure of **33** and stochastic assembly into non-chiral aggregates, with *P* and *M* twists. B) traces of chiral **35R/S** formed upon reaction of **33** with **34R/S** lead to the formation of pure *M* or pure *P* aggregates and consequently to chiral organogels. Images reproduced from ref.[73]

Of particular interest were the results obtained by the use of a chiral dopant, 1-cyclohexyl ethylamine **34** (R/S). The dopant was added to the solution of **33** before gelation in a 1:3 molar ratio and it was possible to observe that the only one type of twist was observed (*P* twists for the **34R** and *M* twists for **34S**). This demonstrated how the presence of the dopant stabilises only one type of aggregation; furthermore, after the removal of **34**, the system observed the same aggregation pattern and retained the previous configuration, as a small amount of it had reacted with **33** through amide-ester exchange. These traces of

35 were not detectable by NMR spectroscopy, but still directed the aggregation, leading it to retain the chirality.

Another example of system containing an increased π surface area was reported by George *et al.*[74] In their study, they designed and characterised a BTA functionalised with a highly conjugated aromatic system, a naphtalenediimide (NDI), **33**.

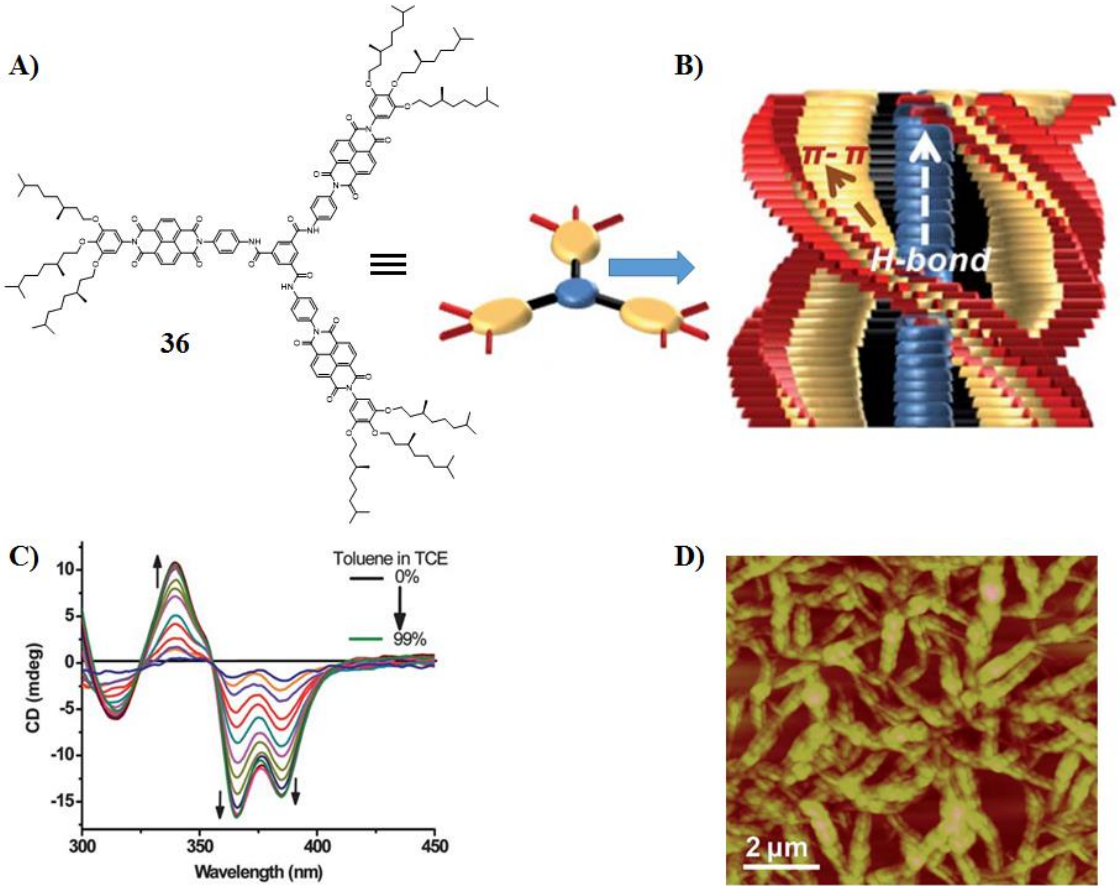

Figure 1.20 A) Schematic structure and B) aggregation model for **36**. C) CD spectra of **36** in TCE and upon addition of toluene as anti-solvent. D) AFM heigh image of the left-handed twisted coils formed in the TCE/Toluene mixture. Images reproduced from ref.[74]

The NDI was connected to the BTA *via* an aromatic spacer and possessed a gallate extremity bearing three chains containing a chiral centre, in order to direct the chiral aggregation process. Compound **36** was found to form organogels in methylcyclohexane (MCH) and toluene, while no macroscopic signs of aggregation were found in more polar solvents such as tetrahydrofuran (THF) or 1,1,2,2-tetrachloroethane (TCE). **36** was shown to exist in a completely dissolved state in pure TCE, as evident from the characteristic NDI absorption features, and the absence of a circular dichroism (CD) signal (**Figure 1.20**). Upon increasing the percentages of toluene in the toluene–TCE mixtures, the absorption spectra showed a gradual decrease in the maxima of NDI at 358 and 378 nm, with a concomitant increase in the blue-shifted absorption at 344 nm, characteristic of the

H-aggregates of NDI,[75] was observed, which confirmed the formation of the aggregates. By plotting the CD intensity at 365 nm as a function of the toluene content (of the solution mixture), it is possible to observed sigmoidal behaviour, indicating the isodesmic nature of the process, rather than a cooperative one. The quantum mechanical calculation showed that in the optimal disposition for the aggregation, the hydrogen bonds from the core were not oriented in the same direction. This was speculated by the authors to be related to the aromatic spacer that determines the configuration of the amide bonds. Furthermore, X-ray diffraction experiments show that the aggregation was strongly directed by π-π stacking interactions and the hydrophobic interactions of the peripheral chains.

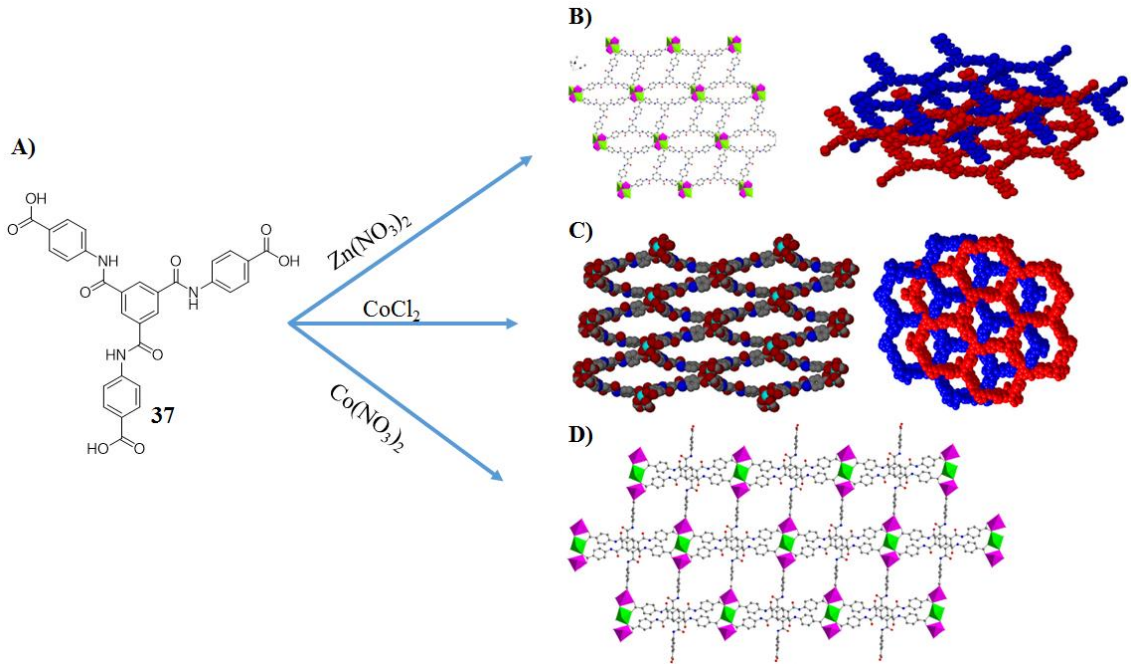

Figure 1.21 A) Chemical structure of **37.** B) layered (left) and double interpenetrated framework formed by the Zn(II) complex. C) three-dimensional model and double interpenetrated network formed by **37** with $CoCl_2$. D) polyhedral representation of the network formed upon reaction of **37** with $Co(NO_3)_2$. Images reproduced from ref.[76]

In a study presented by Zhao *et al.* on compound **37** (**Figure 1.21**, **A**), the intermolecular H-bonding interactions drove the aggregation process leading to coordination polymers with different structures upon solvothermal reaction with Zn(II), Co(II) and Cd(II) (**Figure 1.21 B**, **C** and **D** respectively).[76] The systems all formed a core-rosette, but reactions with the various salts differentiated the final structures. As an example, the addition of zinc nitrate formed a twofold interpenetrating architecture, while the use of cobalt chloride formed a twofold interpenetrating three-dimensional architecture. Cobalt nitrate and cadmium nitrate formed grid layered architecture with interplanar π-π stacking

interaction. The work demonstrated the potential ability to form a large variety of structures with the use of coordination chemistry.

Lloyd, Tan and co-workers designed and studied the properties of a family of BTAs functionalised with aromatic carboxylic acids, including **37**.[54] The eight derivatives were all found to be insoluble in deionised water, but upon addition of three equivalents of NaOH they became solubilised, with the exception of **43**, which was found to be insoluble even in highly basic pH conditions. Upon protonation with diluted HCl, **44** formed an insoluble precipitate, while compounds **37**-**41** formed hydrogels. Solutions of deprotonated **42** showed no changes upon protonation; over a few weeks, crystallization of trimesic acid was observed, pertaining to the hydrolysis of the amide bond. Gels obtained from **36**-**40** were found to be dishomogeneous, which was considered to be due to a kinetic factor. The gelators were then protonated using glucono-δ-lactone (GδL), yielding homogenous hydrogels. Analysis of rheological measurements determined the Avrami constants for these systems, which suggests that the gelation mechanism for compounds **37**-**39** and **41** are based on homogeneous spontaneous nucleation, interfacial control, and one-dimensional growth. On the other hand, **40** show a gelation mechanism based on heterogeneous nucleation, interfacial control, and one-dimensional growth.

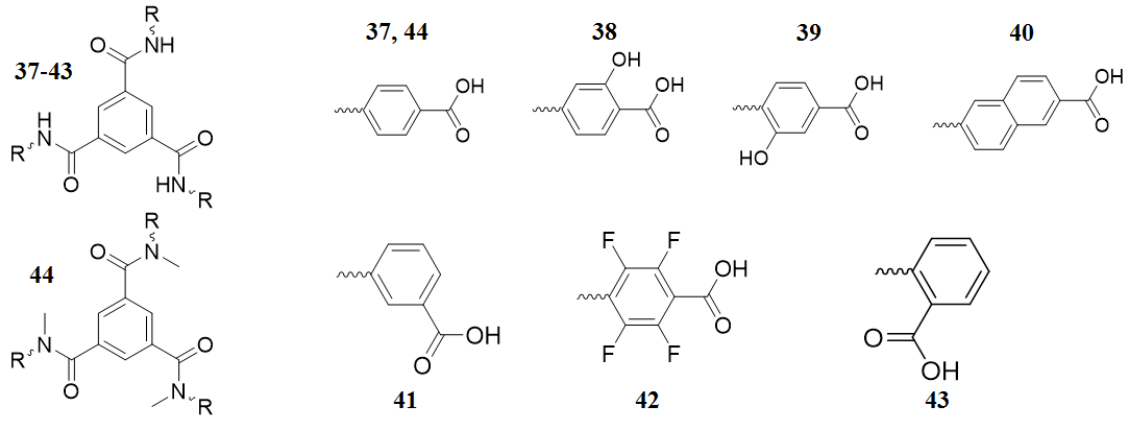

Figure 1.22 Structures of BTA tricarboxylic derivatives **37 - 44**. Reproduced from ref.[54]

Electronic microscopy images show the fibrous nature of the systems and while electron diffraction confirms that such fibres are amorphous, they allowed to verify that the d distance for **37 - 41**, which was found compatible with the average distance for H-bonding, indicating that this interaction, integrated with the π-π stacking, are happening among the gelators units inside the fibres.

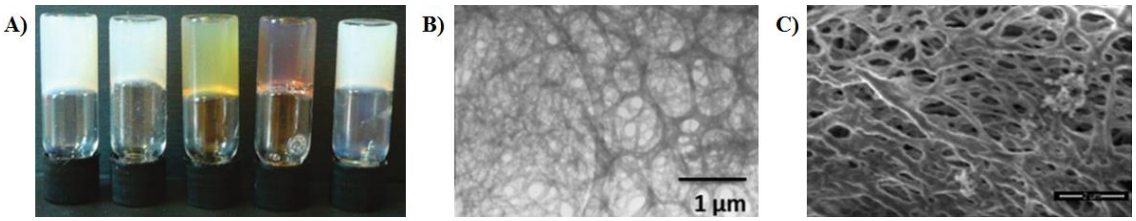

Figure 1.23 A) hydrogels of compounds **37 - 41**. B) TEM and C) Cryo-SEM of the hydrogel formed by **36** that show the fibrous nature of the aggregate. Images reproduced from ref.[54]

In a recent work, Webber and co-workers expanded on the use of carboxylic moieties to trigger the gelation process.[55] In their work, they designed **45** (**Figure 1.24 A**), a derivative of **37**, functionalised with glutammic acid. This allowed for the evaluation of the effect of the addition of a chiral centre and two carboxyl groups on the gelation in a buffered environment. Compound **45** was present in a transparent sol state in aqueous environment at neutral pH; upon alteration of pH and ionic forces, the formation of supramolecular aggregates was observed. **45** was dissolved in tris(hydroxymethyl)aminomethane (Tris) buffer in the presence of $CaCO_3$ and NaCl, in its fully deprotonated form; the acidification step was performed with a strong, fast reacting acid such as HCl and with a slower-reacting acid, GδL. Upon maturation of the samples to their observable steady state, SEM was used to examine the bulk material for evidence supporting the presumed pathway dependence, visible on the macroscopic scale. Measured diameters in the GδL-treated sample are comparable to the dimensions reported in previous works.[77]

The electron microscopy (TEM and SEM) imaging on the bulk of the aged hydrogels (**Figure 1.24 C**) showed the formation of hierarchical superstructures that were reminiscent of some of the wide, smooth structures formed under the HCl stimulus, differing in the size, with the first reaching up to 1 µm in diameter against the typical 30 nm observed in the latter. Chiroptical measurements show that the presence of the chiral centre on the side chain induces chirality on the hydrogel formed through GδL protonation, while no Cotton signal was observed for the aggregate formed by HCl.

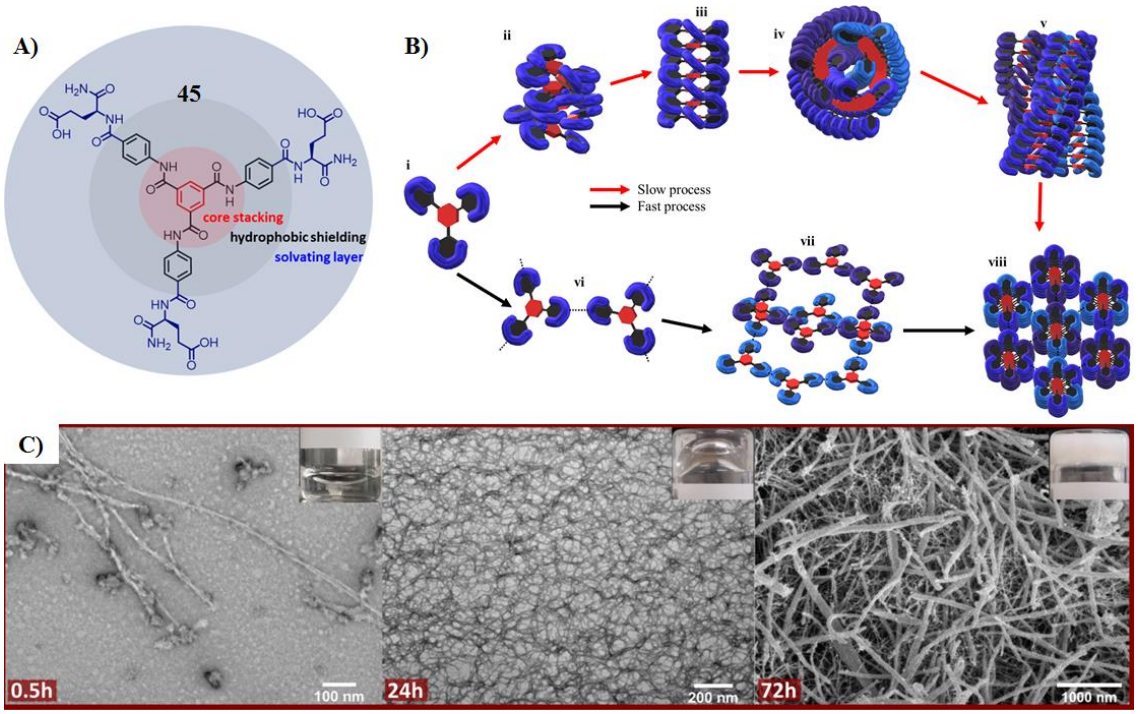

Figure 1.24 A) Structure of **45**. B) Assembly processes of **45** upon protonation with HCl (bottom, "fast" route) or GδL (top, "slow" route): **i. 45**, **ii.** disordered nuclei, **iii.** chiral nuclei, **iv.** helical fibril (top view), **v.** helical fibril (side view), **vi.** oligomers, **vii.** honeycomb lattice, **viii** crystalline fibers. C) TEM (left, middle) and SEM (right) images of the **45** hydrogel obtained using the "slow" route. Images reproduced from ref.[55]

Considering all of the results discussed above, allowed for speculation on the aggregation mechanisms involved in the two processes. Under fast kinetic condition, it was proposed that protonated monomers undergo a lateral association through H-bonding, together with the axial stacking of monomers through core amide H-bonds. This results in the formation of short oligomers that position themselves into a honeycomb lattice arrangement and ultimately to crystalline fibers with hexagonal columnar packing with high aspect ratios, on the order of 10 molecules wide. The slow GδL route instead, proceeds through a nucleation-elongation pathway where the stacking is the favoured process after the formation of aggregation seeds; the single helices will then form higher order triple or multihelical bundles. Eventually the slow-catalysed pathway manifests the same hexagonal columnar packing structure as is observed in the fast pathway, albeit with width dimensions more than an order of magnitude greater, much higher crystallinity and regularity.

1.4 Lanthanide Metal ions

As previously mentioned, the coordination of metals in supramolecular chemistry has been largely explored by many research groups.[41] In the recent years, particular attention

has been given to lanthanide ions due to their unique physical and coordination properties,[78-79] leading to the design of novel structures. These novel structures allowed to obtain materials functional for specific applications.[80-81] The properties of the lanthanides have been explored unveiling their abilities to interact with organic ligands to form hybrid materials such as gels with luminescent properties,[82] organic light emitting diodes (OLEDs),[83] sensors[84-85] and even MRI contrast agents, to name just a few.[86-87]

1.4.1 Properties

The lanthanides comprise elements of the first row of the f-block in the periodic table, from the first, lanthanum (^{57}La, from which they bear their name) through to lutetium (^{71}Lu). Although in the recent years systems containing stable lanthanides in different valence states have been explored,[88] lanthanides are most stable in the trivalent state. Lanthanides gradually fill the 4*f* orbitals, shielded by 5*s* and 5*p* subshells, with a general electronic configuration of: [Xe]4f^{n} (n = 0 - 14). A gradual decrease of the ionic radii is observed with increasing atomic number, a characteristic referred to as *lanthanide contraction*.[8, 89]

The lanthanides are usually referred to as strong Lewis acids (due to their +3 oxidation state), as they possess high ionisation potentials and high charge densities that enables them to interact with a wide variety of ligands containing atoms with Lewis basic behaviours, such as oxygen, nitrogen and fluorine. The lanthanides usually have high coordination requirements, reaching from 9 in solution to 12, and that the formation of stable complexes is usually achieved through the use of several chelating ligands, or the use of macrocyles with high number of coordination sites (such as cyclen, which will be feature later in this Thesis).[90-91] These atomic and ionic characteristics translate into very distinctive photophysical properties that will be discussed in the following sections.

1.4.2 Photophysical properties of the lanthanides

As previously mentioned, lanthanides possess 4*f* valence electrons that are shielded by their filled 5s^2 and 5p^2 orbitals, which translates into minor changes to the electronic configuration through the interaction with ligands.[92] These shielded electrons have the ability to undergo *f-f* transitions, which is observed as sharp singlet-like signals in their emission spectra, characteristic of each specific Ln ion, covering the spectrum from the ultraviolet-visible (UV-vis) to the near-infrared (NIR) regions.[93-94] The ability to undergo such transitions renders all of the ions luminescent, which is either fluorescent or phosphorescence in nature,[89] with the obvious exceptions of La(III) (empty *f* shell) and

Lu(III) (full *f* shell). The colour of the observed emission is characteristic of the single ion, with Eu(III) being red and Tb(III) being green, for example.

Although both fluorescence and phosphorescence are radiative relaxation processes, they are fundamentally quite different. In the case of fluorescence, the emission of a photon is due to the radiative decay of the $S_1 \rightarrow S_0$ transition; in this case, there is no variation of the spin multiplicity ($\Delta S = 0$), making it a spin-allowed transition and therefore, the process is quite fast, with the decay happening in a timeframe of 10^{-12} to 10^{-6} s. On the other hand, phosphorescence is a process involving a variation of the spin multiplicity ($\Delta S \neq 0$), making this kind of transition spin-forbidden; the $T_1 \rightarrow S_0$ transitions thus require more time, occurring between 10^{-6} s and 1 s.[89] The characteristic *f-f* transitions of Ln(III) ions are also Laporte forbidden, as they do not involve a change in the symmetry for the system; this puts their lifetimes closer to the latter time frame, with the longest emission lifetimes being in the range of milliseconds for Eu(III) and Tb(III) and the shortest being in the microsecond range for Yb(III) and Nd(III). Such long lifetimes can be exploited for the design of luminescent probes for systems where a delay between the excitation of the probe and the detection of the luminescence emission is needed, such as for *in vivo* measurements on biological materials, in order to bypass the background signal due to the autofluorescence of the probe, resulting in more accurate time gated measurements (**Figure 1.25**).[95-96]

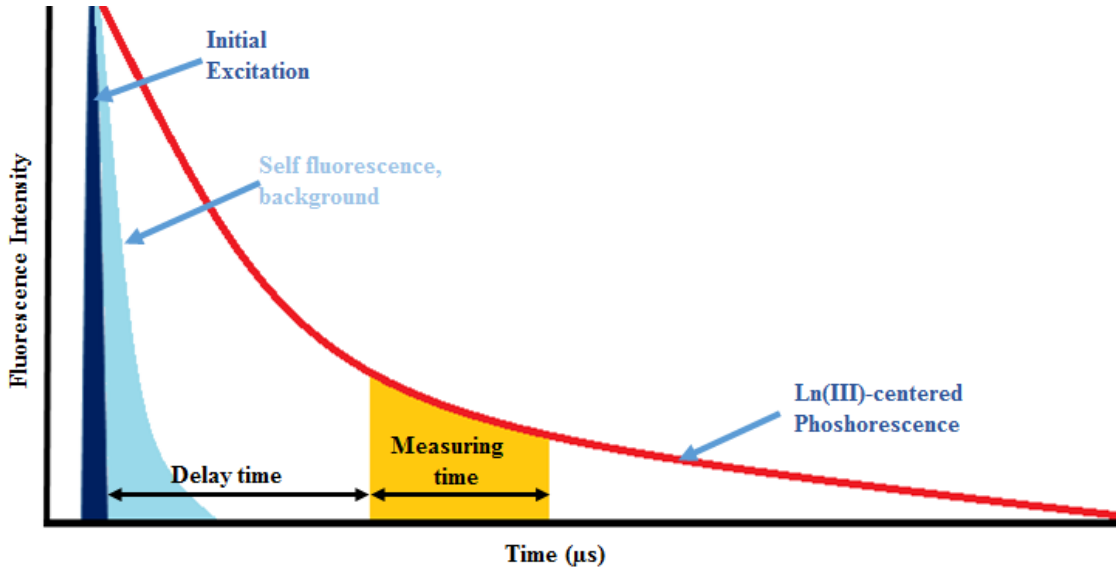

Figure 1.25 Illustration of the time gated setup to measure Ln(III)-centred emissions avoiding autofluorescence. Image reproduced from ref.[96]

Although Ln(III) ions may seem like ideal candidates for the development of optical probes, they do not lack drawbacks; the main of these being their relatively low molar

absorption coefficients, ε, often lower than 1 M^{-1} cm^{-1}, making direct excitation of the metal an inefficient process. The most effective way around this issue, is the so called "antenna effect", which involves the use of an organic chromophore, or a metal ion complex (such as Ru(II) based polypyridyl complexes) with high absorptivity that acts as a "light harvester" for the metal ion that is then excited indirectly.[97-98]

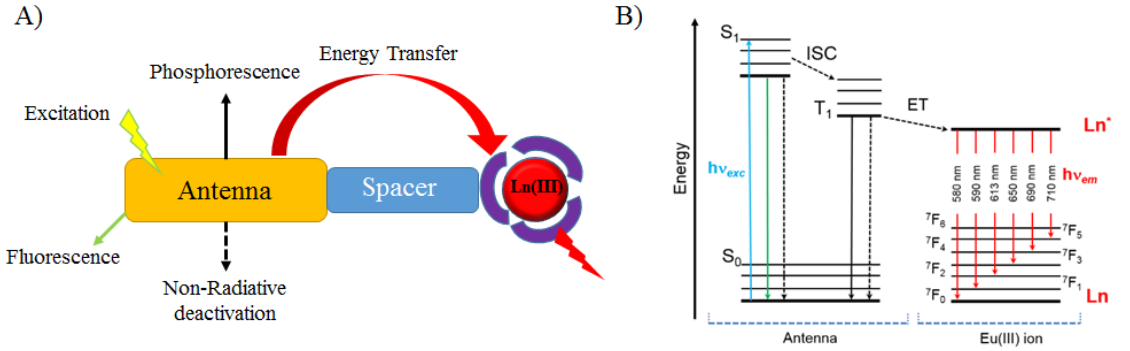

Figure 1.26: A) Representation of the processes involved in the antenna-driven sensitization of Ln(II) ions. B) Jablonski diagram representing the pathways for the sensitization of Eu(III) ions. Images reproduced from ref.[99]

The schematic representation shown in **Figure 1.26: B)** illustrates the sequence of processes involved in the sensitization of Eu(III) ions using a modified Jablonski diagram. The exciting radiation first hits the sample and a photon elevates the chromophore from the singlet ground state, S_0, to the singlet excited state, S_1, (blue transition). From S_1, the system can completely dissipate the energy *via* non-radiative processes (dashed transition) and decay back to the ground vibrational state of the electronic excited state and then either decay through fluorescent emission or undergo *intersystem crossing* (ISC) to the excited triplet state, T_1. From T_1, the system can again decay without radiating, emit molecular phosphorence transitioning from T_1 to S_0, or finally, transfer the energy to the metal centre in a non-radiative process of energy transfer (ET) which populates the lowest excited state of the lanthanide. In the case of Eu(III), this state is $^5D_0$, from which it will dissipate the energy, emitting phosphorescence. As the ground state electronic levels ^7F_J ($\Delta J = 0 - 5$) are quantized, the transitions are therefore discreet and give rise to the line-like emission spectra.[89, 99]

In order for the energy transfer to be effective, the ligand needs to be designed so that the energy gap (ΔE) is in a suitable frame. This ΔE needs to be then close enough to maximize the quantum yield of the process, but steep enough to minimize the chance of back-transfer processes; suitable values to avoid this range between 2500 cm^{-1} and 3500 cm^{-1} for the two most explored ions, Eu(III) and Tb(III), and similar values can be expected

for the onther Ln(III) ions. On the other hand, where efficient ISC takes place, the energy gap between the singlet and triplet states is around 5000 cm^{-1}. Therefore, to design efficient ligands, the two parameters requested are that $\Delta E(^1S^*–^3T^*) \approx 5000\ cm^{-1}$ and $\Delta E(^3T^*–Ln^*$ emissive level) is in the 2500–3500 cm^{-1} range.[100-102]

As previously discussed, the radiative processes are in competition with the non-radiative decays. The two most commonly observed forms of decay are the quenching of the triplet excited state, T_1, by molecular oxygen and the deactivation of the singlet excited state, S_1, through collisional and vibrational quenching.[9, 87] The following section will describe these processes in detail.

1.4.3 Lanthanide luminescence quenching

The process of quenching, as explained in the previous section, involves the decay of the excited state in non-radiative ways. Quenching normally involves molecules that complete the coordination sphere of the metal, or molecules of diffusing solvent[89] and can happen through vibration modes, like stretching of the O-H, N-H and C-H bonds of the coordinating groups. Although these processes could be thought to be parasitic towards the efficiency of the emission of the systems, they allow researchers to obtain precious data regarding the coordination environment of the metal ion. The most common information derived is the number of water molecules that are bound to the Ln(III) ion, or the hydration state, also called the *q* value of the complex. Horrock and *et al.*[103-104] were the first to propose a method that would determine a mathematical relationship between the *q* value of a system and the life times of Eu(III) complexes coordinated by H_2O and D_2O. The hypothesis they presented was based on the fact that the stretching motion along the O-H axis of coordinated molecules of H_2O and D_2O would differently affect the deactivation of the Eu(III) excited state, as the heavier deuterium atoms would contribute less toward the process.[105] This idea was expanded upon by Parker and co-workers[106] in order to consider the vibrational contribution of N-H and C-H groups and the parametric equation was obtained (***Formula 1.1***).

$$q^{\mathrm{Eu(III)}} = \mathrm{A}\left[\left(\frac{1}{\tau_{\mathrm{H_2O}}}\right) - \left(\frac{1}{\tau_{\mathrm{D_2O}}}\right) - 0.25 - 0.075x\right] \qquad \textbf{\textit{Formula 1.1}}$$

In the equation, which was derived using amidic ligands, the τ terms represent the lifetime of the Eu(III) species recorded in H_2O and D_2O and A is a proportionality constant equal to 1.2 ms. The remaining terms are correction factors for the effect induced by second

sphere water molecules and the contribution of N-H oscillators, with *x* being the number of amidic N-H oscillators bound to the metal.

The information presented in the last two sections shows that to minimise the vibrational deactivation of the Ln(III) luminescence and maximise the emission, it is important to focus on choosing and designing ligands able to stabilise the system while minimising the vibrational energy contributions, as well as selecting solvents with a low tendency to coordinate. This can be achieved using multidentate ligands capable of stabilising the complex while shielding the metal ion from solvent coordination. Ligands containing suitable chromophores are therefore the best choices for the development of functional supramolecular materials based on Ln(III) luminescent emission.[107] The Gunnlaugsson research group has been a major contributor in this field, developing several functional luminescent materials, a few examples of which will be discussed in the following section.

1.4.4 Advances in the Gunnlaugsson Group

In recent years, the Gunnlaugsson group has centred its research on the design and development of supramolecular soft materials, such as gels and polymers. These materials were integrated with the use of *d*-block and Ln(III) ions able to emit luminescence with ligands in order to use metal-directed aggregation and integrate optical properties to such materials.

Kotova *et al.* firstly combined the use of BTA and metal-directed gelation processes to obtain a luminescent hydrogel.[108] In this work, the use of tripodal BTA core unit, the properties of which were described in section 1.2, was conjugated with the ligand properties of three 2,2';6',2''-terpyridyl (**tpy**) moieties, a chelating tridentate ligand, to obtain **46**. The **tpy** ligand was chosen because of its ability to form supramolecular aggregates, which has been reported widely[109-110] and the ability to bind Ln(III) ions and form higher-order aggregates. **46** showed the ability to form gels in hydroalcoholic mixtures. In particular, a 70:30 water:methanol mixture and 0.25-0.3 wt% **46** led to the formation of a transparent gel upon slow evaporation of the solvent at room temperature. When the ligand was dissolved with a $EuCl_3 \cdot 6H_2O$ salt in various stoichiometries (1:1, 1:2 and 1:3 L/Eu ratios), the resulting gels were luminescent, confirming the ability of the tpy ligand to act as an antenna to populate the $^5D_0$ excited state of the Eu(III) ion. The systems were investigated spectroscopically in solution and morphologically as a gel, leading to interesting results. Spectroscopic studies of the solutions revealed that initially

the main species to form are the 1:1 and the 3:2 Eu:**46** complexes. This showed that the interaction between the ligand and metal ion is regulated by an equilibrium that can be pushed towards the formation of higher-order supramolecular aggregates. Electron microscopy (SEM and HRTEM) imaging confirmed this, as the two gels showed drastically different morphologies.

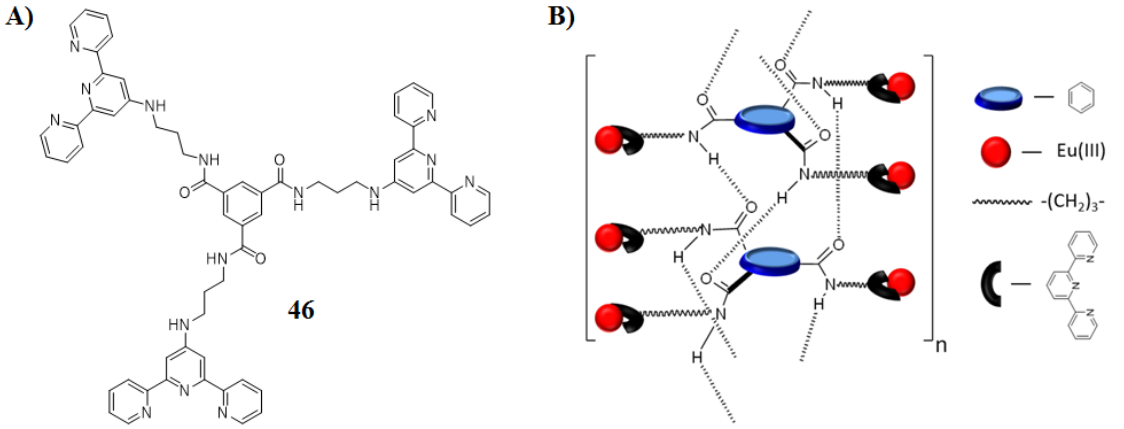

Figure 1.27 A) Molecular structure of BTA-tpy ligand **46**. B) Schematic representation of the triple H bonding in helices of **46**, with the Eu-binding tpy units are directed outside the helix. Reproduced from ref.[108]

The gel formed by the ligand presented intertwining bundles of strings, while the metallogel was shown to possess a more ordered structure, where the strings are aligned locally; a schematic model for the aggregate is shown in **Figure 1.28**. It was also found to be more mechanically robust.

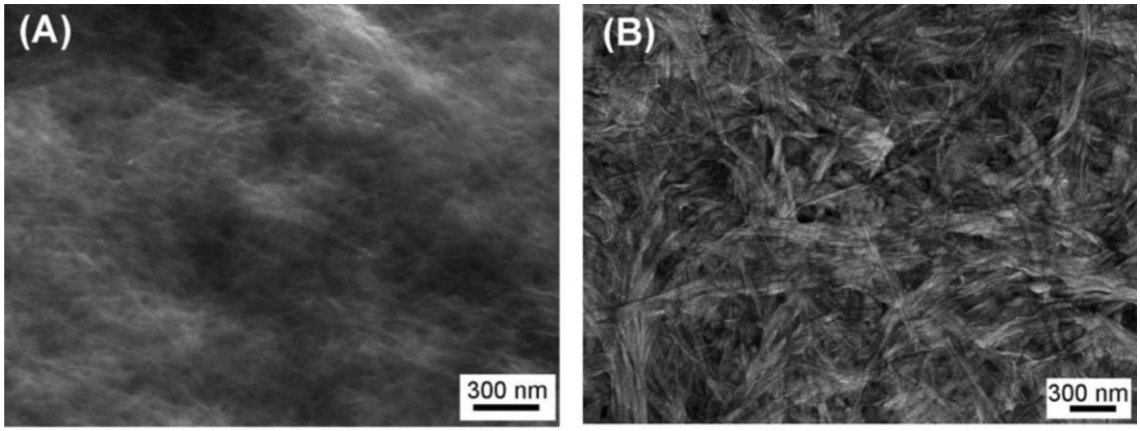

Figure 1.28 SEM imaging of the gels formed from (A) **46** and (B) Eu·**46**. Images reproduced from ref.[108]

A following study[111] also performed in collaboration with the Boland team at TCD and co-workers revealed a peculiar behaviour of the systems. On the surface of the gel, it was possible to observe the growth of halide salts into nanowires with high aspect ratios; this was obtained by dropcasting the supramolecular gel formed from solutions containing the corresponding halide salt (NaCl, KCl or KI) and slowly allowing the gel to dry over three

to four days. The resulting wires had diameters of 130-200 nm and a length of up to 10 µm. Although the role of the supramolecular gel within this process was not completely defined, it was speculated that the gel affected the diffusion of the ions inside its matrix, leading to the crystallisation of the ions at the interface with the gel, with the wires growing by being 'pushed' from the bottom up. These "supramolecular nanogardens" could therefore be used as a model for studying the growth and the properties of highly ordered nanomaterials.

A series of Eu(III) and Tb(III) metallogels were also reported by Gunnlaugsson *et al.*[82] which displayed self-healing properties. Ligand **47** was initially designed to induce the formation of aggregates with 1:3 and 1:2 (M:L) stoichiometries that would afterwards bundle into luminescent supramolecular gels. The precipitation of the gels was achieved by irradiating the formed complex in the presence of excess Ln(III). The gels obtained were opaque in natural light and highly luminescent under UV light irradiation; and their deposition on quartz slides allowed for spectroscopic and morphological studies. UV-Vis absorption analysis showed the line-like spectra expected for Eu(III) and Tb(III) complexes; upon simple mechanical mixing, it was possible to observe an emission spectrum which could be considered the sum of the spectra from the single components, with an overall yellow-orange emission.

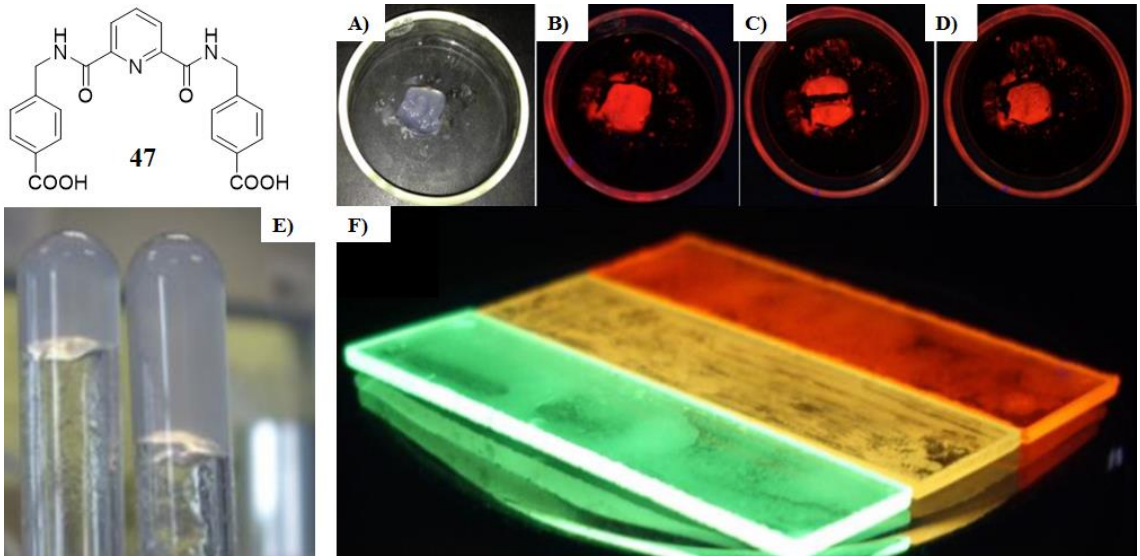

Figure 1.29 Molecular structure of **47**. Top right) Gel resulting from Eu(III):**47** under normal light (A), UV irradiation (B), immediately after cutting (C) and after self-healing over time (D). E) Comparison between Tb(III):**47** (left) and Eu(III):**47** (right) gels. F) Samples of the Tb(III) (left), Eu(III) (right) and Tb(III)/Eu(III) mix gels on quartz slides. Images reproduced from ref.[82]

TEM analysis of the gels on quartz showed that although similar, Eu(III) and Tb(III) led to slightly different cotton-like fibrous aggregates. Interestingly, the Tb(III) metallogels displayed more densely packed fibers in comparison with the Eu(III) analogue, which

correlated with the difference in volume when they are prepared under the same conditions. Finally, the systems ability to self-heal was verified by comparing its rheological properties before and after cutting a sample of each of the gels.

The work presented in the PhD Thesis of Dr. Savyasachi AJ gave further insight on the properties of the behaviour of BTA-terpyridine systems where a variety of amino acids had been introduced on the side arms (**Figure 1.30 A**). The use of the achiral amino acid glycine led once more to the formation of a robust gel in MeCN/H_2O mixtures (**Figure *1.30* B**), but the use of similar conditions with chiral amino acid derivatives only yielded viscous solutions in several different solvents, suggesting the formation of aggregates. To get a better understanding of the nature of such aggregates, the samples were investigated using several techniques and the most conclusive results were yielded by microscopy studies. In fact, the SEM images revealed that the molecules had assembled into spheres, with diameters of 0.5 and 2 µm in MeOH and EtOH respectively (**Figure 1.30 C**). In MeCN, the systems displayed the most uniformity where upon addition of Ln(III) ions, a network of cross-links among the spheres was observed. The microspheres were also investigated using Atomic Force Microscopy (AFM), which showed solid-like behaviour.

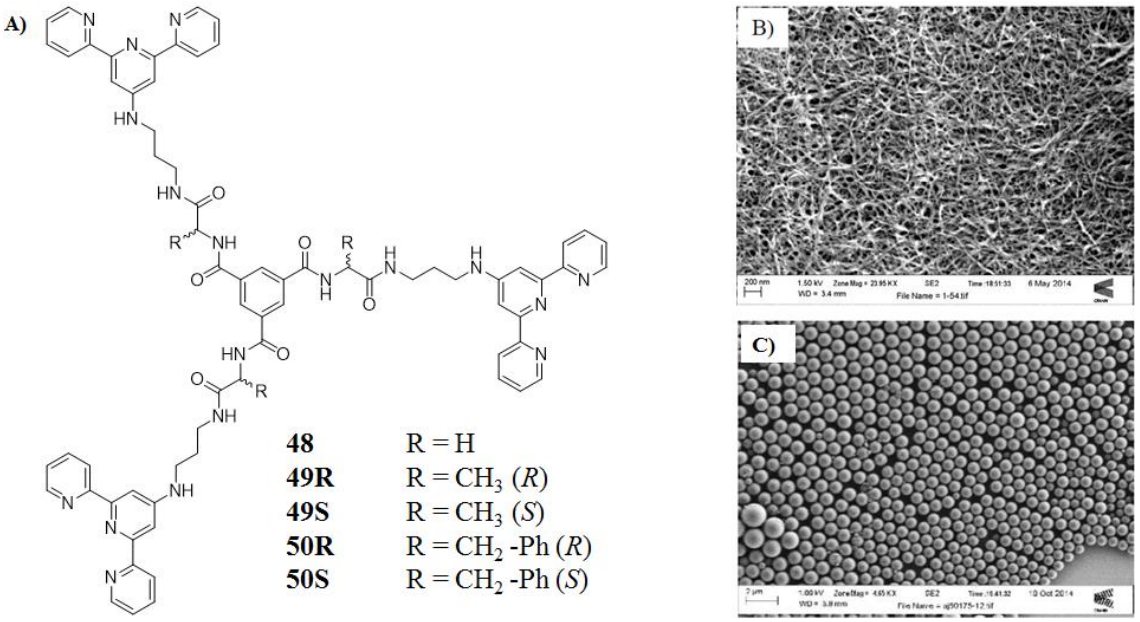

Figure 1.30 A) Molecular structures for compound **48** - **50** presented by Savyasachi in his thesis work. B) SEM imaging performed on the gels formed from **48**. C) SEM of the microspheres formed by **49**. Reproduced from ref.

A remarkably different behaviour was observed in a family of BTA derivatives presented by Dr. Amy Lynes in her PhD thesis (**Figure 1.31**).[112]

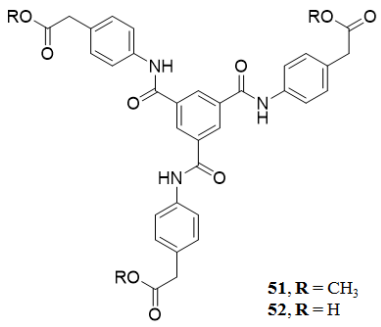

Figure 1.31 Molecular structure for compounds **51** and **52**. Reproduced from ref.[112]

In these systems, the BTA core had been functionalised using an aromatic substituent, a phenylacetate group, to study the effect of these bulky and structurally rigid blocks on the aggregation behaviour. In fact, the presence of the phenyl ring completely blocked the ability of these system to form stable gels; instead, it was observed that **51** and **52** had the ability of forming complex structures while coordinating Cd(II) ions. These structures were found to be porous and **52** was found to be able to adsorb high quantities of CO_2, because of its higher structural flexibility.

1.5 Work described in this PhD Thesis

As discussed in the previous sections, the ability of controlling the self-assembly processes of supramolecular "soft" materials is an area of increasing importance. The BTA motif, presented in section 1.3, has been proved to be a very interesting and versatile tool for the understanding the processes that through supramolecular interactions lead to the formation of these soft materials, thanks to the possibility of binding different moieties to a scaffold able to form hydrogen bonds *via* its amidic units. Previous work in the Gunnlaugsson group also demonstrated, as was outlined above, that minor changes in the BTA structures can have major impact on the materials output and there clearly exists a need to further study and understand what factors governs that. In particular, the differing results by Savyasachi and Lynes attracted particular interest; this project was designed in order to combine the properties of amino acids functionalised BTAs together with the structural rigidity introduced by a phenyl ring in proximity to the BTA core.

Chapter 2 will describe the design and development of a family of BTA derivatives containing a rigid aromatic spacer, an amino acid component and a metal-binding terpyridine moiety, as well as the formation of a Eu(III) complex with one of these derivatives. An alternative synthetic pathway will also be shortly presented.

Chapter 3 will focus on spectroscopic and morphologic studies performed on these BTA derivatives both as free ligand and as Eu(III) complex.

Chapter 4 will describe a work in collaboration with a fellow Gunnlaugsson group member where a BTA derivative will be used to form a higher order structure with a cyclen-based Tb(III) complex.

Chapter 5 will present a series of different aggregators designed within the Gunnlaugsson group or in collaboration with it, that were studied morphologically to highlight the differences induced by the different interaction in the final aggregates on a micro- and nanoscopic scale.

Chapter 2

Synthesis of tripodal BTA systems functionalised with tpy moieties

2.0 Introduction

As seen in Chapter 1, compounds **48 - 50** (**Figure 2.1 A**) were found to aggregate forming complex structures, with the achiral derivative forming organogels and microspheres through the formation of the threefold hydrogen bonds and π - π stacking of the BTA cores. It was found that the side interactions through the tpy moieties and the amino acidic components also directed the aggregation. It was speculated that the introduction of an aromatic spacer would induce a shielding of the core of the ligands and therefore influence the properties of the resulting supramolecular systems. The aim of the work described in this thesis is to study these effects by building on the knowledge and expertise previously obtained within the Gunnlaugsson group in this field.

In order to achieve this aim, the following considerations were taken into account:

- Design of the ligand in order to have a BTA core, an aromatic spacer, achiral (glycine) and chiral (alanine and phenyl alanine) amino acid connected *via* a short aliphatic chain to the terpyridine moiety;
- Synthesise and characterisation of the ligands spectroscopically and morphologically;
- Complexation and spectroscopic studies with Ln(III) ions;
- Aggregation studies of the new ligands and complexes into gels and nanostructured materials.

The result of such rationale was the design of ligands **53 - 55**. The structure for these ligands is shown in **Figure 2.1 B**, where the different "building blocks" that make up these ligands are color-coded.

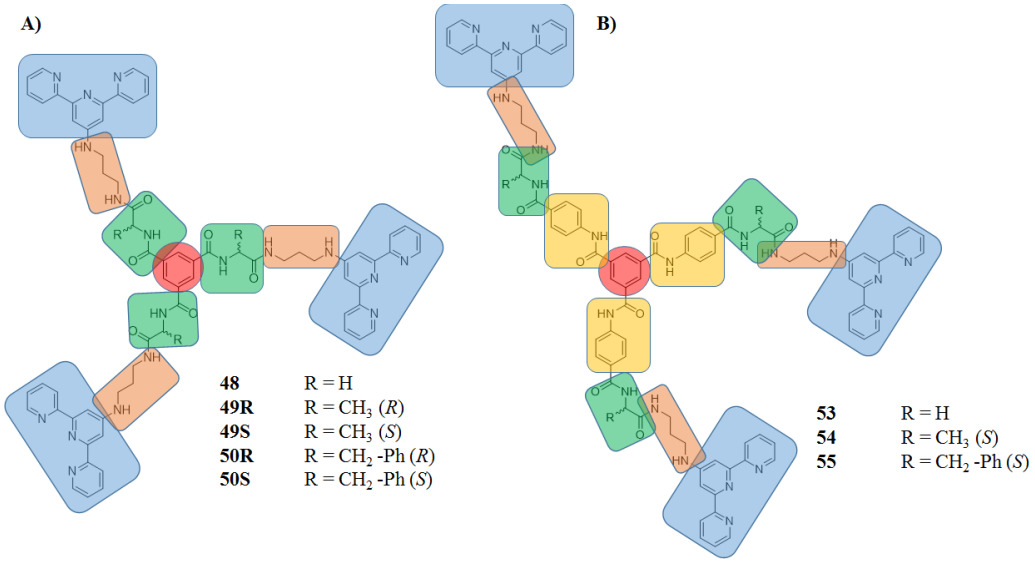

Figure 2.1 Schematic structures of tripodal compounds **48 - 50** synthesised in previous works in the Gunnlaugsson group (A) and **53 - 55** including an aromatic spacer, highlighted in yellow (B).

The central BTA core is shown in red; the use of this core will ensure the C_3 symmetry for the final systems and ensure the ability of the various ligands to interact. The novel aromatic spacers are highlighted in yellow; their introduction will allow for an understanding of the effect that an extra aromatic ring would induce on the aggregation of the final ligands. Following that, the amino acid components are highlighted in green; their presence will allow for an introduction of a chiral centre in the final ligands, together with the ability to further increase the complexity of the system. The tpy moieties are highlighted in sky blue; their photophysical properties, together with their chelating capabilities can be exploited for the binding of lanthanide ions. Finally, connecting the amino acid groups to the terpy moieties are short aliphatic chains, highlighted in orange; their presence allows for a moderate mobility for the terpy moieties.

The following sections will follow the step-wise addition of all these components, beginning with the aromatic core and following a building-up procedure.

2.1 Synthesis of tripodal ligand 37

The first step for the formation of the target molecules involved the synthesis of **37**. To do so, the literature method developed by Zhang[76] was used with some slight modifications as shown in **Scheme 2.1**; full description for the synthesis can be found in the Experimental Details chapter, while characterization details can be found in the Appendix chapter.

In the first step, 1,3,5-benzenetricarbonyl trichloride (**BTC**) was reacted with an excess of methyl 4-aminobenzoate in hot acetone, using potassium carbonate as base to neutralise the hydrochloric acid formed by the reaction, pushing the reaction to completion.

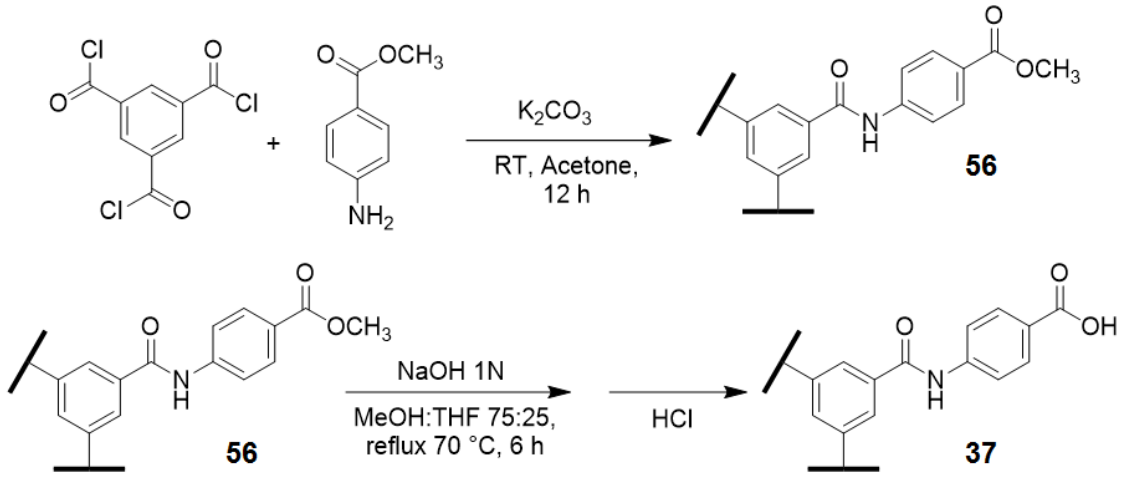

Scheme 2.1 Synthesis of tripodal ligand **37.**

This step proved straightforward and compound **56** provided both high yield (87%) and purity. The methyl ester was hydrolysed with an aqueous solution of NaOH in a MeOH/THF mixture and the carboxylate was later obtained pure as a precipitate as a hydrochloride salt from the mixture upon acidification with HCl in a 80% yield. Both ^{1}H-NMR and HRMS analysis confirmed the formation of pure product and the full characterisation for these compounds can be found in the Appendix chapter.

The ability of **37** to form MOFs had been reported by Zhang *et al.*[76] and as such, an attempt at replicating the solvothermal syntheses of such systems using several *d*- and *f*-block metals was made. In particular, two *d*-block ions, Zn(II) and Cu(II) and three lanthanides, Eu(III), Tb(III) and Gd(III) were employed. Solutions of **37** and the relative ion salt (nitrate for Zn(II) and Eu(III), trifluoromethyl sulfonate for Tb(III) and Gd(III) and sulphate for Cu(II)) in DMF containing traces of water were sealed in Teflon capped vials and heated at 100 °C for 24 and 48 hours in a heat block. In all cases, the process lead to the precipitation of solids that were found to be amorphous in nature. This inability to obtain such MOFs, or even a simple crystalline structure for **37**, was speculated to be due to the nature of the ions used, the lack of a controlled cooldown ramp from 100 °C to RT, or a combination of the two factors. The aggregation properties of **37**, and in particular, its ability to form hydrogels, will be discussed further in Chapter 3. The investigation to expand the use of **37** in the formation of coordination polymers and MOFs was not pursued any further after this attempt.

2.2 Design and synthesis of amino acid-functionalised derivatives

Once **37** was obtained, the following step involved the functionalization with three different alpha amino acids, namely: achiral glycine, and chiral L-alanine and L-phenylalanine. To do so, the rationale was to form amide bonds between the carboxylic moieties of **37** and the amine groups of the protected amino acids, and then remove those protecting groups from the amide product. The coupling reaction occurs in two steps: first, activation of the carboxyl group; followed by reaction of the resulting activated species with the desired amine. The activation of the carboxyl group could be achieved using acid halides, azides, anhydrides, or carbodiimides; it is also possible to form active esters *via* pentafluorophenyl or hydroxysuccinimido as reactive intermediates; some of these approaches were explored. Reactive intermediates derived from generation of acyl

chlorides or azides are highly efficient for amide coupling; however, these processes involve harsh condition and the resulting compounds have very high reactivity, leading often to formation of side products. Therefore, the use of reagents which operate in milder conditions are broadly preferred.

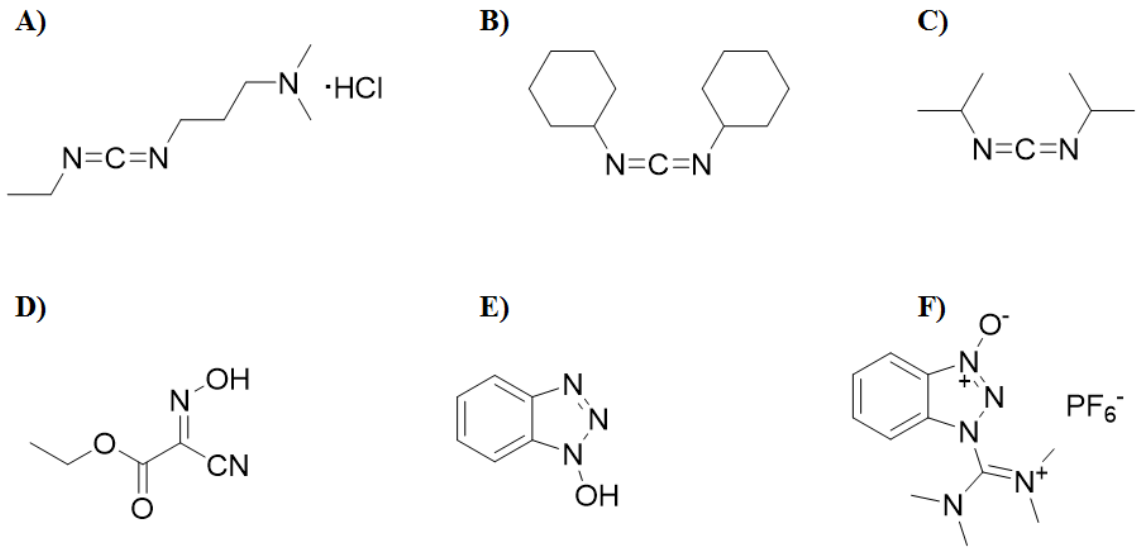

Figure 2.2 Chemical structure of reagents and co-reagents used in amide coupling reactions. A) **EDCI·HCl**, B) **DCC**, C) **DIC**, D) **OxymaPure**, E) **HOBt**, F) **HBTU**.

Figure 2.2 shows some of the reagents broadly used for amide coupling reactions; among them, there are carbodiimides such as *N*-ethyl-*N'*-(3-dimethylamino-propyl)carbodiimide hydrochloride (**EDCI·HCl**), dicyclohexylcarbodiimide (**DCC**) or diisopropylcarbodiimide (**DIC**), as well as ethyl cyano(hydroxyimino) acetate (**OxymaPure®**), benzotriazol derivatives such as 1-hydroxybenzotriazole (**HOBt**), and *N*,*N*,*N*′,*N*′-tetramethyl-*O*-(1H-benzotriazol-1-yl)uronium hexafluorophosphate (**HBTU**). The coupling reactions require the presence of a base able to act as a proton carrier without interfering with the main reaction mechanism. Examples of such bases are triethyl amine (**TEA**), dimethylamino pyridine (**DMAP**) or diisopropyl ethylamine (**DIPEA**, or Hünig's base). The conditions that maximize the efficiency are not absolute and depend on the nature of the reagents involved.[113]

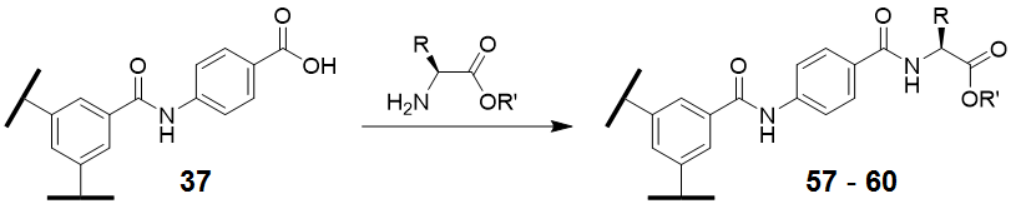

57: **R** = H; **R'** = CH_2CH_3; **58**: **R** = H; **R'** = $C(CH_3)_3$; **59**: **R** = CH_3; **R'** = $C(CH_3)_3$;
60: **R** = CH_2 –Ph; **R'** = $C(CH_3)_3$

Scheme 2.2 General scheme for the synthesis of protected amino acids derivatives **57** - **60**.

In this work, the amide coupling reactions involving **37** (**Scheme 2.2**) proved to be challenging. The reactions with the three different amino acids were tuned using alanine as a model system. This allowed for optimisation of the protocol while ensuring that the absolute configuration of the chiral centres would be maintained. The summary of the synthetic protocols used in this case is represented in **Table 2.1**.

Table 2.1 Synthetic protocols and their efficiency for the synthesis of **59**.

Coupling Reagents	Organic Base	Solvent	Yield (%)	Reaction time
EDCI·HCl; HOBt	TEA	DCM	28	72 hrs
EDCI·HCl; HOBt	TEA	THF	16	72 hrs
EDCI·HCl; HOBt	TEA	3:1 DCM:DMF	10	72 hrs
EDCI·HCl	DMAP	DCM	N/A	72 hrs
DCC; Oxyma Pure	DIPEA	DMF	N/A	12 hrs
HBTU; HOBt	DIPEA	DMF	37	12 hrs

The first reaction involved the use of **EDCI·HCl** in conjunction with **HOBt**. **37** was stirred at 0 °C in anhydrous DCM under argon atmosphere, for 15 min with **EDCI·HCl**, **HOBt** and **TEA** for 15 min before adding L-Alanine as *tert*-butyl ester hydrochloride. The reaction was left to stir at RT for 72 hours under inert atmosphere, after which the solvent and most of **TEA** were removed under reduced pressure, forming an oil, which was dissolved in DCM and washed with a sat. solution of $NaHCO_3$, H_2O, a sat. solution of NaCl and then dried over Na_2SO_4. The solid sulphate was removed by gravity filtration and the dried organic layer was reduced *in vacuo* to yield a yellow oil. The oil was slightly diluted and added dropwise to diethyl ether (Et_2O) to obtain a white precipitate, which was filtered and dried *in vacuo*. This procedure was the initial choice because **EDCI·HCl** and its by-product are water soluble, making it easy to remove with simple washes; **HOBt** is effective in suppressing racemization;[114] and both **TEA** and DCM are easy to remove under reduced pressure.

Although the desired products were obtained successfully in this way, this procedure presented several issues. The reaction and work-up times were not optimal and the

reaction presented a low yield, reaching a maximum of 28%. The work-up, in fact, proved to be extremely difficult because of the excessive amount of emulsions formed upon addition of the washing solutions to the organic phase, which could not be broken by addition of small quantities of sat. NaCl solution or MeOH, and would not break up completely, ultimately causing the loss of product and longer times to complete the workup. The main cause for the low yield was speculated to be due to issues with the solubility of **37**, which is only fully soluble in dimethyl sulfoxide (DMSO), dimethylformamide (DMF) and dimethylacetamide (DMA), other than basic aqueous solutions. To overcome this, the reaction was repeated using both neat anhydrous THF and a 3:1 DCM/DMF mixture. In the first case, the reaction produced an even lower yield of 16%, while in the second case the reaction was found to be unsuccessful, with no product isolated.

These unexpected issues led to attempting the reaction using different coupling reagents combinations. Initially, **EDCI·HCl** was kept as the carboxyl group activator, while **HOBt** was removed, and as organic base either **TEA** or 4-(Dimethylamino)pyridine (**DMAP**) were used in DCM. These experiments were designed to probe if **HOBt** was affecting the overall reaction efficiency, or if **TEA** was not favouring the reaction itself. The lack of **HOBt** was instead found to lower the efficiency of the reaction, with the yield capping at 10%, while the use of **DMAP** seemed to worsen the conditions and made the reaction unsuccessful. This was speculated to be due to the nucleophilic catalytic action of **HOBt**, which favoured the reaction completion.

The following step replaced **EDCI·HCl** with a different carbodiimide; the choice fell on **DCC**, which when reacted, formed an insoluble by-product, dicyclohexyl urea (**DCU**), which could be removed by filtration. To suppress racemization, **DCC** was paired with the use of **Oxyma Pure®** (ethyl 2-cyano-2-(hydroxyimino) acetate); **TEA** was replaced by **DIPEA** and DCM was replaced with DMF as solvent, to allow for higher reaction temperatures (80 °C) and reduce the reaction time down to 12 hours. Once again, the results did not show any significant improvement when compared to those obtained using the **EDCI**/**HOBt** system. Although the protocol reduced sensibly the reaction time, the work-up presented further challenges in line with those outlined in the first synthetic protocol. Furthermore, the yield proved to be only slightly better, at 32% and the ^{1}H-NMR showed traces of impurities over several attempts.

After all these attempts failed to give a highly efficient synthesis, the use of carbodiimide was set aside and attention was drawn to the use of uronium salts. In particular, **37** was dissolved in anhydrous DMF and an excess of **HBTU** was added in conjunction with **HOBt** and **DIPEA**. The resulting mixture was stirred at 0 °C for 10 min; the protected amino acid was then added and the reaction was left stirring at RT for 24 hours, after which the reaction was quenched by pouring it onto an ice/water mixture. The resulting white solid was isolated by using suction filtration. The NMR spectra (400 MHz, DMSO-d_6) of the crude product showed the successful formation of compound **59**, with traces of protected amino acid still present. Compound **59** was dissolved in DCM and this solution was then washed with a sat. solution of $NaHCO_3$, H_2O, sat. NaCl solution and then dried over Na_2SO_4. The dried organic layer was reduced *in vacuo* to give a yellow oil. The oil was slightly diluted again with DCM and added dropwise to diethyl ether (Et_2O) to obtain a white precipitate, which was filtered and dried *in vacuo*. The use of this protocol was found to give the highest yield among the ones attempted, at 37% of the desired product and allowed for scaling up without a loss in efficiency, as it was observed through several attempts that used up to 1 gram of **37** as starting material. The same protocol was then used with the other two amino acids and characterisation of **57 - 60** (see the Experimental Details and Appendix Chapter) was performed. A comparison of these various methods is shown in **Table 2.1**. The work-up procedure for the following reaction step, *i.e.* the deprotection of the carboxyl group, involved a precipitation of the solids in H_2O. This step eliminates the purification processes of **57 - 60**, as the unreacted excess of protected amino acids become deprotected and were subsequently removed due to the high water solubility of Gly, Ala and Phe (249.9, 167.2 and 29.6 g/L, respectively) in the precipitation step.

As stated previously, the carboxylic moieties of the amino acids were protected using their esters. Tertiary butyl ester was used for alanine and phenylalanine, in both cases as their hydrochloride salts. Initially, methyl and ethyl esters were also employed for glycine. The use of aqueous solutions of NaOH and KOH was initially chosen in the design for the deprotection of the methyl and ethyl esters, but an appropriate condition for the ester cleavage was not found. At lower temperatures ($T < 70$ °C) no formation of the product was observed, while at higher temperatures ($T \geq 70$ °C) a degradation of amino ester derivatives was observed. The use of *tert*-butyl ester was then extended to glycine derivatives, initially as dibenzenesulfonimide salt, then as hydrochloride salt.

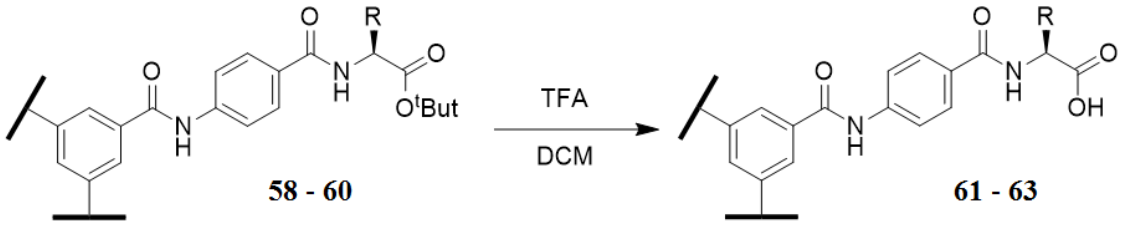

58, **61**: **R** = H; **59**, **62**: **R** = CH_3; **60**, **63**: **R** = CH_2 –Ph

Scheme 2.3 Reaction scheme for the cleaving of the *tert*-butyl esters from compounds **58** - **60** to obtain **61** - **63**.

The formation of **57** - **60** was confirmed by the use of various characterisation techniques; in **Figure 2.3** the ^{1}H-NMR spectrum (400 MHz, DMSO-d_6) of **59** is shown as an example. It is also possible to observe the presence of unreacted alanine *tert*-butyl ester by observing the presence of an impurity multiplet next to the quintet for proton 6, as well in the integration value relative to the protons 7 and 8.

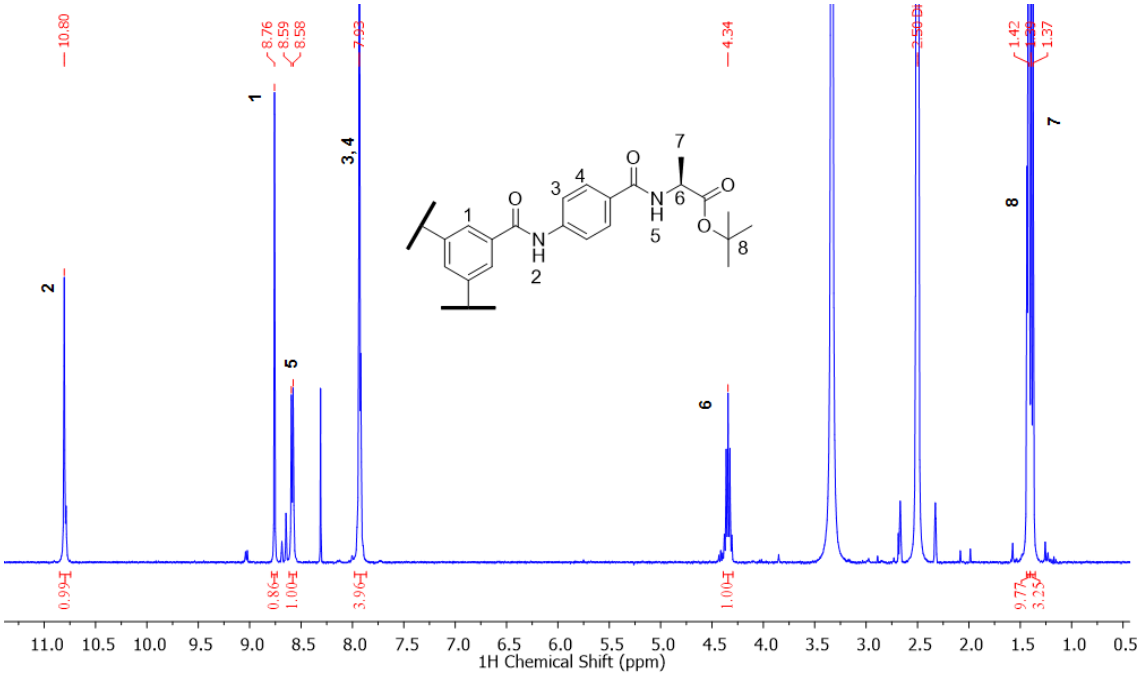

Figure 2.3 ^{1}H-NMR (400 MHz, DMSO-d_6) spectrum of **59**. It is possible to see the presence of unreacted alanine as contaminants in the peaks at 4.34, 1.42 and 1.38 ppm.

Figure 2.4 ^{1}H-NMR (400 MHz, DMSO-d_6) spectrum of **62**. No *tert*-butyl protons or unreacted alanine observed.

The deprotection of *tert*-butyl esters was performed using trifluoroacetic acid (**TFA**) in anhydrous DCM overnight, with a $CaCl_2$ drying tube. Upon reaction completion, the solvent was removed in *vacuo*, and the resulting solid was redissolved in MeOH and reprecipitated in water. This process was designed taking into account the solubility of the used amino acids in water after their deprotection. The deprotected amino acids,

become solubilised in water and allow to by-pass the necessity of separating the unreacted amino acids, used in excess to ensure the full functionalization of **37**, from **58 - 60**.

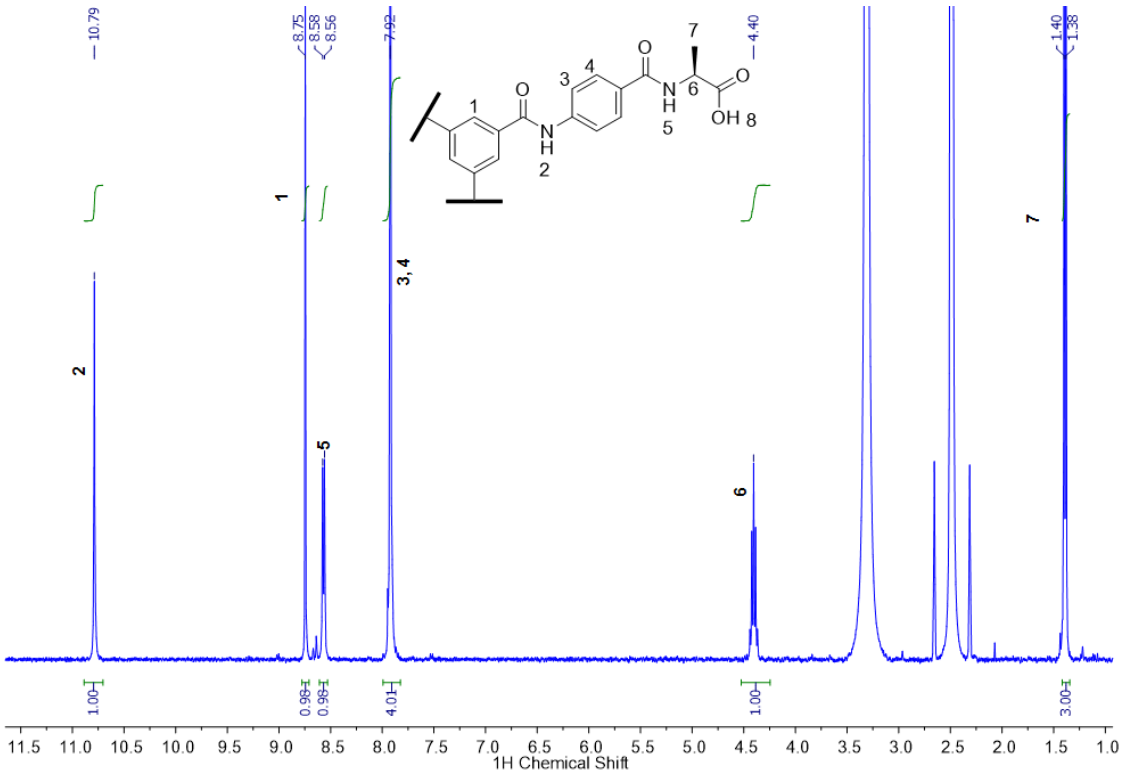

This design obtained **61**, **62** and **63** in high yields (≥ 80%) and purity. An experimental proof of this can be seen in **Figure 2.4**, where the ^{1}H-NMR spectrum for **62** is shown. It is in fact possible to observe, comparing this spectrum to the one shown in **Figure 2.3** the lack of the peak relative to the *tert*-butyl protons and, more importantly, the lack of signals relative to unreacted alanine impurities, confirming the effectiveness of the method.

2.3 Synthesis of the terpyridine moiety and ligands 53 - 55

As explained in Section 1.3, a ligand capable of sensitising Ln(III) ions needs to fulfil certain requirements. Section 1.4 detailed how the terpyridyl unit has been reported to possess such requirements and have been investigated in several previous works in the Gunnlaugsson group. This work builds upon advancements achieved previously and also uses these moieties in the ligands **53 - 55**. The synthetic strategy used was the same as reported,[115] shown in **Scheme 2.4**, and confirmed after characterisation (see Experimental Details and Appendix Chapters).

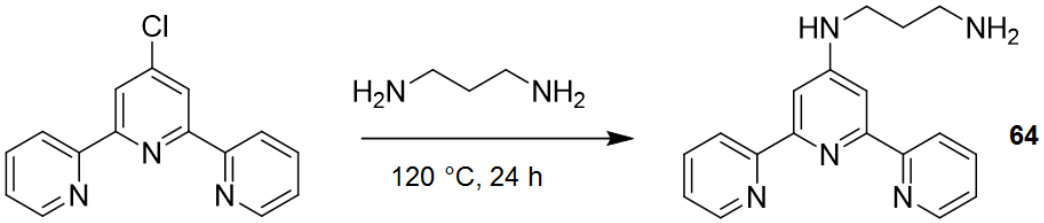

Scheme 2.4 Synthesis of terpyridine moiety in **64**.

The terpyridyl moiety **64** was to be coupled with ligands **61** - **63** *via* its amino group, therefore, once more employing amide coupling reactions. Again, this proved to be quite challenging. The coupling was attempted using several different combinations of reagents and conditions, to optimize the results. Initially, the use of **EDCI·HCl** in conjunction with **HOBt** and **TEA** in a 3:1 DCM:DMF mixture for 72 hours was investigated. The reaction showed low efficiency, with a low yield, inferior to 10%, and a constant metal impurity issue. This was quite evident in the work-up procedure where the solutions displayed a bright, purple colour, characteristic of $[Fe(tpy)_2]^{3+}$ complexes. These solutions were washed using the disodium salt of 2,2′,2″,2‴-(Ethane-1,2-diyldinitrilo)tetraacetic acid (**EDTA**) solutions, but no effect was observed. A reason for this can be found with the binding constant of such complexes, which is well known to be very high,[116-117] reaching logβ of 20.9 in water. Such strong interaction was found extremely difficult to break and therefore these impurities would reduce the yield of the reaction further.

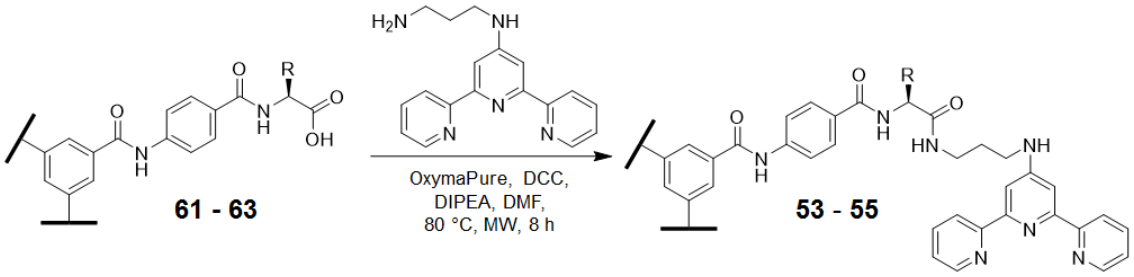

Scheme 2.5 Synthesis of tripodal ligands **53** - **55**.

Despite previous drawbacks, the target molecule was obtained in good yield and very high purity using **DCC** together with **OxymaPure** and **DIPEA** in anhydrous DMF under microwave irradiation at 80 °C for 8 hours; this allowed to speculate that the Fe^{3+} ions would be present as contaminant in traces either in the reagents used for the previous protocol, or in the ones used for the workup. The reaction mixture, after cooling to RT, was poured into an ice/water mixture. The resulting precipitate was filtered to obtain the target molecule. The ^{1}H-NMR spectrum (600 MHz, DMSO-d_6) showed the successful

formation of the desired product, as well as the presence of **DCU** impurities in the precipitate obtained this way. To completely remove the presence of such impurities, the low solubility of DCU in organic solvents was exploited. The solid was dissolved in DMF (first cycle) or DCM (second and third cycle) and exposed to sub-zero temperature for 6 hours; the solution was then filtered to remove the precipitated DCU and the solvent was removed under reduced pressure. The schematic representation of this process and the effect on the ^{1}H-NMR of **57** is depicted in **Figure 2.5**. In the orange circles the signals relative to the DCU and starting material impurities that were not found in the purified compound.

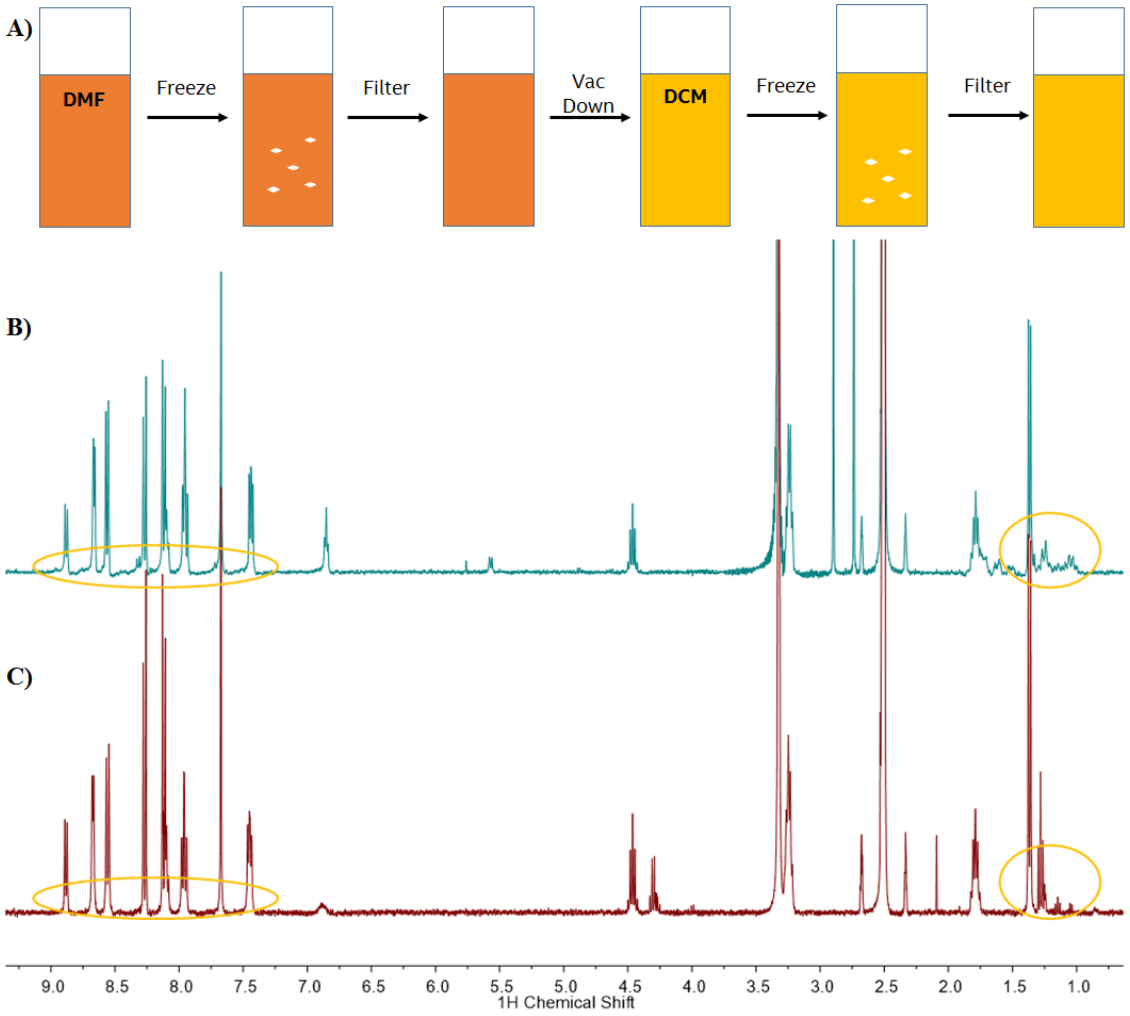

Figure 2.5 Schematic representation for the removal of the **DCU** impurities from solutions of **54** (**A**). Comparison between the (^{1}H-NMR 600 MHz, DMSO-d_6) before (**B**) and after (**C**) the purification process.

After three cycles, the compound was further purified by column chromatography on silica gel using a 90:10 $CHCl_3$/EtOH mixture, achieving a high degree of purity, as shown by the ^{1}H-NMR, in **Figure 2.6** and was further confirmed by Elemental Analysis (see Experimental Details and Appendix Chapters for further characterisation).

A further confirmation of the purity of **54** was obtained by means of elemental analysis, which confirmed the percentage quantities of carbon, hydrogen and nitrogen atoms within experimental error.

Although it was possible to use this method to obtain **54** in high purity, as confirmed by elemental analysis and other characterisation techniques, high purity samples of **53** and **55** eluded isolation; further studies will thoroughly investigate the purification of such compounds and to expand the library of these tripodal systems.

The use of this method was attempted for the synthesis of compounds **61** - **63**, but the spectra showed products with major impurities, which led to ceasing this study and focus turned to the HBTU derivative.

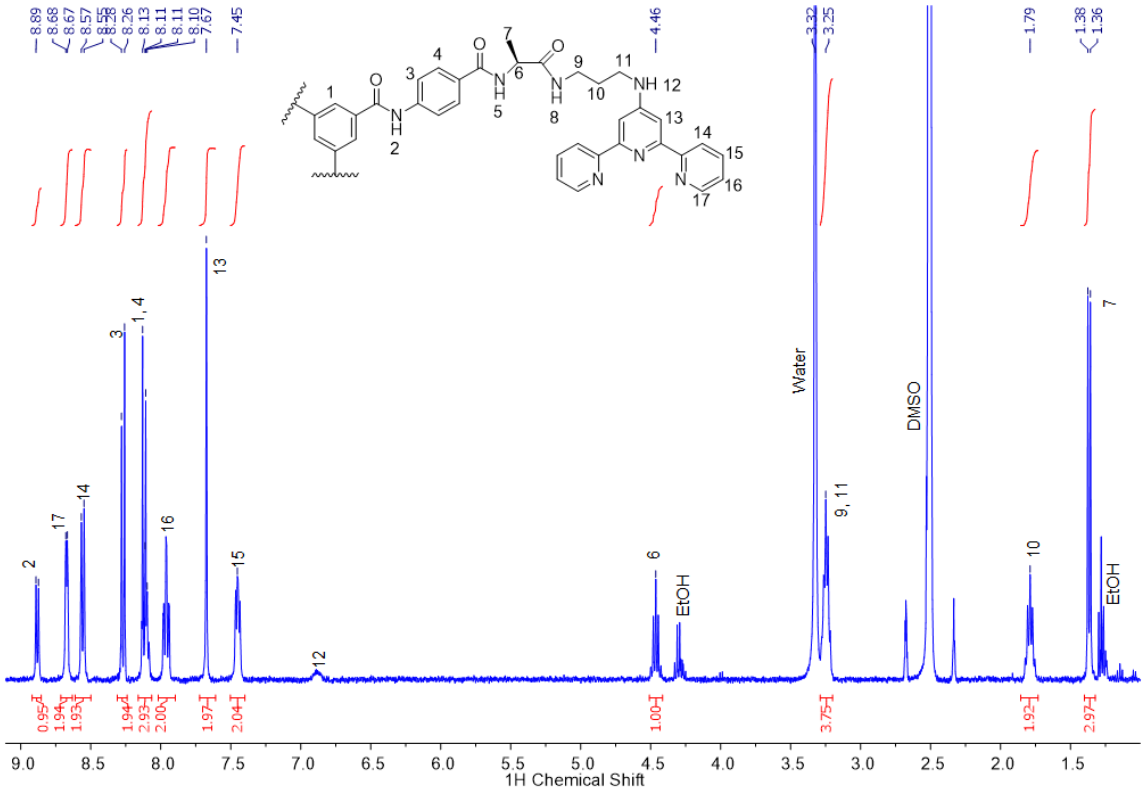

Figure 2.6 ^{1}H-NMR (600 MHz, DMSO-d_6) spectrum of **54** after the purification cycles.

2.4 Alternative synthetic pathways

The synthesis of compound **54** was also attempted through a slightly different synthetic approach from the one described above. Having assessed the formation of the amide units as the most difficult to achieve, a different strategy was devised, which would involve the synthesis of the single moieties and to couple them on a **BTC** core as the final step of the

synthesis. This would be possible by building up the moieties using 4-nitrobenzoic acid as a starting block. The nitro group would in fact be an oxidised amino group, that could be reduced to the desired amine group, which in turn, would be able to react with the acid chloride. To further facilitate these reactions, the 4-nitrobenzoic acid was replaced with its acid chloride, which was reacted with the protected amino acids in freshly distilled $CHCl_3$, in the presence of a base (NEt_3) to neutralise the excess of hydrochloric acid formed *in situ* (**Scheme 2.6**). The reaction was left stirring at RT for 16 hours, after which the solvent was removed under reduced pressure. The resulting solid was redissolved in DCM and washed with a sat. solution of $NaHCO_3$, H_2O, a sat. NaCl solution and dried over Na_2SO_4. The dried organic layer was reduced to give a yellow oil. The oil was slightly diluted and added dropwise to diethyl ether (Et_2O) to obtain **65** - **68** as a white precipitate which was filtered and dried *in vacuo* as described previously.

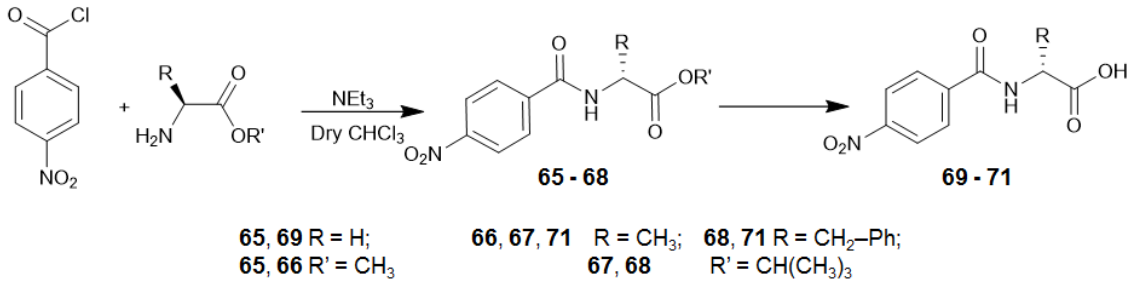

Scheme 2.6 Synthesis of compounds **69** - **71**. The deprotection of the carboxylic moieties for **65** - **68** varies depending on the protecting group.

Figure 2.7 ^{1}H-NMR (400 MHz, DMSO-d_6) spectrum of **70**.

The derivatives obtained were deprotected using methods chosen as a function of the individual protecting groups. For **65** and **66**, the method chosen was a basic hydrolysis in methanol using NaOH at RT for 8 hours. The reaction mixture was quenched by dropwise addition of TFA to precipitate white solids. For **67** and **68** the protecting *tert*-butyl groups were cleaved using TFA in anhydrous DCM for 8 hours. The solvent was then removed at reduced pressure to obtain target molecules **70** and **71** (**Scheme 2.6**).

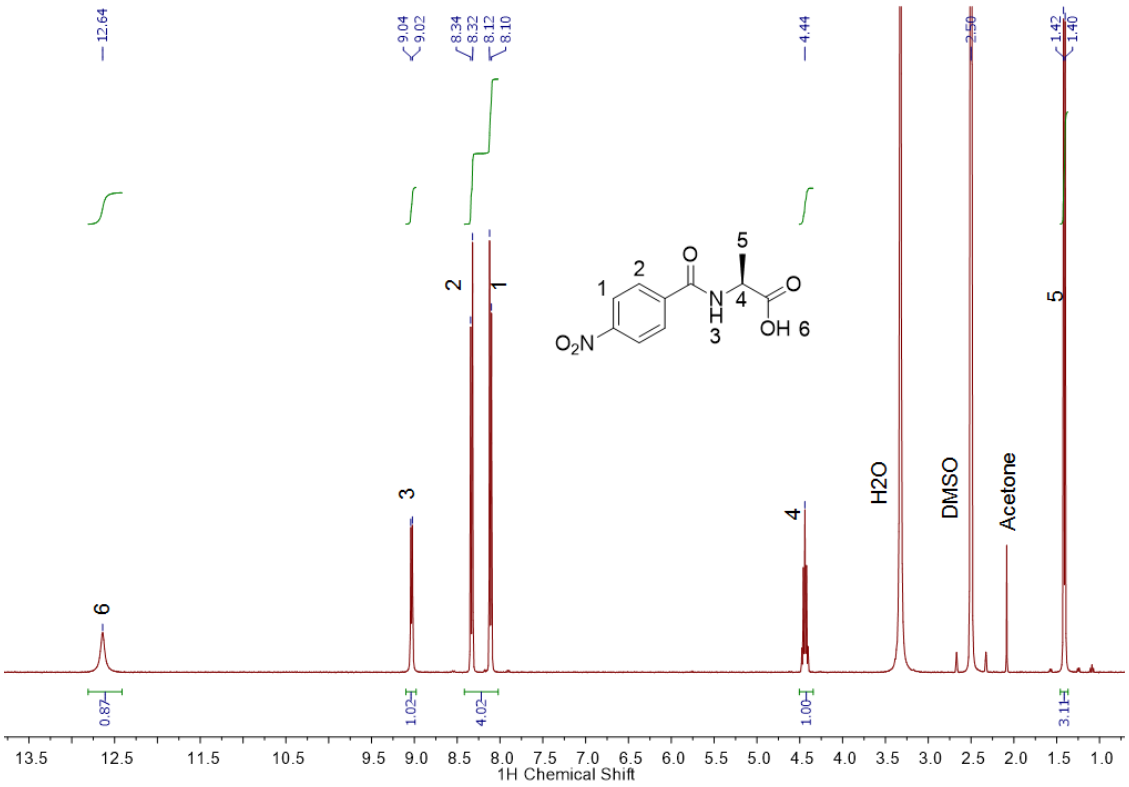

Scheme 2.7 Synthesis of **72 - 74**. The reactions were performed using a Biotage microwave reactor.

Once deprotected, **70** was reacted with **64** in microwave reactor, using the same conditions used to obtain **54** (**Scheme 2.7**). The reaction was far easier to work up; the urea by-product solubility was extremely low compared to the target molecule, precipitating completely from the reaction mixture and removed by gravity filtration.

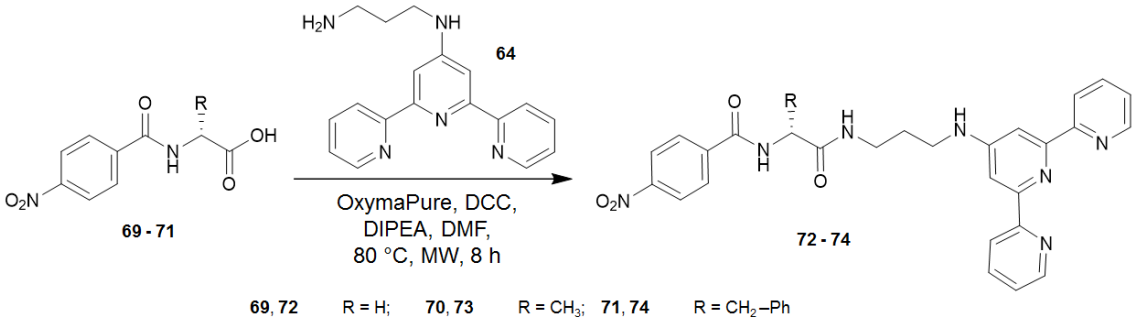

The DMF reaction mixture was then added to cold water, yielding compound **73** as beige precipitate that was recovered by suction filtration, with the ^{1}H NMR shown in **Figure 2.8**. The reaction, which yielded good results for both **73** and **74**, did not show the successful formation of **72**. Further studies will help understand the reason for this. Complete characterisation for **73** and **74** can be found in the Experimental Details and Appendix chapters.

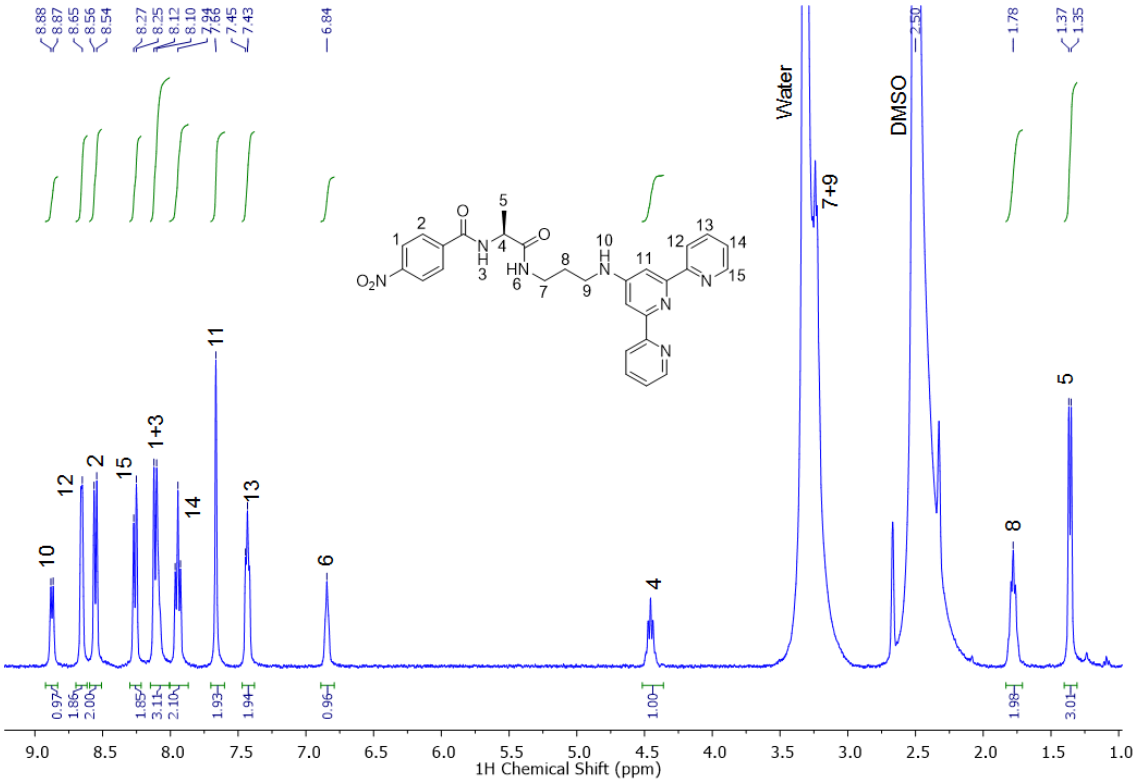

Figure 2.8 ^{1}H-NMR (400 MHz, DMSO-d_6) spectrum of **73**.

In order to obtain the tripodal ligand, the nitro group of **73** had to be reduced to amino and reacted with **BTC**. To do so, the hydrogenation reaction was performed using a Parr Hydrogenation Shaker apparatus. A solution of **73** in MeOH was placed in the apparatus together with palladium on carbon catalyst (20% w/w) and it was exposed to 3 atm of gaseous H_2 for 24 hours while shaking.

Scheme 2.8 Synthesis of compound **75**. The reaction was performed in a Parr Hydrogenation Shaker.

The reaction mixture was diluted using ethyl acetate and filtrated on celite to remove the solid catalyst. The resulting solution was then washed using a solution of ethylenediaminetetracetic acid disodium salt (Na_2H_2EDTA) in ammonium buffer, to remove traces of metal that could "poison" the tpy ligand. The organic layers were then dried over $MgSO_4$ and the solvent was removed under reduced pressure and then further *in vacuo* to obtain a bright yellow solid with a yield of 48%. **Figure 2.9** shows the ^{1}H-NMR spectrum of **75** as an example of such solid in DMSO-d_6, further characterisation can be found in the Experimental Details and Appendix chapters.

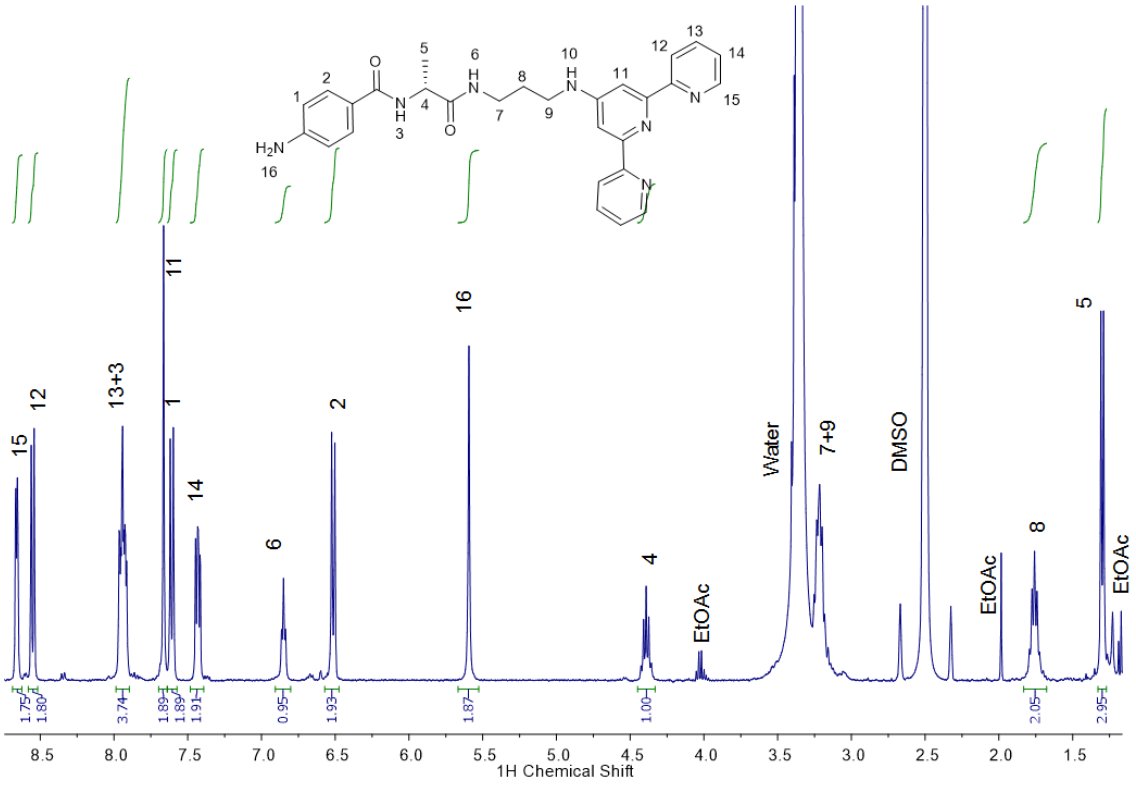

Figure 2.9 ^{1}H-NMR (600 MHz, DMSO-d_6) spectrum of **75**.

The solid was dried *in vacuo* and stirred with **BTC** and NEt_3 in anhydrous DCM for 24 hours. Upon assumed reaction completion, the solvent was removed under reduced pressure to obtain a yellow oil. The oil was diluted using a small amount of DCM and then precipitated using Et_2O to obtain a solid. Upon ^{1}H-NMR analysis, it became evident that the reaction had actually yielded a mixture of the mono-, bi- and trifunctionalised **BTC** product. The use of chromatography on both silica and alumina stationary phase failed to issue a separation of the various fractions upon the use of simple eluent mixtures ($CHCl_3$ or DCM with cyclohexane, MeOH, EtOH or iPrOH, EtOAc with hexane). The issue was then addressed by varying the reaction conditions, by both using longer reaction times (48, 72 and 96 hours) and larger equivalents of **75** (3.5, 4.5 and 5 equivalents) to further the reaction towards the formation of the tripodal ligand, however, with no success. This behaviour was speculated to be to the reduced reactivity of the aromatic amine in the 4 position from an amide group; the presence of the carbonyl prevents the delocalization of the electrons over the aromatic ring, activating it instead towards electrophilic substitution.

The use of *d*-block metals, and in particular Zn(II), to form supramolecular polymers has been reported in a previous work from the Gunnlaugsson group.[118] An attempt at using **75** as a ligand to form a Zn(II) complex was made with the aim of obtaining a

"supramolecular monomer" suitable for the formation of supramolecular polymers. **75** was dissolved in MeOH and stirred for 24 hours in presence of $ZnCl_2$, after which the solvent was removed under reduce pressure and the resulting solid was characterised. In **Figure 2.10** the mass spectrum obtained using an ESI instrument is shown.

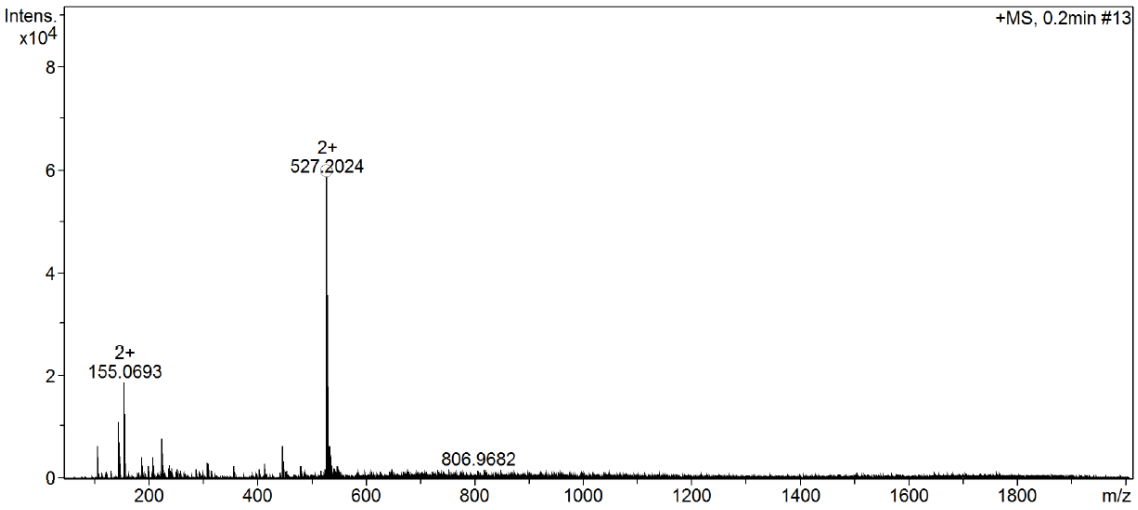

Figure 2.10 ESI^+ Mass spectrum for Zn·**75** complex, with the [M+Zn] peak.

The mass spectrum shows clearly the formation of the 1:1 M:L complex, but not the formation of the 1:2, or higher molecular weight aggregates. This confirmed the ability of **75** to bind to the metal, but nothing seemed to hint at the formation of higher complexity structures. Further studies will be performed using different metals and conditions to attempt to achieve the supramolecular polymerization.

Although this method did not prove too suitable in obtaining ligands **53 - 55**, it still yielded some interesting building blocks that could be used for different project in the Gunnlaugsson Group. Furthermore, it was possible to obtain the crystal structures for intermediates **66** and **70** using X-Ray Diffraction (XRD) neither of which had been reported before. More details about this, will be discussed in the following section.

2.5 Crystallographic studies of 66 and 70

Suitable single crystals of **66** were obtained from vapor diffusion of Et_2O into MeOH. Crystallographic data and refinement parameters, resolved by fellow Gunnlaugsson group member June Lovitt, are summarised in **Table 2.2**. The X-ray diffraction analysis of white block crystals provided a structural model in the triclinic *P*1 space group. The asymmetric unit contains two unique molecules of the ligand with full chemical occupancy and no solvent or guest molecules present within the unit cell lattice as illustrated in **Figure 2.11 A**.

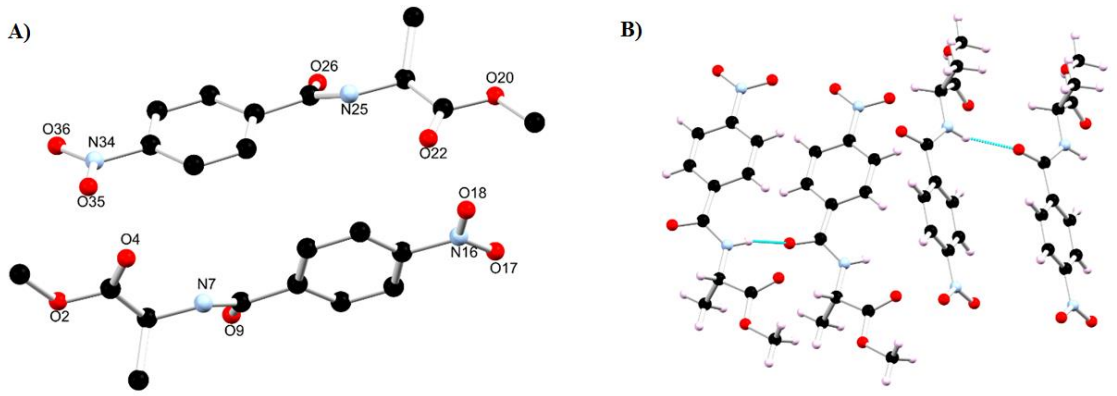

Figure 2.11 Structure of **66** with heteroatom labelling scheme. Asymmetric unit (**A,** Hydrogen omitted for clarity) and extended structure (**B**) with H-bonding among adjacent units highlighted in cyan.

The extended structure of **66**, shown in **Figure 2.11 B**. features a hydrogen bond interactions between the N-H of one ligand molecule and the carbonyl group of the neighbouring molecule with (N7···O9) distance of 2.91721(18) Å and (N7···H7···O9) angle of 153.805(2)°. There are also weak C-H···heteroatom interactions between adjacent molecules, for instance there are C-H···O interactions with a (O22···C23) distance of 3.4780(2) Å and an angle of 170.2158(7)° (O22···H23···C23 angle). Finally, there are C-H···O interactions between the nitro group of one ligand molecule and the ester group of the neighbouring ligand molecule (O36···C1) distance of 3.39685(17) Å and an angle of 141.378(3)° (O36···H1A···C1). These interactions support the adjacent ligand units assembling in a head to tail arrangement as illustrated in **Figure 2.12**.

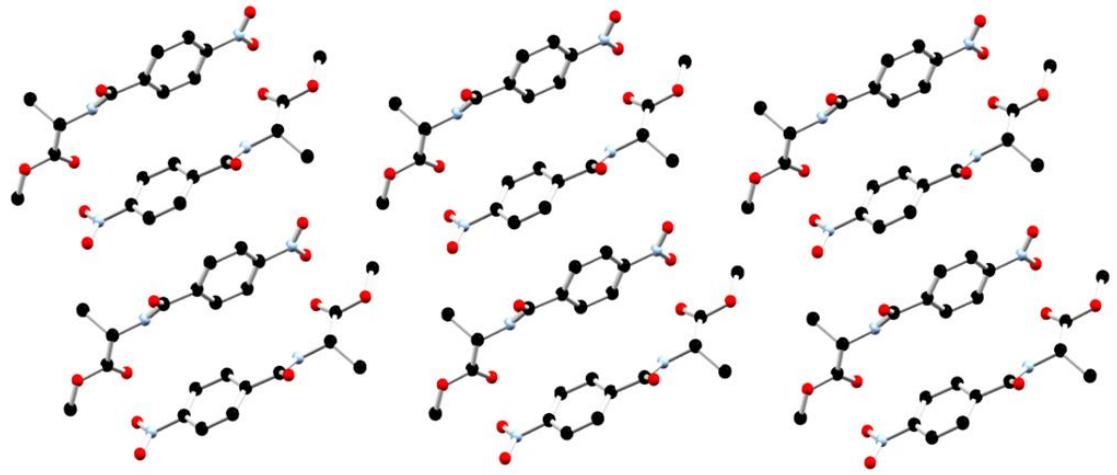

Figure 2.12 Extended structure of **66** illustrating the head to tail packing interactions of the ligand supported through H-bond and C-H···O interactions.

Suitable single crystals of **70** from Et_2O diffusion from MeOH solutions. Crystallographic data and refinement parameters are summarised in **Table 2.2**. The X-ray diffraction analysis of white block crystals provided a structural model in the monoclinic $P2_1$ space

group. Again, the asymmetric unit contains two unique molecules of the ligand with full chemical occupancy and no solvent or guest molecules present within the unit cell lattice as illustrated in **Figure 2.13 A**.

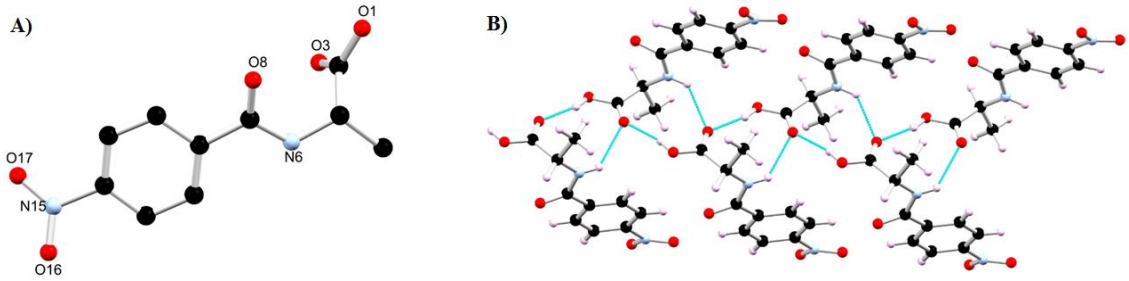

Figure 2.13 Structure of **70** with heteroatom labelling scheme (**A,** Hydrogen omitted for clarity) and extended structure (**B**) with H-bonding among adjacent units highlighted in cyan.

Again, looking at the extended structure of **70**, it is possible to observe hydrogen bond interactions. In this case, these interactions form between the carboxylic acid groups of adjacent ligand molecules and the carbonyl group of the neighbouring molecule with (O3···O1) distance of 2.673(3) Å and (O1···H1···O3) angle of 162.63(16)°. There are also weaker hydrogen bonds between the amine N-H in one ligand molecule and the carbonyl group of the adjacent molecule with a (N6···O3) distance of 2.926(4) Å and an angle of 132.48(19)° (O3···H6···N6 angle). These interactions support the adjacent ligand units assembling as illustrated in **Figure 2.13 B**.

Table 2.2 Crystal data and structure refinement for **68** and **72**.

Identification code	**66**	**70**
Empirical formula	$C_{12}H_{12}NO_5$	$C_{20}H_{20}N_4O_{10}$
Formula weight	250.23	476.40
Temperature/K	100.0	273.15
Crystal system	triclinic	monoclinic
Space group	P1	$P2_1$
a/Å	4.9378(3)	6.9360(4)
b/Å	8.5248(5)	7.1749(4)
c/Å	14.3646(9)	10.4969(6)
α/°	75.251(4)	90
β/°	89.912(4)	96.510(4)
γ/°	89.924(4)	90
Volume/Å^3	584.74(6)	519.01(5)
Z	2	1

ρ_{calc}g/cm^3	1.421	1.524
μ/mm^{-1}	0.951	1.068
F(000)	262.0	248.0
Crystal size/mm^3	0.03 × 0.04 × 0.03	0.04 × 0.1 × 0.05
Radiation	CuKα (λ = 1.54178)	CuKα (λ = 1.54178)
2Θ range for data collection/°	6.362 to 119.248	19.142 to 117.846
Index ranges	-5 ≤ h ≤ 5, -9 ≤ k ≤ 9, -15 ≤ l ≤ 15	-7 ≤ h ≤ 7, -7 ≤ k ≤ 7, -11 ≤ l ≤ 11
Reflections collected	6189	3149
Independent reflections	3255 [R_{int} = 0.0366, R_{sigma} = 0.0487]	1462 [R_{int} = 0.0434, R_{sigma} = 0.0500]
Data/restraints/parameters	3255/3/329	1462/1/157
Goodness-of-fit on F^2	1.052	1.060
Final R indexes [I>=2σ (I)]	R_1 = 0.0322, wR_2 = 0.0830	R_1 = 0.0390, wR_2 = 0.1028
Final R indexes [all data]	R_1 = 0.0334, wR_2 = 0.0844	R_1 = 0.0407, wR_2 = 0.1042
Largest diff. peak/hole / e Å^{-3}	0.17/-0.17	0.27/-0.21
Flack parameter	0.06(10)	-0.1(2)

2.6 Synthesis of Eu·54 1:1 complex

The formation of the Ln(III) complexes was achieved employing the procedure established in the Gunnlaugsson group for the synthesis of 1:1 L:M Ln(III) complexes under thermodynamic control. The ligand was reacted with 1 mole equivalent of Eu(CF_3SO_3)$_3$ in CH_3OH at 70 °C under microwave irradiation for 60 minutes (**Scheme 2.9**). The reaction mixture obtained was then concentrated under reduced pressure and then the complexes were precipitated by ether diffusion to yield **Eu·54** as off-white solid in near quantitative yield.

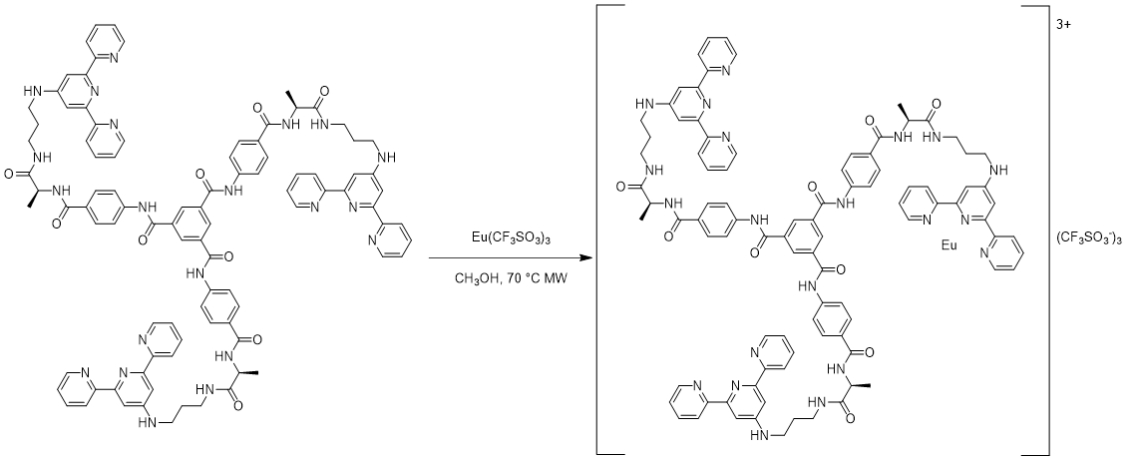

Scheme 2.9 Synthesis for complex **Eu·54**. The reaction was performed in a Biotage microwave reactor.

Ln(III) complexes, due to the paramagnetic nature of these ions, make the use of magnetic-based techniques such as ^{1}H-NMR very limited, as the proton resonances broaden and shift significantly, resulting in spectra that are hardly interpretable.

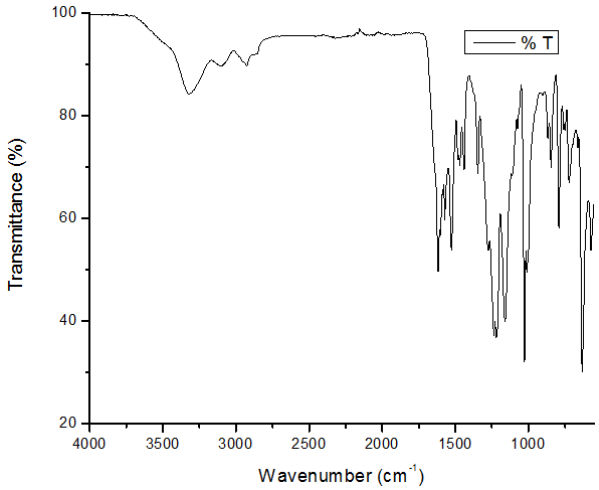

Figure 2.14 FTIR spectrum of **Eu·54** complex formed upon MW irradiation.

The complex was then characterised using infrared (IR) spectroscopy (**Figure 2.14**) and the formation of the complex was further confirmed by the appearance of the Eu(III) characteristic peaks in emission spectroscopy. The presence of a very broad pyridinic signal at 3500 cm^{-1} shows the formation of the complex through the tpy units. UV-Vis spectroscopy, shown in **Figure 2.15**, allowed to confirm the formation of **Eu·54** from the emission spectrum in phosphorescence mode, where it is possible to see (orange curve) the presence of peaks relative to the $^{5}\mathbf{D_0}\rightarrow{}^{7}\mathbf{F_n}$ transition between 460 and 600 nm. A characterization though mass spectrometry was also attempted, through MALDI-MS. Unfortunately, using different matrices it was not possible to observe signals, relative to the complex, with the characteristic peak distribution for Europium complexes.

The spectroscopic and morphologic characterization of the complex will be widely discussed in the following chapter together with that of the free ligand, to show further evidence of the formation of the complex.

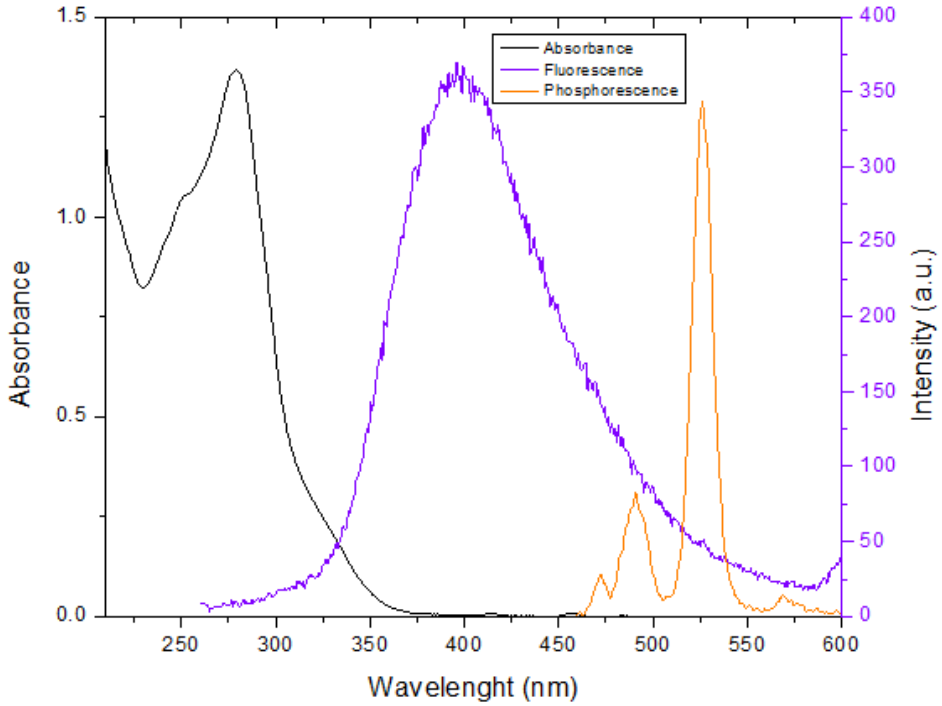

Figure 2.15 Absorbance (black), fluorescence (purple) and normalised phosphorescence (orange) spectra for **Eu·54** (c = 10 µM) obtained in microwave reactor. Phosphorescence low-intensity was increased four times to be comparable to fluorescence.

2.7 Conclusion

The synthesis of a family of tripodal ligands containing a rigid aromatic group, an amino acid moiety and a metal-binding terpyridine functionality was outlined in this chapter. Numerous setbacks were encountered during the development of adequate and satisfying synthetic procedures and in the characterization of these systems. These issues were addressed and a synthetic procedure capable of overcoming such setbacks was obtained and described. The use of this procedure to further widen the library of tripodal ligands, in order to further study their potential aggregator properties was detailed and will continue to be employed in future studies.

An alternative synthetic pathway to the target molecule was also presented. Although this desired goal was not fully achieved, another series of potential building blocks were also presented and synthesized, with a specific synthetic protocol. Two of such derivatives were recrystallized and the structure, which had not yet been reported, was obtained and resolved through the use of single crystal X-Ray crystallography. An attempt at obtaining

supramolecular complexes through the use of metal ions was also performed and will be further investigated in the future.

The following chapter will further introduce characterization techniques involved in probing the behaviour of the tripodal system synthetized herein both spectroscopically and morphologically.

Chapter 3

Spectroscopic and morphologic studies of BTA-based tripodal systems

3.0 Introduction

Once the synthesis of ligands **53 - 55** was achieved as described in the previous chapter, these ligands were investigated to gain a better understanding of their self-assembly behaviour in solution. In this Chapter, the study will focus on the behaviour of **54**, which was chosen for the smaller size of the side group linked to the chiral atoms, by using various spectroscopic studies, such as monitoring the changes in the ground and the excited states upon formation of supramolecular self-assemblies in methanol. Previous studies in the Gunnlaugsson group have demonstrated that probing these changes can lead to information about stoichiometry, distribution of the species in solution, etc., while the use of Circular Dichroism (CD) and NMR spectroscopy can get information about changes in the local environment of some parts of the ligands.

Hence, this would allow to evaluate the effect of the chiral group on the aggregation while not increasing further the complexity of the system. To do so, the ligand was initially investigated in solution at low concentration, both as a free ligand and while forming metal complexes or conjugates (supramolecular polymers). These same solutions were then dropcasted on to silicon wafers and studied using morphologic techniques such as Scanning Electron Microscopy (SEM).

Overall, the studies described in this Chapter will highlight the behaviour of ligand **54** and for complex **Eu·54** in solution, from where the properties such as the molar attenuation coefficient, **ε**, the number of solvent molecules bound to the metal in the complex, ***q value***, the life times for the species in solution, **τ**, emissive behaviour and the binding constant for the **1:1**, **1:2** and **1:3** (**L:M**) complexes. The morphology studies allowed to gain an understanding of the structure that the system acquires on the micro- and nano-scale. Further spectroscopic and morphologic studies, in particular for compound **55**, will be shown and discussed in Chapter 4, as they adopt particular relevance to the work described there.

3.1 Dilution studies for 54 as a free ligand

For these studies it was decided to use competitive and hydrogen bonding solvents. Hence, at first instance the use of MeOH was decided upon. A 10 μM solution of **57** in CH_3OH was prepared and the absorbance spectrum was recorded between 200 and 400 nm. The spectrum showed the presence of a band centred at 277 nm, indicating the presence of a $\pi \rightarrow \pi^*$ transition. The solution was then progressively diluted to 0.52 μM while monitoring the behaviour of absorbance and emission as a function of the

concentration. Upon dilution, it was possible to observe a linear decrease in absorbance, with no shifts in the λ_{max} of the band (**Figure 3.1 A**). This would indicate that no ground states interactions were observed within this concentration range, in this competitive medium.

Hence, this behaviour seems to exclude the formation of aggregates in the concentration range studied, which makes such concentration range ideal for single molecule solution spectroscopic studies. Absorbance values at 277 nm were plotted as a function of concentration (**Figure 3.1 B**), and through linear fitting, it was possible to obtain the molar extinction coefficient at 277 nm, $\boldsymbol{\varepsilon_{277nm}}$. The value averaged over three measurements was found to be 119450±1260 M^{-1} cm^{-1} ($\log\varepsilon_{277nm}$ = 5.077±3.100).

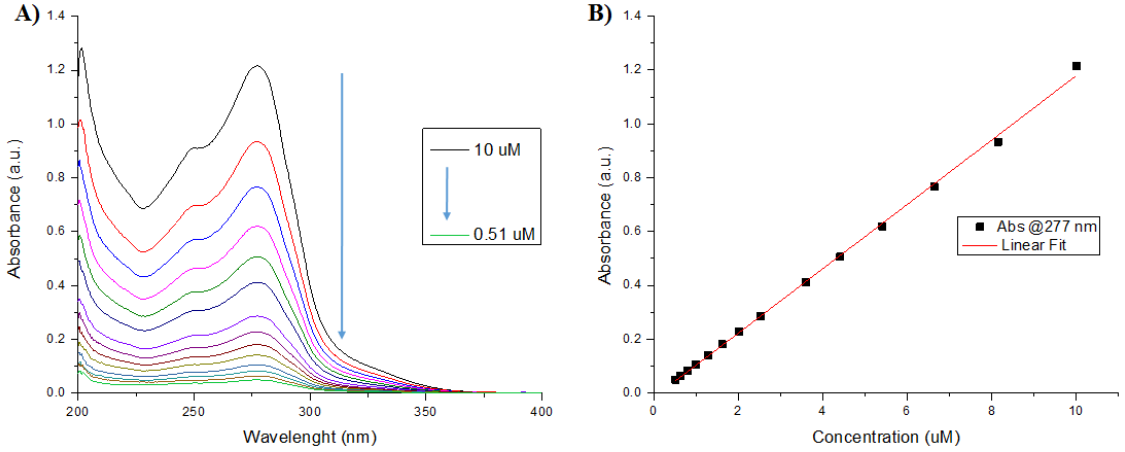

Figure 3.1 Absorbance spectra (**A**) and binding isotherm at 277 nm (**B**) for **54** in MeOH (*0.52 μM→*10 *μM).*

Upon exciting at 277 nm, a fluorescence emission centred at 408 nm was observed in MeOH. Concomitantly to the absorbance studies, the emission spectra were recorded (**Figure 3.2 A**). Plotting the intensities at 408 nm against concentration (**Figure 3.2 B**) it was possible to observe a linear behaviour at low concentration range (c = 0.5 – 3.5 μM) that reaches the saturation at higher values (c ≥ 8.15 μM) (**Figure 3.2**). This result was initially considered as an effect of inner filters induced by interactions between the molecules in the solution; this hypothesis was contested by the absence of a shift in the wavelength of the maximum. It was then considered that over the threshold found (8.15 μM) molecules of **54** undergo a self-assembly processes to form supramolecular aggregates.

To address the two different behaviours observed in the fluorescence isotherms, two separate sets of titrations at different initial concentration for ligand **54** were performed.

This choice was made in order to gain a better understanding on the self-assembly processes happening at different concentration ranges.

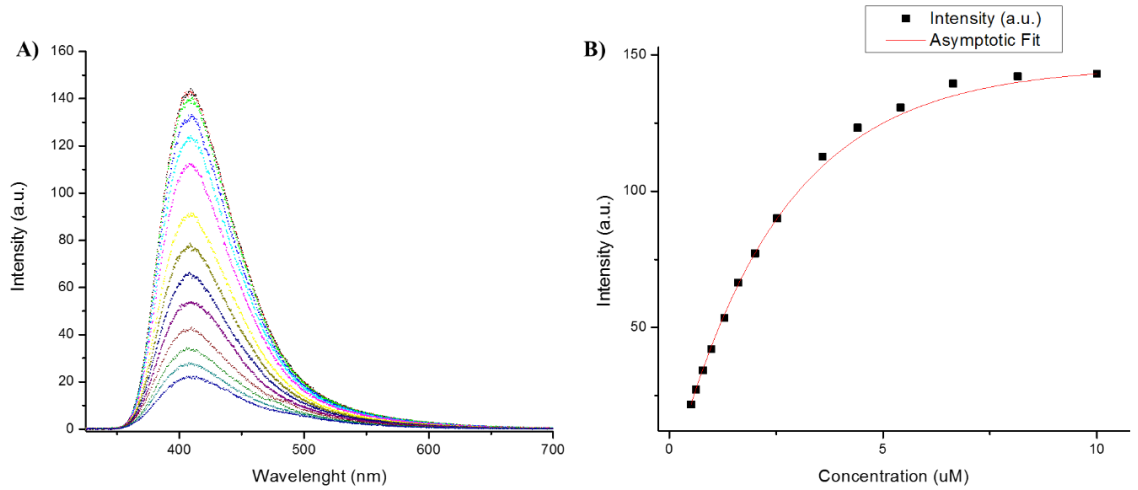

Figure 3.2 Fluorescent spectra of **54** upon dilution (A) and fitted isotherm (B) with the intensity at 408 nm against concentration (B, black dots) and asymptotic fit (B, red line).

3.2 Lifetime studies for Eu·54 complexes and q values

Having studied the ground and excited states properties of **54**, the **Eu·54** complex, synthesized in Chapter 2 was investigated next. The optical properties of the Ln(III) complexes were investigated using various spectroscopic techniques in CH_3OH solution. Initially, the complexes investigated were formed under thermodynamic control and followed by kinetic control. In this section, the focus will be on the complex formed under thermodynamic control.

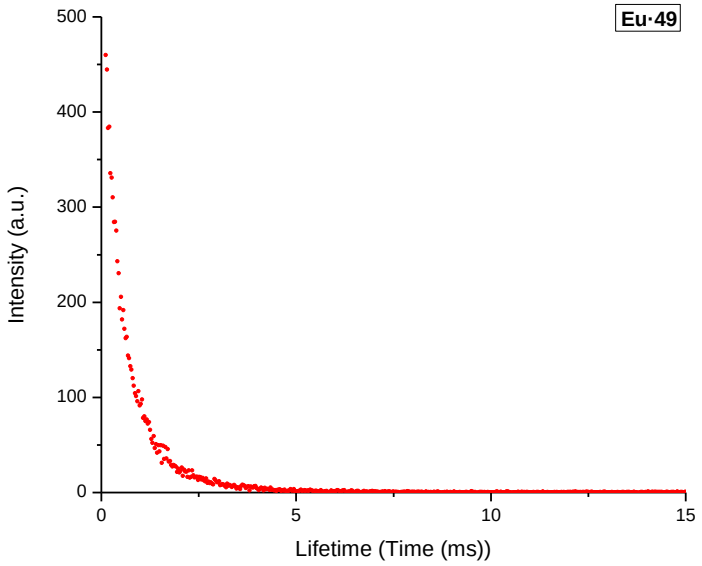

Figure 3.3 Eu(III)-centred emission decay recorded for **Eu·54** solution (c = 10 μM) in CH_3OH (λ_{ex} = 277 nm).

Solutions of **Eu·54** were prepared as described in **Section 2.6** with the concentration of 10 μM in CH_3OH and their absorption, fluorescence and phosphorescence spectra, were recorded at 21 °C and have been shown in Chapter 2.
The Ln(III) ions, as discussed in Chapter 1, **Section 1.3.1** possess high coordination requirements; in particular, Eu(III) and Tb(III) have a coordination number of nine.[90] When the donor atoms of the ligands are unable to fulfil the coordination sphere of the Ln(III) ion, it is completed by solvent molecules. To determine the presence of solvent molecules bound to the metal ion core, the excited state of **Eu·54** at 1:1 (**L:M**) stoichiometry was investigated. The hydratation state, or the number of bound water molecules, *q value*, was derived following Formula 1.1 by Parker *et al*,[106] shown already in the Introduction Chapter, presented using the luminescence lifetimes of each complex in both in CH_3OH (τ_{CH3OH}) and CD_3OD (τ_{CD3OD}).

$$q = A\left[\left(\frac{1}{\tau_{CH3OH}} - \frac{1}{\tau_{CD3OD}}\right) - 0.25 - 0.075x\right] \qquad \textbf{\textit{Formula 3.1}}$$

The life times were determined upon fitting the of Eu(III) excited state decay profiles, using the most intense Eu(III) transition, corresponding to the $^5D_0 \rightarrow {}^7F_2$ band centred at 617 nm. The decays were fitted using monoexponential curves that yielded a value averaged over three measurements resulting in τ_{CH3OH} = 0.56±0.01 ms and τ_{CD3OD} = 0.83±0.01 ms. In the **Formula 3.1** the term A is a proportionality constant relative to the solvent used, equal to 2.1 ms in the case of methanol, while the final term, 0.075*x*, was introduced by Parker and it takes into account the quenching induced by second sphere solvent molecules and the vibration relative to the N–H bonds. Parker, who was using an amide functionalised cyclen as ligand, defined *x* as the number of amide N–H oscillators bound directly to the metal *via* the oxygen atom of the carbonyl group; in the case of terpyridine ligand, this contribution becomes irrelevant as in this case *x* = 0. The q values calculated for the 1:1 complex **Eu·54** showed the value of 0.4±0.5, indicating that the terpyridine groups are able to saturate the metal, as it had been previously reported.[108, 119] Furthermore, this is consistent evidence of the 1:1 stoichiometry, as each Eu(III) ion would complex three different terpyridine units of one ligand, and each ligand would be binding one Eu(III) ion overall.

3.3 Spectroscopic Titration of 54 with $Eu(CF_3SO_3)_3$

The formation of the Ln(III) complexes under kinetic control was investigated performing spectroscopic titrations of the ligand with $Eu(CF_3SO_3)_3$ in CH_3OH solution at 25 °C. To perform these measurements, stock solutions of the ligand were prepared and then diluted to the desired final concentration in the (1 cm) cuvette. As reported in **Section 3.1**, the different behaviour of the isotherms for absorbance and fluorescence spectra suggests the possibility of the ligand aggregation at higher concentration, initiated the solution self-assembly studies at different concentrations with the goal to understand how the behaviour would change upon addition of the metal ions.

Initially, the titration was performed with a starting concentration of **54** of 10 μM in MeOH, at which absorbance was found to be within linear range of the absorbance *vs* concentration curve (**Figure 3.1 B**) while on the plateau for the same fluorescence curve (**Figure 3.2 B**) suggesting the possibility of supramolecular polymer formation between ligand molecules. These solutions were then titrated using a stock solution of the metal in MeOH at 1 mM for the additions. The second set of measurements was performed using solutions of **57** at a concentration of 3 μM in MeOH, to which solutions of the *f*-metal ions were added. In this case, the ligand concentration is within linear range of absorbance and fluorescence changes *vs* concentration suggesting the presence of the ligand in solution as the single molecule (i.e. no aggregation occurs).

In both cases, the absorbance, excitation, fluorescence and phosphorescence spectra were recorded upon every addition. The titration was repeated several times for both conditions to ensure the reproducibility of the behaviours observed as stated above. These measurements would obtain titration data for the complexes formed under kinetic control and would be compared to those obtained for the complex formed under thermodynamic conditions. This would enable the similarities and differences in the nature of these systems to be directly compared.

3.3.1 UV-Vis absorption titration of 54 (c_L = 10 μM) with $Eu(CF_3SO_3)_3$

The absorbance spectra at a higher concentration range (**Figure 3.4 A**) confirmed the presence of a band centred at 277 nm that upon addition of *f*-metal ions showed hypochromic effect, decreasing until reaching a minimum value of absorbance. Furthermore, it was possible to observe an hyperchromic effect that leads to the formation

of a shoulder around 320 nm. This becomes particularly evident observing the binding isotherms at different wavelengths (**Figure 3.4 B**), as they clearly show the presence of the absorbance values reaching a plateau after 2 equivalents of metal ions added.

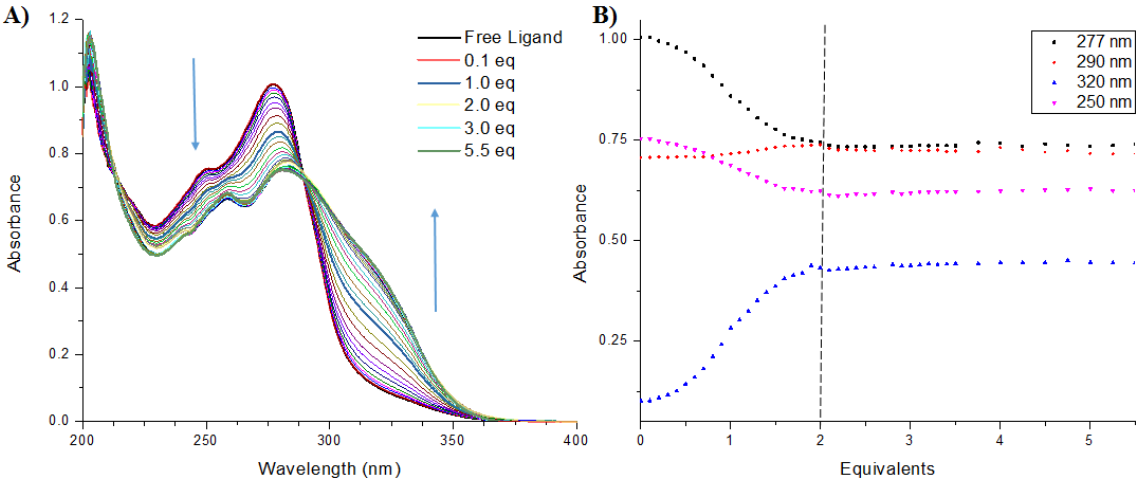

Figure 3.4 Absorbance spectra (A) and binding isotherm curves at different wavelengths (B) upon the addition of $Eu(CF_3SO_3)_3$ to ligand **54** (c = 10 µM). The titration, performed at 25 °C, was repeated several times and showed the trend to be fully reproducible.

From the absorption spectra it is possible to see what initially appeared to be an isosbestic point at 290 nm; upon magnification, as well as observing the isotherms in **Figure 3.4 B** (red dots), the absorbance at 290 nm remains constant up to until 1 eq of Eu(III) added, followed by a slow increase up to 2 eq, after which the absorbance is constant again.

This kind of spectroscopic changes indicate the formation of species with a different stoichiometry upon the addition of the metal; in particular, judging by the isotherms, it would seem that in this concentration range, the system does not undergo any changes after two equivalents of the metal are added. The distribution of the species as a function of the metal equivalents will be further discussed in section **3.4.7** as this data was further analysed using non-linear regression analysis software, which would allow further understanding of the process that leads to the formation of the Eu(III) complex.

3.3.2 Fluorescence titration of 54 (c_L = 10 µM) with $Eu(CF_3SO_3)_3$

Concomitantly to the recording of the absorption spectra, the ligand-centred emission was also studied upon the addition of Eu(III) ions. Fluorescence spectra were recorded using an excitation wavelength of 277 nm. The ligand fluorescence spectra (**Figure 3.5 A**) show the same band centred at 408 nm already observed in **Section 3.1**, which upon the addition of the metal ions undergoes a progressive quenching. At the same time, excitation spectra, exciting at 408 nm, were recorded and are shown in the Appendix chapter. The quenching

progresses up to a minimum value of intensity after about 2.1 equivalents of metal are added. This is also in agreement with the changes observed in the absorption spectra. Contextually with such quenching, it is also possible to observe a change in the spectra shape, indicating the formation of a different species as shown as a function of added Eu(III). This behaviour becomes more evident observing the binding isotherm at 408 nm, plotted in **Figure 3.5 B**. The emission intensity of **54** decreases until about 2 equivalents of Eu(III) are added; after such value, it is possible to observe the intensity to increase again with a different trend, indicating a different species forming in solution. This data, which is consistent with the one observed for the absorption titration, further confirms the formation of the Eu(III) complex.

This behaviour is associated with a different processing of the energy absorbed after the irradiation: initially, the free ligand would emit fluorescent radiation after vibrational decay; after the addition of the metal, the energy is transferred from the excited level of the ligand to the metal centre, resulting in the quenching of the direct emission from the ligand. Although no signal relative to the Eu(III)-centred emission was observed in fluorescence mode, it was still possible to speculate that the quenching is proof of the close proximity of the metal ion centre to the ligand and, consequently, to the formation of the complexes; further confirmation of this will be given in the following section, where the metal-centred emission in phosphorescence mode was observed.

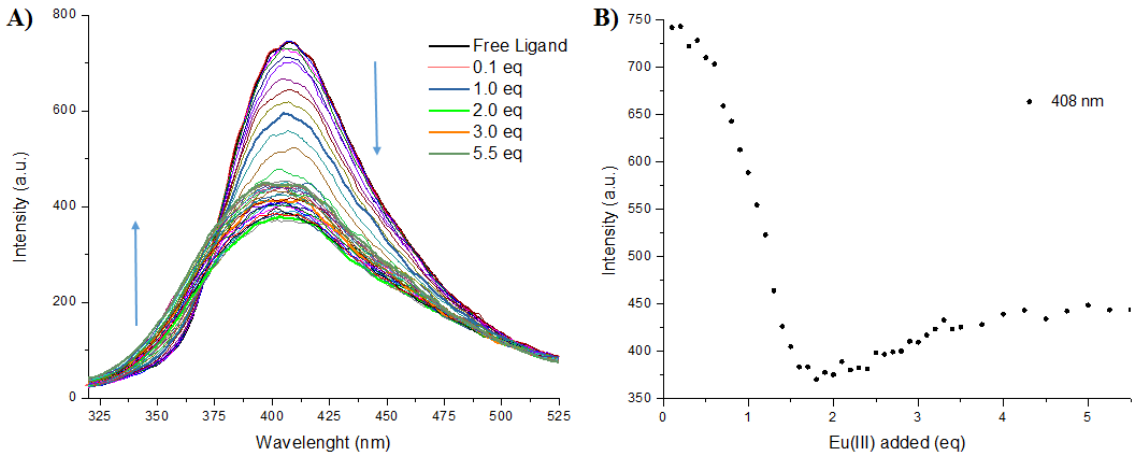

Figure 3.5 Fluorescence spectra (A) and isotherm at 408 nm (B) upon the addition of $Eu(CF_3SO_3)_3$ to ligand **54** (c = 10 μM), λ_{ex} = 277 nm. The titration, performed at 25 °C, was repeated several times and showed the trend to be reproducible.

3.3.3 Phosphorescence titration of 54 (c_L = 10 μM) with $Eu(CF_3SO_3)_3$

The emission of Eu(III) was recorded and measured in phosphorescence mode upon excitation at 277 nm as a function of increasing Eu(III) concentration. The

phosphorescence of the Eu(III) emission spectra are shown in **Figure 3.6, A**. The most intense signal is the one relative to the $^5D_0 \rightarrow ^7F_2$ transition, with a band centred at 617 nm; note, it is possible to see all the five transition, although the $^5D_0 \rightarrow ^7F_3$ transition is low in intensity. The high intensity of the band relative to the $^5D_0 \rightarrow ^7F_2$ transition is due to the band being a so-called "**hypersensitive transition**". These transitions, that have a $|\Delta J| \leq 2$, are strongly dependent on the geometry of the Eu(III) ion and in particular of the local asymmetry around it.[120] It is particularly interesting to observe the phosphorescence isotherms for the bands centred at 591, 617 and 690 nm, plotted in **Figure 3.6 B**. The emission intensity increases with the addition of 1 equivalent of Eu(III) added, after which it reaches a plateau for the bands at 591 and 690 nm; while 617 nm trends show a slow decrease. This was speculated to be related to small changes in the coordination environment around the metal ion.

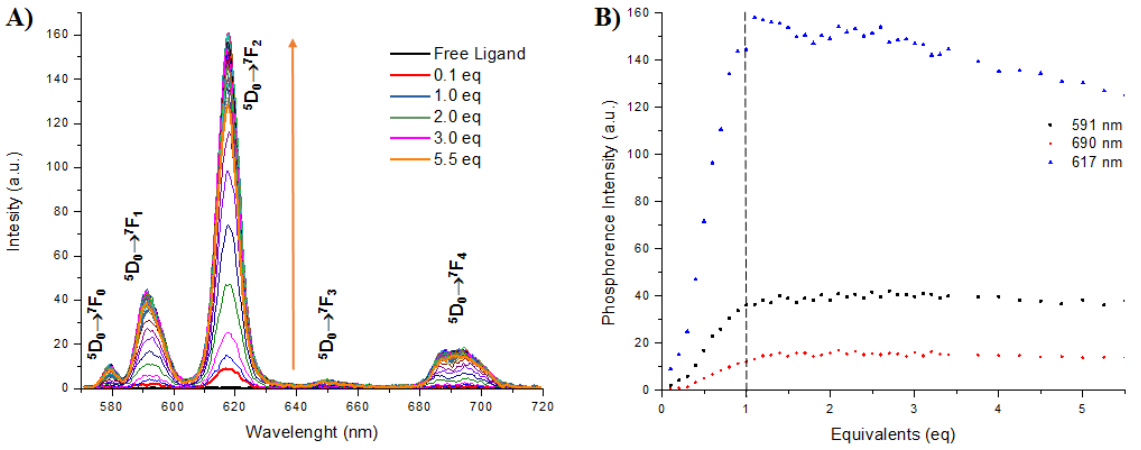

Figure 3.6 (A) Phosphorescence spectra for the titration of **54** (c = 10 µM) with Eu(III), λ_{ex} = 277 nm. The five Laporte-forbidden transitions can be observed. (B) Binding isotherms for the bands at 591, 617 and 690 nm. It is possible to notice a linear increase up to about 1 equivalent of Eu(III) added.

These results suggest that the species with 1:1 stoichiometry are the most emissive in solution. It is important to consider that a single ligand molecule of ligand possesses three binding moieties; this in fact leads to the consideration that a 1:1 M:L stoichiometry effectively means that every metal ion is bound by three terpyridine units. This result is in line with what was observed in previous works in the Gunnlaugsson group.[108]

The isotherms show a slow decrease of the intensity for the $^5D_0 \rightarrow ^7F_2$ transition, while the $^5D_0 \rightarrow ^7F_1$ and $^5D_0 \rightarrow ^7F_4$ remain substantially constant; this confirms that the species formed in the 1:1 stoichiometry have the most effective LMCT, while further addition of the metal ions induce the formation of species where the energy transfer is not as effective. This behaviour is reflected in the absorbance and fluorescence spectra; the disparity may be related to a series of factors, such as a change in the efficiency of the

energy transfer between ligand and metal centres and self-quenching processes taking places. To gain a better understanding of this, the results will be compared to the ones obtained for the system at lower concentration and processed using non-linear regression analysis.

3.3.4 UV-Vis absorption titration of 54 (c_L = 3 µM) with $Eu(CF_3SO_3)_3$

Upon first inspection, the behaviour at lower concentration was found to be similar to the one at higher concentration. As expected, examining the spectra, **Figure 3.7 A**, it is possible to see the band centred at 277 nm gradually decreases its absorption values upon the addition of the metal: while simultaneously the shoulder appears at around 320 nm. Conversely, when plotting the binding isotherms at four different wavelengths (**Figure 3.7 B**), it is possible to observe a marked difference in the behaviour of the system. At lower concentration the plot shows significant changes in the absorbance values with the addition of two equivalents of metal ions; while a plateau is observed after the addition of three and a half equivalents.

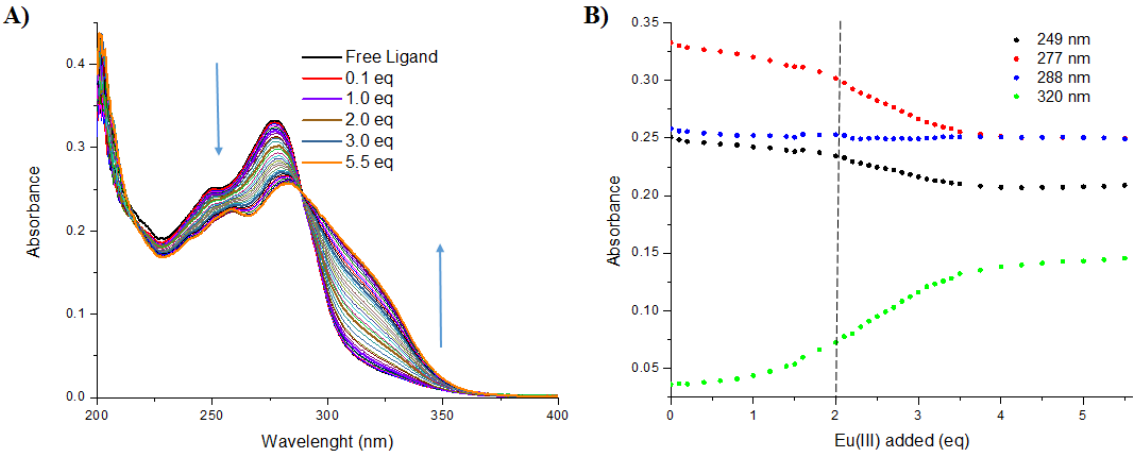

Figure 3.7 Absorbance spectra (A) and isotherm curves at different wavelengths (B) upon the addition of $Eu(CF_3SO_3)_3$ to ligand **54** (c = 3 µM), λ_{ex} = 277 nm. The titration, performed at 25 °C, was repeated three times and showed the trend to be reproducible.

These differences will be further analysed in the later sections, after investigating the emission spectra.

3.3.5 Fluorescence titration of 54 (c_L = 3 µM) with $Eu(CF_3SO_3)_3$

The ligand-centred emission was recorded and studied upon the addition of Eu(III) ions for the low concentration system. Once again, fluorescence spectra were recorded using an excitation wavelength of 277 nm. Due to the low concentration, the intensity recorded

for the fluorescence spectra was subsequently quite low; hence, the spectra shown on **Figure 3.8 A** details quite high levels of background noise.

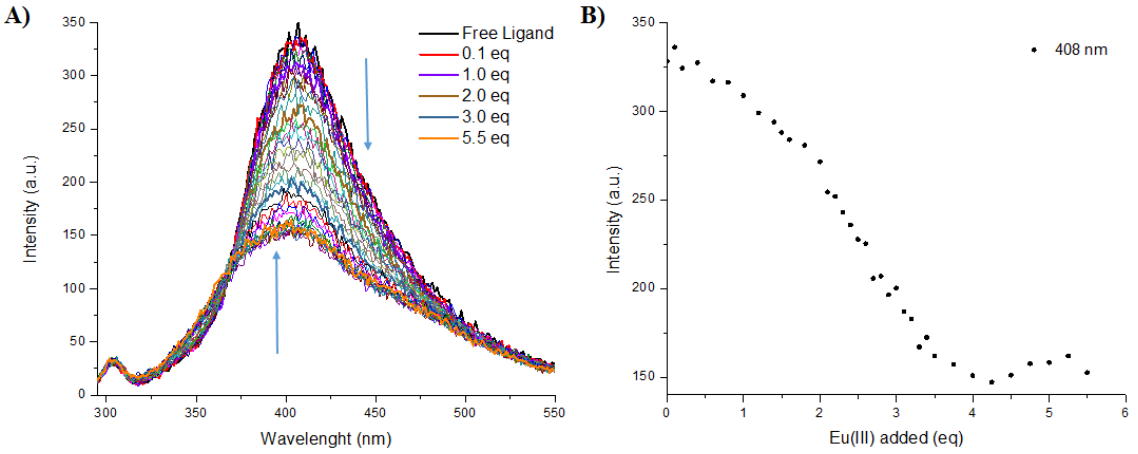

Figure 3.8 Fluorescence spectra (A) and isotherm at 408 nm (B) upon the addition of $Eu(CF_3SO_3)_3$ to ligand **54** (c = 3 μM), λ_{ex} = 277 nm. The titration, performed at 25 °C, was repeated three times and showed the trend to be reproducible.

In this case, as well, it was possible to observe the quenching of the ligand-centred emission. Analogously to findings observed for the absorbance spectra, the changes in the emission induced by the presence of the metal come at higher equivalents when compared to the higher concentration system. The slight increase in the luminescence after the quenching was observed after about 3.5 equivalents of metal had been added to the ligand.

3.3.6 Phosphorescence titration of 54 (c_L = 3 μM) with $Eu(CF_3SO_3)_3$

Finally, the metal-centred emission was investigated for the low concentration system, once again using an excitation wavelength of 277 nm. The phosphorescence spectra, shown in **Figure 3.9 A**, demonstrate an enhancement in the emission for all of the ΔJ values, with $^5D_0 \rightarrow {}^7F_3$ being the less intense and $^5D_0 \rightarrow {}^7F_2$ being the more prominent. As with the results witnessed in the fluorescence spectra, the initial emission intensity recorder was low; it is hypothesised that this was induced by a significant instrument noise, and upon revised instrumental tuning, it was possible to obtain satisfying intensity values.

Nonetheless, the emission spectra, and in particular the binding isotherms (**Figure 3.9 B**), confirm the trend shown by absorbance and fluorescence. The system demonstrates a linear trend up to 2 equivalents, particularly for the intensity at 617 nm (red dots), where

a plateau is observed between 2 and 3.5 equivalents, thereafter the intensity starts increasing again (although at a different rate).

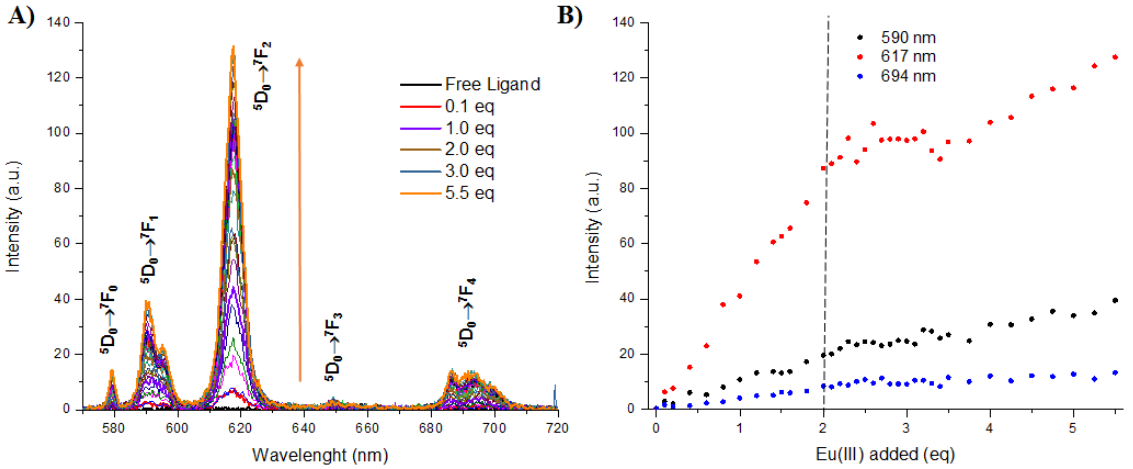

Figure 3.9 (A) Phosphorescence spectra for the titration of **54** with Eu(III) (c = 3 μM), λ_{ex} = 277 nm. The five Laporte-forbidden transitions can be observed. (B) Binding isotherm for the bands at 590, 617 and 694 nm. It is possible to notice a linear increase up to about 2 equivalent of Eu(III) added.

This seems to suggest a weaker influence of the metal at lower concentration, subsequently yielding lower amount of **M:L** assemblies in the solution and in turn to a lower binding constants of the species formed. Having examined the ground state and the excited state properties of **54**, the changes in the absorption and emission spectra were studied using non-linear regression analysis; these results will be discussed below.

3.3.7 Non-linear regression studies for the spectroscopic data

The spectroscopic data shown so far allowed to gain an insight on the behaviour for the ligand **54** both free and upon the addition of metal ions. In order to deepen this understanding and gain behavioural knowledge of the various species distribution in solution, the data was further processed using the SPECFIT software.[121] The program, which makes use of non-linear regression analysis, applies mathematical methods in order to minimise the differences between the experimental data and theoretical curves that the software generates according to a user-defined model; therefore, it was necessary to define the equilibria and the consequent species that could form. The equilibria take into account the formation of the different **M:L** species:

$$Eu + L \leftrightarrows EuL \qquad K_{1:1} = \frac{[EuL]}{[Eu][L]} \qquad \textit{Formula 3.2}$$

$$EuL + L \leftrightarrows Eu_2L \qquad K_{2:1} = \frac{[Eu_2L]}{[EuL][L]} \qquad \textit{Formula 3.3}$$

$$Eu_2L + L \leftrightarrows Eu_3L \qquad K_{3:1} = \frac{[Eu_3L]}{[Eu_2L][L]} \qquad \textit{Formula 3.4}$$

and so on; it is possible to write a single equilibrium equation that takes into account the formation of consecutive species, such as

$$nEu + mL \leftrightarrows Eu_nL_m \qquad \textbf{\textit{Formula 3.5}}$$

For which it is possible to write a global aggregation constant, $\beta_{n:m}$:

$$\beta_{n:m} = \frac{[Eu_nL_m]}{[Eu]^n[L]^m} \qquad \textbf{\textit{Formula 3.6}}$$

As the software yielded the association constants as their logarithmic values, the global aggregation constant will also be addressed as its logarithmic value, $\log\beta_{n:m}$. The software models were compiled with data obtained in both concentrations ranges in absorbance. Initially, the data from the high concentration was processed. The initial model used for the fitting program considered three different species, the complexes in 1:1, 1:2, and 1:3 (**L:M**) stoichiometries, together with the free ligand. **Figure 3.10 A** shows the recalculated and consolidated spectra of the four different species. The quality of the fitting was initially valued by plotting the binding isotherms together with the relative fits (**Figure 3.10 B**).

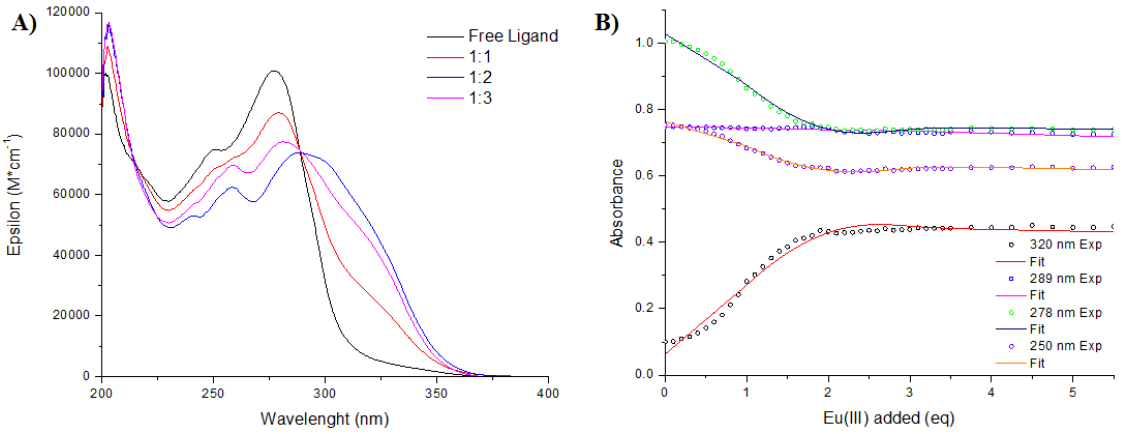

Figure 3.10 Recalculated spectra of the single species (**A**) and experimental binding isotherms (and relative fitting) (**B**) obtained processing the system at c_{57} = 10 μM using the fitting model which included the 1:1, 1:2 and 1:3 **L:M** complexes.

Table 3.1 Binding constants obtained for the titration of **54** (c = 10 μM) with $Eu(CF_3SO_3)_3$ showing three species using the SpecFit software

Stoichiometry (L:M)	logβ	StD
1:1	10.03	±1.02
1:2	17.13	±1.03
1:3	23.59	±1.03

Upon obtaining the fitting, the software successfully delineated the binding constants for the three species, that are summarised in **Table 3.1**. The value obtained for

these constants show that the 1:1 complex is the most stable, with a constant of 10.03; the 1:2 and the 1:3 are less stable, with constants of respectively 7.10 and 6.46. Comparing these values with the ones obtained in a previous work from the Gunnlaugsson group,[122] it can be seen that the three binding constants for **54** are generally greater than the ones for both **49R** and **49S** ($\log\beta_{1:1}$ = 8.49 ± 0.16, $\log\beta_{1:2}$ = 7.11 ± 0.17, $\log\beta_{1:3}$ = 5.0 ± 0.19 and $\log\beta_{1:1}$ = 8.51 ± 0.36, $\log\beta_{1:2}$ = 7.59 ± 0.40, $\log\beta_{1:3}$ = 5.5 ± 0.41 respectively), with the only exceptions being the $\beta_{1:2}$, which was greater in both cases. This seems to suggest that, in this three species model, **54** binds Eu(III) more strongly when compared to **49R/S**. These values allowed the software to plot the formation diagram for the three species, shown in **Figure 3.11**. The speciation distribution diagram reflects the overall changes in solution upon adding Eu(III). The formation of the 1:3 species is favoured at higher equivalents of metal added, being formed in over 90% after adding 3.5 equivalents of Eu(III).

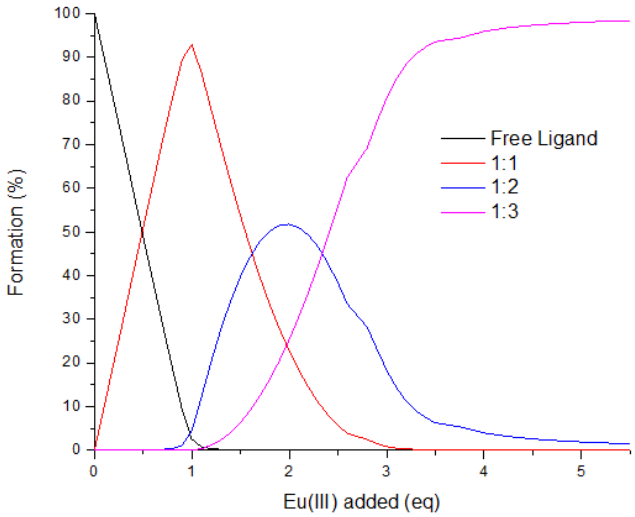

Figure 3.11 The speciation distribution diagram for the species obtained using the binding model which included the formation of 1:1, 1:2 and 1:3 **L:M** complexes.

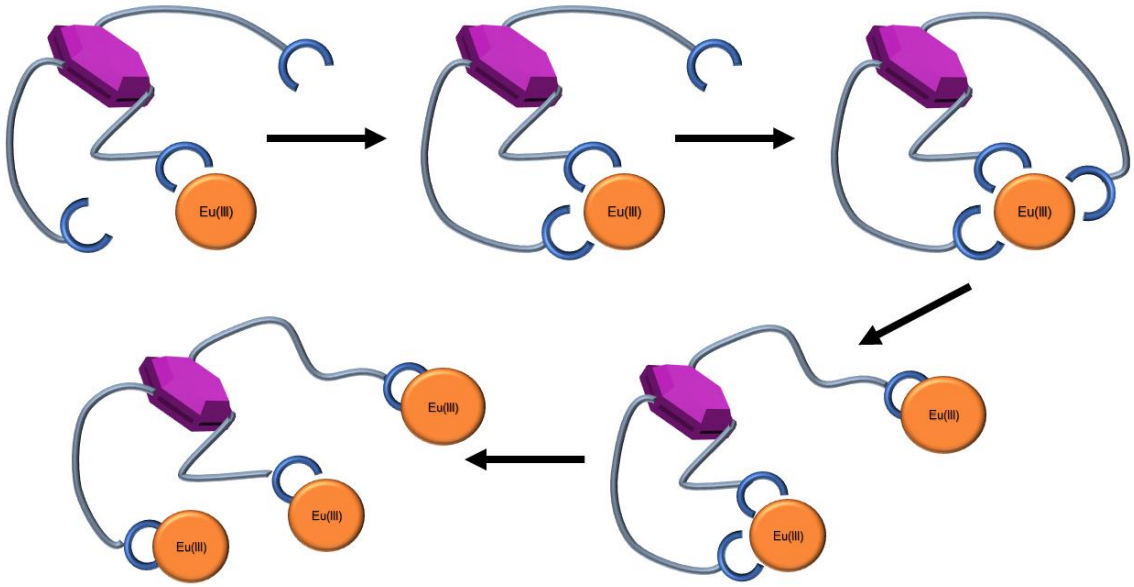

Figure 3.12 Schematic representation of the binding mode for the system that progressively forms the L:M 1:1, 1:2 and 1:3.

The fit, although allowing to obtain the binding constants, presented relatively high values of standard deviations for them; to address this, a fitting attempt that involved a different binding model was attempted. In this case, the species taken into account were the 1:1 and the 3:2; this binding model had been proved successful in describing similar systems previously presented in the Gunnlaugsson group.[108, 122]

This second fit allowed to get, once again, the recalculated spectra of the three species (**Figure 3.13 A**). It is particularly interesting to notice how the molar absorptivity for the 2:3 species was found to be higher than the "simple" species; this is to be expected, considering the 2:3 species contains two absorbing centres. The isotherms and the relative fits, shown in **Figure 3.13 B**, can again be considered a good measure of the quality of the fit.

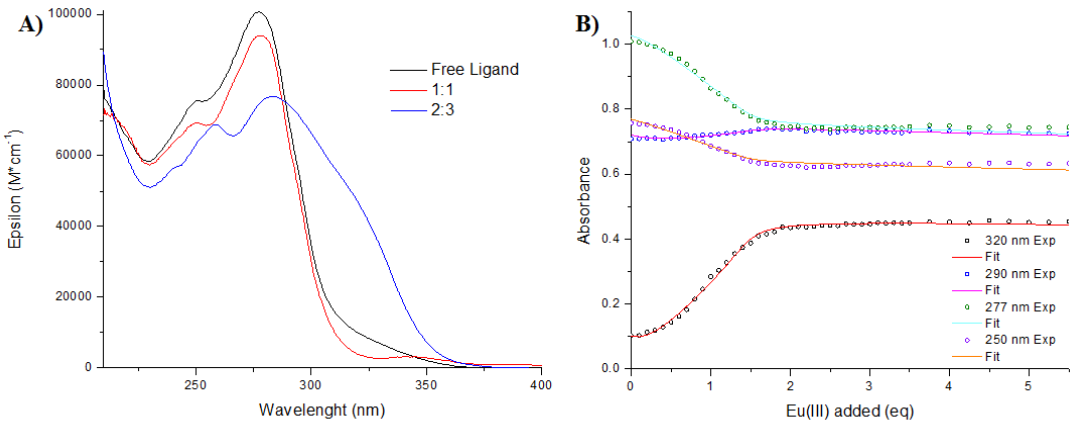

Figure 3.13 Recalculated spectra of the single species (**A**) and experimental binding isotherms (and relative fitting) (**B**) obtained processing the system at c_{57} = 10 μM using the binding model which included the 1:1 and 2:3 **L:M** complexes.

The binding constants obtained from the software are reported in **Table 3.2**. In this case, comparing the values of the binding constants to previous studies in the Gunnlaugsson group[108] ($\log\beta_{1:1}$ = 7.2 ± 0.3, $\log\beta_{2:3}$ = 23.3 ± 0.4), it was possible to see that while the 1:1 species presents $\beta_{1:1}$ lower than the one previously observed; the $\beta_{2:3}$ is almost two order of magnitudes higher for **54**, again hinting a higher stability for this **Eu·54** specie.

Table 3.2 Binding constants obtained for titration of **54** (c = 10 μM) with $Eu(CF_3SO_3)_3$ showing the two complexes obtained fitting absorbance data using the SpecFit software.

Stoichiometry (L:M)	logβ	StD
1:1	6.66	± 0.20
2:3	25.55	± 0.28

The two binding constants demonstrate that in this second model, the 1:1 species has a much lower binding constant, $\beta_{1:1}$ = 6.66, while the $\beta_{2:3}$ species present a very high global aggregation constant, 25.55; this was unsurprising, when considering the exponents that such stoichiometry would introduce using ***Formula 5***. Furthermore, the standard deviations were found to be much lower, indicating a more accurate fitting. Through the constants, it was again possible to obtain the speciation distribution diagram, **Figure 3.14**.

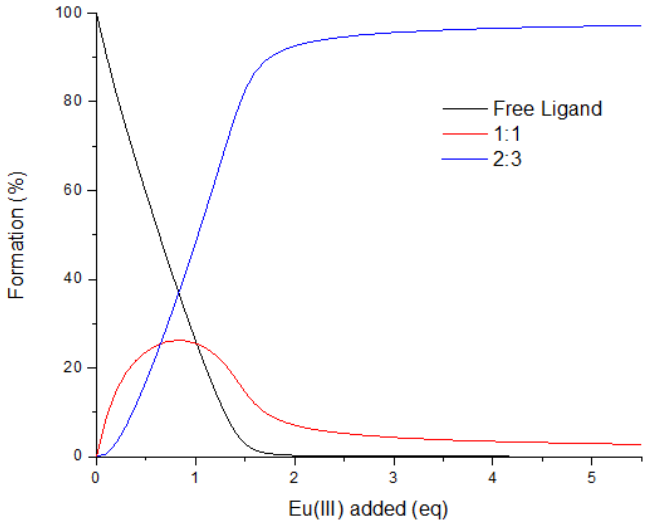

Figure 3.14 The speciation-distribution diagram for the species obtained using the fitting model which included the 1:1 and 2:3 complexes.

Studying the speciation distribution diagram, it was possible to observe that although the 1:1 **L:M** species started forming upon the addition of the metal, shortly after reaching 0.5 equivalents, the formation of the 2:3 species became predominant. The two

species (as well as the free ligand) initially coexist, until a total predominance of the 2:3 species upon reaching 1.5 equivalents of metal added, with a formation over 80 %.

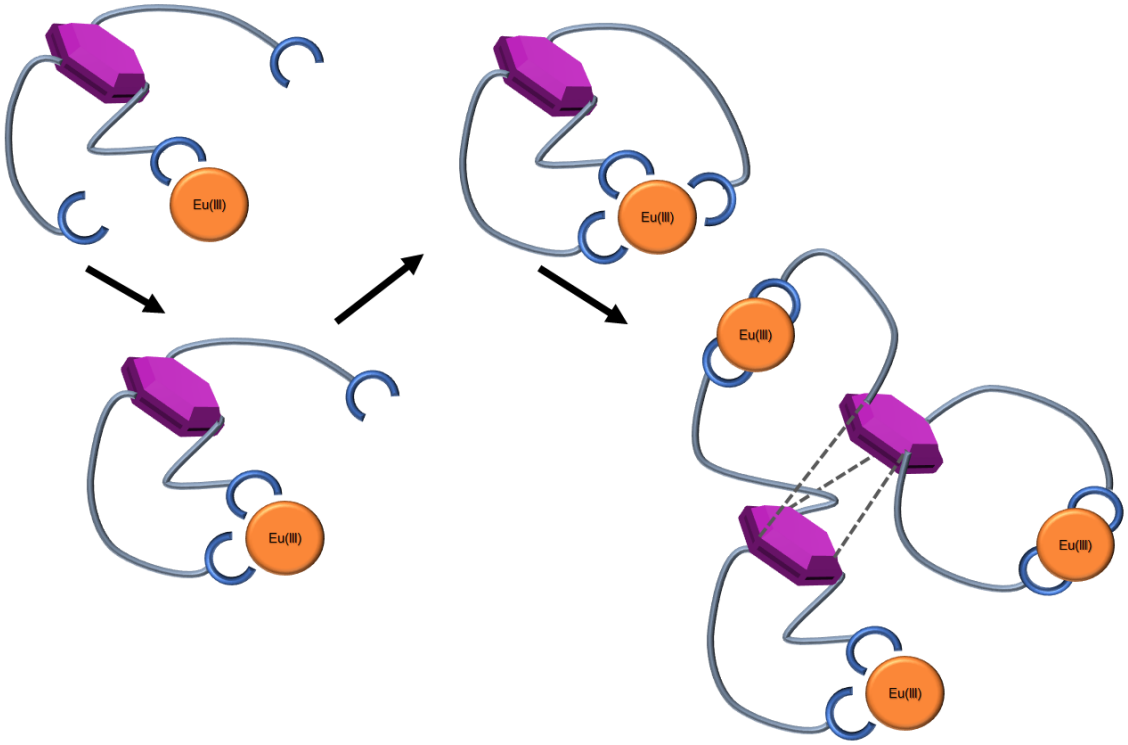

Figure 3.15 Schematic representation of the binding mode for the system that progressively forms the L:M 1:1, and 2:3. The stoichiometry suggests the formation of dimers.

A possible third model to consider involved the formation of the 1:1, 2:3 as well as the 1:3 species. Although mathematically the fit would present reliable values, it was not considered effective in the description of the system from a chemical point of view. Nevertheless, the possibility to use different binding models for this system indicates its complex self-assembly behaviour: not only does one have to consider the interactions between ligand and metal ions that occur in solution; but also the interaction between the ligands themselves, and how they affect the overall metal-ligand species formation.

The information gathered while processing the data for the high-concentration suggested that in such conditions, **54** forms aggregates that involve species with more complex stoichiometries. It was possible to understand that **54**, like other BTA derivatives reported by the Gunnlaugsson group, might undergo self-assembly processes through π - π and hydrogen bonding interactions. It was speculated that the formation of such self-assembly is the defining factor for observing one binding mode over the other in solutions with different concentrations.

To gain further insight, the data obtained at low concentration was then processed. Hence, analogously to the analysis of the changes of **54** at high-concentration, the diluted system

was initially fitted using the 1:1, 1:2 and 1:3 **L:M** species as reference, together with the ligand. The fit allowed consolidated spectra for the single species (**Figure 3.16 A**): where it is again possible observe the binding isotherms and the relative fits in **Figure 3.16 B**. It is possible to consider the quality of the fitting process taking into consideration the sum of the standard deviations for the fitting curves, which was found to be 0.03243, a very low value.

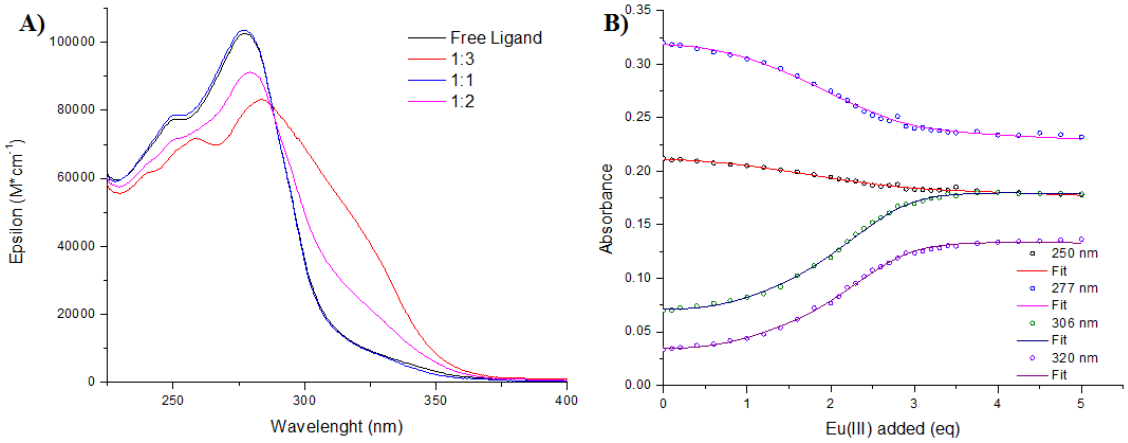

Figure 3.16 (A) Recalculated spectra of the single species (**A**) and binding isotherms (and relative fitting) (**B**) obtained processing the system at c_{57} = 3 μM (lower) concentration using the binding model which included the 1:1, 1:2 and 1:3 **L:M** complexes.

In this case, too, the fit yielded the binding constants, which are shown in **Table 3.3**. From these binding constants, it is possible to see that the most stable system is the 1:1 (logK = 9.06), followed by the 1:2 (logK = 8.42) and finally the 1:3 (logK = 6.72). This is reflected in the speciation distribution diagram that was possible to obtain, shown in **Figure *3.17***.

Table 3.3 Binding constants obtained for titration of **54** (c = 3 μM) with $Eu(CF_3SO_3)_3$ showing the three complexes obtained using the SpecFit software.

Stoichiometry	logβ	StD
1:1	9.06	±0.58
1:2	17.48	±0.76
1:3	24.20	±0.75

The speciation distribution diagram shows how the system main species switch progressively from the free ligand, to the 1:1, 1:2 and 1:3 species at when 0.5, 1.5 and 2.5 equivalents of Eu(III) are added, respectively, as expected considering the exponential dependence to the metal concentration.

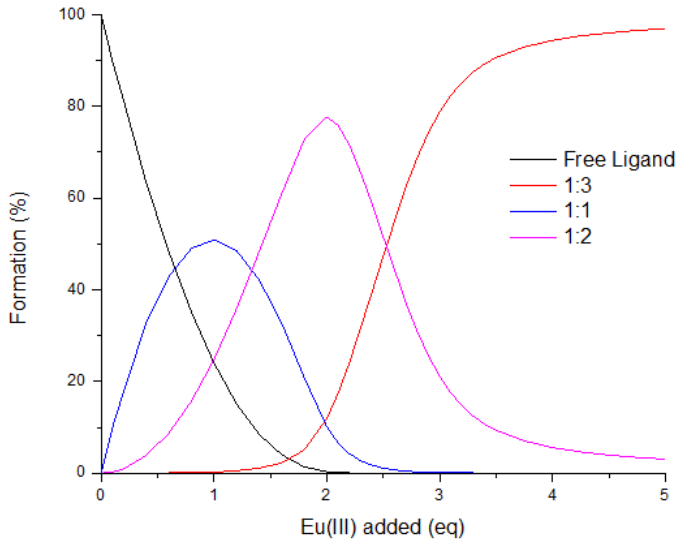

Figure 3.17 Speciation distribution diagram for the species obtained using the fitting model which included the 1:1, 1:2 and 1:3 complexes.

The fitting of the data obtained at low concentration involving the formation of the 2:3 species was attempted; the software was unable to yield data that would support such hypothesis. Therefore it is possible to speculate that the system switches from simpler stoichiometries that involve a single ligand which bind metal ions to more complex ones at higher concentration ranges, as in this case with the formation of supramolecular polymers between the ligand molecules.

The fits, as previously said, were obtained using only the data obtained in the absorbance spectra. Although the fitting of the emission data was attempted several times, the software was unable to fit these data sets. The following hypotheses were proposed to explain such behaviour: for the ligand-centred emission, in the higher concentration range, the fluorescence for the ligand was found not to follow linear trends; this could have impacted the ability of the software to process such data. On the other hand, at lower concentration the fluorescence emission intensity was very low, resulting in very low intensity signals even after enhancement, which would, in any case, lead to weakened signal-to-noise ratio, and hence higher errors. A similar behaviour could be speculated for the metal-centred emission, therefore leading to an inability to gain a further confirmation. Nonetheless, the exclusive use of absorbance data advanced understanding of the stoichiometries for the system in two different concentration ranges.

The spectroscopic studies allowed further insight on the behaviour of **54** in MeOH solution as free ligand and upon addition of Eu(III). Studying the ground and excited state of **54** it was possible to observe a chromophore behaviour for the ligand and a ligand-centred emission in fluorescence mode. The absorption and emission were found

to have a dependency from the concentration, but while the first showed a linear behaviour in the concentration range studied (1 - 10 μM), allowing to obtain the molar extinction coefficient for **54**, the fluorescent emission presented a non-linear behaviour after a concentration threshold (8.15 μM). The spectroscopic titration using Eu(III) that followed were then performed at two different ligand concentration, 3 μM and 10 μM. Processing the data obtained in these titration using non-linear regression analysis, it was possible to find that the ligand prefers to form different species depending on the starting concentration of the ligand. Single-ligand species (1:1, 1:2 and 1:3) were found to form more favourable in diluted conditions upon the addition of Eu(III), while species containing ligand dimers, formed though π-π and hydrogen bonding interactions, are preferred by the system at higher ligand concentration. The behaviour of **54** to form these species and aggregates was found in accordance to previous works in the Gunnlaugsson group[108, 122] and was further investigated with morphology studies, which will be described in the following section.

3.4 Morphologic studies of self-assemblies from tripodal systems

As described in Chapter 1, the ability of the BTA systems to form supramolecular aggregates has been vastly proven and studied,[47, 57] therefore, the ability to form such aggregates was investigated for the systems presented in this thesis. In particular, such molecules were generally (although not always, as seen in the Gunnlaugsson group[52]) able to form helical aggregates through the hydrogen bonding between neighbouring molecules of BTA ligands *via* carbonyl oxygen atom and hydrogen atom of the amide group. Also, the addition of the metal ions to the system brings further complexity to connect ligand molecules together leading to the systems extending in several dimensions with higher hierarchy in its morphology. An example for this, shown in **Figure 3.18**, was observed in a previous study in the Gunnlaugsson group, which this work extends upon.

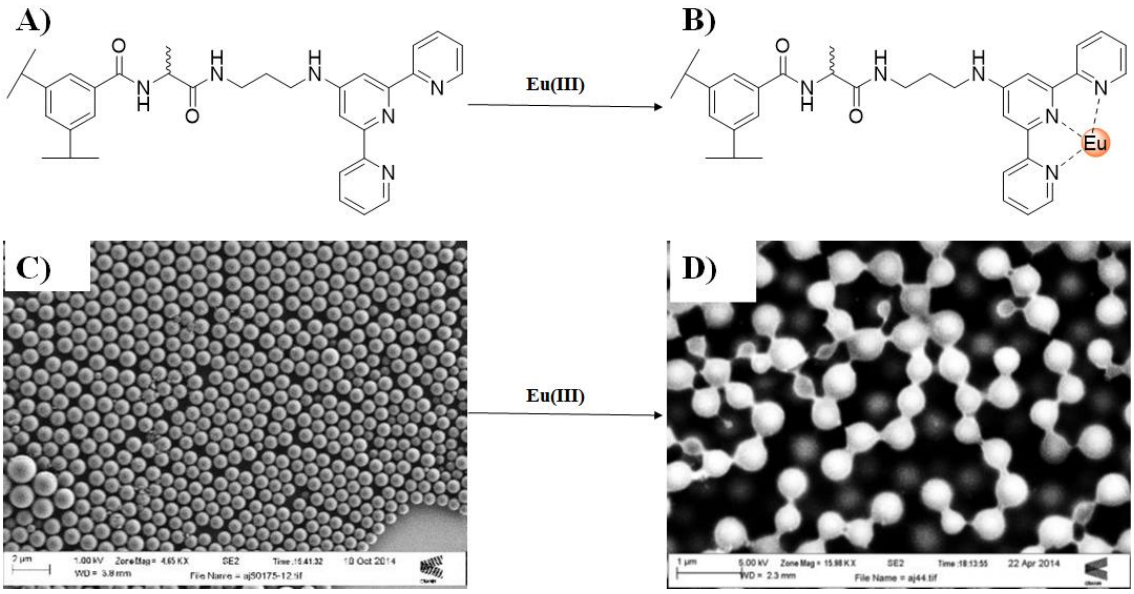

Figure 3.18 Structures for ligands **49R/S** (A) and relative Eu(III) complexes (B). SEM imaging from solutions before (C) and after the addition of the Eu(III) ions. Images reproduced from ref.[122]

3.4.1 Scanning Electron Microscopy (SEM) Studies

The studies described in this section were performed using a Scanning Electron Microscope (SEM).[123] When a material is irradiated with electron beams, a series of outgoing electron particles are generated (**Figure 3.19**) such as backscattered electrons which are beam electrons that emerge from the sample, and also secondary electrons that escape the sample surface. From the energy (and direction) of these particles, it is possible to obtain information of the surface composition of the material hit by the primary electron beam. Different particles will possess different ranges of energy, and consequently, a different **mean free path**, λ(E). The parameter of which is of particular importance, as it defines the depth from the surface, from which each different type of particle is able to escape, following the correlation expressed in ***Formula 3.7***. This means that an appropriate selection of the emitted particle allows to gain an understanding on the characteristics of a specific depth of a material among the ones closest to the surface.

$$\lambda = \frac{143}{E^2} + 0.054\sqrt{E} \qquad \textit{Formula 3.7}$$

In the case of SEM, the particles analysed are secondary electrons, particles with an energy of ~50 eV, which translates, through ***Formula 3.7***, to a mean free path that allows to gain insight on the top ~100 nm from the surface, *i.e.* an ideal depth to gain morphologic information about the surface of a material.

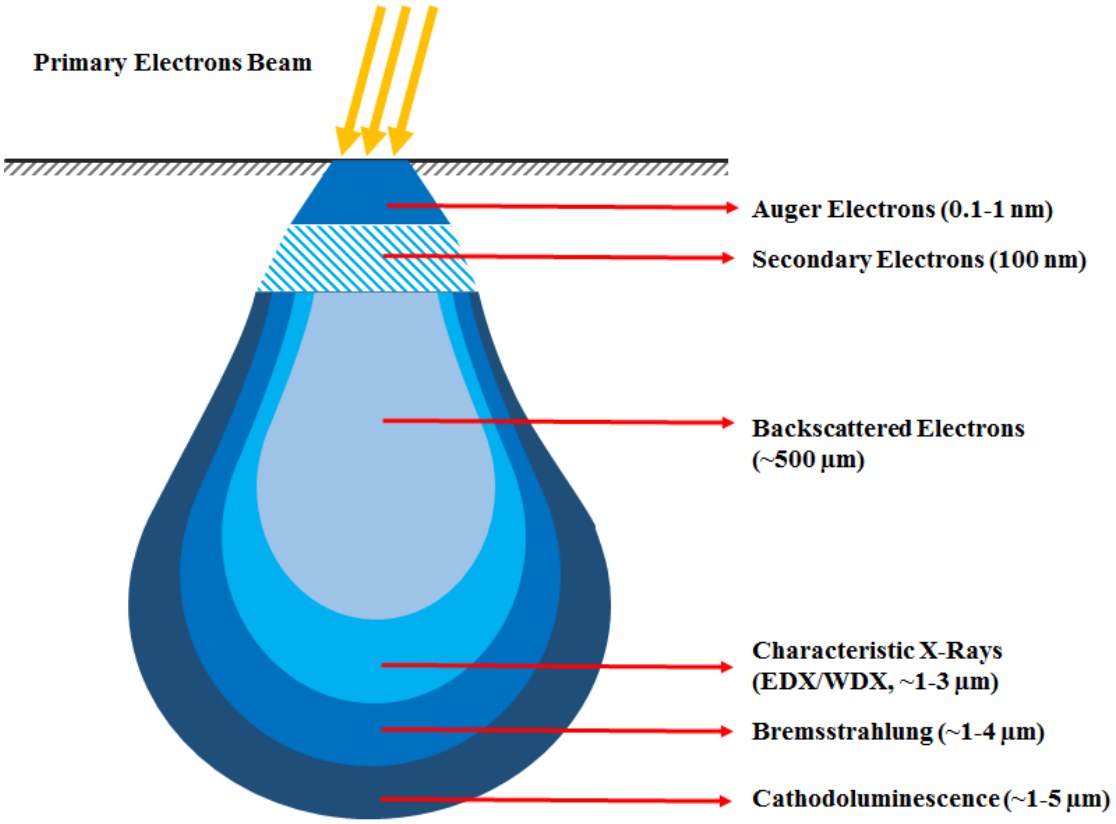

Figure 3.19 Schematic representation of the particles emitted from a surface irradiated with electron beams. Secondary Electrons allow to obtain morphological information on the surface and are detected by SEM.

The quantity of electrons able to escape the surface of the sample in a fixed period is inferior to the amount of primary electrons in the beam used to irradiate the sample. For conductive samples, this does not represent an issue, as the charge is free to move in the bulk of the material and can be discharged on the metallic support that acts as a "ground". For non-conductive samples, like the ones presented in these studies, this is not possible, and therefore charging phenomena are observed.[124-125] These phenomena can have different effects,[124] with the most common result being the presence of extremely bright spots, due to the strongly localised emission from the excess of electrons.

Although different methods to address the charging effects have been proposed,[125-127] the most common solution to charging issues is represented by the coating of non-conductive samples with thin layers of conductive material using techniques that would preserve the aspect ratio and the morphology of the underlying sample. This was the solution of choice in the work presented here, with the samples coated using a magnetron sputtering technique using a Pd/Au target to form the coating layer. This allowed to minimize the charging effects and obtain information of the samples.

The imaging shown in this study was performed using a Carl Zeiss ULTRA instrument in the Advanced Microscopy Laboratory facility from CRANN. More details on the conditions can be found in the Experimental Details Chapter.

3.4.2 Gelation experiments on 37

Among the systems obtained through the synthesis shown in Chapter 2, **37** was the simplest. As mentioned in Chapter 1, it was found able to form hydrogels upon pH tuning by Howe *et al*.[54] The formation of the gel was observed repeating the experiment performed by Howe.

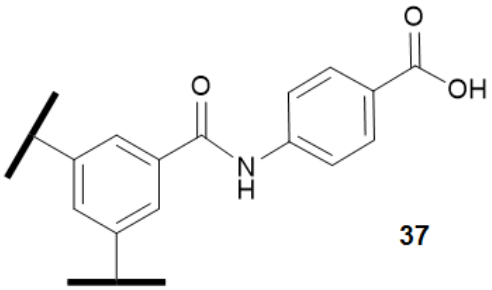

37

Figure 3.20 Chemical structure of gelator **37**.

To obtain the gelator, **37** was initially dissolved in deionised water using 3 equivalents of strong base (NaOH) and then precipitated as sodium salt (Na_3**37**) using a large amount of isopropanol (^{i}PrOH). This salt was dissolved in deionised water and reprotonated by adding the slow-reacting 4 equivalents of solid GδL (glucono-δ-lactone), with the slow formation of a transparent gel observed over the course of 6 hours. The use of GδL allowed for the protonation processes to happen in a slower fashion, allowing the systems to rearrange themselves into aggregates. The hydrogel shows the presence of aggregates that trap the solvent molecules, similar to the ones reported by Howe *et al* (**Figure 3.21**). These aggregates resemble short fibres; the presence of a twisting along the main axis, which is hinted at high magnification (**Figure 3.21**, **C** and **D**). The aggregates were measured to have an average cross-section of 47.7 nm (± 6.0 nm); this value is in line with the one reported by Howe, which found cross-sections ranging between 50 and 200 nm for the systems reported.

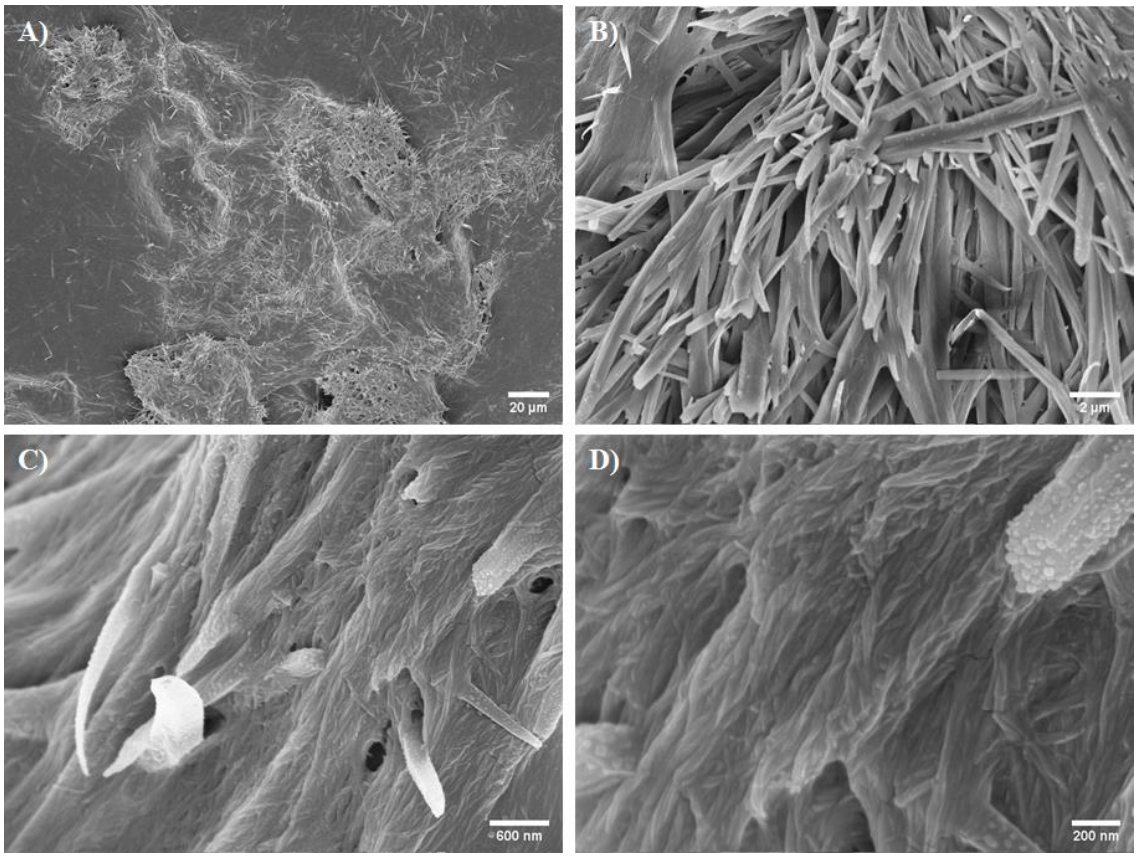

Figure 3.21 SEM images of **37** hydrogel formed upon reprotonation with GδL. Scale bars 20 µm (A), 2 µm (B), 600 nm (C) and 200 nm (D).

Several attempts at modifying these gels were made. Initially, they were exposed to two different metals. In one case, a $CuCl_2$ solution (0.1 eq) was added to observe the ability of the ions to diffuse through the gel. On a macroscopic scale, it was possible to observe the diffusion of the Cu(II) ions through the gel, as the characteristic blue colour diffused through the whole gel (**Figure 3.22**), while on the nanoscale, no major change in the structure of the fibres of the hydrogel was observed.(**Figure 3.23 A**, **B**).

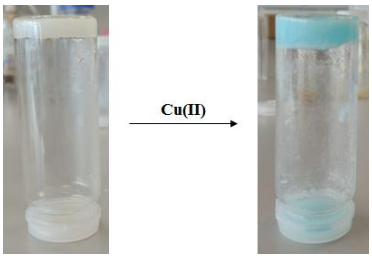

Figure 3.22 Effect on the **37** hydrogel of the diffusion of Cu(II) ions.

A different experimental setup was also attempted in which the Cu(II) would be dissolved in the carboxylate solution before the addition of GδL, though the SEM imaging of these samples did not show significant differences. This setup was then used for the following experiments, as well.

An experiment was designed in which the Cu(II) ions were replaced by Tb(III) ions, in order to exploit its spectroscopic properties. The experiment was performed by adding four equivalents of $Tb(CF_3SO_3)_3$ to solution prior to gelation; although no luminescence was visible to the naked eye under UV irradiation (λ_{ex} = 254 nm), the SEM imaging was performed to investigate the potential effect of the ions to distort or affect differently the structure of the gel.

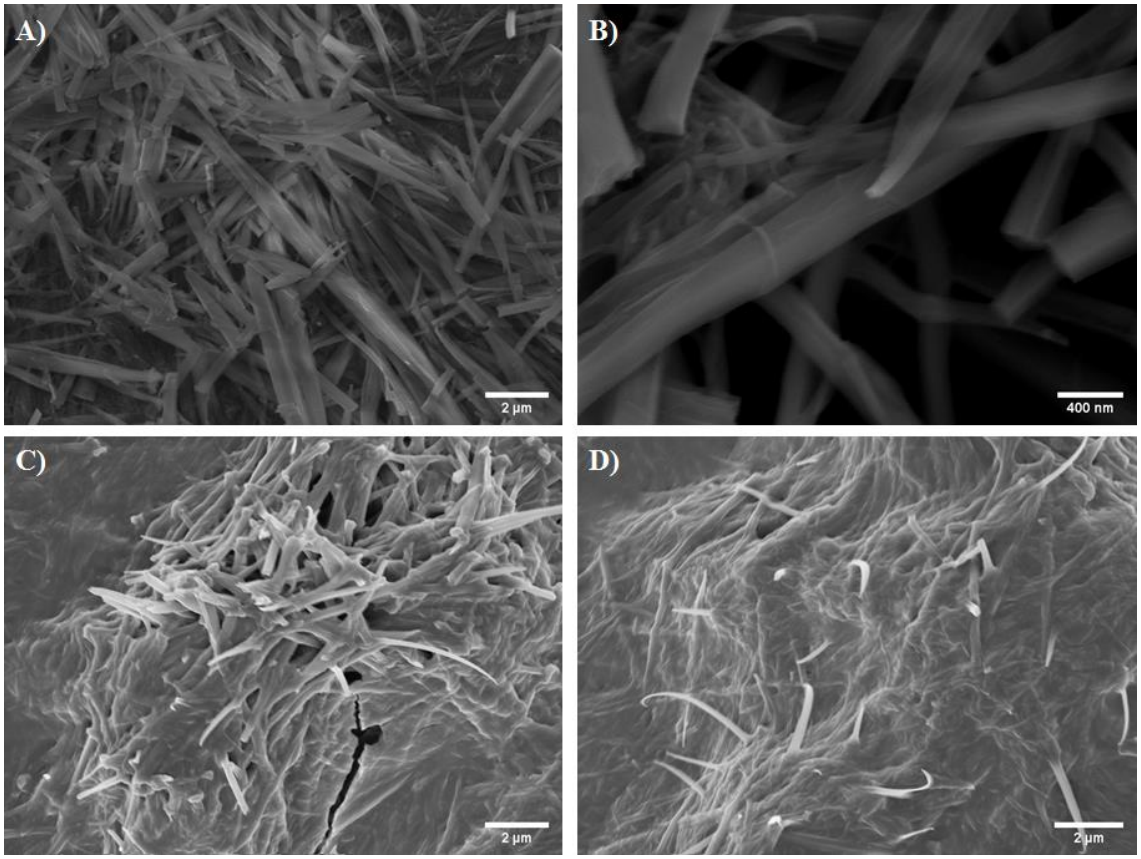

Figure 3.23 SEM images of **37** hydrogel formed in presence of Cu(II) (A, B) and Tb(III) (C, D), after reprotonation with GδL. Scale bars 2 µm (A), 400 nm (B) and 2 µm (C, D).

In this case, a major change in the cross-section was observed (168.1 ± 37.7 nm), with the aggregates maintaining their fibrous nature (**Figure 3.23 C**, **D)**. It was observed that the solvent had not completely been used for the swelling of the gel by **37**, indicating that in presence of the Tb(III) salt, part of the solvent is seized for the solvatation of the ion and the smaller amount of a competitive solvent such as water might induce the formation of longer-range interactions. More experiment to verify such hypothesis will be performed in situation of higher ionic strength.

3.4.3 Synthesis and effect of UPy additive on 37 hydrogels

Even though the gels of **37** sustained the reverse vial test (**Figure 3.22**) they were not strong enough to study their rheological properties, it was thought to use an additive able to enhance its mechanical properties. This kind of strategy has been widely used on materials obtained from macromolecular systems, such as collagen. One method, cited in Chapter 1, is the use of additive containing UPy (Ureido-Pyrimidone) moieties.[128] UPy moieties, as explained in the Introduction Chapter, are able to form 4-fold hydrogen bonds, which are therefore able to form very strong and directional supramolecular "joints". Here we anticipated that UPy could interact with **37**, either covalently, through its isocyanate moiety, or through supramolecular interactions, through hydrogen bonding with partners present on **37**. In this work in order to attempt a strengthening of **37** hydrogels, a UPy additive was synthesised starting from 2-Amino-4-hydroxy-6-methylpyrimidine, **76**, shown in **Figure 3.24**.

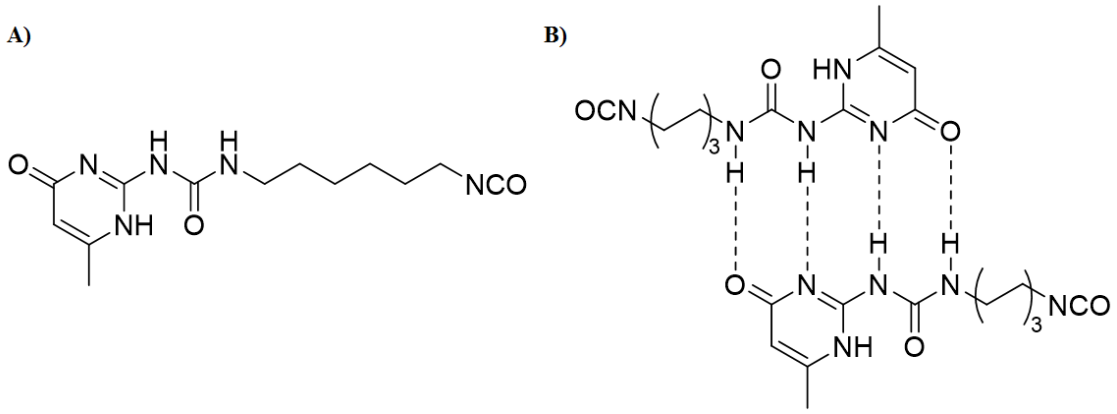

Figure 3.24 A) Molecular structure of UPy-functionalised additive **76**. B) Self-complementary hydrogen bonding interaction in a **76** dimer.

Compound **76** was synthesised following a literature procedure[128]. The pyrimidine precursor was dispersed in an excess of neat 1,6-hexamethylene diisocyanate and the reaction was carried at 100 °C for 18 hours (**Scheme 3.1**). The resulting solution was then diluted 10:1 with hexane to induce the precipitation of a fine white powder which was then suction filtered and dried *in vacuo*. The formation of the additive, was confirmed using ^{1}H-NMR, with the presence of the three NH signals at 7.32, 9.64 and 11.54 ppm (**Figure *3.25***), as well as by mass spectrometry, with the peak at 325.18 (m/z). This signal is due to the formation of the urethane derivative of **76** with methanol used to prepare the sample.

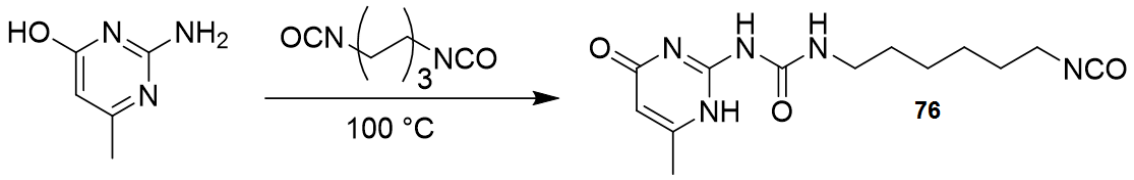

Scheme 3.1 Synthesis of UPy-functionalised additive **76**.

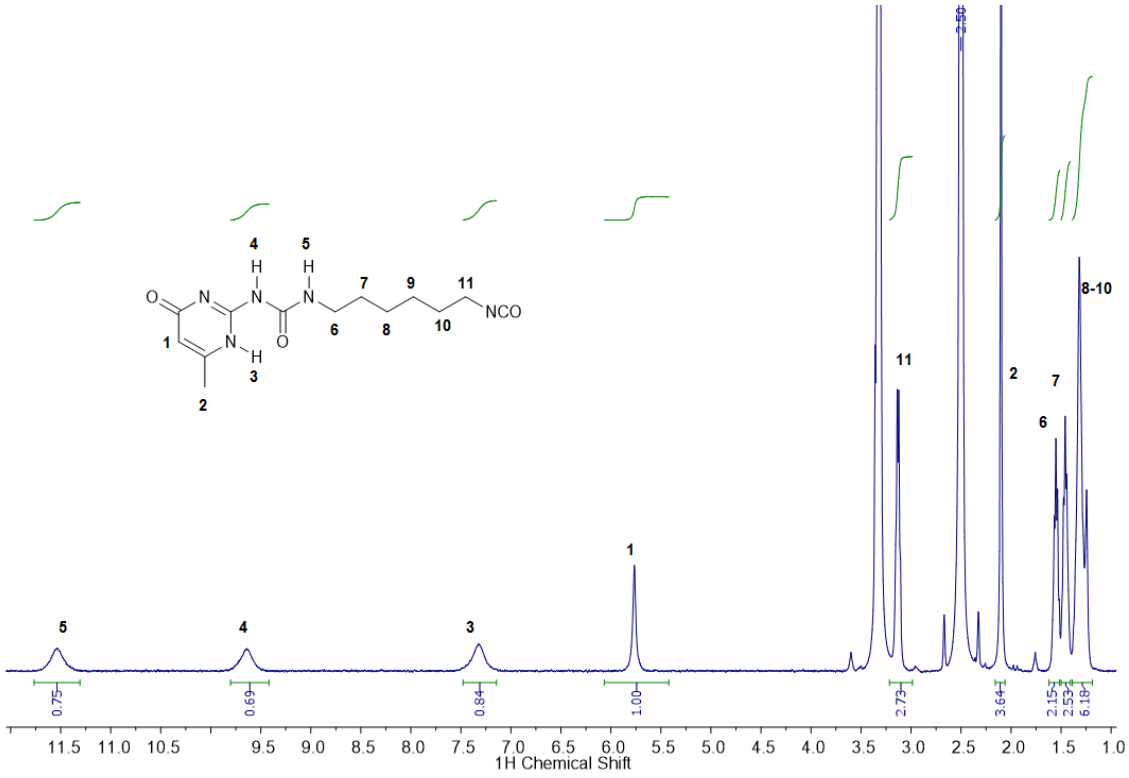

Figure 3.25 ^{1}H NMR spectrum (400 MHz, DMSO-d_6) of **76**.

Following this procedure, **76** was obtained in very high yield (78 %) and was used to observe the effect that its presence would induce on the gelation of **37**. To do so, **76** (0.3 eq) was added to the aqueous solution of Na_3**37** in conjunction with GδL; the resulting suspension was briefly placed in ultrasound bath and the sample was left to rest. The formation of a white, opaque gel was observed over 4 hours, after which it was subjected to the inversion test. In **Figure 3.26** it is possible to see the effect of **76** on the aggregation. The fibres aggregate into a tighter packing, with a measured cross-section diameter of 28.9 (± 6.0 nm), and appeared to be less microcrystalline in nature. These changes on the nanoscale, though, were not met on the macroscopic scale. The formed gel, in fact, did not show to be mechanically stronger, as once more it was not possible to perform rheologic studies on the materials. A possible explanation could be a higher self-affinity of **76** compared to the affinity with the H-bond partners on **37**; this would exclude **76** from interfering with the formation of the fibres, with dimers of **76** acting as inert reinforcing particles.

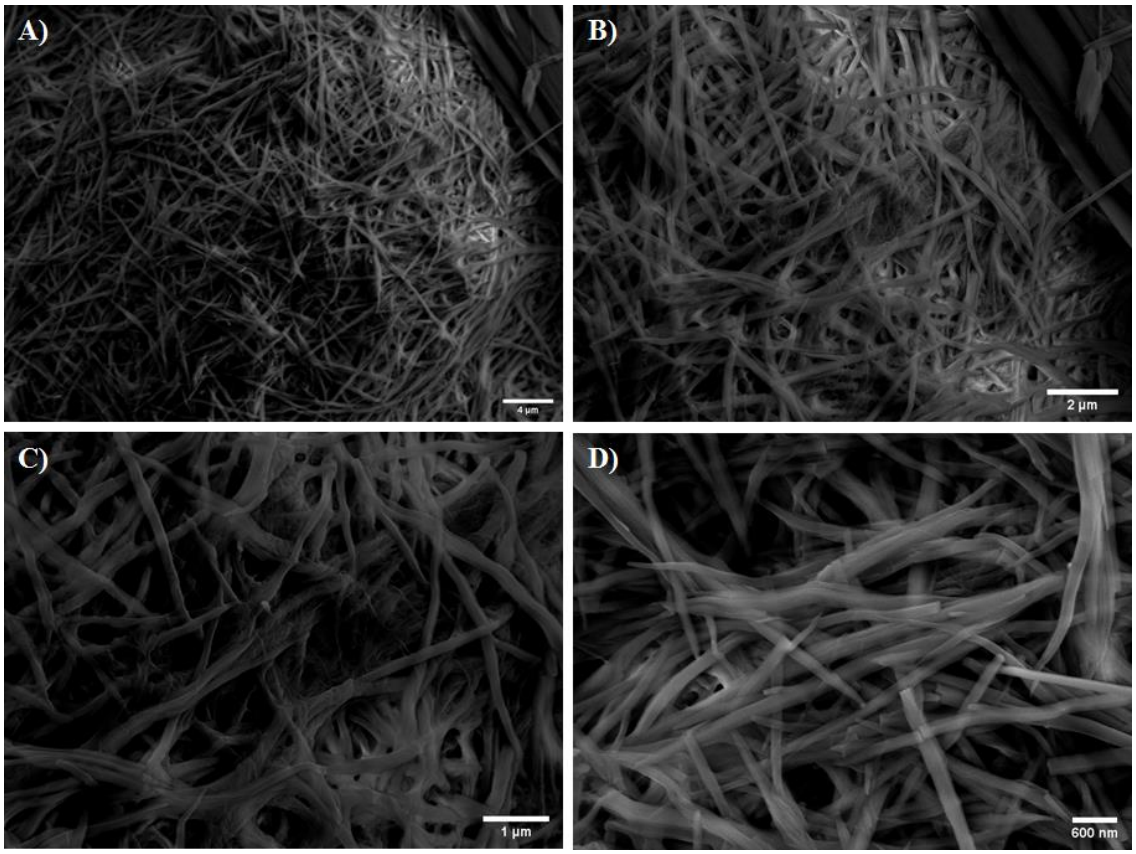

Figure 3.26 SEM images of hydrogels of **37** formed upon protonation with GδL in presence of **76**. A slightly tighter packing of the fibrous aggregate can be seen. Scale bars 4 µm (A), 2 µm (B), 1 µm (C) and 600 nm (D).

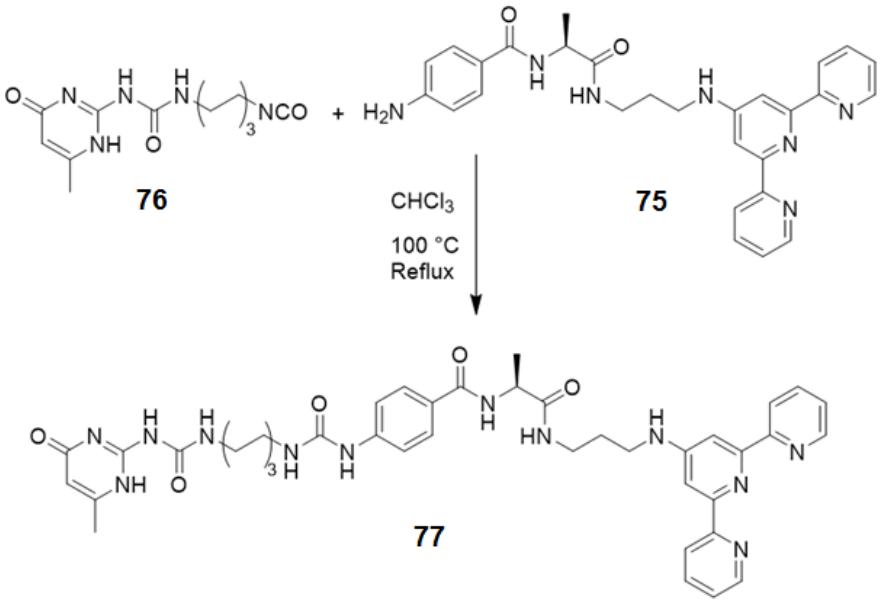

Scheme 3.2 Synthesis of **77**. The reaction was performed at high temperature for 72 hours.

Although it was not found to be able to induce the mechanic properties of the gels **37**, **76** was used as a building block for different structures. In particular, having obtained compound **75** an attempt of forming a supramolecular building block possessing a UPy moiety on one end and a terpy moiety at the other was considered (**77**, **Scheme 3.2**).

Such a design would result in a molecule that would be able to self-interact forming dimers through the hydrogen bonding interaction between UPy moieties of the neighbouring molecules and, through the terpy group, to form supramolecular polymers using metal ions as bridging points or "supramolecular glue" (**Figure 3.27**).

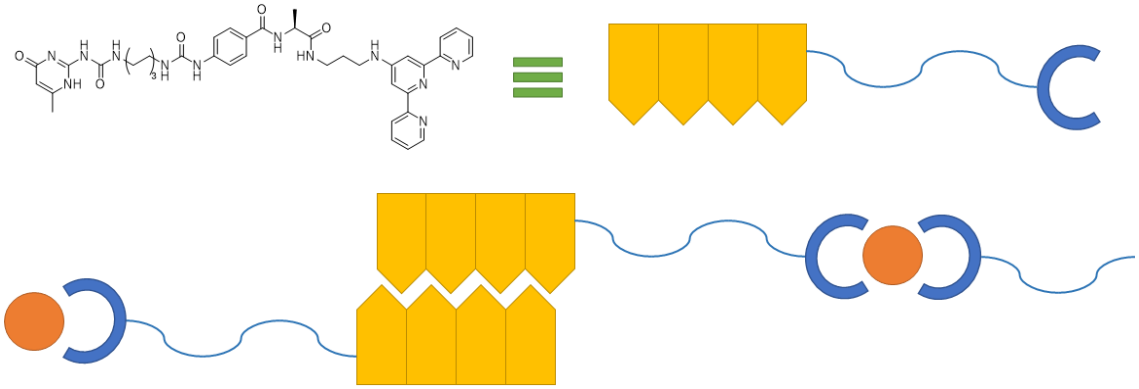

Figure 3.27 Schematic representation of the envisioned aggregation of **77**. In yellow, the UPy self-interacting UPy moiety, in blue the metal-binding terpy moiety and in orange the metal to act as "supramolecular glue".

The reaction, shown in **Scheme 3.2**, was attempted by suspending **76** in an aprotic solvents such as $CHCl_3$, to prevent the isocyanate group to undergo parasite reactions and then adding solid **77** while stirring at high temperature. The reaction mixture remained as a suspension for 72 hours, after which the reaction was stopped and the solid was retrieved by suction filtration. The solid, which was examined using ^{1}H-NMR and mass spectrometry, did not show the signals relative to **77**; once again, the reason for this was speculated to be linked with the low reactivity of the aromatic amine group. Initially, this was thought to be bypassed by the high reactivity of the isocyanate moiety to form a urea group, but this was not seen in the condition used in this experiment. Further studies could optimise the conditions to obtain **77**, as well as other relevant UPy-functionalised derivatives.

3.4.4 Gelation experiments on 62

After confirming the ability of **37** of forming hydrogel upon protonation of the carboxylic groups, a similar experiment was attempted for compound **62**, as it possessed analogous acidic moieties. In this case, though, it was not possible to isolate the tri sodium salt, as the procedure used to obtain Na_3**37** involved precipitating the gelator upon addition of a large quantity of ^{i}PrOH. The equivalent salt for **62**, Na_3**62**, was found very soluble in the organic solvent. The gelation was then attempted by dissolving **62** using 3 equivalents of aqueous NaOH, with the pH then adjusted using HCl or GδL. A slow addition of diluted

solutions of HCl, solid GδL and aqueous GδL solutions lead to the almost instantaneous precipitation of an off-white solid.

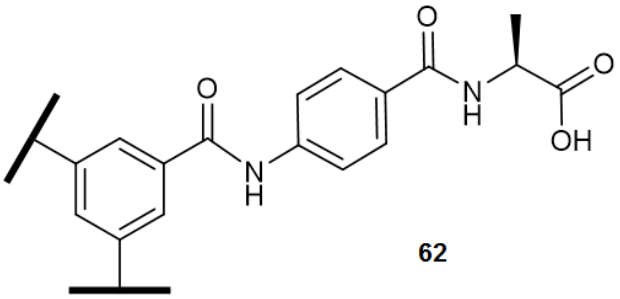

62

Figure 3.28 Chemical structure for **62**.

The aggregation properties of **62** in MeOH solutions will be discussed in detail in Chapter 4; this section will discuss the behaviour of this BTA derivative in mixed solvents. Solutions of **62** were prepared dissolving the solid in MeOH and adding a secondary solvent in different ratios to observe any differences that would arise. The solvents used for these experiments were MeCN, THF, DCM and water, in order of increasing polarity. The behaviour for each potential anti-solvent was observed at 25, 50, and 75% of the total composition; THF and DCM did not show any change in the system, that remained a simple yellow solution; MeCN induced the precipitation of **62** when it consisted of 50% or more of the solvent mixture; the most interesting results were observed in water. In aqueous mixtures, it was possible to observe a change in behaviour at 75%: the system switched from a yellow solution to a gel. At this point, to gain a better understanding, two further solvent mixtures were tested, at 70% and 80% of water, with the first behaving like a slightly viscous solution and the second showing the precipitation of **62** as a solid (**Figure 3.29**).

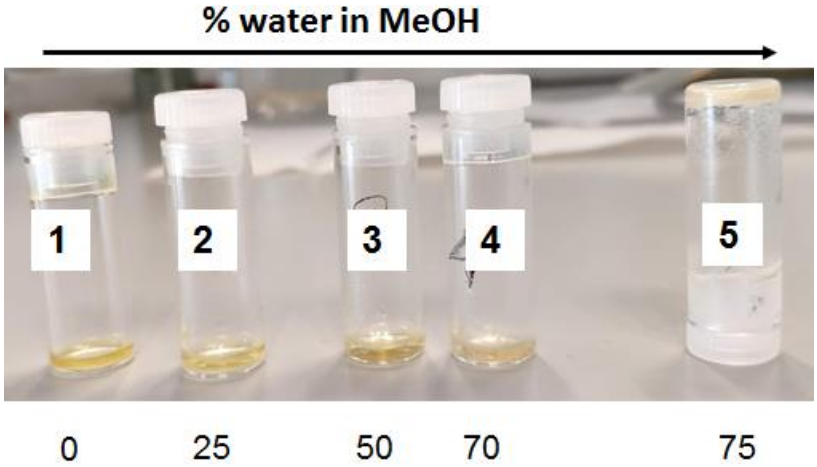

Figure 3.29 Behaviour of **62** in water:MeOH mixtures. The BTA derivative starts precipitating at water fractions of 80% or higher (not shown).

The gel formed using this method was not mechanically strong. And once again, this prevented rheological measurements to be performed. The system was then spotted on a silicon chip and imaged using SEM. The SEM images of the gel, shown in **Figure 3.30**, showed a remarkably different behaviour from **37**. At low magnification, it was possible to observe the formation of layer (**Figure 3.30 A**). Upon increasing magnification, it was found out that such layer is composed by **spherical aggregates**. These aggregates, observed in all the parts of the layer, are not regular in size, but seem to be composed by fibrous aggregates, that can be observed at very high magnification (**Figure 3.30**, **D**).

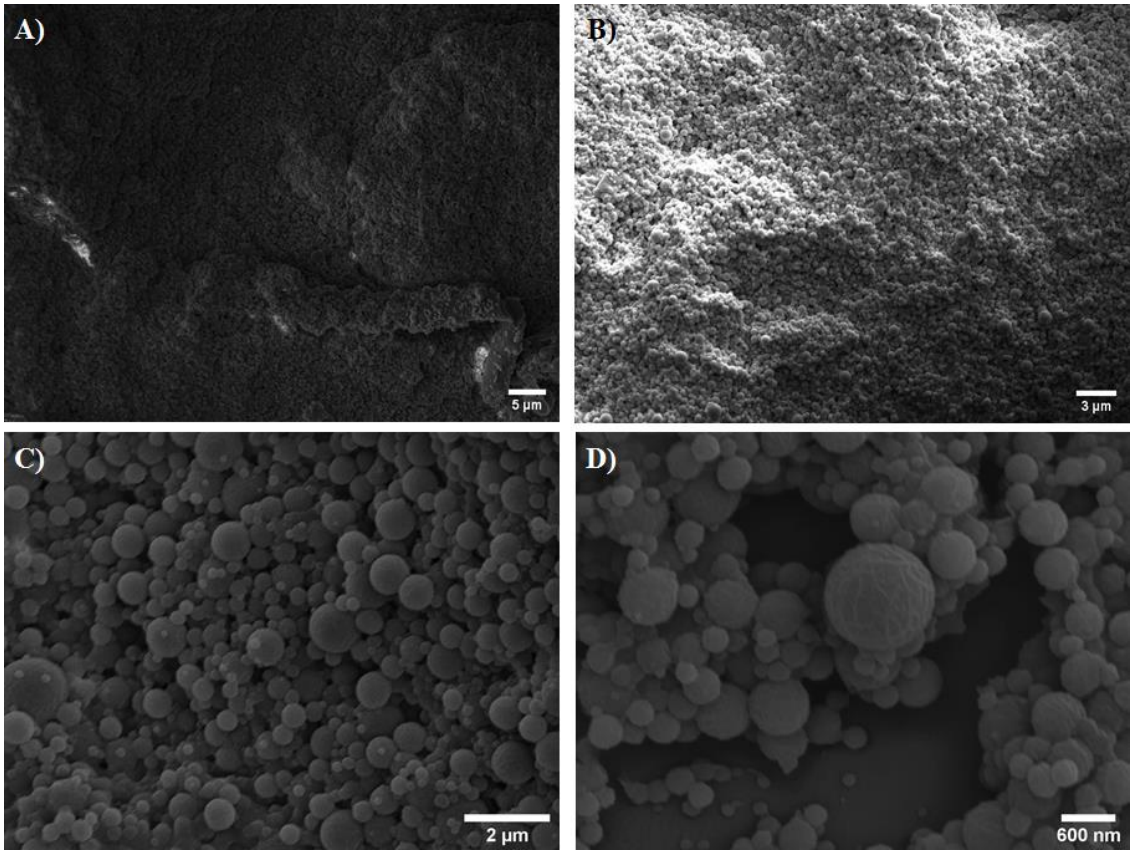

Figure 3.30 SEM images of **64** gel formed in MeOH:H_2O (1:3) mixture. The aggregation into irregular micro- and nano- spheres can be observed. Scale bars 5 µm (A), 3 µm (B), 2 µm (C) and 600 nm (D).

In **Figure 3.31 A** it is possible to see the size distribution diagram for the radii of spherical aggregates, calculated over 143 measurements. The distribution shows that the majority of spheres have a weighted mean radius of 302.6 nm, making them effectively **nanospheres**; the high standard deviation from this average (±179.78 nm) is a further confirmation of the dispersity of the diameters. However, much bigger aggregates, with a diameter over a micron were present. Although it was not possible at this stage to gain a better understanding on the aggregation mechanism leading to the formation of the nanospheres, it would appear when considering the details of the microscopy images in

Figure 3.31 B, that **62** aggregates initially into fibrous structures that in turn form the microspheres possibly indicating an equilibrium between the gelation and precipitation processes due to the hydrophobic nature of the initial gelation assemblies.

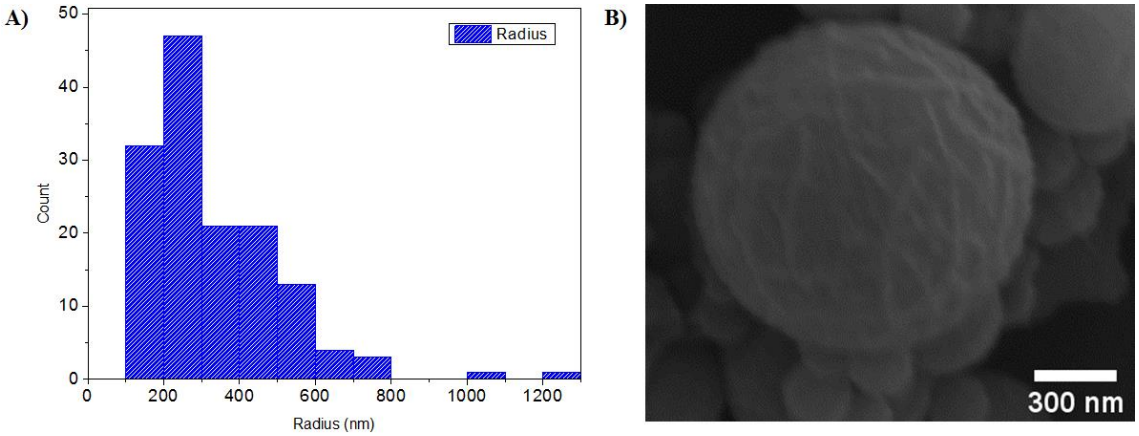

Figure 3.31 Size distribution diagram for the radii of the microspheres composing the gel **62** (**A**). Detail of a microsphere with the fibres composing the nanospheres (**B**).

3.4.5 Morphology studies on 54

Once **54** was obtained, in parallel to the spectroscopic studies, morphologic studies were also performed. Initially, attempts at inducting the gelation of the system were performed that involved pH modulation and MeOH/H_2O mixtures. These attempts, however, did not lead to gelation. At low pH, **54** showed a moderate solubility in water, but upon reaching neutrality or higher pH values, precipitation of **54** was observed. Analogous behaviour was observed attempting to use dilute MeOH solutions in H_2O, with precipitation being observed almost immediately. The focus of the morphology studies was then shifted to the behaviour of **54** in MeOH solutions, and samples were prepared by spotting a **54** solution 10 μM in MeOH onto silicon wafers, which were left to dry in air for 24h and *in vacuo* for 2h prior to the SEM imaging. The wafer would then be sputter-coated with Pd/Au and imaged using SEM, as shown in **Figure 3.32**.

The SEM results demonstrate that upon slow evaporation of the solvent, spotted solutions of **54** formed nanospheres. Like the nanospheres obtained from the gels of **62**, at high magnification (**Figure 3.32 D**), it was possible to observe that these nanospheres appear to form a spheric structure. It was our hypotesys that the formation of such spheres would take place after an initial aggregation into fibers; further studies would allow to verify this. Unlike the nanospheres observed for the gel sample of **62**, though, the size distribution for these nanospheres was found to be much more regular. This behaviour was speculated to be induced by the initial aggregation, furthered by the hydrogen

bonding, into fibres. The hydrophobicity of these fibres could trigger either the precipitation or the formation of a higher order aggregate, *i.e.*, the spheres.

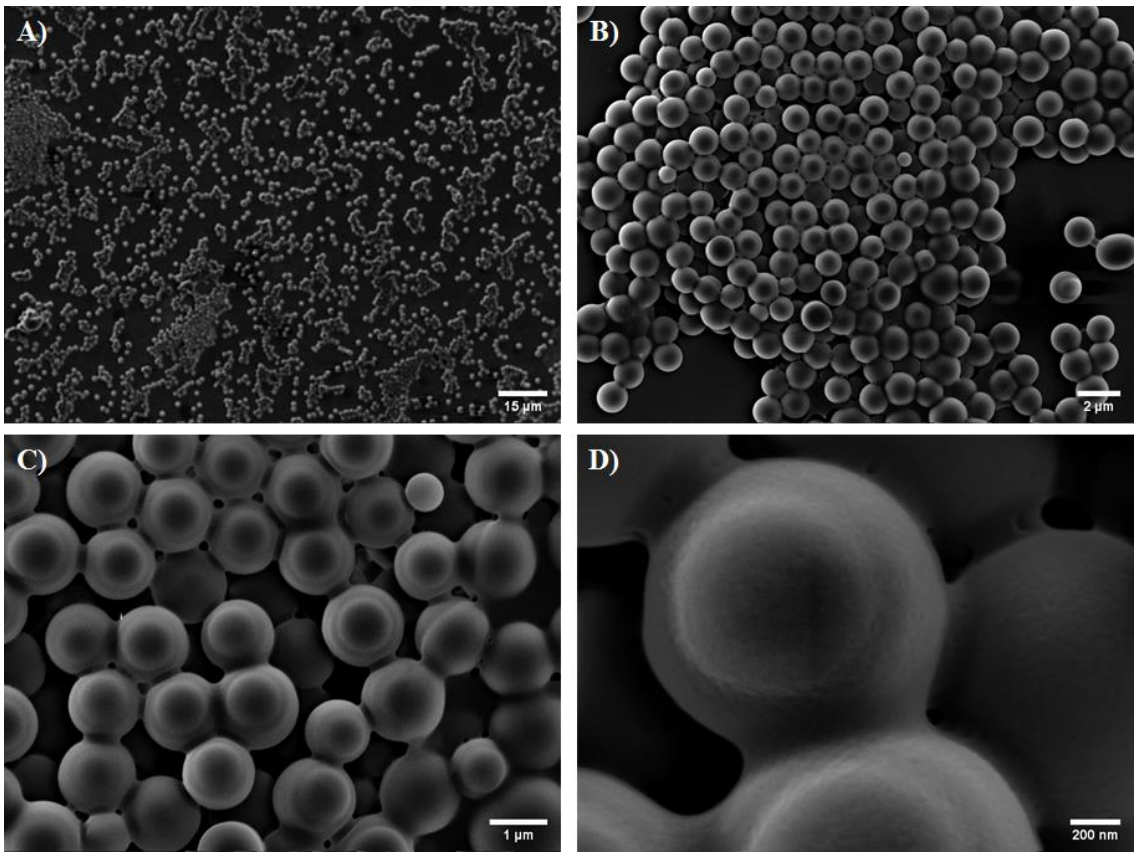

Figure 3.32 SEM images of **54** dropcasted from 10 µM MeOH solution. It is possible to observe the formation of regular nanosphere for this ligand. Scale Bar 15 µm (A), 2 µm (B), 1 µm (C) and 200 nm (D).

In the case of **54**, the radius for the spheres was found to be much lower if compared to the gel of **62**, with a weighted average of 107.2 nm per nanosphere. Looking at the distribution diagram relative to the diameters, **Figure 3.33 A**, it can also be observed that the nanospheres obtained from **54** are more monodispersed (standard deviation ±13.02 nm) when compared to the those obtained for **62**. This could be due to the timescale of the aggregation processes being different. In the case of **62**, it is legitimate to speculate that the formation of the spheres is "forced" during the gelation process, *i.e.* upon the addition of the MeOH solution into water; this would induce a much more repentine change in the system, and subsequently accounting for the formation of more irregular aggregates.

For **54**, on the other hand, the process is slower, as it happens during the evaporation of the solvent after the spotting of the silicon wafer. Furthermore, some of the nanospheres that form appear to be hollow (**Figure 3.33 B**). Understanding the reason for which some samples contain more hollow nanospheres when compared to other, could lead to a grasp

of the process that leads the system to switch from the fibrous structures to the higher order nanospheres.

An additional remark that can be noted is that the nanospheres appear to "pack" further, forming networks and partially merging with each other. This packing, although not close, seems to happen upon different levels, leading to a porous, multi-layered material.

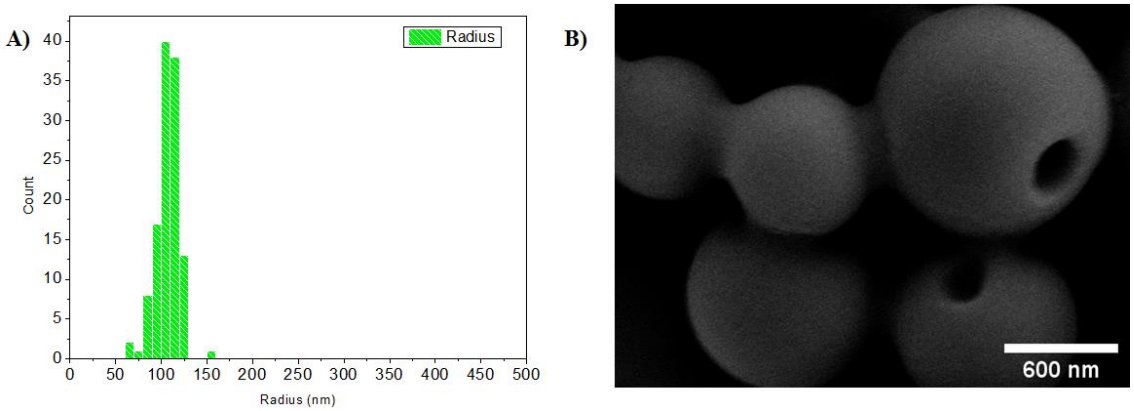

Figure 3.33 Size-distribution diagram for the diameters of the microspheres of **54** (**A**). Detail of some hollow microspheres (**B**).

3.4.6 Morphology studies on Eu·54

The ability of forming supramolecular aggregates of **54** was also investigated after the formation of the Eu(III) complex, in order to gain further understanding of the changes that the presence of the metal would induce in the final structures. The studies were performed both on the system formed under kinetic control, *i.e.* upon mixing of the two species in methanol in 1:1, 1:2 and 1:3 stoichiometries, as well as the 1:1 species formed under thermodynamic control, *i.e.* investigating the aggregates formed upon microwave irradiation as described in section 2.6.

In order to obtain the **M:L** species formed under kinetic control, three different solutions of **54** with the concentration of 10 μM were prepared in MeOH. To each of these solutions one, two or three equivalents of $Eu(CF_3SO_3)_3$ were added at room temperature. These mixed systems were allowed to stand for 2-4 hours before being dropcasted on silicon chips, dried initially in air for 16 hours and later for two hours *in vacuo* prior to coating and imaging, with the SEM images of the samples shown in **Figure 3.34**.

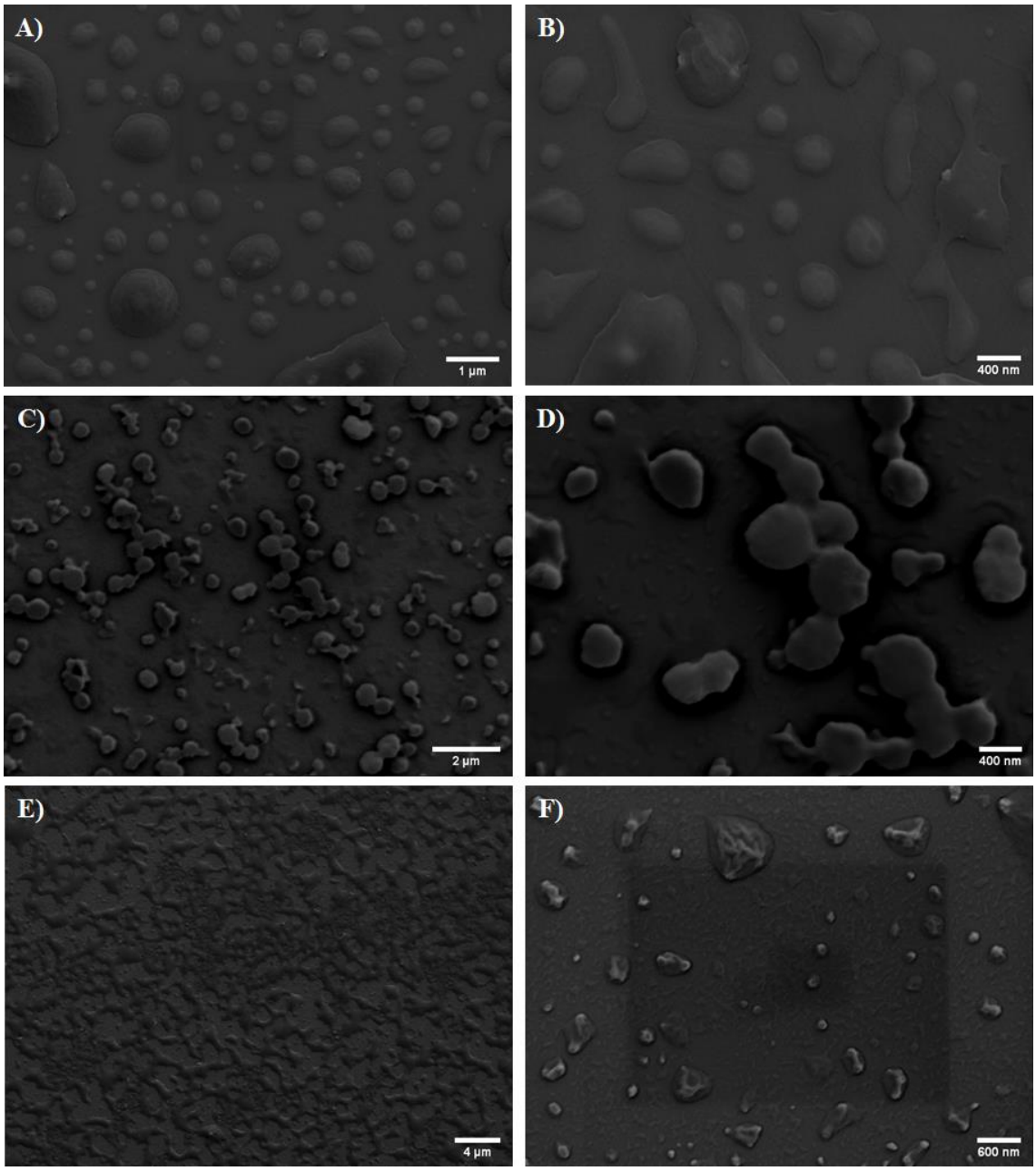

Figure 3.34 SEM images of **Eu·54** (n = 1, 2, 3) dropcasted from 10 µM MeOH solution in various stoichiometries. (A) and (B) 1:1 stoichiometry, scale bars 1 µm and 400 nm. (C) and (D) 2:1 stoichiometry, scale bars 2 µm and 400 nm. (E) and (F) 3:1 stoichiometry, scale bars 4 µm and 600 nm.

The SEM images show different morphologies upon the addition of the metal solutions. Examining the SEM images taken at 1 equivalent of Eu(III) added, it is possible to see that the system switched from the smaller, and monodisperse sized nanospheres formed by **54**, to much less regular spheroidal aggregates. (**Figure 3.34 A**). These bigger aggregates seem to form larger arrangements for which a diameter was averaged over several samples as 519.34 ± 348.57 nm. Furthermore, the aggregates seem to lack the well-defined shapes seen for the free ligand (**Figure 3.34 B**). This loss of order seems to

become more prominent upon adding more Eu(III), as can be seen in the images taken when 2 equivalents of Eu(III) have been added, in **Figure 3.34 C** and **D**, respectively.
For these examples, the images seem to confirm the trend seen for the smaller aggregates, that coalesce into networks composed of units of very irregular shapes. Upon the addition of three equivalents of Eu(III), it was possible to observe the formation of larger layers rather than aggregates, as it can be easily seen in **Figure 3.34 E**. Imaging sections far from the main **Eu·54** layer, it is possible to find amorphous aggregates with a different morphology, in which the fibrous component can be distinguished. It was speculated that this behaviour might be indicative of Eu(III) ions to behave as bridging points between units of **54**, bound by the three terpyridine units; this would be coherent with the reduced hydrophobicity of the complex, caused by the charge of the metal.
Comparing these results to the ones seen previously within the Gunnlaugsson group,[122] it was observed that **54**, like **49R/S**, aggregates into fibrous structure that further arrange themselves to form nanospheres. The main difference between the two systems are noticed in the size distribution of the nanospheres: the structures formed by **57** possessing a diameter much smaller (200 - 300 nm) if compared to the ones from **54** (750 - 1000 nm). The most remarkable difference could be noticed upon the changes induced on the morphology by the addition of Eu(III). While the previous work from Savyasachi[122] showed how the presence of the metal ions would induce the formation of networks of microspheres, the effect on Eu(III) on the spheres of **54** would cause the loss of evident structural features, forming compact films.

3.4.7 Morphology studies on 55

Although, as reported in Chapter 2, it was not possible to obtain compound **55** in high purity, a 10 μM solution of the BTA derivative in MeOH was prepared and imaged. The result of such experiment, although not universally valid, would still allow to gain an insight on the aggregation and on the effect that the presence of small quantities of DCU (impurity identified within compound **55**) would have on the formation of the supramolecular structure. The presence of the urea functionality is proven to interfere with the aggregations in systems that undergo assembly processes based on the formation of H-bonds between amide moieties, such as proteins,[129-130] or J-aggregates.[131-132]

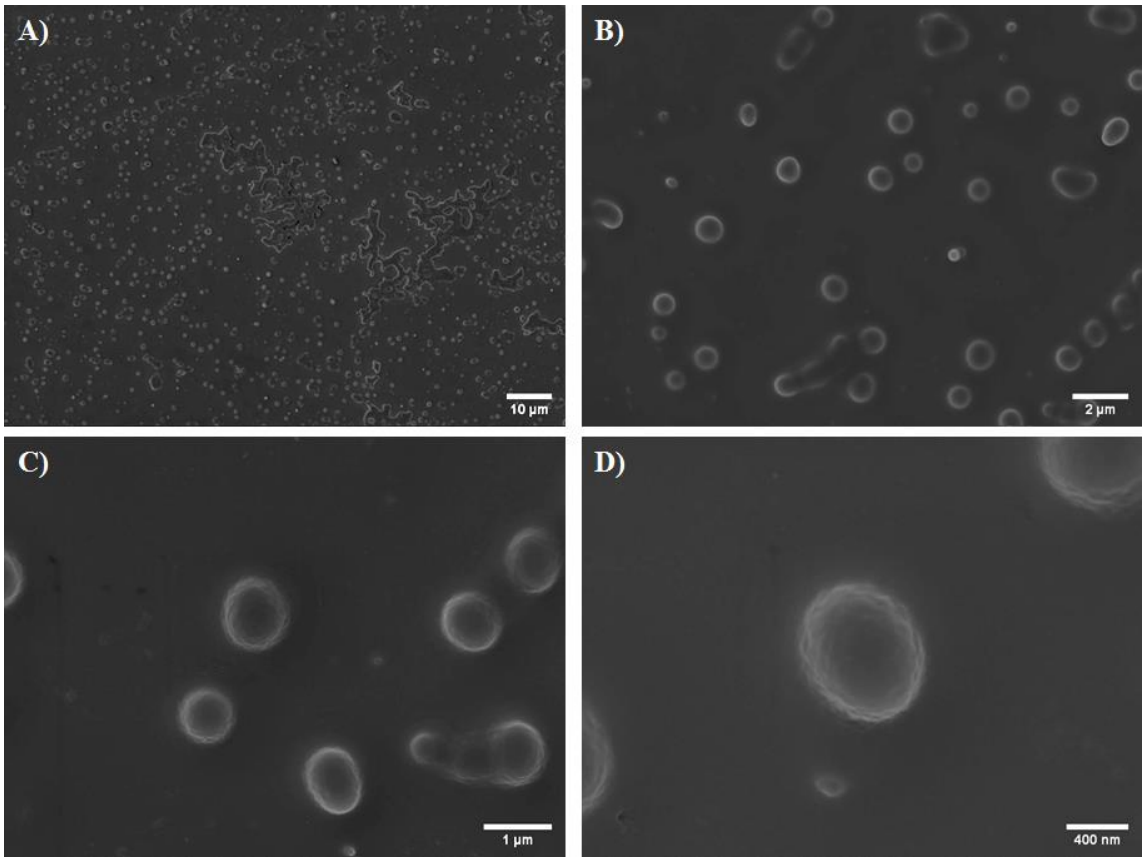

Figure 3.35 SEM images of **55** dropcasted from 10 µM MeOH solution. It is possible to observe once again the formation of spherical aggregates. Scale Bar 10 µm (A), 2 µm (B), 1 µm (C) and 400 nm (D).

Initially, the SEM images show the formation of a system composed of round aggregates similar in shape and size to those formed by **55**, paired with larger layer-like structures (**Figure 3.35 A**); at higher magnification (**Figure 3.35 C** and **D**), the morphology appears less regular. These spheres, although nanoscopic, were harder to measure, as they were quite dispersed on the wafer with the value varying between 371 nm and 845 nm. Furthermore, in the areas were more material was present, they would coalesce to form the larger structures, sizing over the micron (**Figure 3.35 A** and **B**).

Particularly interesting images of the sample were taken when focusing on a different region of the sample; such images, shown in **Figure 3.36**, indicate a possible effect of the urea on the aggregation. In particular, in **Figure 3.36 B** where it is possible to observe a "broken" microsphere. It was speculated that the spheroidal aggregates formed by **55**, and presumably those formed by **54** as well, are actually hollow and the aggregation leads to the formation of a shell rather than a solid sphere. Developing a protocol to obtain **55** in high purity will allow to obtain further understanding on its ability to form complex structures through self-assembly.

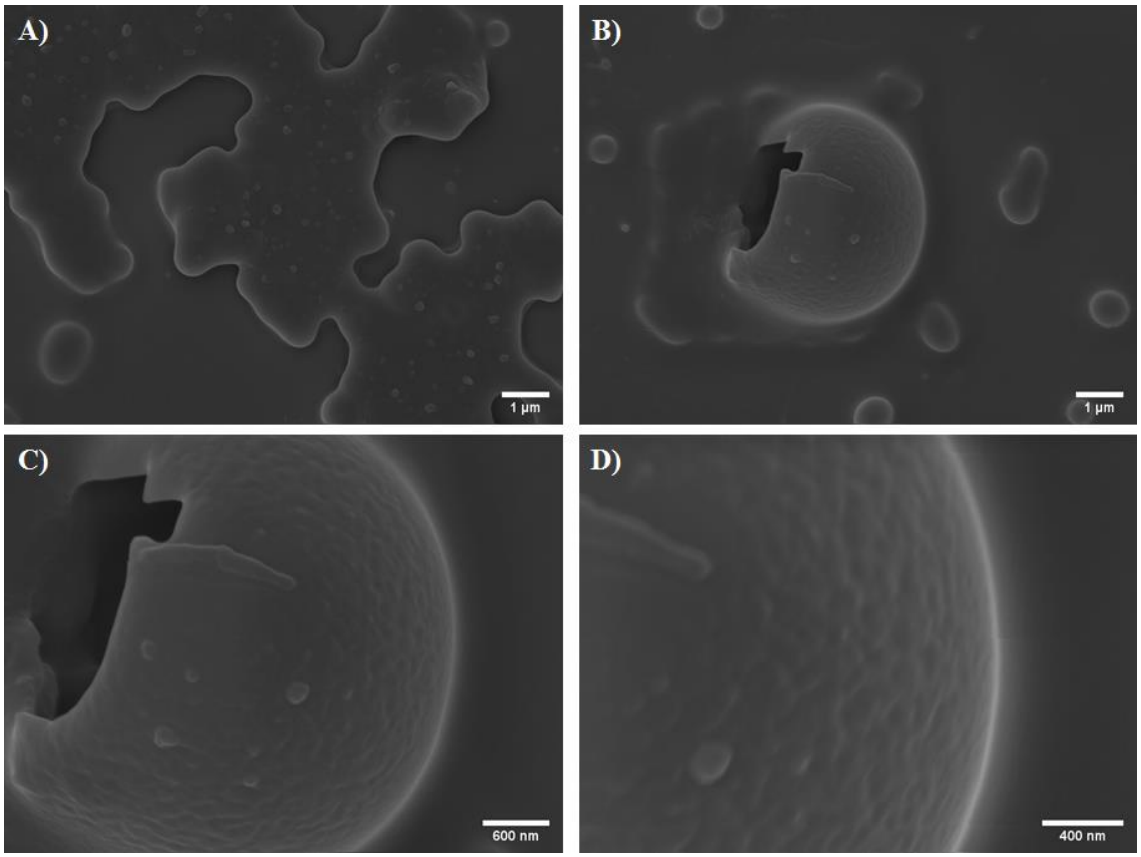

Figure 3.36 SEM images of **57** dropcasted from 10 µM MeOH solution, taken in a region rich in layer-like structures. It is possible to observe a hollow spherical aggregate. Scale Bar 1 µm (A) and (B), 600 nm (C) and 400 nm (D).

3.4.8 Conclusions

In this Chapter the behaviour of the synthesised ligands **37**, **62**, **54** and **55** using spectroscopic and morphologic techniques was shown and discussed. The spectroscopy experiments, focused on **54** and allowed to gain insight on its photophysical properties, both as free ligand and Eu(III) complex.

The ability of the ligand to sensitise the metal centre through the terpy moiety allowed to record Eu(III)-centred phosphorescence emission. These spectra, along with absorbance and fluorescence, were recorded for Eu(III)assemblies with **54** in methanol solution after forming under thermodynamic and kinetic control. This allowed for better understanding of the characteristics of the **M:L** self-assembly formation in the solution. The complex **Eu·54** formed under thermodynamic control was found to have no solvents molecules coordinated to the metal centre (q value), strengthening the hypothesis that in these conditions the complex was formed in 1:1 stoichiometry.

The formation of metal complexes under kinetic control was further studied by performing spectroscopic titration at two different concentrations. This choice was taken

as a consequence of the behaviour observed in the preliminary dilution studies. The process was found to be concentration-dependant, as using solutions at different concentrations lead to different stoichiometries found to be the most likely within this system. After performing non-linear regression analysis on this data it was found that in the presence of an excess of Eu(III), the system would prefer the formation of the 2:3 ligand to metal stoichiometry when measured at higher ligand concentration (10 μM). In contrast, it would prefer the formation of a 1:3 stoichiometry when measured at lower concentration (3 μM).

Morphological studies were performed on **37**, **62**, **54** as well as **Eu·54** using SEM imaging. It was found that **37** formed a hydrogel possessing a fibrous structure upon dissolution in H_2O as trisodic salt and slow reprotonation using glucono-δ-lactone, as literature reports. The functionalisation of such gel with a *d*- (Cu(II)) and *f*- (Tb(III)) metal ions introduced witnessed changes in the size of the resulting fibers, while maintaining the overall structure of the fibres. This was speculated to be related to the high hydrophobicity of the aggregates of **37**, conjugated to a low affinity for the metal used. Addition of **76** containing a UPy moiety to the gel of **37**, in the hope that such a mixed gel might possess different properties, lead to a tighter packing of the fibres, although the final gel did not show improved mechanical properties. Hence, no further modification for these systems was attempted.

76 was also used to attempt the synthesis of novel building block possessing UPy and terpy moieties at opposite ends, ideally able to form supramolecular polymers. Even though the chosen synthetic route did not result in the desired compound, further studies will be attempted in the future to find appropriate conditions that would consent such achievement. The use of activators for the amino groups involved in the reaction, different solvents or performing the reaction at a combination of higher temperature and pressure, such as using a microwave initiator, are all possible options.

Ligand **62** was found to form a weak gel-like system upon addition of water to a MeOH solution in a 75:25 ratio; such gel-like material was found to be composed by irregular nanospheres with an average radius of 167 nm. These nanospheres were hypothesized to be composed by fibres; further investigation will have to be performed on this system to gain a better understanding on the aggregation process that leads to the formation of the gel from the spheres. The behaviour of this system in solution will be discussed in the following chapter.

Ligand **54** was also found to aggregate into very regular nanospheres, almost monodispersed with an average diameter of 50 nm. In this case as well, a fibrous structure could be found to be further aggregate to form the nanospheres. Moreover, it was found, through imaging of Eu(III) assemblies with **54**, in the ratio of 1:1, 2:1 and 3:1, that the presence of the metal ion lead to the coalescence of the nanospheres, corroborating the hypothesis that the ions are able to behave as bridging units between the terpy moieties. The formation of lateral interactions would happen together to the amide core and π stacking, resulting ultimately in the generation of large structures, where the spheroidal shape is lost. At the same time the binding of terpy moieties to the Eu(III) ions would potentially change the overall charge of the system, which would also modify the solvation properties of the overall assembly, its solubility and, hence, lead to the destruction of the nanospheres. These results are in line with the behaviours observed in the spectroscopy studies, as **54** was found to form higher M:L assemblies at higher concentrations. A condition that is met during the slow evaporation of the solvent, the aggregates gain a higher overall charge, which increases with the equivalents of metal added, leading to a more charged (and in turn, more hydrophilic) system, that will consequently form larger, film-like aggregates.

Finally, preliminary imaging of compound **55** in presence of DCU impurities allowed to confirm that the spheres, formed upon the aggregation, are hollow and that the formation of the spheres, hindered by the presence of the urea contaminant is the result of a combination of hydrophobic and hydrogen bonding contribution.

Further studies on these systems will allow to gain a deeper understanding on the aggregation processes involved in their self-assembly, as well as on the mechanical properties of the resulting materials. AFM measurements would allow either confirming or denying the hollowness of the spheres and the use of controlled amounts of urea would allow to understand the mechanism that leads to the formation of the nanospheres.

Chapter 4

Preparation and Characterisation of ternary Ln(III) complexes using BTA and cyclen ligands

4.0 Introduction

The use of lanthanide ions for the formation of hierarchical materials of higher order has attracted growing interest in the recent decades; their high coordination requirements are suitable to direct self-assembly using different ligands, which could lead to desired hierarchy in the aggregation processes.[81] Although various materials were obtained following this rationale, as seen in some of the examples presented in Chapter 1,[80-83] designing such systems presents challenges that make them relatively rare. The Gunnlaugsson group, as reported in Chapter 1, has approached this challenge by designing molecules capable of undergoing self-assembly processes in the presence of Ln(III) ions, where the metal directs the assembly process to form higher-order structures. Exerting control of such processes is highly challenging and one of the main research objectives for supramolecular chemistry. In one of their recently published work in the Gunnlaugsson group,[133] the formation of a higher order material formed using a Ln(III) ions complex was reported. The formation of a higher-order structure was observed *via* the self-assembly of a heptadentate cyclen (1,4,7,10-tetraazacyclodecane)-based ligand, **79**, where the coordination of the Ln(III) ion was completed by a tripodal ligand, 1,3,5-benzene-trisethynylbenzoate, **78** (**Figure 4.1**). The tripodal ligand was found to be a suitable antenna to sensitize the Ln(III) ions through the carboxylic moieties, with the resulting aggregate displaying luminescent properties. The subsequent investigation into the resulting ternary system gave key insights into its properties.

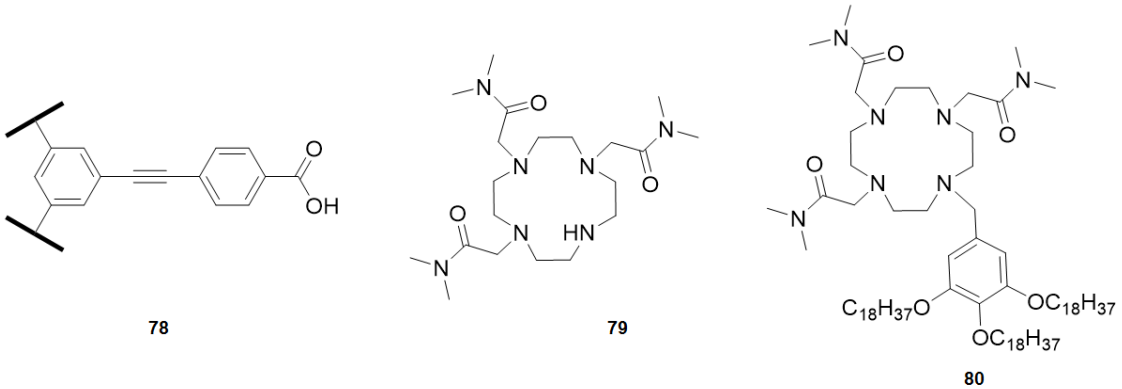

78 79 80

Figure 4.1 Chemical structure of tripodal ligand **78** and cyclen-based ligands **79** and **80**.

In this chapter, a study expanding upon this work will be described. The tripodal ligand **62**, shown in Chapter 2, will be used in place of **78** to saturate the coordination sphere of the Tb(III) ions containing the heptadentate cyclen ligand **80**. Ligand **80** was initially designed as a derivative of **79**, whereby one of the cyclen's NH group is functionalised with a methyl gallate, which is then functionalised with three alkyl chains. The design

and synthesis of **80** was performed by fellow Gunnlaugsson group member Bruno D'Agostino, who was involved in this study, in order to obtain an amphiphilic system capable of forming Langmuir-Blodgett films, with the ultimate goal of obtaining a solid-state sensor.

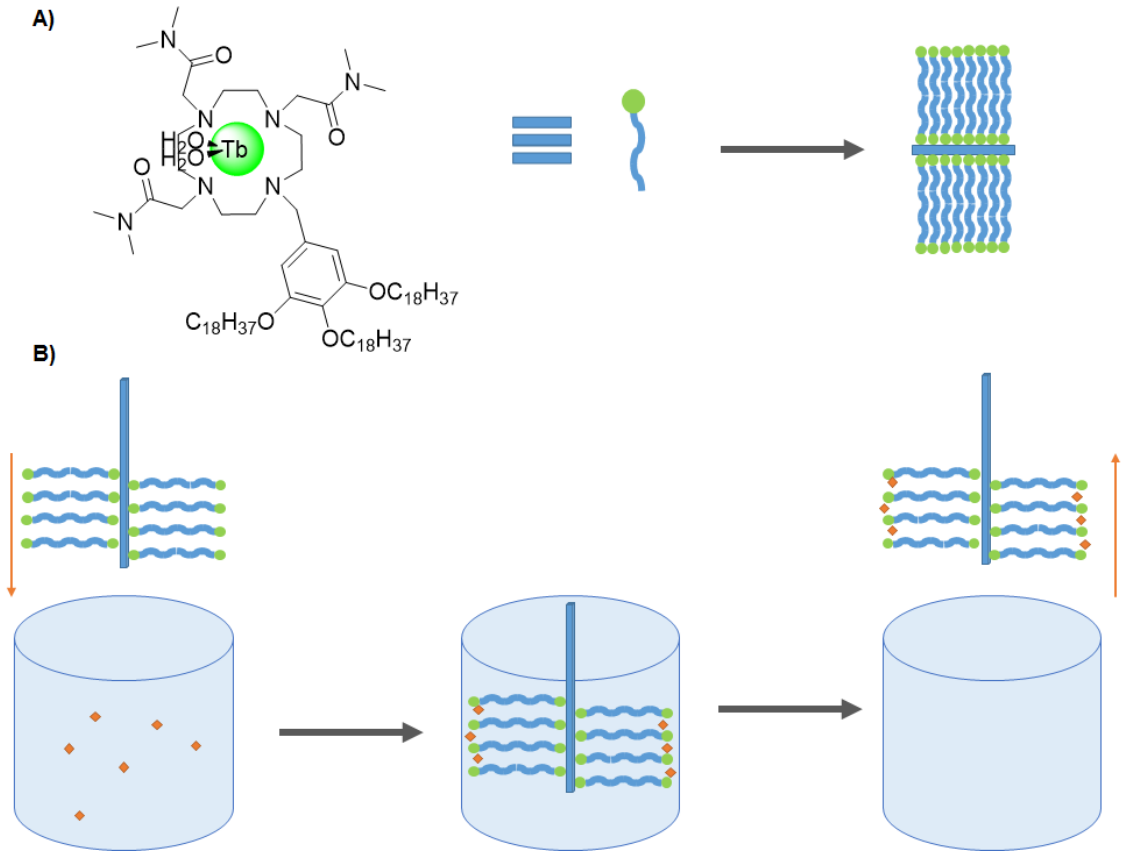

Figure 4. 2 A) Schematic representation of **Tb·80** and the formation of the double layer Langmuir-Blodgett bilayer. B) Schematic representation of the sensing process *via* dipping of the LB films.

In this study, the Tb(III) complex of **80** was used to form a tertiary system with **62** (**Figure 4.3**) in two solvent systems. This was followed by spectroscopic characterization and SEM imaging of the samples, which allowed us to gain a better understanding of the aggregation processes and the effect that a chiral centre could induce onto the final aggregate.

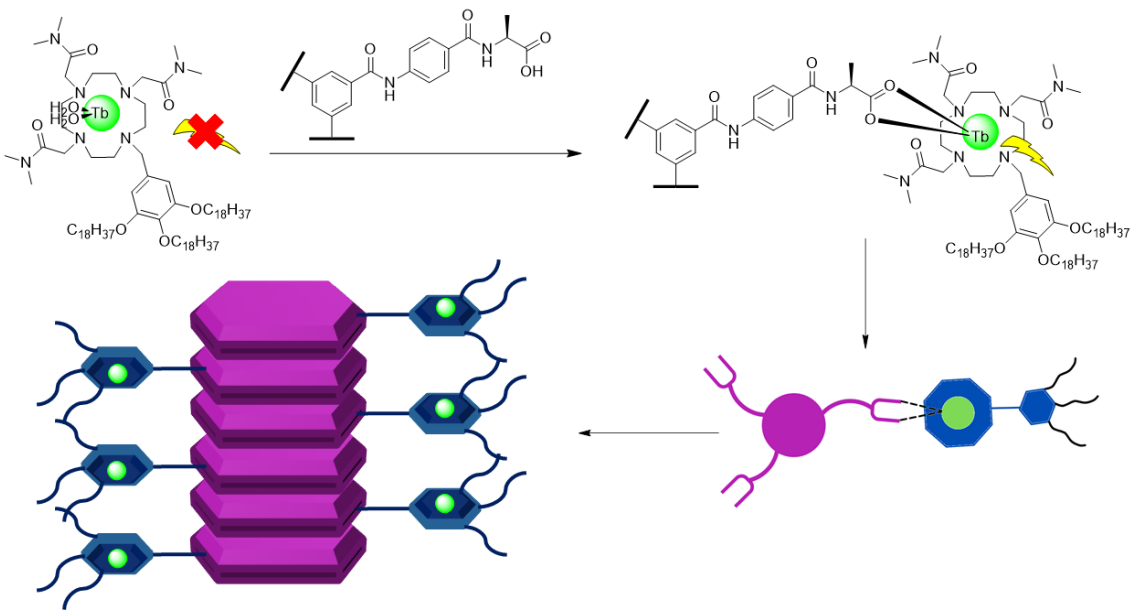

Figure 4.3 Schematic representation of the formation of the ternary system **62**·(**Tb**·**80**) and consequent aggregation model.

4.1 Synthesis of the cyclen ligand

As mentioned previously, the synthesis of **80** was carried out by fellow Gunnlaugsson group member Bruno D'Agostino, however, a short summary of the synthesis and characterization of this ligand will be provided. After the successful synthesis of **80**, the ligand was used to form a Tb(III) complex. The use of the Tb ion results from the fact that the excited state of the tripodal ligand is assumed to be appropriate to populate the ^5D_n excited states of the metal. Hence, it is presumed that we would be able to observe the self-assembly formation between **80** and **62** in real time by performing various spectroscopic titrations. The results of these investigations will be described in section 4.2.

Cyclen-based ligand **80** was obtained through a convergent multistep synthesis, outlined in **Scheme 4.1**. Methyl gallate was initially treated with 1-bromo octadecane to functionalise the ring with long-chain ethers. The methyl ester protecting group was cleaved using KBH_4 in presence of LiCl to obtain the deprotected carboxylic acid, **82**; the carboxylic functionality was then reacted with PBr_3, obtaining the bromo-derivative **83**.

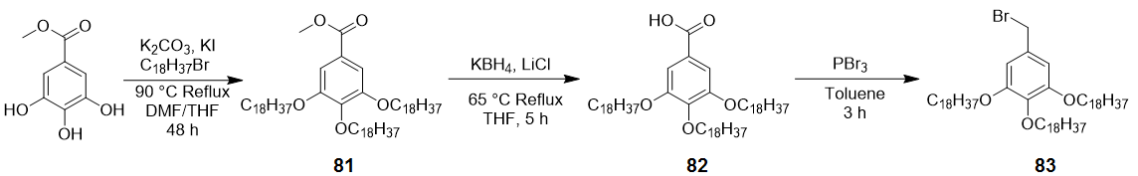

Scheme 4.1 Schematic representation for the synthesis of **83**.

This bromo-derivative was reacted with cyclen using the mono-alkylation procedure developed within Gunnlaugsson group,[134] forming the mono-functionalised derivative **84**, that upon reaction with 2-chloro-dimethylacetamide, formed compound **80 (Scheme 4.2**). This molecule contains four nitrogen atoms possessing a lone electron pair each and three amidic carbonyl groups, allowing it to behave as a heptadentate chelating ligand.

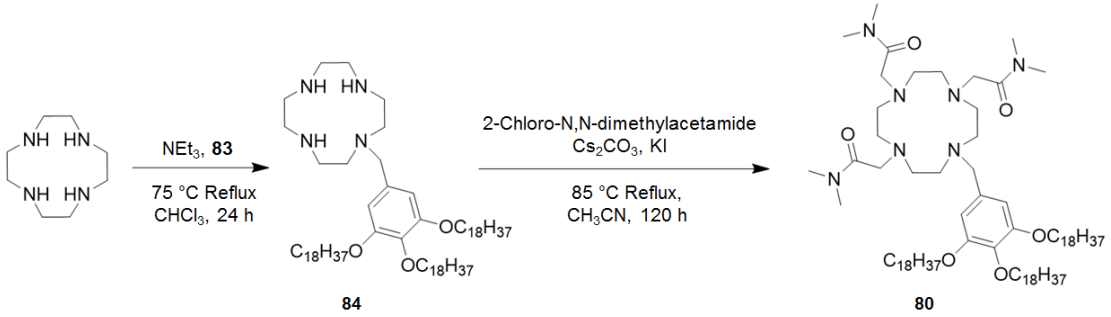

Scheme 4.2 Synthesis of macrocyclic ligand **80**.

The size of the inner cavity of the cyclen has been proven suitable to host various Ln(III) ions, and the presence of the acetamide should increase its ability to stabilise Ln(III) ions that possess very high coordination requirements. Once formed, such complexes possess high binding constants and can be used for various imaging applications *in vivo*.[79, 97, 135] After formation of the ligand, it was used to form the Tb(III) complex by microwave irradiation of a methanol solution of the ligand with a 10% excess of $Tb(CF_3SO_3)_3$. Once the reaction was complete, the solvent was reduced under reduced pressure, and triturated in diethyl ether, yielding a white solid that was isolated by centrifugation.

As seen in Chapter 2, the presence of paramagnetic Ln(III) renders the use of NMR techniques unreliable, and therefore unsuitable, for the characterization of these complexes (see Appendix, FigXX). Instead, FT-IR was used to confirm the formation of the complex. By monitoring the characteristic stretching of the C=O bond, it was observed that the peak for this vibrational mode shifted from 1667 cm^{-1} for **80** to 1643 cm^{-1} for the Tb(III) complex. Further confirmation was obtained by ToF-MALDI mass spectrometry, which confirmed the presence of the Tb(III)-**80** complex (**Figure 4.4**). Further characterisation of ligand **80** and complex **Tb·80** can be found in the experimental and appendix chapter.

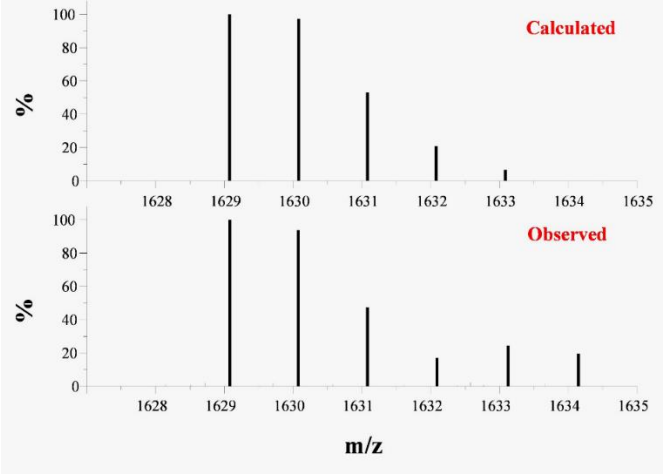

Figure 4.4 Experimental MALDI mass spectrum for **Tb·80** complex (bottom), compared to the calculated one (top). The characteristic molecular weight distribution of Tb complexes can be observed.

4.2 Ternary Tb(III) complex formation

Once the **Tb·80** complex was obtained and characterised, the formation of a ternary complex using ligand **62** was attempted. As discussed in Chapter 1, Tb(III) prefers high coordination numbers, such as 8 or 9, and as a heptadentate chelator, **80** would leave two vacant coordination sites on the Tb(III) ion, which are occupied by solvent molecules. The ternary complex can form upon displacement of these solvent molecules followed by coordination of the carboxyl groups from **62** (**Figure 4.3**).

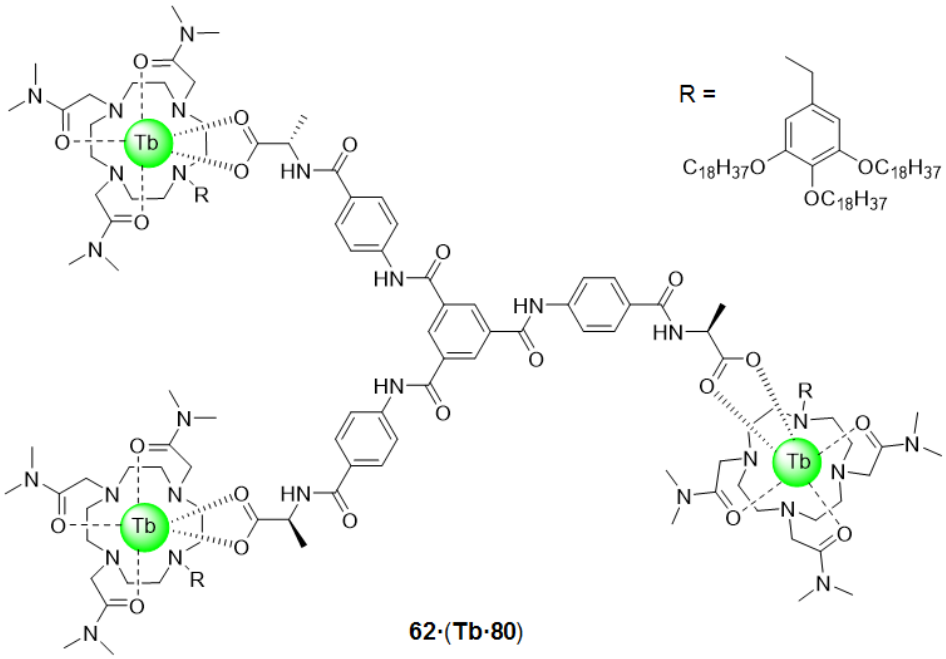

Figure 4.5 Schematic representation of ternary complex **62·**(Tb**·80**), in a 1:3 stoichiometry.

As anticipated in the previous section, the formation of the ternary complex was assumed to enhance the metal-centred emission. The energy gap between the excited state of the

tripodal ligand, and the excited states ^5D_n of the metal ion, would be suitable for ligand-to-metal charge transfers that would populate the latter. The increased population of this state should enable emissive relaxation and, as a result, the phosphorescent emission can therefore be used as a tool to study the aggregation process of this ternary system.

The formation of the ternary system was investigated using spectroscopic and microscopic techniques. Absorbance spectra of a solution of complex **Tb·80** in methanol shows only one absorption band centred at 225 nm which corresponds to the presence of the gallate ring. Although the presence of a benzene ring has been proven to partially sensitize the Tb(III)[136], the intensity of the resulting emission was found to be of very low intensity. A successful displacement of the coordinated solvent molecules by carboxylic groups of **62** would result in coordination of the tripodal ligands to the lanthanide centres through both oxygen atoms, forming a 1:3 stoichiometry between **62** and **Tb·80**, **Figure 4.5**. As a consequence of this coordination, **62** behaves as a light-harvesting antenna and allows for an enhancement of Tb(III)-centred emission in the **62**·(**Tb·80**) assembly.

The method used to investigate the formation of the ternary system was to observe the changes in the absorbance and phosphorescence spectra of a 10 μM methanol solution of **Tb·80** upon the addition of 0.1, 0.2 and 0.3 equivalents of **62** in methanol. The spectra were recorded starting from a solution 10 μM of **Tb·80** to which the equivalents of the tripodal system were added again as methanol solution.

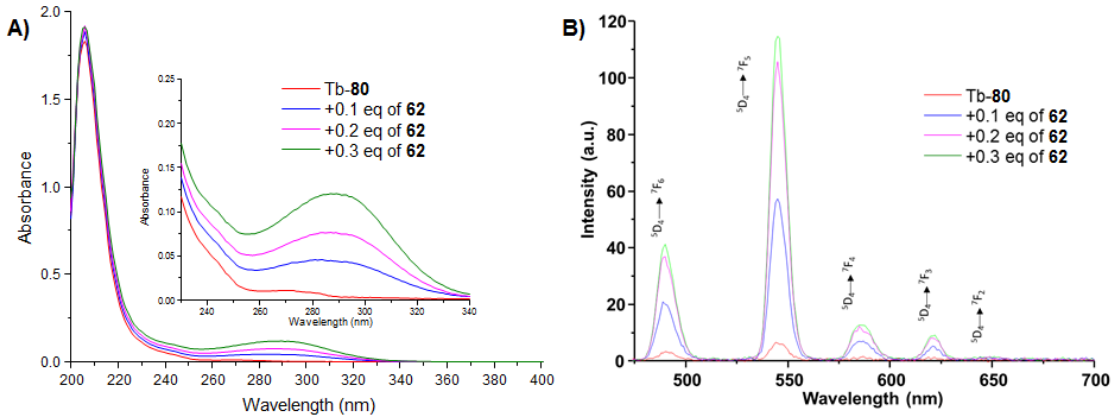

Figure 4.6 A) Absorbance and B) phosphorescence spectra (λ_{ex} = 288 nm) of **Tb·80** (c = 10 μM) upon addition of **62** (0 → 0.3 eq) in MeOH.

As shown in **Figure 4.6 A**, upon the addition of 0.1 equivalents of **62**, it was possible to see the appearance of the absorbance band at 288 nm. This band increases to a maximum when the system reaches a stoichiometry of 1:3 between **62** and **Tb·80** in the range

explored in this study. Simultaneously, the phosphorescence emission spectra were recorded and are shown in **Figure 4.6 B** (λ_{ex} = 288 nm). It was possible to observe the bands associated with the terbium emission, *i.e.* the ones relative to the $^5D_4 \rightarrow {}^7F_{2\text{-}6}$, increase upon the formation of a 3:1 **62**:(**Tb·80**) stoichiometry. To consider the presence of kinetic effects, the spectra were recorded both immediately after the additions of **62**, and after a 10 minute delay. As no difference was found between the two sets of spectra in the three titrations performed, it was concluded that the system is not subject to kinetic effects and hence the titration could be proceeded without any delay between additions. The formation of the ternary complex can be observed by the naked eye through exposing the methanol solution of complex **Tb·80** to **62**. **Figure 4.7** shows pictures taken under UV irradiation (λ_{ex} = 254 nm) of the solution of **Tb·80** before the addition of **62** (A) and when 0.3 equivalents of **62** were added (B), in which the presence of a bright green emission is observed.

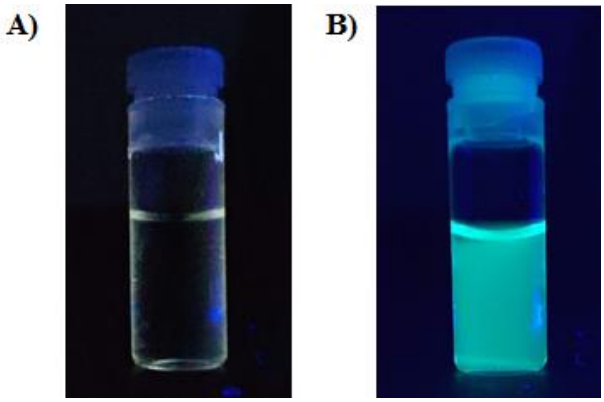

Figure 4.7 Picture of methanol solutions of **Tb·80** before (A) and after (B) the addition of 0.3 equivalents of **62**, under UV light (λ_{ex} = 254 nm) irradiation.

To gain further understanding of the effect that the solvent would have on the self-assembly processes, both UV-Vis absorption and emission (in phosphorescence mode) titrations were carried out using THF as a solvent. Starting from a 10 µM solution of **Tb·82** in THF, 0.1, 0.2 and 0.3 equivalents of **64** were added, and the spectra were recorded immediately after the mixing, and after 10 minutes of the addition. The absorbance spectra (**Figure 4.8 A**) shows the formation of two bands, centred at 296 and 371 nm for **Tb·80**. After the addition of **62**, these bands undergo a hyperchromic effect, as already observed in the methanol spectra. At the same time, it is possible to observe a hypsochromic shift for the bands, which leads to the bands being centred at 288 and 356 nm respectively after the addition of 0.3 equivalents of **62**. Another factor that was considered is that the reduced solubility of **62** in THF might aid to produce a solvophobic

effect on the assembly, which would then facilitate the formation of ternary complexes with 1:1, 1:2 and 1:3 stoichiometries - as these would be charged species and better accommodate **62** in solution.

The phosphorescence spectra in THF (λ_{ex} = 296 nm) are of particular interest (**Figure 4.8 B**) as they also allowed us to monitor the formation of the desired ternary complexes. The initial luminescence spectrum of **Tb·80** shows a small signal for the ($^5D_0 \rightarrow {}^7F_J$, J = 0–4) transitions. Again, it is possible that in THF, the benzene ring of **80** is able to act as an antenna and partially sensitize the Tb(III) metal centre, with consequent phosphorescent emission. Upon the addition of 0.1 equivalents of **62** (solid blue line) and following the mixing of solution, it was possible to observe a hyperchromic effect, with the tripodal ligand acting as an antenna and activating the phosphorescent emission.

Recording the phosphorescence spectrum after a 10 minute delay (blue dashed lines) showed the signal increasing further which hints to kinetic effects occurring in this system. Consequently, the change in the emission were recorded at 10 minute intervals, with the signals increasing at every measurement, until a plateau was reached after 40 minutes from the addition.

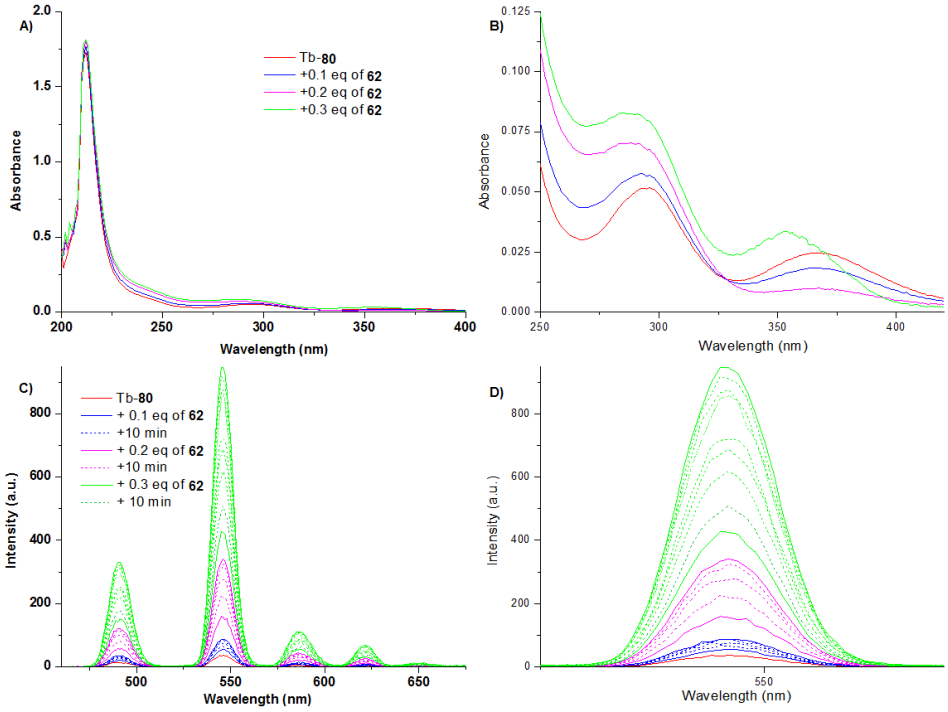

Figure 4.8 Absorbance (A, B) and phosphorescence (λ_{ex} = 296 nm) (C, D) spectra of **Tb·80** (c = 10 μM) upon addition of **64** (0 → 0.3 eq) in THF.

Once the plateau was reached and the signal was stable, a second aliquot of 0.1 equivalents of **62** was added to the solution and the spectrum recorded. Again, the intensity of the signal increases upon this addition (pink solid line), increasing further in

all the spectra recorded after 10 minutes intervals (pink dashed lines), with the plateau reached after a total of 40 minutes from the first addition. The third aliquot of 0.1 equivalents was added and the process was repeated (green solid and dashed lines).
The final emission intensity for the ternary system in THF was almost doubled (90% increase) when compared to the one recorded in methanol under the same conditions. After repeating the titration several times and observing these phenomena, the explanation speculated for this behaviour was, again, connected to the less prominent competitive behaviour of THF. In conjunction with this, the poor solubility of **62** in THF would, through the solvophobic effect, strengthen the binding between **Tb·80** and **62** and possibly modulate the ability to transfer the energy between the antenna and the metal centre. Furthermore, the poor solubility in THF did not allow for satisfying fits for the data, therefore making it impossible to obtain the binding constants in this solvent.

To grasp a better understanding of the stability of the system at various stoichiometries, a different experiment was designed. A methanol solution of **Tb·80** (from 0 to 4 equivalents) was titrated into a solution of **62** (10 µM) and the effect of the addition was studied by recording the absorbance, fluorescence and phosphorescence spectra. Absorbance spectra of **62** shows two bands centred at 279 and 358 nm (**Figure 4.9 A**), which, upon addition of **Tb·80**, increases in absorbance. Two binding isotherms were obtained by plotting the absorbance values at 279 and 358 nm (**Figure 4.9 B**).

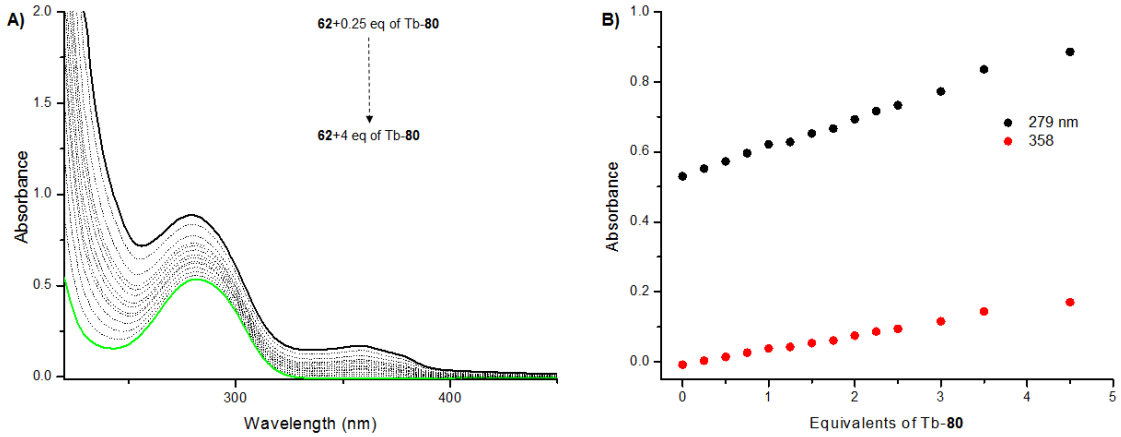

Figure 4.9 A) Absorbance spectra for a 10 µM MeOH solution of **62** upon addition of **Tb·80** (0 → 4 eq). B) binding isotherms for the bands at 279 and 358 nm.

There is a single point change in the slope of the binding isotherm plots corresponding to the addition of 3 equivalents of **Tb·80** and implying the formation of a stable 1:3 ternary system. To further investigate this, we examined the fluorescence data for the same titration (**Figure 4.10 A**). Upon excitation with λ_{ex} = 279 nm, it was possible

to record the fluorescence of **62**, showing a band centred at 352 nm, which was quenched upon the addition of **Tb·80**.

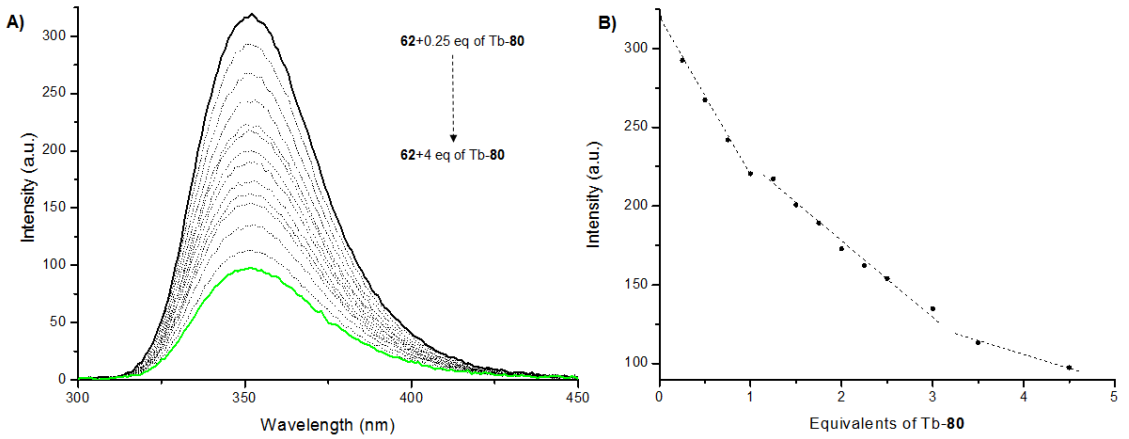

Figure 4.10 A) Fluorescence spectra (λ_{ex} = 279 nm) for a 10 µM MeOH solution of **62** upon addition of **Tb·80** (0 → 4 eq). B) binding isotherm recorded at 352 nm.

Once again, plotting the intensity for the peak at λ = 352 nm against the equivalents added allowed us to obtain a binding isotherm (**Figure 4.10 B**). The quenching of the fluorescence **62** (red) shows two changes in the slope, at 1 and 3 equivalents, indicating the formation of the 1:1 and the 1:3 (M:L) species.

The data was also recorded in phosphorescence mode. Methanol solutions of **62** did not show any signal, as expected. Upon addition of Tb-**80**, the tripodal ligand sensitized the metal centre and activated the phosphorescence emission, which was revealed in the spectra (**Figure 4.11 A**). The binding isotherms (**Figure 4.11 B**), in particular the one relative to the peak at 545 nm, shows two very well-defined changes in the slope, at 1, 2 and 3 equivalents, clearly showing the formation of the 1:1, 1:2 and 1:3 species.

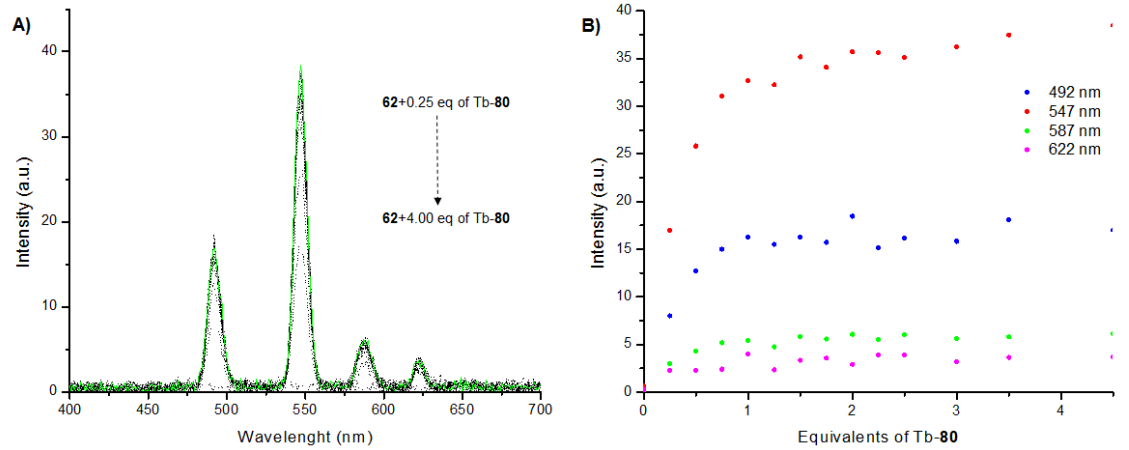

Figure 4.11 A) Phosphorescence spectra (λ_{ex} = 279 nm) for a 10 µM MeOH solution of **62** upon addition of **Tb·80**. B) Binding isotherms recorded at 492, 547, 587 and 622 nm.

The data was analyzed using the non-linear regression analysis software ReactLab to determine the binding constants for the three species formed in the solution.[137] In particular, reliable fitting was obtained using the data recorded in phosphorescence mode, and analogously to what was shown in Chapter 3, the binding equilibria and equations had to be considered:

$$nTb + mL \leftrightarrows Tb_nL_m \qquad \textbf{\textit{Formula 4.1}}$$

$$\beta_{n:m} = \frac{[Tb_nL_m]}{[Tb]^n[L]^m} \qquad \textbf{\textit{Formula 4.2}}$$

The model with the three species was used with the software to yield the constants shown in **Table 4.1**. The values indicate that the three species all present similar stability constants ($\log\beta_{1:1}$ = 7.10; $\log\beta_{1:2}$ = 7.53; $\log\beta_{1:3}$ = 7.37) indicating very limited, if any, cooperativity effects in the formation of the ternary species.

Table 4.1 Binding constants for the formation of the 1:1, 1:2 and 1:3 species for **62·(Tb·80)** complexes. The fitting was performed using the phosphorescence data.

Stoichiometry (L:M)	logβ	StD
1:1	7.10	± 0.03
1:2	14.63	± 0.05
1:3	22.00	±.0.07

The quality of the fit was considered high, as low values for standard deviation were found. Comparing these values to the ones observed in the previous work in the Gunnlaugsson group,[133] a similar trend can be observed - the values obtained for the tripodal benzoate system were found to be close to the ones obtained here: 6.05 ± 0.18, 7.45 ± 0.19 and 6.24 ± 0.39 for the 1:1, 1:2 and 1:3 (L:M) species respectively. Additional details on the fit can be in the Appendix chapter.

From the binding constants, the software was able to produce a species distribution diagram, which is shown in **Figure 4.12**. This allowed some understanding of the dynamics of the complexation process. The first ternary system to form is obviously the 1:1 complex, which reached a maximum of 18% at one equivalent of **Tb·80**. The 1:2 species starts forming almost immediately, reaching a maximum of 28% when 2 equivalents are added. The 1:3 complex starts forming upon the first addition as well and increases quickly to 95% of the ligand-containing species at 3 equivalents, after which the "conversion" from 1:2 to 1:3 species slows down, reaching a plateau at 3.5 equivalents.

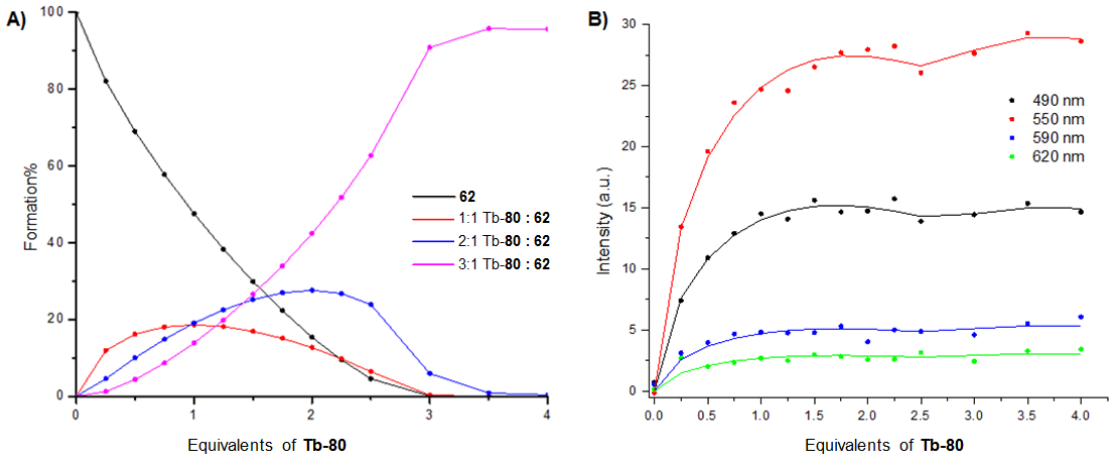

Figure 4.12 (A) Speciation-distribution diagram for the titration of **62** with **Tb·80** performed in methanol and (B) binding isotherms and relative fits obtained from phosphorescence data.

In conclusion, the green emission characteristic of Tb(III) complexes was visible to the naked eye upon irradiation (λ_{ex} = 254 nm), with the spectroscopic studies allowing us to confirm the formation of the ternary system through the emission spectra in phosphorescence mode. The titration in the two solvents allowed to see the difference between a more and less competitive solvent, MeOH and THF, respectively, with the control over the aggregation switching from thermodynamic to kinetic. The non-linear regression data showed the predominance of the 1:3 (L:M) species at 3 equivalents of metal added, although no cooperativity effects were observed when considering the values of the single equilibrium constants. The following section will expand the understanding of the aggregation modes from a morphological point of view.

4.3 Morphology studies

Once **62**·(**Tb·80**) had been obtained under kinetic control and characterised using various spectroscopic techniques, its aggregation properties in organic solvents was studied using SEM technique and compared to **62** and **Tb·80**. As seen in Chapter 3, **62** shows aggregation properties in MeOH/H_2O mixtures and, in this section, the studies will show the behaviour of the ligand in solution. In particular, the role of the two components will be discussed to gain some understanding over the interaction directing the aggregation. The hypothesis proposed for the aggregation involves a preliminary self-assembly of molecules of **62,** that subsequently bind the metal centre.

To test this, samples were prepared using the same procedure described in Chapter 3, by dropcasting 20 µL of 10 µM solutions on silicon wafers (see Experimental Details). The wafers with compounds dropcasted on their surface were left to dry for 24 hours in air

and then under high vacuum for 2 hours prior to the imaging. The fully dried samples, being non-conductive, were sputter coated with an ultra-thin gold film to allow the imaging without incurring any charging effect from primary electrons.

The first sample imaged, obtained by casting a 10 µM solution of **Tb·80** prepared in methanol, **Figure 4.13**, shows no particular order or structured aggregation, with only random aggregation happening on short distance pseudo-bundles.

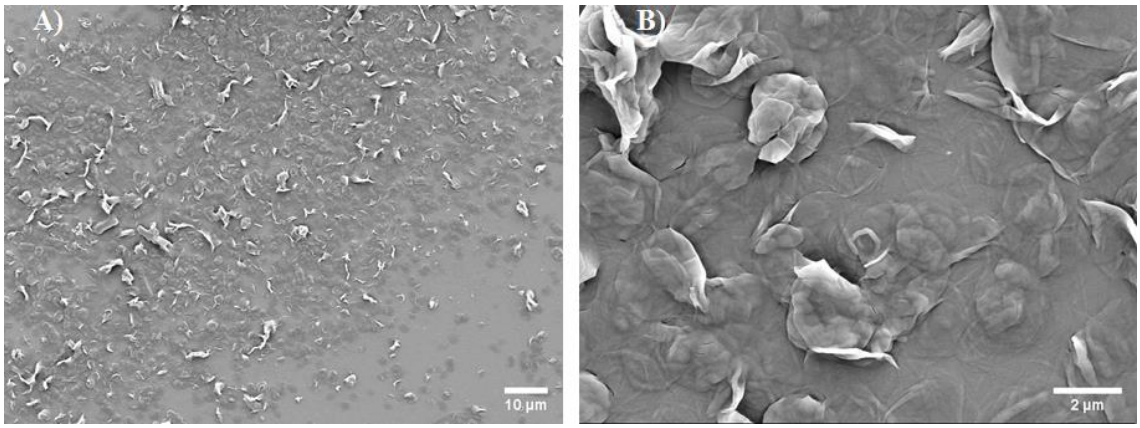

Figure 4.13 SEM images of **Tb·80** (20 µL, 10 µM methanol solution). Scale bar (A) 10 µm and (B) 2 µm.

Conversely, images taken from a **Tb·80** solution in THF seem to show that the complex appears in a rod-like structure, hinting to an early stage of a crystallization process for **Tb·80** (**Figure 4.14**).

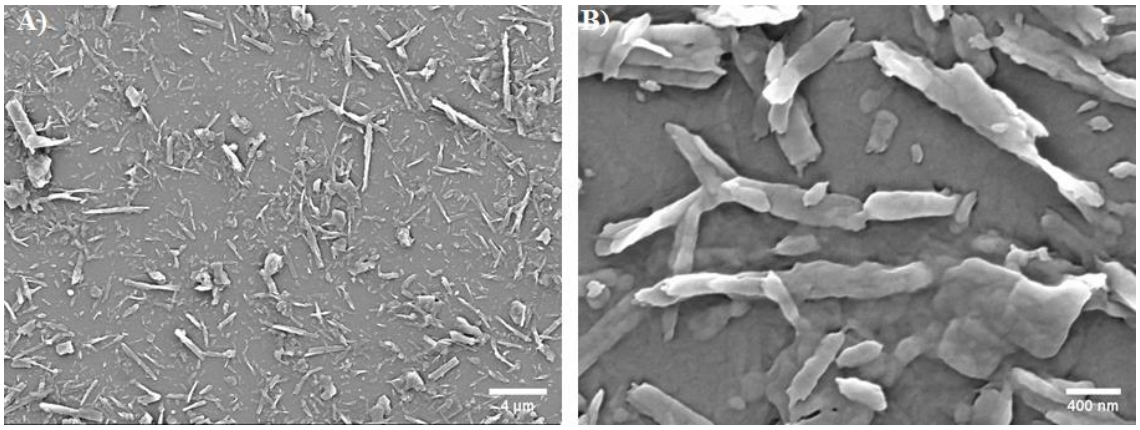

Figure 4.14 SEM images of **Tb·80** (10 µM THF solution). Scale bar (A) 10 µm and (B) 2 µm.

The preliminary imaging of **Tb·80** show that, in MeOH, the intermolecular interactions do not lead to a well-defined structure. This could be related to a high affinity to the polar solvent which is able to interact with the polar "head" of the complex, meaning the non-polar tails do not seem to arrange. On the other hand, in THF a much more ordered structure was observed - the rod-like structure seem to hint to a better

packing, presumably do to a stronger solvophobic effect that allows the molecules to form the rod-like systems.

The imaging was also performed on samples of **62** in solution. In this case, the poor solubility of **62** in THF made it impossible to obtain images from this solvent, limiting the imaging to samples casted from a MeOH solution. The images, **Figure 4.15**, show the formation of a snowflake-like aggregate which are relatively big in size (*ca.* 455 μm).

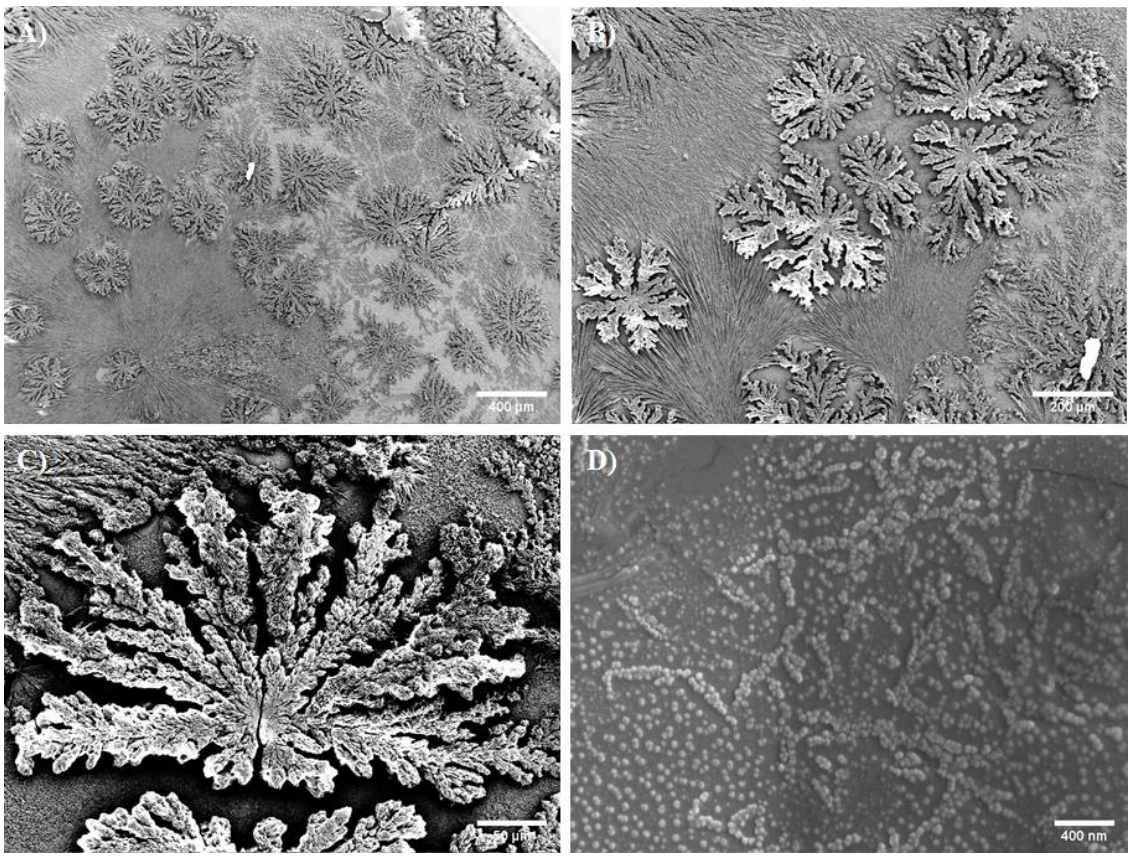

Figure 4.15 SEM images of **62** (10 μM methanol solution). Scale bar (A) 400 μm, (B) 200 μm, (C) 50 μm and (D) 400 nm. A weak charging effect can be observed in (C).

The formation of self-assembled structures is evident, and as seen in Chapter 3, this was not unexpected. Upon magnification, it was possible to observe the formation of smaller spheroidal aggregates that confirm the ability of **62** to aggregate through the hydrogen interactions of the amide groups.

Subsequently, imaging of the 1:3 (L:M) self-assembly was performed on samples casted from methanol and THF solutions, obtained upon addition of 3 equivalents of **Tb·80** to 10 μM solutions of **62**. Although not soluble in THF on its own, **62** completely solubilizes once **Tb·80** is added. The images acquired from the samples casted from a methanol solution show the formation of early aggregates of *ca.* 17 μm in diameter, defined as

micro-coil or micro-urchins (**Figure 4.16**, **B**), with a micro-crystalline structure visible even on a micrometer scale (**Figure 4.16**, **C**). This new structure, different from the ones observed before for the two single components, seems to indicate that the ternary complex units interact in methanol and rearrange themselves into regular structures to a certain extent, as evident from the formation of short-range microcrystalline domains.

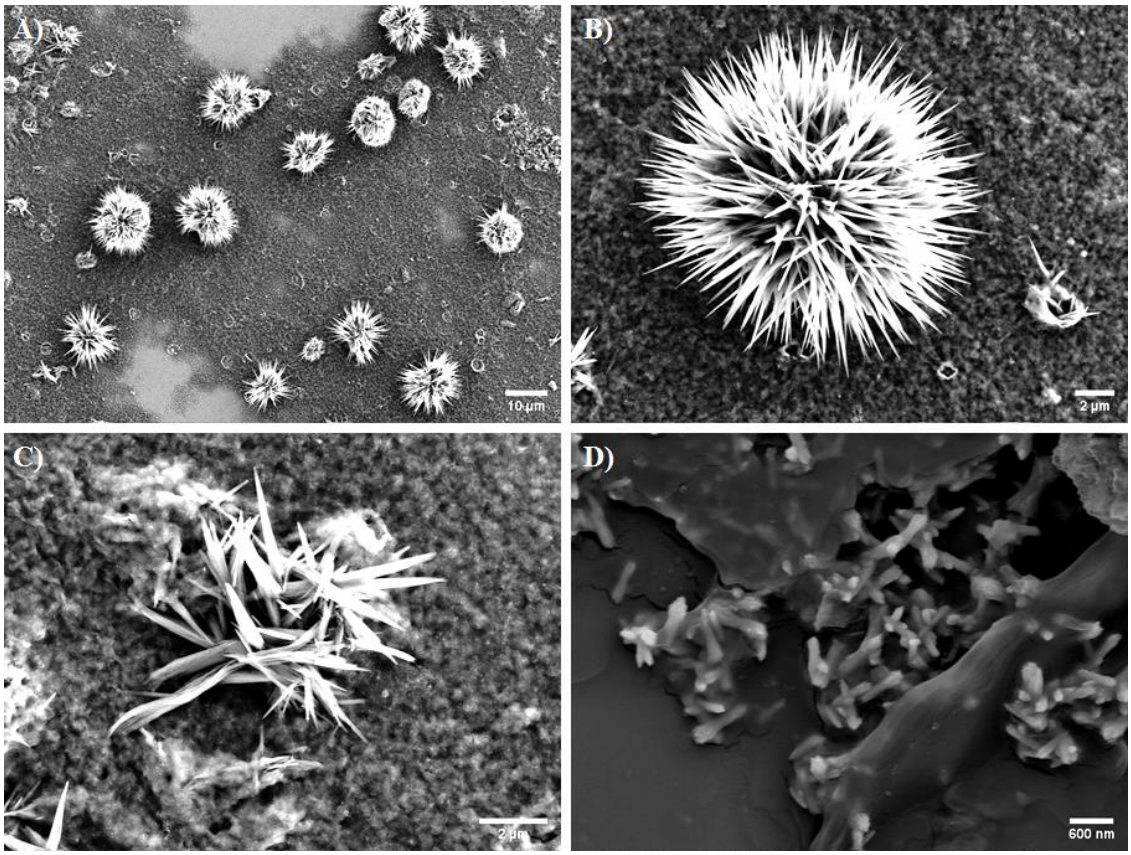

Figure 4.16 SEM images of **62·**(**Tb·80**) 1:3 mixture (10 µM methanol solution). Scale bar (A) 10 µm (B) and (C) 2 µm and (D) 500 nm.

The imaging of **62·**(**Tb·80**) prepared in THF upon mixing (**Figure 4.17**), shows a system that forms compact films in which smaller (300 - 800 nm), irregular aggregates, can be seen. This seems to confirm what was seen during the spectroscopic studies, where an important kinetic effect could be observed in the titrations performed in THF.

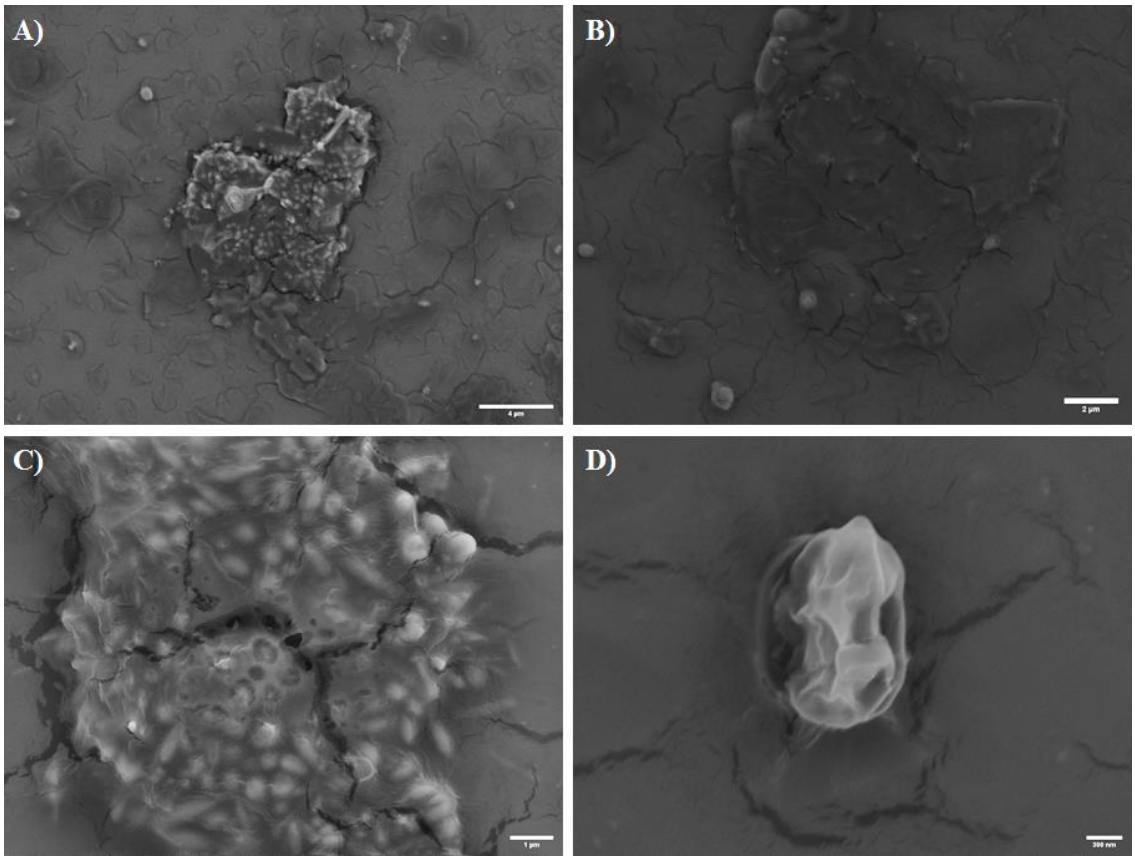

Figure 4.17 SEM images of **62·(Tb·80)** 1:3 mixture (10 μM THF solution). Scale bar (A) 4 μm, (B) 2 μm, (C) 1 μm and (D) 300 nm.

At high magnification (**Figure 4.17 C**) it is possible to see that the larger clusters are composed of smaller, irregular aggregates that form in the nanoscale range, with sections of *ca.* 300/400 nm. This seems to indicate that upon simple mixing, the formation of the complex in THF, confirmed by the luminescence, does not lead to ordered structures. The presence of a much more polar component in the ternary system suggests that in this case, the solvophobic interactions do not allow the complex to form a regular arrangement. At the same time, the tripodal system was not able to form the network of hydrogen bonds necessary for its self-assembly.

The solutions obtained upon simple mixing were then exposed to microwave irradiation; which should allow the systems to rearrange and assemble under thermodynamic control, possibly forming a 1:1 species in higher yield by passing any energy barrier or kinetic traps, reaching the most stable system, *i.e.*, the one at the lowest energy minimum. Once more, it was possible to observe different aggregates in the two solvents. The mixture in methanol casted after the irradiation shows the formation of larger aggregates that completely replace the urchin-like aggregates that were observed

upon simple mixing. These aggregates, shown in **Figure 4.18**, seem to lack a higher-degree order, with a more amorphous nature.

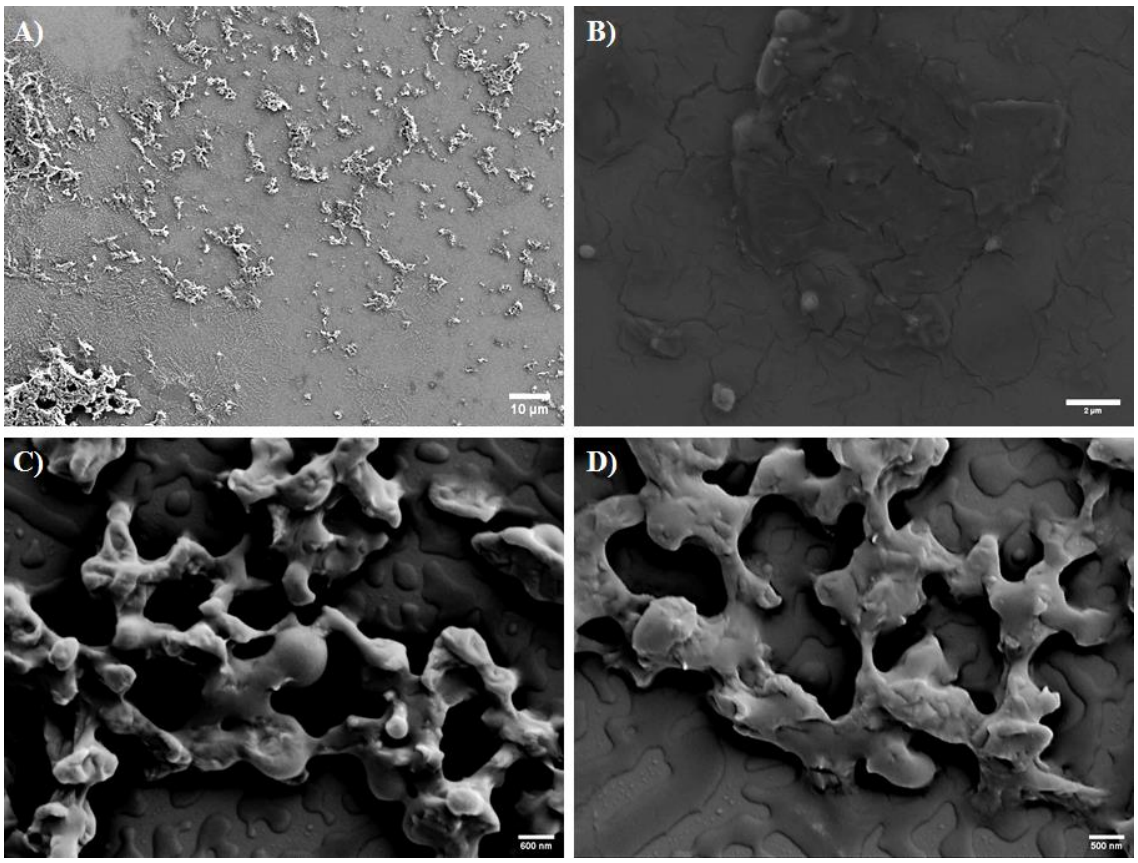

Figure 4.18 SEM images of **62**·(**Tb**·**80**) 1:3 mixture (10 µM methanol solution) after 1 hour MW irradiation at 100 °C. Scale bar (A) 10 µm, (B) 2 µm, (C) 600 nm and (D) 500 nm.

The microwave irradiation shows an even more interesting effect on the final aggregate for the system in THF. In **Figure 4.19** it is possible to observe the formation of a network of fibrous aggregates.

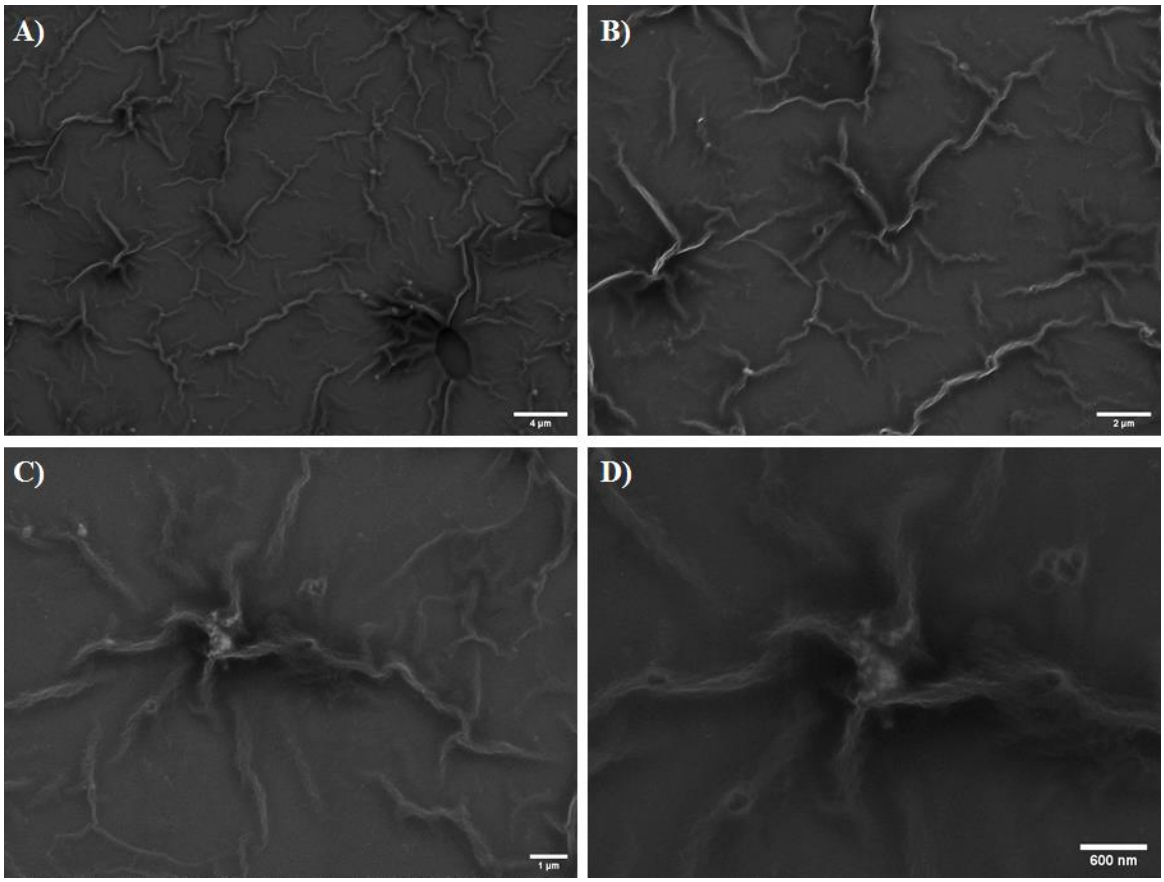

Figure 4.19 SEM images of **62**·(**Tb**·**80**) 1:3 mixture (10 µM THF solution) after 1 hour MW irradiation at 100 °C. Scale bar (A) 4 µm, (B) 2 µm, (C) 1 µm and (D) 600 nm.

The fibres show a relatively small cross-section diameter of *ca.* 290 nm and extend over several µm. The fibres also display a "twist" along their main axis, a behaviour that has been observed previously on aggregates formed from BTA-based systems.[47, 62, 73] They intertwine to form networks that extend over tens of µm, resulting in a much more complex structures compared to the one obtained upon simple mixing and possibly indicating the formation of 1:3 (L:M) complex in the higher yield. The irradiation can be speculated to allow the complex to overcome energy barriers, allowing the system to freely rearrange in THF in such a way that the hydrogen bonds network of the tripodal BTA derivative could form the "backbone" of the aggregate, with the "moieties" containing the **Tb**·**80** unit arranging themselves laterally.

4.4 Conclusions

This chapter focused on the formation and the study of a ternary complex by using one of the tripodal BTA derivatives described in Chapter 2 and a Tb(III) cyclen based complex. The Tb(III) cyclen-based complex was obtained through a multi-step synthetic approach that allowed us to obtain ligand **80** as a yellow solid which was characterized

by ^{1}H NMR spectroscopy, mass spectrometry and elemental analysis. The ligand was then used to form the Tb(III) complex **Tb·80** upon reaction of **80** with $Tb(CF_3SO_3)_3$ under microwave irradiation in methanol solution. The complex was obtained as a white solid, which was characterised with mass spectrometry techniques, ^{1}H NMR and IR spectroscopy. **Tb·80** shows a very small luminescence signal, which was found to be enhanced by the addition of an antenna system. On addition of 0.3 equivalents of ligand **62**, it was possible to observe a significant enhancement of the Tb(III)-centred emission upon ligand excitation at 288 nm. Performing spectroscopic titrations of **62** with **Tb·80** it was possible to obtain consistent absorbance, fluorescence, and phosphorescence spectra and observe the changes that **Tb·80** induced during interaction with **62** in two different solvents, methanol and THF, respectively.

In methanol, the addition of **Tb·80** allowed observation of a hypochromic effect in the absorbance spectrum of **62**. At the same time, quenching is observed in the luminesce spectra for the emission of the ligand **62** centred at 352 nm, while there is an increase in intensity of the band centred at 545 nm. This relates to the emission of the Tb(III) ion and in particular to the ($^{5}D_0 \rightarrow {}^{7}F_J$ J = 1) transition observed in phosphorescence acquisition mode. These effects become more and more pronounced upon every addition, until a plateau was reached at a total of 3 equivalents of **Tb·80**. Fitting the data using the non-linear regression analysis software, ReactLab,[137] allowed us to obtain the binding constants for the 1:1, 1:2 and 1:3 species, with the relative values suggesting the lack of cooperative effects.

The spectroscopic measurements were performed in THF despite the poor solubility of **62** as a free ligand as **Tb·80** allowed the tripodal ligand to dissolve upon the formation of the ternary species. The titrations in this system were therefore performed by titrating a solution of **Tb·80** in THF (10 μM) with 0.1, 0.2 and 0.3 equivalents of **62** from a stock solution prepared in methanol. In this case, the absorbance spectra showed a hypsochromic effect for the two bands, centred at 296 and 371 nm, which shifted to 288 and 356 nm, respectively, upon reaching 0.3 equivalents of **62**, *i.e.* a 1:3 ratio between **62** and **Tb·80**. This behaviour was correlated to the formation of a different species, the ternary complex, that display a strong interaction. A particularly interesting behaviour that was observed during the titrations conducted in THF was the recording of a strong kinetic effect in the phosphorescence spectra, with the signal increasing over 40 minutes after every addition, with a maximum of 60 minutes for the final addition.

The morphology of these systems was also studied using SEM, obtaining images for the 1:3 species in methanol or THF, both before and after microwave irradiation, in order to discriminate between assemblies formed under kinetic and thermodynamic conditions. Imaging of **Tb·80** deposited from both solvents, and **62** from methanol, was also performed. The former did not show the formation of any supramolecular aggregate, with the molecules arranging into rod-like structures, while the latter shows snowflake-like structures.

In methanol, the 1:3 species displayed urchin-like aggregates formed under kinetic control, that replace the seemingly more ordered "snowflake-like" ones. This could be speculated to be a consequence of the fact that the presence of the **Tb·80** complex removes the carboxylate moieties from the aggregation agents, leaving only the BTA core as main drive for the aggregates. After microwave irradiation, the urchin-like structures evolved into more complex and extensive ones, with an inferior microcrystalline character, possibly due to a different rearrangement of the alkyl chains bound to the gallate.

In THF, upon simple mixing, the ternary species displayed irregular aggregates, with the network composed of smaller units lacking visible order. Upon irradiation, it was possible to observe the formation of thin and long fibres capable of intertwining to form an extended and complex network, which could potentially trap solvent efficiently. The formation of such an ordered structure suggests that, due to the low affinity demonstrated by **62** for THF, the overall aggregation can be influenced by a form of the solvophobic effect which drives the process to a higher degree of order.

The work presented here will be expanded by studying the behaviour of the fibrous network formed by the ternary complex in THF at different concentrations in order to gain insight into the aggregation process and the dynamics that lead to these fibres. At the same time, this ternary system could be studied in different solvent systems using spectroscopic techniques to gain a wider understanding of the effect of solvent on the aggregation. This would provide further clarification on the stoichiometry and the binding mode within the assemblies formed. Finally, the use of different Ln(III) ions capable of forming ternary complexes could be attempted to obtain information on the effect on not only the overall spectroscopic properties of the system, but also potentially on the aggregates.

Chapter 5

Morphology studies for aggregators

5.0 Introduction

The work described in this chapter will be a departure from the one described in the previous ones. Herein, a series of aggregating systems will be presented; the various supramolecular structures resulting from the self-assembly processes will be studied morphologically using SEM imaging to highlight the differences arising from the different forces driving the aggregation processes in different solvents. The systems presented here are based on two different architectures. The first is the **1,8-Naphthalimide**, shown in **Figure 5.1**, **A**, a well known aggregator, that has been vastly studied in the Gunnlaugsson group over the years.

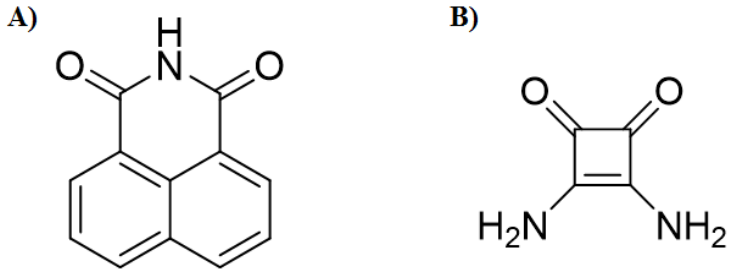

Figure 5.1 Structures of the core architectures for the systems shown in this chapter, 1,8-naphthalimide (**A**) and squaramide (**B**)

The naphthalimide derivatives presented in the studies presented here were synthesised in collaboration with members of the Gunnlaugsson group. The second architecture is based on the **squaramide** core, shown in **Figure 5.1**, **B**. Squaramide derivatives have been attracting increasing attention in the last few years thanks to their combination of structural rigidity, hydrogen bonding abilities, which are similar to those found in ureas and thioureas, which are well known gelators, and electronic properties that make these system increasingly interesting for formation of supramolecular structures.[138] Both the derivatives described in this work were synthesised in the Elmes Group from Maynooth University. As in the case of the naphthalimides, these squaramide derivatives were investigated using SEM, similarly to the compounds presented in the previous chapters. On both occasions, imaging samples were obtained by drop-casting their solutions (from different solvents) on to Silicon wafers after they had been dried in air and under vacuum. The discussion below, begins with the work carried out in collaboration with the Elmes research group.

5.1 Squaramide derivatives

Squaramides are a family of conformationally rigid cyclobutene ring derivatives. This small molecular scaffold is comprised of two carbonyl hydrogen-bond acceptors in close

proximity to two NH hydrogen-bond donors rendering it extremely useful as a tool in areas as diverse as catalysis, molecular recognition, bioconjugation, and self-assembly, which is particularly interesting for the scope of this work.[139-140]

These scaffolds possess impressive bonding properties, which arise from a combination of two factors. The delocalization of a nitrogen lone pair into the cyclo-butenedione ring system confers the four-membered ring with aromatic character, and at the same time, the presence of the carbonyl and amidic groups, respectively, acts as acceptors and donors of hydrogen bonds. This combination makes these systems highly advantageous in self-assembly processes, as well as molecular recognition ones, as the aromatic character brings about an increased thermodynamic stability from which these processes benefit, while the hydrogen bonding character enables these systems to self-associate in a 'typical' tape like manner often seen for their related urea systems.[141] These properties have attracted a lot of attention towards the squaramidic architectures, especially considering that they possess conformational rigidity and synthetic versatility, thereby lending themselves as effective model-systems to deepen the insight of aggregation processes.

In this work, the tetrabutylammonium salts of two anionic squaramides derivatives, **85** and **86** shown in **Figure 5.2**, were studied. Both these systems were designed in order to include an aromatic moiety, that would be able to act as a sensitising antenna, which would absorb in the UV-Vis region, as well as possessing an electron withdrawing effect (in position 4 for **85** and in positions 3 and 5 for **86**). The system also has a methylsulfonate group which will make these overall anionic structures more soluble in competitive polar solvents. Such a design allowed these systems to overcome the low solubility issues from which squaramides derivatives usually suffer. Indeed, **85** and **86** were found to be fully soluble in polar organic solvents such as DCM, MeCN and DMSO; furthermore, they were found to be dissolvable in highly competitive solvents such as MeOH, EtOH and H_2O.

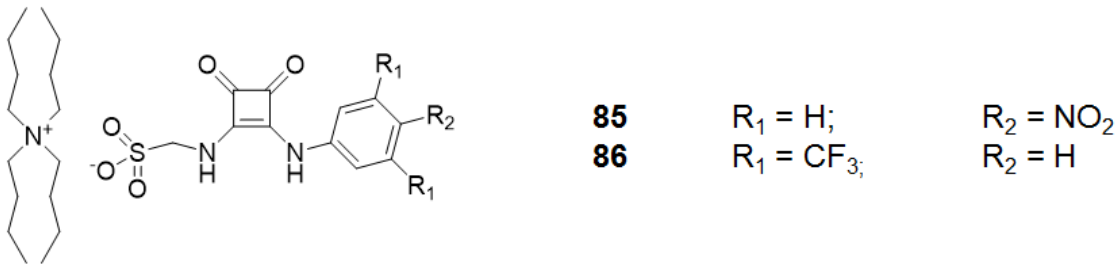

Figure 5.2 Chemical structures of the two squaramides presented in this work, **85** and **86**.

The presence of both hydrogen bond donor and acceptor groups on the squaramides was found to induce the formation of two-dimensional hydrogen bonds that in turn lead to the formation of centrosymmetric dimeric units by Ashton *et al.*[142] and the same behaviour was speculated to be operative for compounds **85** and **86**. Immediate confirmation of this was obtained by the Elmes group upon resolving the XRD structure of **85**, which was obtained by recrystallization from high concentration solutions of DMSO. **Figure 5.3 A** shows the formation of the dimer between the anions of **85**. Adjacent dimers further interact, due to π-π stacking interactions between the aromatic rings of the neighbouring units (**Figure 5.3 B**). The structural analysis was carried out by Dr Chris Hawes at Keele University UK.

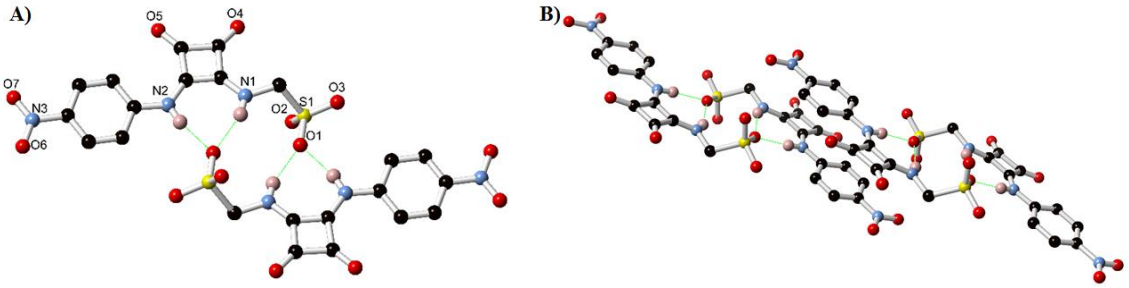

Figure 5.3 Crystal structure of the $^{+}NBu_4$ salt of **85** with heteroatom labelling scheme obtained using XRD. Cations and selected hydrogen atoms are omitted for clarity. (**B**) Interaction of adjacent dimers of **85**, with the π-π stacking between conjugated units.

The solution behaviour of the two structures was studied by the Elmes group using ^{1}H-NMR as sell as UV-Vis absorption spectroscopies. The NMR analysis showed that for both the chemical shifts for the two amidic N-H protons would change as a function of concentration. This would indicate a different chemical environment at different concentration (show in **Figure 5.4** for **85**), which supports the hypothesis that both **85** and **86** were forming self-aggregates in solution.

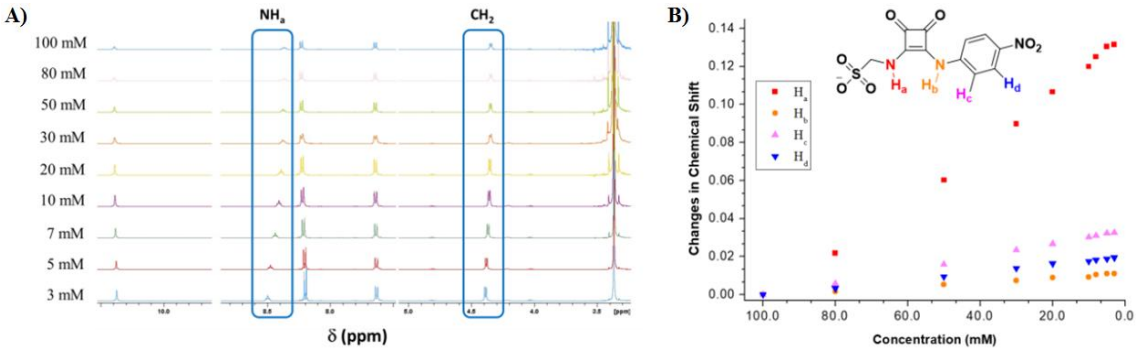

Figure 5.4 A) ^{1}H-NMR dilution studies (100 mM → 3mM) of **85** in performed in DMSO-d_6 (0.5 % D_2O) by the Elmes group. B) Plot of the changes in chemical shift of the four different protons against **85** concentration.

With the view of probing this on the micro-scale, the two systems were studied using SEM imaging to gain further understanding of the behaviours and morphology of these aggregates in different solvent or solvent mixtures. The imaging was performed on samples spotted on the wafers using 1 µM solutions (in different solvents), with the same experimental methods used for the imaging detailed in the previous chapters, repeating the measures 3 - 5 times to ensure reproducibility.

The images obtained from MeCN, shown in **Figure 5.5**, seem to indicate that both of these squaramide derivatives tend to form compact films in which the presence of aggregates networks can be seen (**A**, **C**). Furthermore, it is possible to observe the presence of very regular micro domains with (**B**, **D**) which further confirm the ability of these systems to form regular, microcrystal-like structures, possibly through the formation of rigid dimeric unit discussed above.

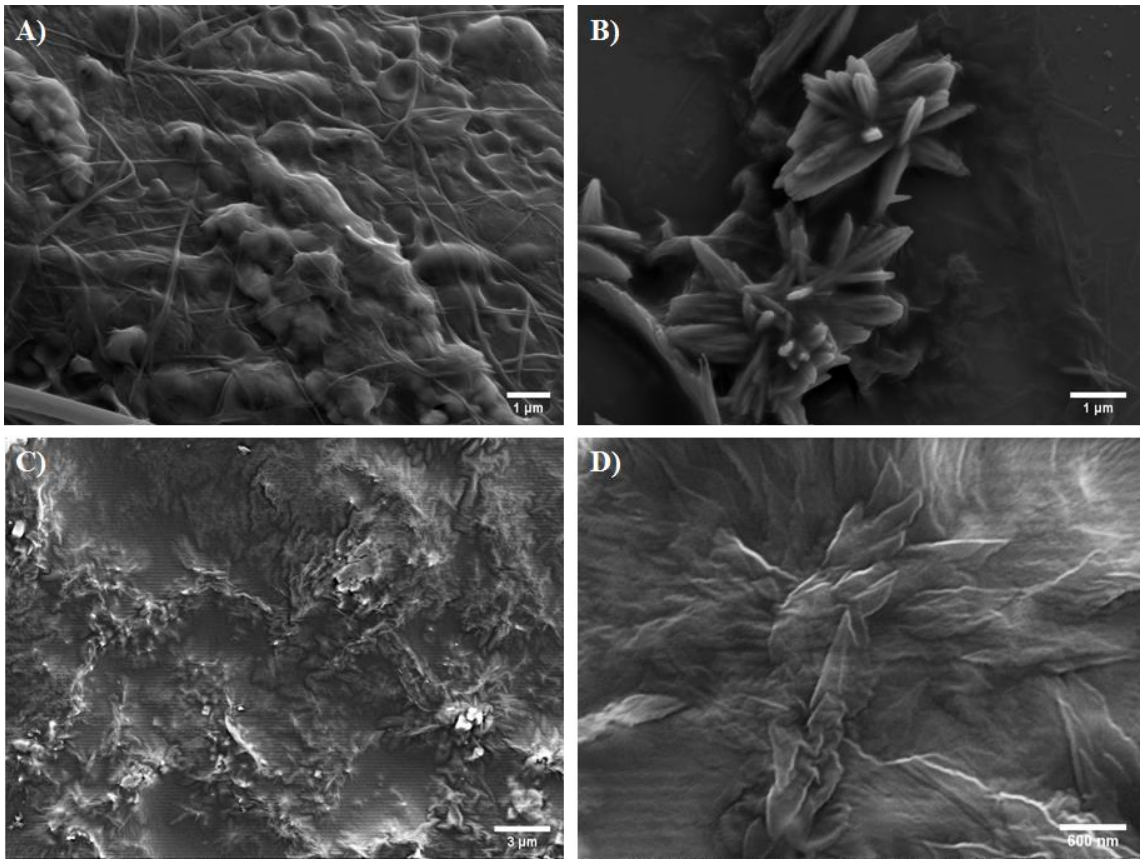

Figure 5.5 SEM images obtained from solutions in MeCN of **85** (A, B) and **86** (C, D). The formation of layers with microcrystalline domains can be observed. Scale bar 1 µm (A, B), 3 µm (C) and 600 nm (D).

Switching to a more competitive H-boning solvent such as EtOH (**Figure 5.6**), it is possible to observe differences between the two squaramides. Here, **85** formed more compact films, more amorphous in nature as can be seen in **Figure 5.6 A** and **B**. In contrast to these results, **86** presented a much more microcrystalline nature, with

micro-domains possessing regular feature visible at low magnification (**Figure 5.6 C** and **D**).

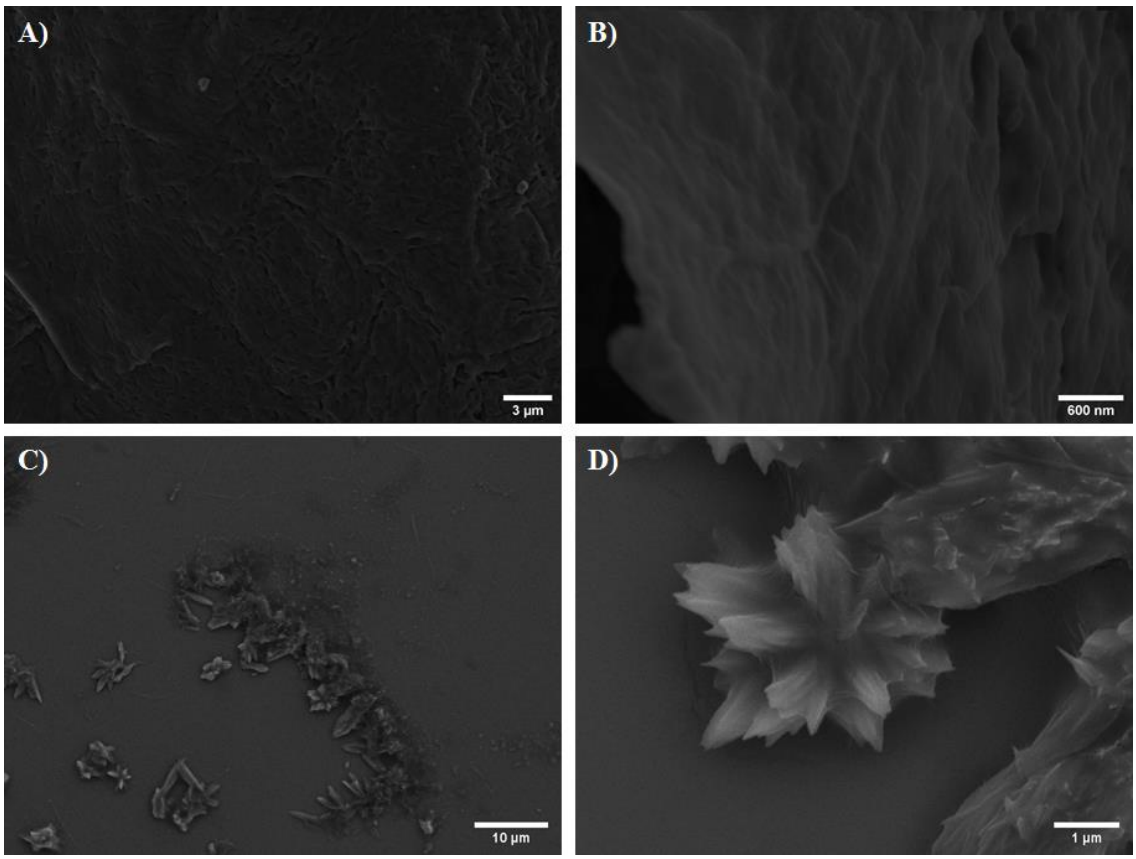

Figure 5.6 SEM images obtained from solutions in EtOH of **85** (A, B) and **86** (C, D). The formation of fibrous layers can be observed for **85**, while more crystalline domains are visible for **86**. Scale bar 3 µm (A), 600 nm (B), 10 µm (C) and 1 µm.

The systems were also investigated in highly competitive solvents, such as H_2O and DMSO:H_2O mixtures. In these solvents, it was possible to again observe the formation of aggregates, with **85** forming aggregate particle systems, and **86** assumed more rod-like conformations (**Figure 5.7**). While it is clear that the solvent has a major effect on the morphological output, one can also speculate that in such highly polar and hydrogen bonding solvents, the self-association seen above would very likely not exist to the same extend due to competition from the local environment. Hence, it is possible that other forces, such as hydrophobic and polar effect might have a major role in this case. Nevertheless, the self-association cannot be excluded as such aggregation could take place due to hydrophobic effect, and subsequently, formation of the dimers might occur due to close packing, which further stabilises the aggregation formation. However, while we were unable to confirm that hypothesis, it is clear that given the structure of **85** and **86**, i.e. aromatic, hydrogen bonding donor/acceptor abilities and anion character, such multiple supramolecular interactions are clearly operational.

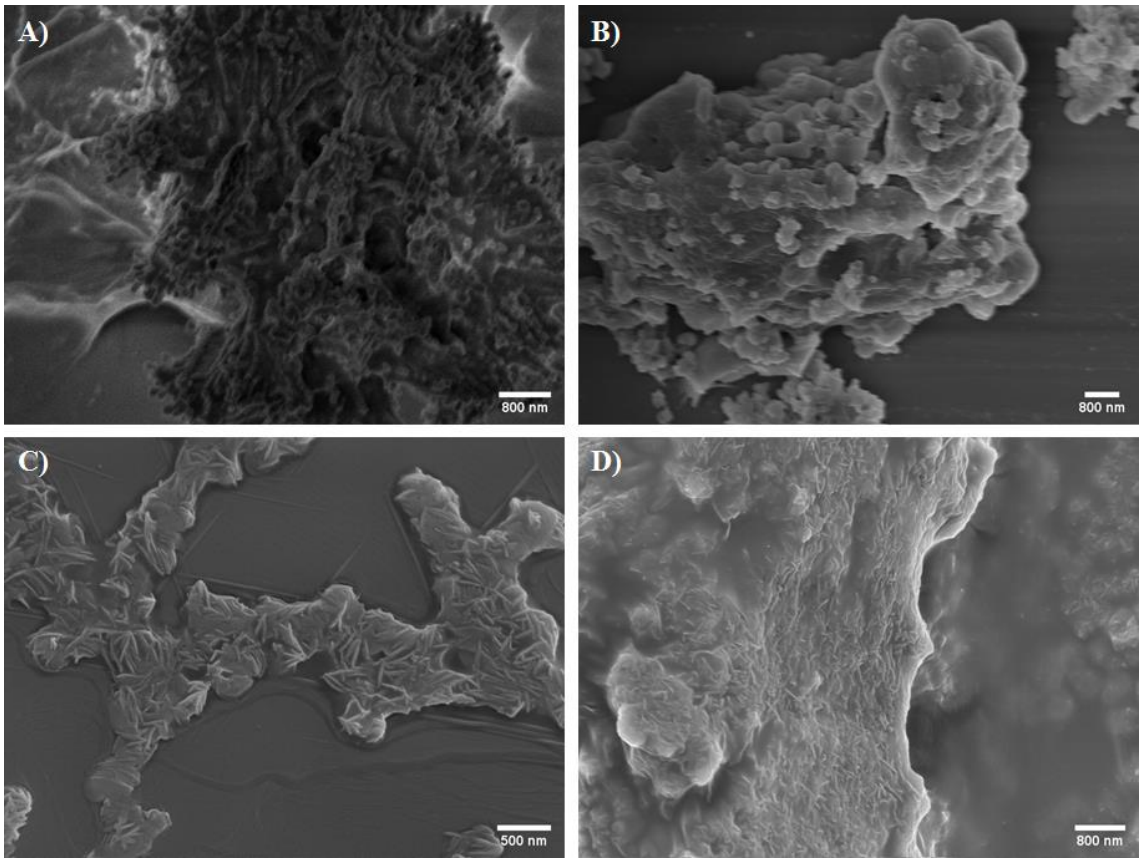

Figure 5.7 SEM images obtained from solutions in **85** and **86** in H_2O (A and C respectively) and H_2O:DMSO 0.5:99.5 (B and D respectively). It is possible to observe the predominance of irregular particles for **85** and rod-like structures for **86**. Scale bar 800 nm (A, B, D) and 500 (C).

In summary, the spectroscopic in conjunction with the morphological imaging investigations, collected through the various experiments outlined above, confirmed that the two systems **85** and **86** are able to aggregate into complex and diverse structures as a function of the solvent, and their appility to capitalise on their aromatic, hydrogen bonding/acceptor abilities and anionic character in these solvents. Furthermore, the use of different substituents (and patterns) strongly affects the properties of the hydrogen bonding which in turn, results in different aggregated system, indicating its vital role in directing the self-assembly processes.

5.2 1,8-Naphthalimide derivatives

The 1,8-naphthalimide fluorophore is a building block commonly employed in modern supramolecular chemistry, and it has been extensively used in sensor design, and to develop organic ligands for use in self-assembly, and in the construction of metal-organic motifs.[143-144] The relative ease of functionalisation and advantageous photophysical properties, for systems such as thio-, oxo- or amino-1,8-naphtlimide, that such framework

possesses have found a wide range of diverse applications.[145-146] Functionalising the "base" structure with different substituents, at the 3- and in particularly the 4-positions of the ring, allows for facile modulation of the electron density of the system, making it possible to induce changes to the electronic properties of the system and ultimately in the spectroscopic and aggregation properties of these system. Recently the Gunnlaugsson group in collaboration with the Scanlan research team at TCD, have explored such self-assembly processes for glycosylated amino- and bromo-naphthalimide structures.[147] The studies presented in this chapter are an extension of that work, and will focus in particular on naphthalimides that have been functionalised both on the aromatic rings and at the imide site; the latter possessing either a benzyl, or pyridine units. It is worth mentioning, that other ongoing work in the group focuses on the incorporation of polypyridine units in to the naphthalimide structure and the effect that has on their material properties of such building blocks.

5.2.1 Morpholine functionalised Naphthalimides

The first naphthalimide derivative studied builds on work previously published by the Gunnlaugsson group,[148] in which the use of several different *N*-picolyl functionalised 1,8-naphthalimides were found to be capable of forming stimuli-responsive gels. When the gelators were further functionalised in the 4th position of the ring, using a piperidinyl functionality, the resulting gels were found to be highly coloured; giving rise to typical green ICT based emission in variety of solvents. However, despite this, it was not possible to measure the photophysical effects of the gels in full. In this work, the piperidinic group in the same position was replaced with a morpholinic one, with the *N*-position functionalised with a benzyl or picolyl substituent. The synthesis, which yielded derivatives **87** and **98**, the chemical structures of which are shown in **Figure 5.8**, was performed by June Lovitt a PhD student in the Gunnlaugsson group.

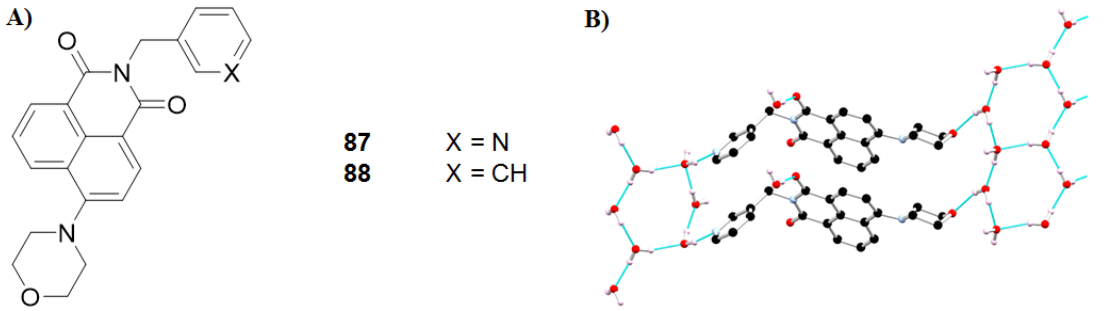

Figure 5.8 Chemical structures of the two morpholinic-functionalised naphthalimides, **87** and **88** (A). Crystal structure of **88** with adjacent units interconnected by H-bonding.

Although the use of 4-morpholino-1,8-naphthalimides is not unknown,[149-150] the studies involving such derivatives mainly focuses on their use as probes for sensing and medicinal chemistry applications, especially for biological systems, while the investigation in this work will focus on their coordination behaviour and the effect that has on their material properties. The pyridyl derivative **87** was found to form colourless needle-like crystals; upon resolution of the structure using XRD, performed again by Ms. June Lovitt, it was possible to see that the unit undergoes π-π stacking in a face-to-face fashion, with the morpholine ring extending the structure through hydrogen bonding with several water molecules.

To study the ability of the ligand to interact with *d*-metal ions, **87** was dissolved in MeCN solution, and $MnCl_2$ was added, upon which the system was observed to switch to a green-coloured metallogel (Mn·**87** metallogel), which was found to revert to solution state upon additions of diluted solutions of HCl (0.1M, 10μL) or NaOH (0.1M, 10μL). To gain an understanding on the aggregation process, the gel and the solutions were investigated using SEM imaging. The results are shown in **Figure 5.9**. The Mn·**87** metallogel (**Figure 5.9**, **A** and **B**) shows a morphology composed of irregular reticulate networks, through which the system is able to trap solvent molecules to gelate. When the gel is acidified or basified, as said, it reverts to solution state. Hence, these metallo-gels are stimuli responsive soft-materials. From these solutions, it was possible to obtain samples suitable for single-crystal XRD, where the structure was resolved and leading to a very interesting result. The structure for crystals of **87** obtained from the broken metallogels were found to be remarkably different from the ones obtained initially. The molecules of **87**, in fact, undergo π-π stacking to form a head-to-tail array between adjacent sheets of ligand, rather than the head-to-head structure that was observed initially; furthermore, no solvent, water or guest molecules were found in the structure, preventing the extension of the structure through hydrogen bonding, as seen in the crystal structure obtained initially.

It was speculated that the reason for this behaviour could be related to the presence of the pyridinic nitrogen. To gain a better understanding of this phenomenon, the focus of the study was moved toward the benzyl derivative, **88**. It was possible to resolve the crystal structure of the ligand by performing XRD measurements on crystals that were obtained from ethyl acetate, and it was possible to observe from this structure that the extended

packing was more similar to the one observed for **87,** obtained above from the metallogel, than to the one formed directly and discussed above.

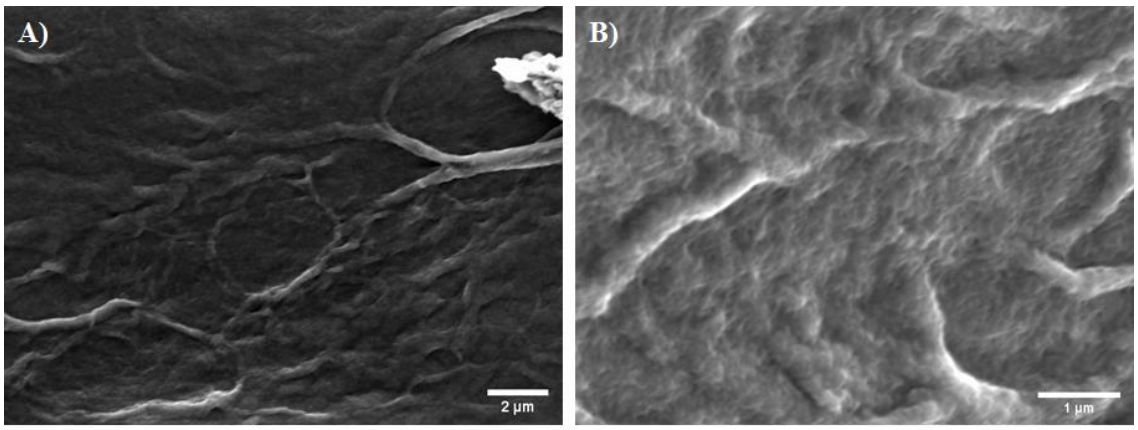

Figure 5.9 SEM imaging of Mn·**87** metallogel swelled in MeCN. Scale bar 2 µm (A) and 1 µm (B).

Importantly, in this example, the π-π stacking between adjacent naphthalimide molecules was, in this instance, in the form of head-to-tail arrays. Furthermore, the presence of the pyridinic nitrogen was also found instrumental to the formation of supramolecular interactions, as the use of different *d*-metals (Co(II), Mn(II) and Ni(II)) chloride salts did not lead to the formation of metallogels for **88**. The system aggregation properties were then studied in solution at three different pH values (4, 6 and 8) and spiked using different acids (CH_3COOH, HNO_3 and HCl) as shown in **Figure 5.10**.

From the SEM imaging carried out on these samples, it was possible to observe that from solutions spiked with acetic acid, **88** formed mostly amorphous structures containing geometrically regular microdomains at pH 4 and 8 (**Figure 5.10 A** and **C**), while the aggregates formed at pH 6 (**Figure 5.10**, **B**) seem to lack such domains. In the images of solutions of **88** spiked with nitric acid, the ligand seem to aggregate into branched structures at lower pH (**Figure 5.10**, **D**) that increase in density and lose definition when the pK is higher (**Figure 5.10**, **E** and **F**). Importantly, an analogous trend was observed for the solutions spiked with HCl (**Figure 5.10**, **G - I**).

These results show the importance of the pyridinic nitrogen, as it was found that the two ligands are able to form crystal structures in which the π-π interaction between the naphthalene rings is strongly affected by its presence, leading ultimately to opposite modes of stacking; head-to-head *vs* head-to-tail. Furthermore, both systems were found to have different levels of pH-responsiveness in their LMWG-behaviours, with **87** forming pH-responsive metallogels and **88** assuming different aggregation modes. These results demonstrate that the substituted naphthalimide systems possess wide range of

possibilities to self-associate and form supramolecular aggregates. This area of research is now being actively perused within the Gunnlaugsson group.

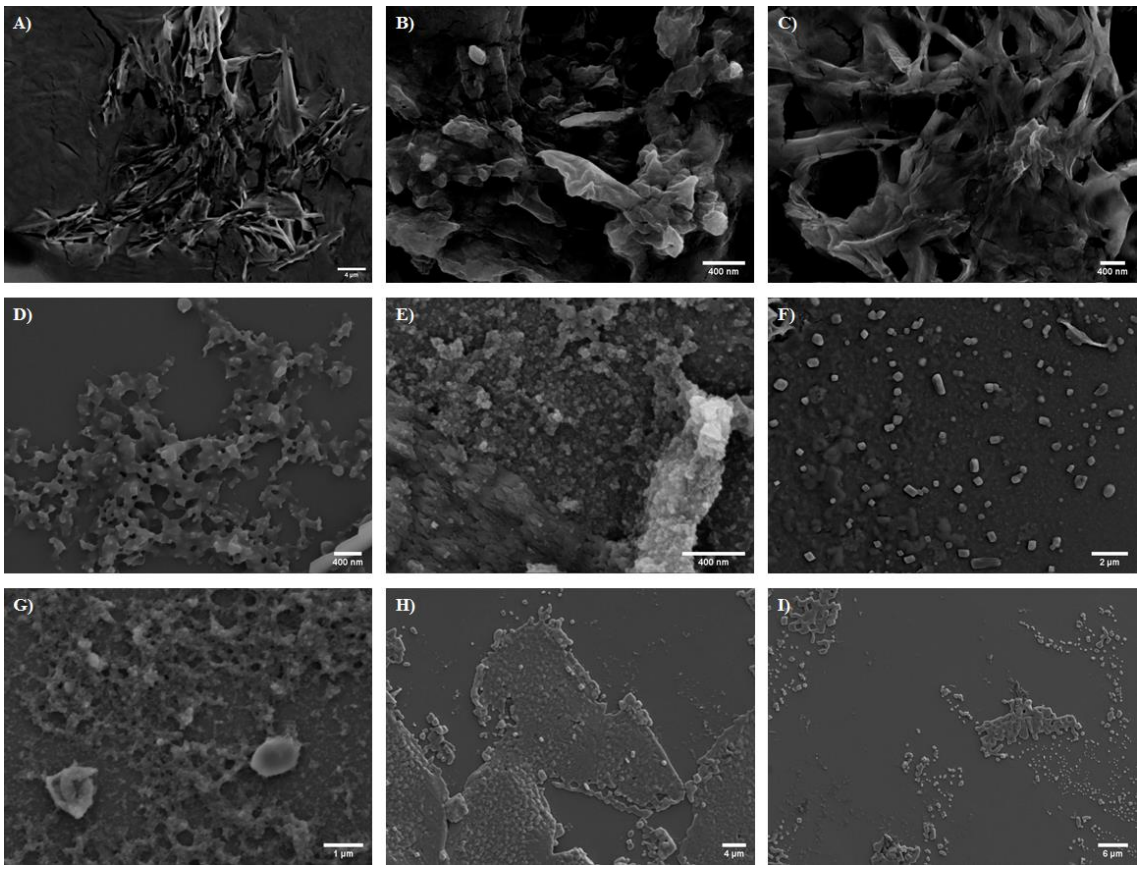

Figure 5.10 SEM imaging of **88** solutions spiked with CH_3COOH (A, B, C), HNO_3 (D, E, F) and HCl (G, H, I) at pH = 4 (A, D, G), 6 (B, E, H) and 8 (C, F, I). Scale bar 4 µm (A, H), 400 nm (B-E), 2 µm (F) and 1 µm (G).

5.2.2 Triphenylamino-functionalised Naphthalimides

As previously mentioned, the naphthalimides have been extensively used as fluorescent probes in biological systems, thanks to their chemical and thermal stability together with high fluorescence quantum yields.[151-152] Such properties make naphthalimides excellent tools for solution studies, but often fail to translate in the switching to solid state systems, or for poor solvents, due to a phenomenon called aggregation-caused quenching (**ACQ**).[153] In the case of naphthalimides, the highly planar and conjugated aromatic region undergoes π-π stacking (as was discussed above) and the resulting systems are able to relax from their excited states through non-radiative pathways, which become preferred to the fluorescence in the aggregated state, causing the ACQ.

Many strategies have been attempted to overcome ACQ phenomena. Tang *et al.*[154] were the first to observe an opposite phenomenon to ACQ when they reported the photophysics of a propeller-shaped silole derivative containing five aromatic substituents. For such a system, the aggregation would force a planarization of the molecule and

activate the radiative emission for the system. This phenomenon was given the name aggregation-induced emission (**AIE**). Chang *et al*.[155] were the first to firstly report that naphthalimides functionalised with aromatic substituents that were out-of-the plane with the ring, could give rise to **AIE** properties that were directly correlated to the angular shape that the substituent would cause to the molecule. This was considered a successful model and many studies followed this method; these in turn, overcoming the ACQ phenomena upon carefully designing the structure modifications, including the study that will be presented here.

In particular, the derivative presented in this study, **89**, was functionalised with two triphenylamine substituents, as shown in **Figure 5.11**, that were chosen to introduce AIE properties in the final compound. The synthesis and purification was achieved by Louisa Sigurvinsson, a visiting master student in the Gunnlaugsson group, under the supervision of Dr. Adam Henwood. The triphenylamine groups normally assume a propeller shape, with the central nitrogen atom being on the same plane of the naphthalimide rings and the individual aromatic rings twisting out of the plane in order to minimise steric repulsion. In polar solvent systems, that structure favour solvation, the phenyl groups become increasingly twisted, limiting the capacity of the nitrogens to donate electron density into the imide accepting unit, which has an effect on the ICT character of the molecule. This translates to red-shifted, low intensity (and sometimes fully quenched) emission. By contrast, in apolar solvents, which are nevertheless capable of solvating this compound, induce planarization in the phenyl groups that facilitates conjugation throughout the π-system. This then extends over the entire molecule, blue-shifting the emission and enhancing its intensity greatly. However, since aggregation can control the proximity of neighbouring fluorophores, and thus their structural conformation, it is of interest to see if competing aggregating effects might induce different photophysical behaviour contrary to these established patters of solvatochromism.

Compound **89** was found to be fully soluble in chlorinated solvents, as well as THF and DMSO; while it did not show good solubility in MeOH, EtOH and H_2O. This is not surprising given the presence of the two propeller units. Nevertheless, it was possible to obtain a crystalline solid by vapour diffusion of hexane into a DCM solution.

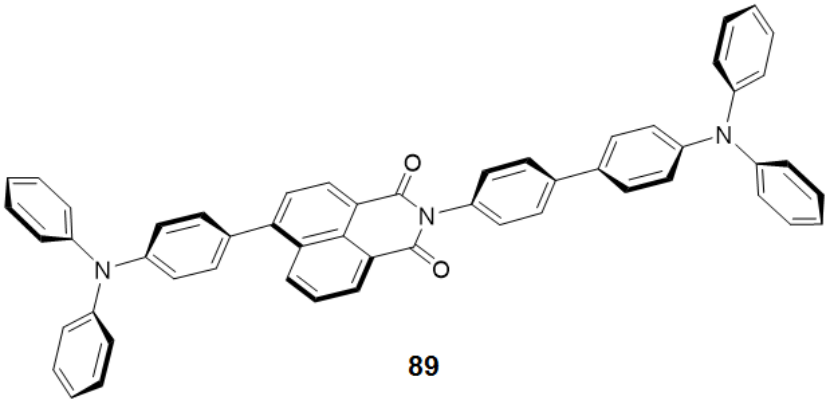

89

Figure 5.11 Chemical structure of naphthtalimide derivative **89**. The planarization of the normally propeller-shaped triphenyl amino groups enhances the emissive properties.

The crystal structure, obtained by XRD measurements solved by fellow Gunnlaugsson Group member Deirdre McAdams, is shown in **Figure 5.12**. The structure confirms that upon crystallization in compound **89** both the triphenylamino groups assume the anticipated propeller-like conformation, with the two phenyl rings closest to the NI core that are twisted from the plane of the naphthalene rings. The packing arrangement shows that the molecules form head-to-tail arrays, in which π-π interactions are formed along the molecule axis, between neighbouring triphenylamino groups.

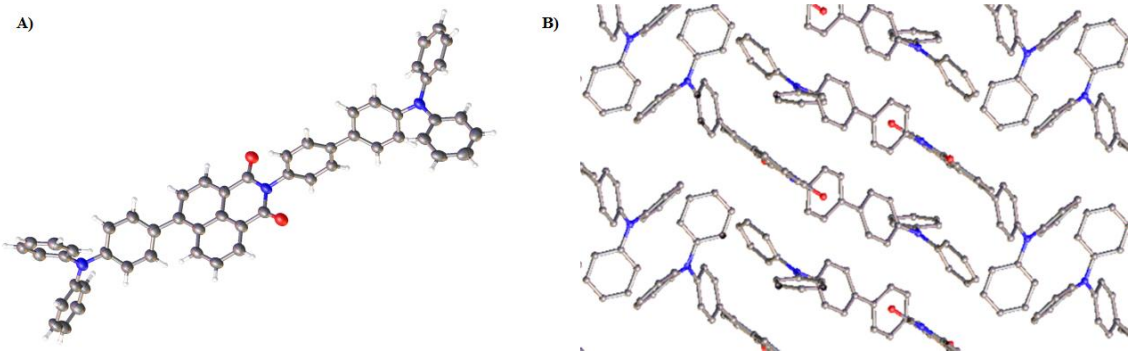

Figure 5.12 Crystal structure of compound **89** obtained using XRD (**A**). Packing arrangement of **89** in the crystal structure.

In order to study the aggregation properties further, two different experiments were carried out. In both cases, **89** was dissolved in a favourable solvent, DCM and THF; and then to these samples, was added to two anti-solvents (MeOH and H_2O) in different ratios. The resulting solutions were then dropcasted on silicon wafers and the samples were prepared for SEM imaging using analogous methods to those described previously in this Thesis. It was foreseen that this would allow interpretation of the system morphologies as the ratio of good solvent was changed to anti-solvent, which is understood to encourage aggregation of **89**. The results from these imaging experiments are shown in **Figure 5.13**.

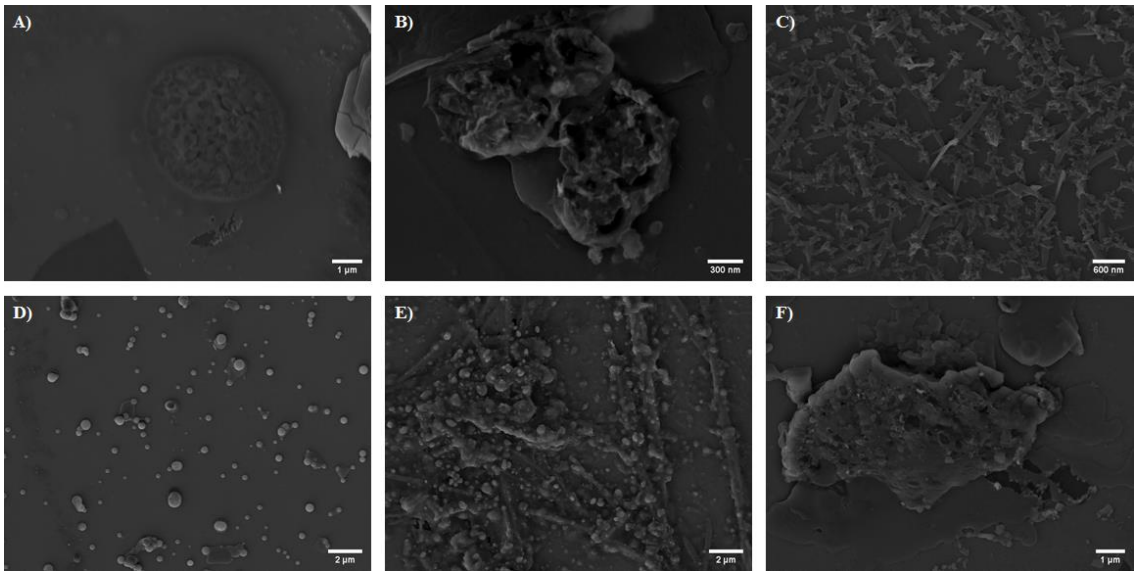

Figure 5.13 SEM imaging of **89** solutions in DCM (A), 50% MeOH in DCM (B), 0.5% DCM in MeOH (C), THF (D), 50% H_2O in THF (E), 0.5% THF in H_2O (F). Scale bar 1 µm (A), 4 µm (A, H), 2 µm (F), 1 µm (G) and 400 nm (B-E).

From the SEM imaging it was possible to observe that in the various solvent systems, **89** show markedly different behaviour; as had been anticipated, it was clearly highly solvent dependent. The SEM images from the sample casted from a DCM solution (**Figure 5.13**, **A**) show that the system formed a compact film, without showing the formation of a well defined supramolecular aggregates. A remarkable difference was noticed when **89** was cast from a 1:1 DCM:MeOH solution (**Figure 5.13**, **B**), as it was possible to observe the formation of a structure with sharper features, although these were not well defined. The starkest change was, however, observed with the sample spotted from 0.5% DCM in MeOH (**Figure 5.13**, **C**), as it was quite clear that the large excess of anti-solvent gave rise to the formation of very regular microcrystalline domains. On the other hand, it was possible to observe the formation of irregular spheroidal aggregates from the sample of **89** when spotted from a THF solution, (**Figure 5.13**, **D**). These seem to coalesce into more irregular aggregates than the sample spotted from the more polar 1:1 THF:H_2O solution (**Figure 5.13**, **E**). This aggregation becomes extremely evident by observing the imaging of the sample spotted from a 0.5% THF in H_2O solution (**Figure 5.13**, **F**), as in this case, the excess of the very competitive anti-solvent leads to the formation a higher density film lacking definition or peculiar shape.

These results indicate two different possible scenarios for the spectroscopic studies to deepen the understanding of the AIE properties of these systems, as the relative ratios of solvent and anti-solvent gave stark differences in the morphology, and presumably in the

assembly, of the final supramolecular aggregate, which will translate to diverse emissive properties. This investigation is currently underway in our laboratory.

5.3 Conclusions

A series of different types of aggregators were presented in this Chapter; two of these were based on the squaramide, and three were based on the 1,8-naphthalimide building motives. These systems have demonstrated that the aggregation processes in solutions can be tuned in a variety of ways; and factors such as small substituent changes or solvent are able to affect, or direct, the resultant assemblies in solution or in aggregated states. For example, it was observed that switching from a "simple" benzyl substituent to a pyridyl one allows pH tunable or depended aggregation formation to a LMWG; and that the use of dopant additives impacts the aggregation modes. Although further studies will be conducted, it was possible to obtain very valuable information on the ability of these two very versatile building blocks to create novel aggregators, and gain a deeper understanding of the processes that lead to the formation of their supramolecular architectures. As indicated above, this work is currently on-going in the Elmes and Gunnlaugsson research groups.

Chapter 6

Experimental Details

6.0 General

All chemicals were purchased from Sigma-Aldrich Ireland Ltd., Acros Organics, TCI Ltd., and Chematech, and were used without further purification, unless otherwise stated. Dry solvents were prepared in accordance with standard procedures described by Vogel, with distillation prior to each use. Thin-layer chromatography (TLC) was conducted using Merck Kiesegel 60 F254 silica plates, and the separation was observed by UV light or developed in an iodine chamber. Chromatographic columns were run on a Teldyne Isco Combiflash Rf200 automatic machine using pre-packed silica columns. Melting Points were determined using an Electrothermal IA900 digital melting point apparatus.

Deuterated solvents for NMR analysis were purchased from Apollo Scientific. NMR spectra were recorded using either a Bruker DPX-400 Avance spectrometer, operating at 400.13 MHz for ^{1}H NMR and 100.60 MHz for ^{13}C NMR, or a Bruker AV-600 spectrometer, operating at 600.10 MHz for ^{1}H NMR and 150.90 MHz for ^{13}C NMR. All NMR spectra were measured at 293 K. Tetramethylsilane (TMS) was used as an internal standard and chemical shifts were referenced relative to the internal non-deuterated solvent signal, with chemical shifts being expressed in parts per million (ppm or δ). For ^{1}H NMR spectra, the number of protons, splitting pattern, coupling constant where applicable, and proton assignment are also reported (in that order). Multiplicities are abbreviated as follows; singlet (s), doublet (d), triplet (t), quartet (q), quintet (qu), multiplet (m), and broad (br).

Electro spray mass spectra were recorded on Bruker microTOF-Q III spectrometer connected to Dionex UltiMate 3000 LC detector using HPLC grade CH_3CN or CH_3OH as carrier solvents. Accurate molecular weights were determined by a peak-matching method, using Agilent Technologies ESI-1 low concentration tuning mix as the internal lock mass. Maldi-Q-Tof mass spectra were carried out on a MALDI-Q-TOF-Premier (Waters Corporation, Micromass MS technologies, Manchester, UK). High-resolution mass spectrometry was performed using leucine enkephaline (H-Tyr-Gly-Gly-Phe-Leu-OH) as the standard reference (m/z = 556.2771); all accurate mass were reported with in ± 5 ppm of the expected mass.

Infrared spectra were recorded on a Perkin Elmer Spectrum One FT-IR spectrometer fitted with a universal ATR sampling accessory. Elemental analysis were performed on an Exter Analytical C3440 elemental analyser at the Microanalysis Laboratory, School of Chemistry and Chemical Biology, University College Dublin.

6.1 Ultraviolet-visible Spectroscopy

The UV-visible absorption spectra were recorded at room temperature using 1.0 cm path length quartz cell in Varian Cary 50 spectrometer. The solvents utilised were of spectrophotometric grade. The wavelength range was set from 200 to 400 nm with a scan rate of 300 nm/min. The blank used was a sample of the solvent system in which the titration was carried out, *i.e.* CH_3OH. Before the start of the titration baseline correction was used in all spectra. Stock solution of ligand with concentrations either 1×10^{-3} or 2×10^{-3} M for the titration in CH_3OH were prepared and then diluted to desired concentration before titration to *ca.* 1×10^{-5} or 3×10^{-6} M. The $Eu(CF_3SO_3)_3$ stock solution was prepared in CH_3OH (1×10^{-3} M) and diluted to 5×10^{-4} M for the titration. The titrations were repeated 3-5 times in order to ensure the reproducibility of the results.

6.1.1 Fluorescence measurements

The fluorescence measurements were carried out on a Varian Cary Eclipse Fluorimeter equipped with a 1.0 cm path length quartz cell at room temperature (293 K). The solvents used were all of spectroscopic grade. Fluorescence data were collected between 320 to 700 nm. The concentration of the ligands and the complexes were the same as those used for the UV-vis absorption measurements.

Table 6.1 *Settings of the Varian Cary Eclipse Fluorimeter for ligand-centered emission measurements*

Mode: Fluorescence	**Excitation:** 278 nm	**Scans:** 320 - 700 nm
Excitation Slit: 20 nm	**Emission Slit:** 5 nm	**PMT Voltage:** 750 V
Averaging time: 0.1 s	**Scan rate:** 600 nm/min	**Data Interval:** 0.5 nm

6.1.2 Eu(III) centred emission measurements

The phosphorescence measurements were carried out on a Varian Cary Eclipse Fluorimeter equipped with a 1.0 cm path length quartz cell at room temperature (293 K). The solvents used were all of spectroscopic grade. The emission data were collected between 320 to 700 nm. The concentration of the ligands and the complexes were the same as those used for the UV-vis absorption measurements.

Table 6.2 *Settings of the Varian Cary Eclipse Fluorimeter for Eu(III)-centered emission measurements*

Mode: Phosphorescence	**Excitation:** 278 nm	**Scans:** 575 - 720 nm
Excitation Slit: 20 nm	**Emission Slit:** 5 nm	**PMT Voltage:** 750 V
No. of flashes: 1	**Gate Time:** 5 ms	**Delay Time:** 0.2 ms
Averaging time: 0.1 s	**Total decay time:** 0.02 s	**Data Interval:** 0.5 nm

6.1.3 Lifetime measurements for Eu(III) complexes emission

The Eu(III) centred lifetime emission measurements of **Eu·57** in CH3OH and CD3OD were conducted on a Varian Cary Eclipse Fluorimeter. The settings of the fluorimeter for the lifetime measurements carried out in Chapter 3 are shown in **Table 6.3**.

Lifetime values of Eu(III) ($^5D_0$) excited state were measured in solution in time-resolved mode. For each system the lifetime values are averages of three independent measurements relative to the emission decay at 617 nm, relative to the $^5D_0 \rightarrow {}^7F2$ transition, enforcing a delay.

Table 6.3 *Settings of the Varian Cary Eclipse Fluorimeter for measuring Eu(III) centred luminescence decay*

Indirect excitation: 278 nm	**Emission:** 617 nm	**Delay:** 0.01 ms
Excitation Slit: 20 nm	**Emission Slit:** 10 nm	**Gate:** 0.02 - 0.03 ms
No. of flashes: 1	**Total decay:** 600 nm/min	**No. of Cycles: 50**

6.2 Experimental Details for Chapter 2

Synthesis of Tris-Methylbenzoate-benzene-1,3,5-tricarboxamide (56)

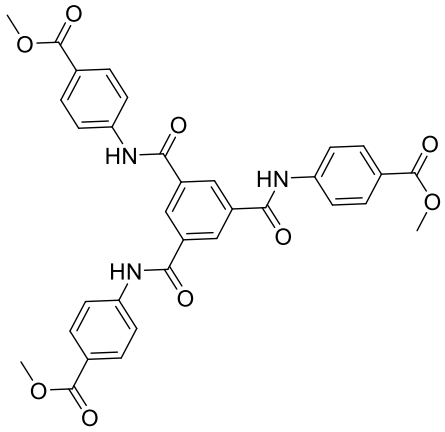

Compound **56** was synthesised using a method reported by Zhang et *al*.[76] A solution of 500 mg 1,3,5-benzenetricarboxylic acid chloride (1.88 mmol, 1 eq), 1 g of methyl 4-aminobenzoate (6.59 mmol, 3.5 equivalents), and K_2CO_3 911 mg (3.5 eq) in 200 ml of acetone was stirred for 12 h at 80 °C. The resulting solid was suction filtrated, then washed with CH_3OH water and then air-dried to obtain a white solid in 87% yield. The clean white solid is then collected. **HRMS** (*m/z*) (ESI MS+) calculated for $C_{33}H_{28}N_3O_9$ *m/z* = 610.182006 [M+H], found *m/z* = 610.180513. **^{1}H NMR** (400 MHz, DMSO-d_6) δ 10.90 (3H, s, N-H), 8.73 (9H, s, Ar-H), 8.00 (12H, dd, Ar-H, J = 8 Hz), 3.83 (9H, s, OCH_3). **^{13}C NMR** (100 MHz, DMSO-d_6) δ 166.25, 165.26, 143.77, 135.62, 130,75, 130.68, 125.15, 120.17, 55.42; **IR υ** mac (cm^{-1}): 3305.55, 2950.1, 1721.26, 1682.83, 1648.10, 1600.50, 1531.79, 1511.30, 1435.32, 1407.26, 1296.70, 1248.92, 1171.41, 1110.58, 851.67, 767.50, 694.99.

Synthesis of Tris-Benzoic acid-benzene-1,3,5-tricarboxamide (37)[54]

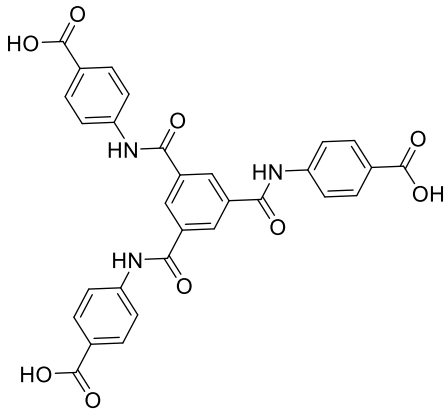

Compound **37** was obtained by basic hydrolysis of **56**. One equivalent of **56** (200 mg, 0.33 mmol) was suspended in a 3:1 MeOH/THF mixture (40 ml total) to which an excess of 1 M NaOH (26 eq, 8.5 mL) was added and the resulting solution was left stirring for 6 hours at reflux (60 °C). The reaction mixture was then left to cool to room temperature and subsequently acidified with aqueous HCl (36% v/v) till pH is about 1. The resulting suspension was filtrated under reduced pressure using a Buchner funnel to obtain a white solid that was washed with water and then left to dry in air. The resulting beige solid was collected with a yield of 90%. **HRMS** (*m/z*) (ESI MS^-) calculated for $C_{30}H_{20}N_3O_9$ *m/z* = 566.120503 [M-H], found *m/z* = 566.119247. **^{1}H NMR** (400 MHz, DMSO-d_6) δ: 12.78 (br, OH), 10.93 (3H, s, N-H), 8.77 (3H, s, Ar-H), 7.98 (12H, s, Ar-H). **^{13}C NMR** (100 MHz, DMSO-d_6) 167.36, 165.18, 143.62, 135.37, 130.91, 130.68, 126.24, 120.03, 67.46. **IR** υ max (cm^{-1}): 3049.76, 1668.94, 1593.98, 1526.30, 1404.22, 1315.99, 1237.24, 1173.35, 1113.26, 852.34, 766.00, 713.50.

6.2.1 General procedure for the synthesis of compounds 57 - 60

One equivalent of **37** (250 mg, 0.44 mmol) was dissolved in anhydrous DMF. The system was cooled down to 0 °C (using an ice bath) and 4 equivalents (1.76 mmol) of the relevant amino acid ester (^{t}But for **58**, **59** and **60**, Et for **57**, all as HCl salts) as well as 10 equivalents of HOBt (666 mg, 4.41 mmol), HBTU (1.671 g, 4.41 mmol), and DIPEA (770 µL, 4.41 mmol), were added. The bath was subsequently removed and the flask left to react at RT under Ar atmosphere. The reaction was stopped and quenched after 36 hours pouring the reaction mixture into a water/ice mixture, leading to the formation of a precipitate, which was collected by suction filtration. The resulting solid was redissolved in fresh DCM (50 mL) and washed with a sat. $NaHCO_3$ solution (10 mL) three times, then with H_2O (10 mL) once and finally with brine (sat. NaCl solution, 10 ml) three times. The layers were then dried on $MgSO_4$ and the solvent removed under reduced pressure. The resulting oil was then redissolved once again in the minimum amount of DCM and

then added to Et_2O (200 mL) to obtain white solids, which were filtrated and dried in air and *in vacuo*.

Tris-(Glycine-EthylEster Benzoic amide)-benzene-1,3,5-tricarboxamide (57)

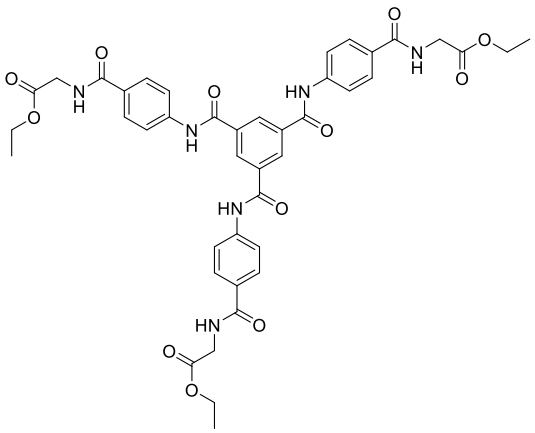

Compound **57** was obtained following procedure described in section 6.2.1 using glycine ethyl ester. Compound **37** (250 mg, 0.441 mmol, 1 eq) was dissolved in anhydrous DMF (15 ml) and then reacted with Glycine Ethyl ester (250 mg, 0.21 mmol, 4 eq), HOBt (595 mg, 4.41 mmol, 10.0 eq), HBTU (1.671 g, 4.41 mmol, 10 eq) and DIPEA (770 µL, 4.41 mmol, 10 eq). Following the workup described above, compound **57** was obtained as a fine white solid (278 mg, 0.167 mmol) in 38 % yield. **^{1}H NMR** (600 MHz, DMSO-d_6) δ: 10.82 (3H, s, N-H), 8.75 (3H, s, Ar-H), 8.88 (3H, b, N-H), 7.93 (12H, s Ar-H), 4.12 (2H, dd, J = 4.13 Hz, CH_2), 4.00 (6H, d, J = 4 Hz, CH_2), 1.21 (9H, t, J = 1.22 Hz, C-H3); **^{13}C NMR** (151 MHz, DMSO) δ 170.46, 170.46, 166.54, 166.54, 165.20, 165.20, 142.25, 142.25, 128.63, 128.63, 120.09, 120.09, 60.92, 60.92, 41.79, 41.79, 40.52, 40.40, 40.26, 40.12, 39.99, 39.85, 39.71, 39.57, 14.59, 14.59.

Tris-(L-Alanine-tButEster Benzoic amide)-benzene-1,3,5-tricarboxamide (59)

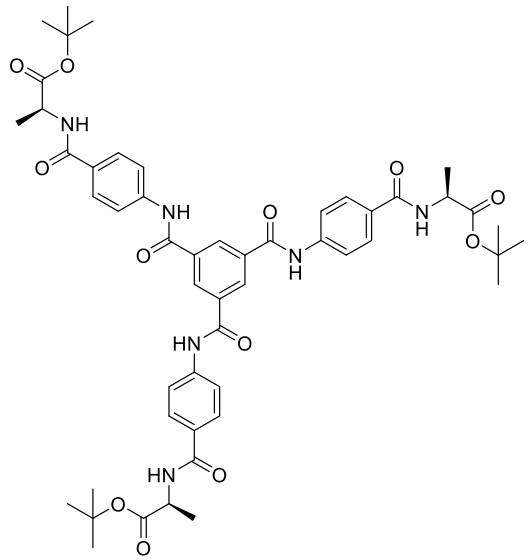

Compound **59** was obtained following procedure described in section 6.2.1. Starting material **37** (250 mg, 0.441 mmol, 1 eq) was dissolved in anhydrous DMF (15 ml) and then reacted with L-Alanine ^{t}But ester (640 mg, 1.76 mmol, 4 eq), HOBt (453 mg, 4.41 mmol, 10.0 eq), HBTU (1.672 g, 4.41 mmol, 10 eq) and DIPEA (770 µL, 4.41 mmol, 10 eq). Following workup, the desired product was obtained as a white solid (334 mg, 0.1762 mmoles) in 40 % yield. **m.p.** Decomp > 197

°C; **^{1}H NMR** (400 MHz, DMSO-d_6) δ 10.81 (3H, s, N-H), 8.76 (3H, s, Ar-H), 8.58 (3H, d, N-H), 7.94 (12H, s Ar-H), 4.35 (3H, q, CH), 1.41 (27H, s, C-H3), 1.38 (9H, d, C-H3). **^{13}C NMR** (100 MHz, DMSO-d6) δ 172.47, 166.14, 165.11, 142.09, 135.70, 130.57, 129.60, 128.73, 119.93, 80.73, 49.36, 28.13, 17.27. **IR υ** max (cm^{-1}): 3305.21, 2980.77, 1731.50, 1637.99, 1600.43, 1499.05, 1313.62, 1249.80, 1153.15, 846.11, 764.95

Synthesis of Tris-(L-Phenylalanine-tButEsterBenzoic amide)-benzene-1,3,5-tricarboxamide (60)

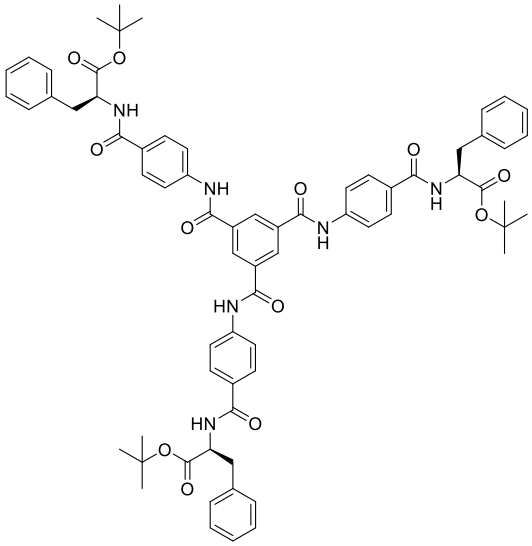

Compound **60** was obtained following procedure described in section 6.2.1. Starting material **37** (250 mg, 0.441 mmol, 1 eq) was dissolved in anhydrous DMF (15 ml) and then reacted with L-Phenylalanine ^{t}But ester (582 mg, 1.76 mmol, 4 eq), HOBt (453 mg, 4.41 mmol, 10.0 eq), HBTU (1.672 g, 4.41 mmol, 10 eq) and DIPEA (770 µL, 4.41 mmol, 10 eq). Following workup, the desired product was obtained as a white solid (mg, 41.3 % yield). **m.p.** Decomp > 221 °C; **HRMS** (*m/z*) (ESI MS+) calculated for $C_{69}H_{72}N_6NaO_{12}$ *m/z* = 1199.510042 [M+Na], found *m/z* = 1199.511027; **^{1}H NMR** (400 MHz, DMSO-d6) δ 10.80 (3H, s, N-H), 8.74 (3H, s, Ar-H), 8.64 (3H, d, J = N-H), 7.90 (12H, q, Ar-H), 7.30 (12H, q, Ar-H), 7.20 (3H, t, Ar-H), 4.57 (3H, q, CH), 3.11 (6H, m, CH_2), 1.36 (27H, s, CH_3). **IR υ** max (cm^{-1}): 3290.22, 2972.13, 2926.14, 2161.94, 1997.91, 1725.19, 1650.77, 1599.96, 1525.54, 1497.99, 1455.41, 1404.25, 1366.32, 1313.01, 1251.35, 1150.23, 839.61, 698.12.

6.2.2 General procedure for the synthesis of compounds 62 - 63

One equivalent of the respective precursor (**59** - **60**) was dissolved in anhydrous DCM, cooled at 0 °C and the solution was added an excess of trifluoroacetic acid. The mixture was left at RT to react overnight. The reaction was then stopped, the DCM was removed under reduced pressure and the TFA solution was added to an ice/water mixture to form a white precipitate that was recovered by suction filtration and washed with water, and dried in air and *in vacuo*.

Synthesis of Tris-(L-Alanine)-benzene-1,3,5-tricarboxamide (62)

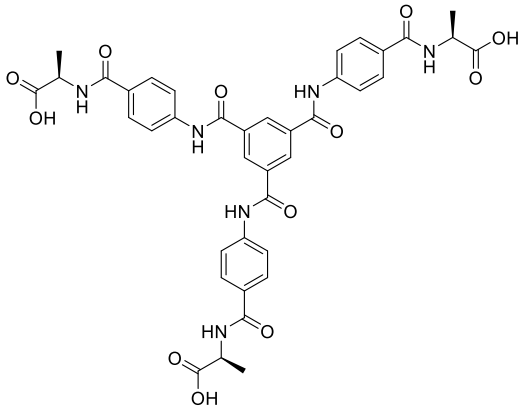

Compound **62** was obtained following the procedure 6.2.2. Compound **59** (200 mg 0.211 mmol, 1 eq) were dissolved in 20 ml of anhydrous DCM and reacted with 3 ml of TFA (excess). After removal of DCM and precipitation in water, the compound was retrieved as a white powder (150 mg, 0.190 mmol) in 91.3 % yield. **m.p.** Decomp > 204 °C; **HRMS** (*m/z*) (ESI MS-) calculated for $C_{39}H_{34}N_6O_{12}$ *m/z* = 389.112284 [M-2H], found *m/z* = 389.113096; **^{1}H NMR** (400 MHz, DMSO-d_6) δ 10.77 (3H, s, N-H), 8.72 (3H, s, Ar-H), 8.55 (3H, d, N-H), 7.90 (12H, s, Ar-H), 4.38 (3H, q, C-H), 1.3 (9H, d, C-H3). **^{13}C NMR** (100 MHz, DMSO-d_6) δ: 174.73, 166.00, 165.12, 142.07, 135.72, 130.55, 129.60, 128.74, 119.92, 49.04, 17.39. **IR** υ max (cm^{-1}): 3318.74, 2990.75, 1720.34, 1637.12, 1604.58, 1521.02, 1498.75, 1453.89, 1403.20, 1311.76, 1250.80, 1187.78, 846.33, 764.82.

Synthesis of Tris-(L-Phenylalanine)-benzene-1,3,5-tricarboxamide (63)

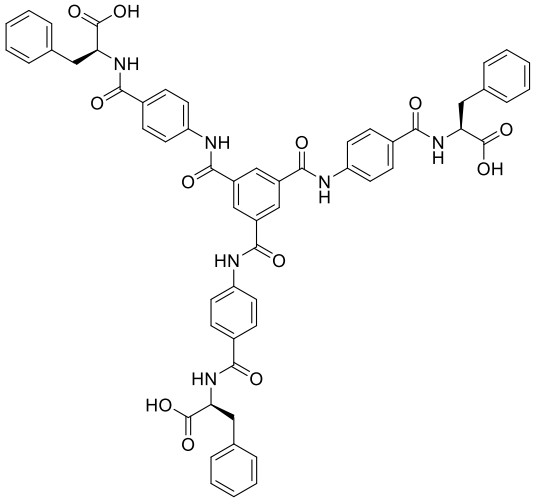

Compound **63** was obtained following the procedure 6.2.2. Compound **60** (200 mg 0.170 mmol, 1 eq) were dissolved in 20 ml of anhydrous DCM and reacted with 3 ml of TFA (excess). After removal of DCM and precipitation in water, the compound was retrieved as a powder (149.7 mg, 0.150 mmol) in 88% yield. m.p. **^{1}H NMR** (400 MHz, DMSO-d_6) δ 10.79 (3H, s, NH), 8.74 (3H, s, Ar-H), 8.61 (3H, d, NH), 7.88 (12H, q, Ar-H), 7.30 (12H, q, Ar-H), 7.18 (3H, t, Ar-H), 4.62 (3H, q, CH), 3.14 (6H, m, CH2).

Synthesis of N-[2,2';6,2"]terpyridin-4'-yl-propane-1,3-diamine (64)[115]

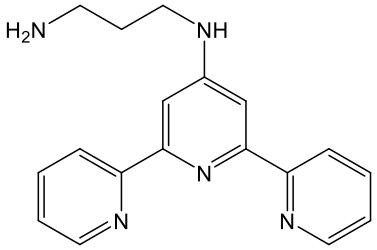

Compound **64** was obtained following the method established by Chichak *et al.*[115], by reacting 400 mg (1.49 mmol, 1 eq) of 4"-chloro-[2,2';6,2"]terpyridine in 4 ml (excess) 1,3-diamino propane. The initial suspension heated at 130 °C under reflux for 18 hours. After cooling to RT, the reaction mixture was added to ice-cold H_2O, forming a white precipitate that was filtrated under reduced pressure, redissolved in DCM and washed with H_2O. Organic phase was dried on $MgSO_4$ filtered and the solvent removed under reduced pressure to obtain a white solid (360 mg, 80% yield). **m.p.** 147 - 149 °C; **HRMS** (*m/z*) (ES MS+) calculated for $C_{18}H_{19}N_5$ *m/z* = 306.3734 [M+H], found *m/z* = 305.3728; **^{1}H NMR** (400 MHz, DMSO-d_6) δ: 8.68 (2H, d, Ar-H), 8.62 (2H, d, Ar-H), 7.84 (2H, t, Ar-H), 7.68 (2H, s, Ar-H), 7.31 (2H, t, Ar-H), 4.09 (1H, t, N-H), 3.47 (2H, m, NHC-H2), 2.68 (2H, t, C-H2), 1.68 (2H, m, C-H2). **^{13}C NMR** (400 MHz, DMSO-d_6) δ: 156.46, 156.08, 149.36, 137.44, 124.25, 121.03, 32.81; **IR** υ max (cm^{-1}): 3286.55, 2976.95, 2545.51, 1606.17, 1582.69, 1564.30, 1496.97, 1463.59, 1403.05, 1317.33, 1228.50, 1109.11, 1089.03, 1045.46, 988.31, 790.28, 622.23

6.2.3 General procedure for the synthesis of compounds 54 - 55

One equivalent of the respective precursor was dissolved in anhydrous DMF in a 20 ml microwave vial, which was cooled down to 0 °C (using an ice bath). 3 equivalents of Oxyma Pure, DCC and DIPEA were added initially, then followed by 3 equivalents of **64**. The vial was then sealed and the reaction was performed under microwave irradiation at 80 °C for 8 hours. The flask content was filtrated to remove crystals of DCU and poured in a mixture of water and ice, leading to the formation of a precipitate, which was then suction filtered. The remaining DCC traces were removed by redissolving the compounds in DMF, lowering the temperature below 0 °C and filtrating the residue, then proceeding to column chromatography using neutral silica as stationary phase and 90 % $CHCl_3$/EtOH as mobile phase to yield the pure product.

Synthesis of N1,N3,N5-Tris-(L,L,L)-1-(3-(2,6-di(pyridine-2-yl)pyridine-4-ylamino)-alanine)-benzene-1,3,5-tricarboxamide (54)

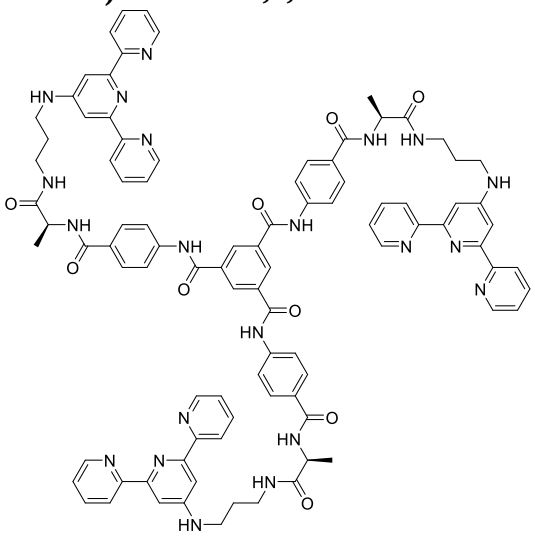

Compound **57** was obtained following the procedure described in section 6.2.3. **62** (200 mg, 0.256 mmol, 1 eq) were reacted with **64** (235 mg, 0.768 mmol, 3 eq), Oxyma Pure (110 mg, 0.768 mmol, 3 eq), DCC (160 mg, 0.768 mmol, 3 eq) and DIPEA (0.140 ml, 0.768 mmol, 3 eq) in 15ml of anhydrous DMF. After column chromatography, the desired compound was obtained as a yellow solid by precipitation from Et_2O (x ml) and dried in vacuum (98 mg, 23.3 % yield). **m.p.** 195 - 199 °C; **HRMS** (*m/z*) (MALDI$^+$) calculated for $C_{93}H_{88}N_{21}O_9$ *m/z* = 1642.7074 [M+H], found (traces) *m/z* = 1642.7141. **^{1}H NMR** (600 MHz, DMSO-d_6) δ 11.13 (3H, s, NH), 9.18 (3H, s, NH), 8.90 (6H, d, Ar-H), 8.87 (3H, s, Ar-H), 8.73 (3H, d, NH), 8.53 (3H, d, NH), 8.19 (12H, d, Ar-H), 7.98 (12H, q, Ar-H), 7.77 (6H, s, Ar-H), 7.73 (6H, d, Ar-H), 4.45 (3H, quint, CH), 3.27 (12H, m, CH_2), 1.85 (6H, quint, CH_2), 1.38 (9H, d, CH_3). **^{13}C NMR** (600 MHz, DMSO-d_6) δ 173.26, 166.16, 165.01, 159.99, 150.19, 149.99, 146.76, 146.70, 142.31, 142.27, 135.32, 129.56, 128.74, 127.47, 127.24, 119.75, 49.89, 40.95, 36.62, 28.65, 18.44; **IR** υ max (cm^{-1}): 3422.96, 3323.33, 3041.33, 2950.13, 2863.54, 2494.94, 2163.11, 2017.51, 1972.30, 1665.09, 1639.82, 1604.33, 1582.47, 1563.73, 1521.71, 1466.06, 1341.42, 985.94, 862.72, 790.31, 685.86, 621.95. **Elemental Analysis:** Calculated for $C_{93}H_{87}N_{21}O_9 \cdot 9H_2O$ = C, 61.89; H, 5.86; N, 16.30. Found: C, 61.45, H, 4.79, N, 17.91

Synthesis of N1,N3,N5-Tris-(L,L,L)-1-(3-(2,6-di(pyridine-2-yl)pyridine-4-ylamino)-phenylalanine)-benzene-1,3,5-tricarboxamide (55)

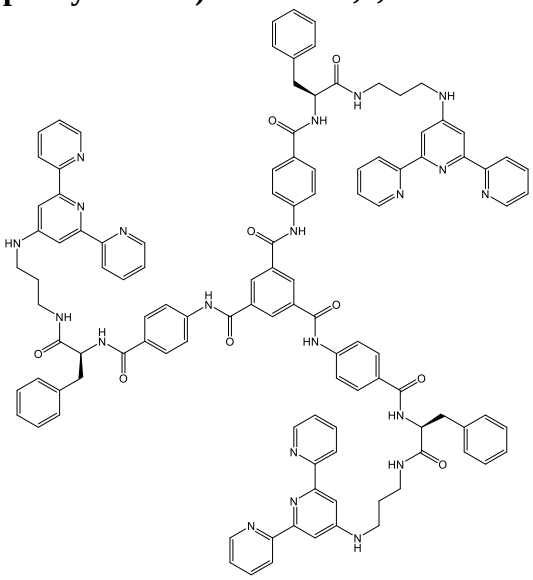

Compound **55** was obtained following the procedure described in section 6.2.3. 200 mg of **63** were reacted with 235 mg of **64** (0.768 mmol, 3 eq), 110 mg of Oxyma Pure (0. 768 mmol, 3 eq), 160 mg of DCC (0. 768 mmol, 3 eq) and 0.140 ml of DIPEA (0. 768 mmol, 3 eq) in 15ml of anhydrous DMF. After column chromatography the compound was obtained as a yellow solid by precipitation from Et_2O and dried in vacuo (98 mg, 23.3 % yield). **m.p.** Decomposed > 230 °C. **HRMS** (m/z) (MALDI) calculated for $C_{93}H_{87}N_{21}O_9$ *m/z* = 1870.8013 [M−H], found (traces) m/z = 1870.8046. **^{1}H NMR** (600 MHz, DMSO-d_6) δ 11.09 (3H, s, NH), 9.16 (3H, s, NH), 8.91 (6H, d, Ar-H), 8.86 (3H, s, Ar-H), 8.64 (3H, d, NH), 8.32 (3H, d, NH), 8.18 (6H, d, Ar-H), 7.99 (6H, d, Ar-H), 7.86 (6H, d, Ar-H), 7.78 (6H, s, Ar-H), 7.74 (6H, t, Ar-H), 7.35 (6H, d, Ar-H), 7.26 (6H, t, Ar-H), 7.16 (6H, t, Ar-H), 4.68 (3H, q, CH), 3.58 (6H, t, CH_2), 3.30 (6H, t, CH_2), 3.09 (6H, m, CH_2), 1.88 (6H, d, CH_3). **^{13}C NMR** (600 MHz, DMSO-d_6) δ 172.0 (C=O), 166.3 (C=O), 165.0 (C=O), 160.2 (Ar-C-NH), 154.0 (Ar-C-Ar), 150.5 (Ar-C-N-Ar), 144.0 (Ar-C-C=O), 142.4 (N-C-Ar), 139.3 (Ar-C), 139.1(CH2-C-Ar), 130.8 (Ar-C), 129.6 (Ar-C), 129.2 (Ar-C-C=O), 128.6 (Ar-C), 127.4 (Ar-C), 126.8 (Ar-C), 123.0 (Ar-C), 121.0 (Ar-C)119.8 (Ar-C), 107.1 (Ar-C), 102.0 (Ar-C), 55.8 (CH), 41.0 (CH_2-NH-tpy), 37.8 (CH_2-Ar), 36.7 (NH-CH_2), 28.4 (CH_2-CH_2-CH_2).

Synthesis of Eu(III) complex (Eu·54)

Complex **Eu·54** was prepared following the procedure established within the Gunnlausson group. 30 mg (0.0183 mmol, 1 eq) of **54** were reacted with 11 mg of $Eu(CF_3SO_3)_3$ (1 eq) in 8 ml of CH_3OH at 70 °C under microwave irradiation for 60 minutes. The reaction mixture was subsequently cooled to room temperature and concentrated to about 2 ml and the complex was precipitated by ether diffusion. The resulting white solid was collected by decanting the liquid and dried *in vacuo*.

6.2.4 General procedure for the synthesis of compounds 65 - 68

One equivalent of 4-nitrobenzoyl chloride was dissolved in anhydrous $CHCl_3$. The system was cooled down to 0 °C (using an ice bath) and 1.1 equivalents of the relevant amino acid ester (Me for **65** and **66**, ^{t}But for **67** and **68**, all as HCl salts) as well as 1.1 equivalents of NEt_3, were added after which the bath was removed and the flask left to react at RT under Ar atmosphere. The reaction was stopped and quenched after 36 hours. The solvent was removed under reduced pressure and the resulting solids were dried further *in vacuo*. Solids where subsequently redissolved in the minimum amount of CH_3OH and then added to Et_2O to obtain white solids, which were filtrated and dried in air and *in vacuo*.

Synthesis of Methyl (4-Nitrobenzoyl)glycinate (65)[156]

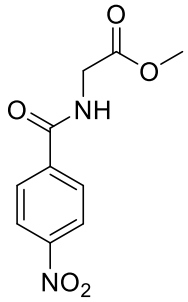

Compound **65** was obtained following the procedure described in section 6.2.4. 200 mg of 4-nitrobenzoyl chloride (1.08 mmol, 1 eq) were reacted with 149 mg of methyl glycinate (1.1 eq) and 350 µl of NEt_3 (2.5 eq) in 200 ml of anhydrous $CHCl_3$. The reaction succeded yielding a white solid (218 mg, 84.7% yield). **m.p.** 151-154 °C; **^{1}H NMR** (400 MHz, DMSO-d_6) δ 9.31 (1H bs, NH), 8.22 (4H, dd, J = 8.22 Hz, Ar-H), 4.06 (2H, d, J = 4.06 Hz, N-CH_2), 3.67 (3H, s, OCH_3).

Synthesis of Methyl (4-Nitrobenzoyl)-*L*-alaninate (66)[157]

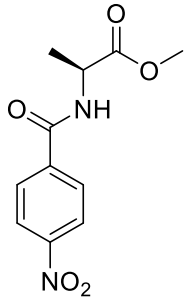

Compound **66** was obtained following the procedure described in section 6.2.4. 200 mg of 4-nitrobenzoyl chloride (1.08 mmol, 1 eq) were reacted with 166 mg of methyl *L*-alaninate (HCl salt) (1.1 eq) and 350 µl of NEt_3 (2.5 eq) in 200 ml of anhydrous $CHCl_3$. The reaction succeded yielding a white solid (234 mg, 91.2% yield). **m.p.** (127-129 °C); **HRMS** (ESI MS^-) (*m/z*): calculated for $C_{10}H_9N_2O_5$ (M -H) *m/z* = 237.051695, found 237.051636 **^{1}H NMR** (400 MHz, DMSO-d_6) δ 9.16 (1H, d, NH), 8.22 (4H, dd, Ar-H), 4.51 (1H, quint, N-CH_2), 3.66 (3H, s, OCH_3), 1.42 (3H, d, CH-CH_3); **^{13}C NMR** (100 MHz, DMSO-d_6) δ 173.24, 129.38, 123.99, 52.43, 48.91, 17.06.

Synthesis of *tert*-butyl (4-Nitrobenzoyl)-*L*-alaninate (67)

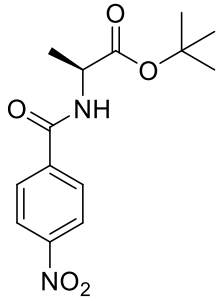

Compound **67** was obtained following the procedure described in section 6.2.4. 200 mg of 4-nitrobenzoyl chloride (1.08 mmol, 1 eq) were reacted with 215 mg of *tert*-butyl *L*-alaninate (1.1 eq) and 350 µl of NEt_3 (2.5 eq) in 200 ml of anhydrous $CHCl_3$. The reaction succeded yielding a white solid (230 mg, 72.3 % yield). **m.p.** 134-138 °C; **^{1}H NMR** (400 MHz, DMSO-d_6) δ 9.03 (1H, d, NH), 8.22 (4H, dd, Ar-H), 4.36 (1H, quint, N-CH_2), 1.41 (9H, s, C(CH_3)$_3$), 1.39 (3H, d, CH-CH_3); **^{13}C NMR** (100 MHz, DMSO-d_6) 171.98, 165.15, 149.56, 139.98, 129.35, 123.96, 80.97, 49.63, 28.08, 17.08.

Synthesis of *tert*-butyl (4-Nitrobenzoyl)-*L*-phenylalaninate (68)

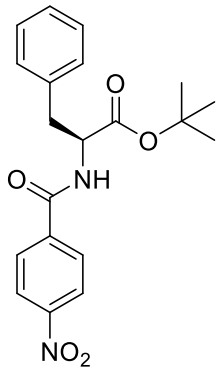

Compound **68** was obtained following the procedure described in section 6.2.4. 200 mg of 4-nitrobenzoyl chloride (1.08 mmol, 1 eq) were reacted with 392 mg of *tert*-butyl *L*-alaninate (1.1 eq) and 350 µl of NEt_3 (2.5 eq) in 200 ml of anhydrous $CHCl_3$. The reaction succeded yielding a white solid (278 mg, 69.4% yield). **m.p.** 148-151 °C; **^{1}H NMR** (400 MHz, DMSO-d_6) δ 9.08 (1H, d, NH), 8.14 (4H, dd, Ar-H), 7.22 (5H, m, Ar-H), 4.56 (1H, dd, N-CH), 3.10 (2H, dq, C-CH_2), 1.34 (9H, s, C(CH_3)$_3$); **^{13}C NMR** (100 MHz, DMSO-d_6)δ 170.89, 165.30, 149.57, 139.88, 138.00, 129.54, 129.27, 128.65, 126.92, 124.00, 81.31, 55.46, 46.02, 36.82, 28.01.

Synthesis of Methyl (4-Nitrobenzoyl) glycine (69)[158]

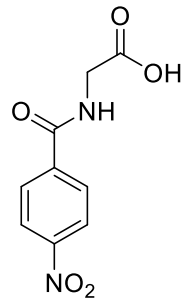

Compound **69** was obtained by basic hydrolysis of **65**. 50 mg of **65** (0.21 mmol, 1 eq) were dissolved in CH_3OH 1 ml acqueous 1 M NaOH (5 eq) and stirred at room temperature for 8 hours. The solution was quenched adding TFA dropwise, to induce the precipitation of off-white solid, that was retrieved by suction filtration (36 mg, 76.2% yield). **m.p.** 128-131 °C; **^{1}H NMR** (400 MHz, DMSO-d_6) δ 9.20 (1H, d, NH), 8.22 (4H, dd, Ar-H), 3.96 (2H, d, CH_2).

6.2.5 General procedure for the synthesis of compounds 70 - 71

One equivalent of the respective precursor (**67** and **68**) was dissolved in anhydrous DCM, cooled at 0 °C and the solution was added an excess of TFA with a $CaCl_2$ drying tube. The mixture was left at RT to react overnight. The reaction was then stopped, the DCM was removed under reduced pressure and the TFA solution was slightly diluted in CH_3OH added to an ice/water mixture to form a white precipitate that was recovered by suction filtration and washed with water, and dried in air and *in vacuo*.

Synthesis of (4-Nitrobenzoyl)-*L*-alanine (70)[158]

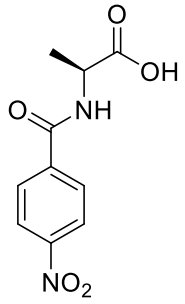

Compound **70** was obtained following the procedure described in section 6.2.5. 200 mg of **68** (0.68 mmol, 1 eq) were reacted with 1 ml of TFA (excess) in 50 ml DCM solution. The reaction succeded giving a white solid (145 mg, 89.6% yield). **m.p.** 168-170 °C; **HRMS** (*m/z*) (ESI MS^-) calculated for $C_{10}H_9N_2O5$ *m/z* = 237.051705 [M -H], found *m/z* = 237.051695; **^{1}H NMR** (400 MHz, DMSO-d_6) δ 12.64 (1H, bs, COOH), 9.03 (1H, d, NH), 8.22 (4H, dd, Ar-H), 4.44 (1H, quint, N-CH), 1.41 (3H, d, C-CH_3); **^{13}C NMR** (100 MHz, DMSO-d_6) δ 174.28, 164.99, 149.55, 139.97, 129.37, 123.95, 48.83, 17.21.

Synthesis of (4-Nitrobenzoyl)-*L*-phenylalanine (71)[158]

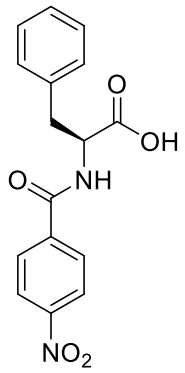

Compound **73** was obtained following the procedure described in section 6.2.5. 200 mg of **69** (0.54 mmol, 1 eq) were reacted with 1 ml of TFA (excess) in DCM solution. The reaction succeded giving a white solid (87.9 % yield). **m.p.** 167-171 °C; **^{1}H NMR** (δ 12.82 (1H, bs, COOH), 9.09 (1H, d, NH), 8.16 (4H, dd, Ar-H), 7.21 (5H, m, Ar-H), 4.65 (1H, dq, N-CH), 3.14 (2H, dq, C-CH_2); **^{13}C NMR** (100 MHz, DMSO-d_6) δ 173.23, 165.19, 149.55, 139.89, 138.38, 129.46, 129.23, 128.66, 126.86, 123.99, 54.80. 36.66.

6.2.6 General procedure for the synthesis of compounds 73 - 74

One equivalent of the respective precursor was dissolved in anhydrous DMF in a 20 ml microwave vial, which was cooled down to 0 °C (using an ice bath). 1 equivalent of Oxyma Pure, DCC and DIPEA were added initially, then followed by 1 equivalent of **64**. The vial was then sealed and the reaction was performed under microwave irradiation at 80 °C for 8 hours. The flask content was filtrated to remove crystals of DCU and poured in a mixture of water and ice, leading to the formation of a precipitate, which was then suction filtered. The solid was dissolved in CH_3OH and then added to Et_2O to obtain an orange (**73**) or yellow (**74**) solid which was dried in air and *in vacuo*.

Synthesis of (S)-N-(1-((3-([2,2':6',2''-terpyridin]-4'-ylamino)propyl)amino)-1-oxopropan-2-yl)-4-nitrobenzamide (73)

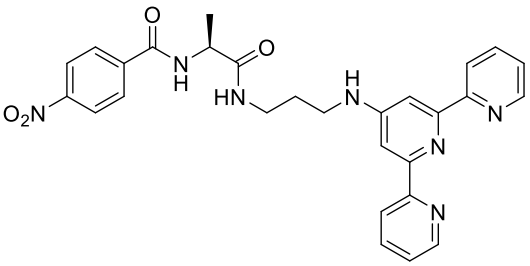

Compound **73** was obtained following the procedure described in section 6.2.6. 100 mg of **70** (0.42 mmol, 1 eq) were reacted with 128 mg of **64**, 60 mg of OxymaPure, 87 mg of DCC. An orange solid was obtained (83 mg, 37.8 % yield). **m.p.** Decomp. 175-180 °C; **HMRS**: (*m/z*) (ESI MS^-) calculated for $C_{28}H_{27}N_7NaO_4$ = 548.201673 (M+Na), found (*m/z*) 548.202102; **^{1}H NMR** (400 MHz, DMSO-d_6) δ 8.87 (1H, d, NH), 8.65 (2H, d, Ar-H), 8.32 (4H, dd, Ar-H), 8.26 (2H, d, N-Ar-H), 7.95 (2H, d, Ar-H), 7.66 (2H, s, C-CH-C), 7.44 (2H, dd, Ar-H), 6.84 (1H, bd, NH), 4.46 (1H, quint, N-CH), 3.24 (4H, m, C$\underline{H}_2$- CH_2-C$\underline{H}_2$), 1.78 (2H, dt, CH_2- C$\underline{H}_2$-CH_2), 1.36 (3H, d, CH_3). **^{13}C NMR** (100 MHz, DMSO-d_6) δ 172.49, 164.93, 149.40, 140.19,

137.54, 129.49, 124.42, 123.73, 121.11, 49.83, 36.93, 28.92, 18.33, 16.13, 14.36. **IR** υ max (cm^{-1}): 3326.25, 2975.96, 2930.74, 2848.72, 1730.16, 1640.84, 1599.37, 1523.67, 1339.52, 1222.35, 864.48, 842.14, 723.24, 699.17, 638.85.

Synthesis of (S)-N-(1-((3-([2,2':6',2''-terpyridin]-4'-ylamino)propyl)amino)-1-oxo-3-phenylpropan-2-yl)-4-nitrobenzamide (74)

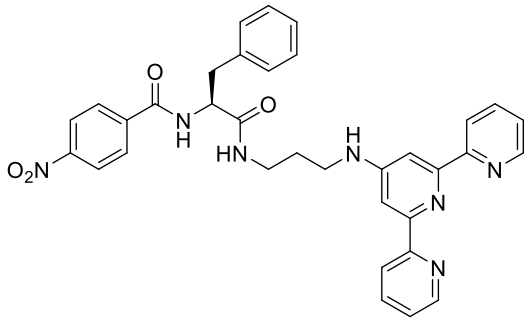

Compound **74** was obtained following the procedure described in section 6.2.6. 100 mg of **73** (0.32 mmol, 1 eq) were reacted with 97 mg of **64**, 45 mg of OxymaPure, 66 mg of DCC. A yellow solid was obtained (68 mg, 35.4 % yield). **m.p.** Decomp. > 173 °C; **^{1}H NMR** (400 MHz, DMSO-d_6) δ 8.96 (1H, d, NH), 8.63 (2H, d, Ar-H), 8.37 (4H, dd, Ar-H), 7.99 (2H, d, N-Ar-H), 7.93 (2H, dd, Ar-H), 7.65 (2H, s, C-CH-C), 7.41 (2H, dd, Ar-H), 7.22 (5H, m, Phe-H), 6.82 (1H, bd, NH), 4.67 (1H, m, N-CH), 3.18 (4H, m,z C$\underline{H}_2$-CH_2-C$\underline{H}_2$), 3.06 (2H, m, CH-C$\underline{H}_2$-Ar), 1.75 (2H, dt, CH_2- C$\underline{H}_2$-CH_2), 1.36 (3H, d, CH_3).

Synthesis of (S)-N-(1-((3-([2,2':6',2''-terpyridin]-4'-ylamino)propyl)amino)-1-oxopropan-2-yl)-4-aminobenzamide (75)

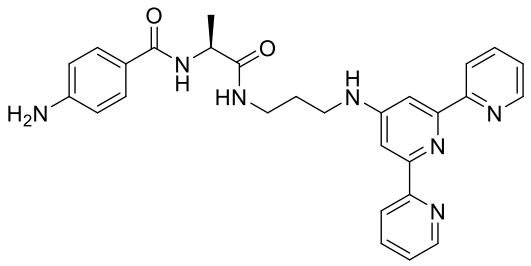

Compound **75** was synthesised using a Parr Hydrogenation Shaker apparatus. 50 mg of **73** (0.095 mmol, 1 eq) were in MeOH and transferred to the apparatus flask, together with palladium on carbon catalyst (10 mg, 20% w/w) and it was exposed to 3 atm of gaseous H_2 for 24 hours while shaking. The reaction was quenched, the flask vented and the suspension filtrered on celite. The solvent was removed under reduced pressure and the resulting solid was redissolved in EtOAc. The resulting solution was washed with solution of ethylenediaminetetracetic acid disodium salt (Na_2H_2EDTA) in ammonium buffer (20 ml, three times), H_2O (20 ml, once) and a sat. solution of NaCl (20 ml, three times). The organic layers were collected, dried over Na_2SO_4 and the solvent was removed to give a yellow solid (18 mg, 38.2 %). **m.p.** Decomp. 147 °C. **HMRS**: (*m/z*) (ESI MS^-) calculated for $C_{28}H_{30}N_7O_2$ = 496.245550 (M+H), found (*m/z*) 496.245686; **^{1}H NMR** (400 MHz, DMSO-d_6) δ 8.67 (1H, d, NH), 8.55 (2H, d, Ar-H), 7.94 (3H, m, Ar-H+NH), 7.66 (2H, s, Ar-H), 7.56 (4H, dd, N-Ar-H), 7.44 (2H, dd, Ar-H), 6.84 (1H, bd, NH), 5.59 (2H, bs, NH_2), 4.39 (1H, quint, N-CH), 3.22

(4H, m, C<u>H</u>$_2$- CH$_2$-C<u>H</u>$_2$), 1.76 (2H, dt, CH$_2$- C<u>H</u>$_2$-CH$_2$), 1.30 (3H, d, CH$_3$); **^{13}C NMR** (400 MHz, DMSO-d$_6$) δ 173.29, 166.43, 156.42, 155.96, 152.12, 149.36, 137.45, 129.49, 124.27, 121.18, 121.04, 112.85, 49.23, 36.91, 28.96, 18.70. **IR** υ max (cm^{-1}): 3317.82, 3208.21, 3076.37, 2926.14, 2161.94, 2025.51, 1980.28, 1603.93, 1584.49, 1564.77, 1499.88, 1265.75, 1184.69, 1095.15, 984.79, 844.87, 791.19.

Synthesis of Zn(II) complex (Zn·75)

Complex Zn·**75** was prepared dissolving 30 mg (0.06 mmol, 1 eq) of **75** in CH$_3$OH, to which 8 mg of ZnCl$_2$ were added and left stirring for 24 hours at room temperature. The reaction was then quenched and the solvent removed under reduced pressure. The resulting solid (24 mg, 63.1% yield) was collected and characterised. **HMRS**: (*m/z*) (ESI MS$^+$) calculated for C$_{56}$H$_{58}$N$_{14}$O$_4$Zn = 527.202296 (M+Zn), found (*m/z*) 527.202396

6.3 Experimental Details for Chapter 3

6.3.1 Gelation tests on 37

Gelation tests were carried out by dissolving a known amount (% weight/volume) of the gelator (Na$_3$·**37**) in millipore quality H$_2$O in a sealable vial (*d.* 25 mm, *l.* 60 mm), to which 4 equivalents of glucono-δ-lactone were added and the system was closed and left undisturbed at room temperature. The attempts that involved the use of Cu(II) and Tb(III) ions were performed as described in section 3.4.2.

6.3.2 Gelation tests on 62

Gelation tests were carried out by dissolving a known amount (% weight/volume) of the gelator (**62**) in CH$_3$OH and adding different amount of millipore quality H$_2$O in a sealable vial (*d.* 5 mm, *l.* 30 mm). The system was closed and left undisturbed at room temperature.

6.3.3 Imaging

The samples were all imaged using a Carl Zeiss ULTRA Plus, field emission scanning electron microscope (FE-SEM) using beam current of 3 - 8 kV with an SE2 or InLens detector. Prior to the recording of the images, all the samples were gold coated using a magnetron sputter to ensure conductivity of the surface.

6.3.3.1 Scanning Electron Microscopy of gels

Gel samples were prepared by placing a small amount of the relative gel (~10 - 15 µL by vol.) on silicon wafers and making a thin film by smooth smearing. The samples were dried initially in air for 5 - 6 hours followed by drying in high vacuum for 2 - 3 hours.

6.3.3.2 Scanning Electron Microscopy of solutions

Solution samples were prepared by dropcasting a small amount of the relative solution (5 - 20 µL) on silicon wafers. The samples were dried in air for 8 hours followed by drying in high vacuum for 2 - 3 hours.

Synthesis of 1-(6-isocyanatohexyl)-3-(6-methyl-4-oxo-1,4-dihydropyrimidin-2-yl)urea (76)[128]

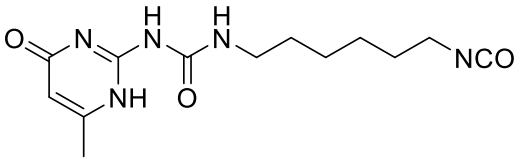

Compound **76** was obtained following the procedure reported by Folmer *et al*.[128] 300 mg (2.4 mmol, 1 eq) of 2-amino-6-methylpyrimidin-4-ol were suspended in 2 ml (excess) of 1,6 hexamethylene diisocyanate and reacted under reflux at 100 °C for 18 hours. The resulting solution was cooled down to room temperature and diluted 10:1 with hexane to induce the formation of a fine white precipitate which was suction filtered and dried *in vacuo* (549 mg, 78.1% yield). **m.p.** 191 - 193 °C; **HRMS** (*m/z*) (ESI MS^+) calculated for $C_{13}H_{19}N_5NaO_3$ *m/z* = 316.138010 [M+Na], found *m/z* = 316.138568; **^{1}H NMR** (400 Hz, DMSO-d_6) δ 11.54 (1H, bs, NH), 9.64 (1H, bs, NH), 7.32 (1H, bs, NH), 5.76 (1H, s, Ar-H), 3.13 (2H, dd, NCO-CH_2), 2.10 (3H, s, Ar-CH_3), 1.55-133 (10H, m, C$\underline{H}_2$).

6.4 Experimental Details for Chapter 4

6.4.1 Tb(III) centred emission measurements

The fluorescence measurements were carried out on a Varian Cary Eclipse Fluorimeter equipped with a 1.0 cm path length quartz cell at room temperature (293 K). The solvents used were all of spectroscopic grade. Fluorescence data were collected between 300 and 450 nm. The concentration of the ligands and the complexes were the same as those used for the UV-vis absorption measurements.

Table 6.4 *Settings of the Varian Cary Eclipse Fluorimeter for ligand-centered emission measurements*

Mode: Fluorescence	**Excitation:** 278 nm	**Scans:** 300 - 450 nm
Excitation Slit: 20 nm	**Emission Slit:** 5 nm	**PMT Voltage:** 750 V
Averaging time: 0.1 s	**Scan rate:** 600 nm/min	**Data Interval:** 0.5 nm

6.4.2 Tb(III) centred emission measurements

The phosphorescence measurements were carried out on a Varian Cary Eclipse Fluorimeter equipped with a 1.0 cm path length quartz cell at room temperature (293 K). The solvents used were all of spectroscopic grade. The emission data were collected between 400 and 675 nm. The concentration of the ligands and the complexes were the same as those used for the UV-vis absorption measurements.

Table 6.5 *Settings of the Varian Cary Eclipse Fluorimeter for Eu(III)-centered emission measurements*

Mode: Phosphorescence	**Excitation:** 278 nm	**Scans:** 400 - 675 nm
Excitation Slit: 20 nm	**Emission Slit:** 2.5 nm	**PMT Voltage:** 750 V
No. of flashes: 1	**Gate Time:** 5 ms	**Delay Time:** 0.2 ms
Averaging time: 0.1 s	**Total decay time:** 0.02 s	**Data Interval:** 0.5 nm

6.4.3 Scanning Electron Microscopy imaging

The imaging performed in this chapter was performed using the same modalities discussed in section 6.3.3.

6.5 Experimental details for Chapter 5

6.5.1 Scanning Electron Microscopy imaging

The imaging performed in this chapter was performed using the same modalities discussed in section 6.3.3.

Chapter 7

References

1. Steed, J. W. T., D. R.; Wallace, K., Core Concepts in Supramolecular Chemistry and Nanochemistry. **2007**, 1-2.
2. Lehn, J.-M., Supramolecular Chemistry—Scope and Perspectives Molecules, Supermolecules, and Molecular Devices (Nobel Lecture). *Angew. Chem. Int. Ed. Engl.* **1988,** *27* (1), 89-112.
3. Lehn, J.-M., From supramolecular chemistry towards constitutional dynamic chemistry and adaptive chemistry. *Chem. Soc. Rev.* **2007,** *36* (2), 151-160.
4. Lehn, J.-M., Supramolecular chemistry: Where from? Where to? *Chem. Soc. Rev.* **2017,** *46* (9), 2378-2379.
5. Whitesides, G.; Mathias, J.; Seto, C., Molecular self-assembly and nanochemistry: a chemical strategy for the synthesis of nanostructures. *Science* **1991,** *254* (5036), 1312-1319.
6. Plush, S. E.; Gunnlaugsson, T., Solution studies of trimetallic lanthanide luminescent anion sensors: towards ratiometric sensing using an internal reference channel. *Dalton Trans.* **2008,** (29), 3801-3804.
7. de Silva, A. P.; Moody, T. S.; Wright, G. D., Fluorescent PET (Photoinduced Electron Transfer) sensors as potent analytical tools. *Analyst* **2009,** *134* (12), 2385-2393.
8. Bünzli, J.-C. G.; Comby, S.; Chauvin, A.-S.; Vandevyver, C. D. B., New Opportunities for Lanthanide Luminescence. *J. Rare Earths* **2007,** *25* (3), 257-274.
9. Binnemans, K., Lanthanide-Based Luminescent Hybrid Materials. *Chem. Rev.* **2009,** *109* (9), 4283-4374.
10. Parker, D.; Dickins, R. S.; Puschmann, H.; Crossland, C.; Howard, J. A. K., Being Excited by Lanthanide Coordination Complexes: Aqua Species, Chirality, Excited-State Chemistry, and Exchange Dynamics. *Chem. Rev.* **2002,** *102* (6), 1977-2010.
11. Surender, Esther M.; Comby, S.; Cavanagh, B. L.; Brennan, O.; Lee, T. C.; Gunnlaugsson, T., Two-Photon Luminescent Bone Imaging Using Europium Nanoagents. *Chem* **2016,** *1* (3), 438-455.
12. Elmes, R. B. P.; Orange, K. N.; Cloonan, S. M.; Williams, D. C.; Gunnlaugsson, T., Luminescent Ruthenium(II) Polypyridyl Functionalized Gold Nanoparticles; Their DNA Binding Abilities and Application As Cellular Imaging Agents. *J. Am. Ceram. Soc.* **2011,** *133* (40), 15862-15865.
13. McMahon, B. K.; Pal, R.; Parker, D., A bright and responsive europium probe for determination of pH change within the endoplasmic reticulum of living cells. *Chem. Commun.* **2013,** *49* (47), 5363-5365.
14. Terech, P.; Weiss, R. G., Low Molecular Mass Gelators of Organic Liquids and the Properties of Their Gels. *Chem. Rev.* **1997,** *97* (8), 3133-3160.
15. Sangeetha, N. M.; Maitra, U., Supramolecular gels: Functions and uses. *Chem. Soc. Rev.* **2005,** *34* (10), 821-836.
16. George, M.; Weiss, R. G., Molecular Organogels. Soft Matter Comprised of Low-Molecular-Mass Organic Gelators and Organic Liquids. *Acc. Chem. Res.* **2006,** *39* (8), 489-497.
17. Buerkle, L. E.; Rowan, S. J., Supramolecular gels formed from multi-component low molecular weight species. *Chem. Soc. Rev.* **2012,** *41* (18), 6089-6102.
18. Hooper, A. E.; Kennedy, S. R.; Jones, C. D.; Steed, J. W., Gelation by supramolecular dimerization of mono(urea)s. *Chem. Commun.* **2016,** *52* (1), 198-201.
19. Lehn, J.-M., Perspectives in Supramolecular Chemistry—From Molecular Recognition towards Molecular Information Processing and Self-Organization. *Angew. Chem. Int. Ed. Engl.* **1990,** *29* (11), 1304-1319.

20. Sang, Y.; Liu, M., Nanoarchitectonics through supramolecular gelation: formation and switching of diverse nanostructures. *Molecular Systems Design & Engineering* **2019,** *4* (1), 11-28.
21. Jenkins, A. D.; Kratochvíl, P.; Stepto, R. F. T.; Suter, U. W., Glossary of basic terms in polymer science (IUPAC Recommendations 1996). **1996,** *68* (12), 2287.
22. Painter, P. C.; Coleman, M. M., *Fundamentals of polymer science : an introductory text*. 2nd ed. ed.; Lancaster: 1997.
23. De Greef, T. F. A.; Smulders, M. M. J.; Wolffs, M.; Schenning, A. P. H. J.; Sijbesma, R. P.; Meijer, E. W., Supramolecular Polymerization. *Chem. Rev.* **2009,** *109* (11), 5687-5754.
24. Fouquey, C. L., J.-M.; Levelut, A.-M. , Molecular Recognition Directed Self-Assembly of Supramolecular Liquid Crystalline Polymers from Complementary Chiral Components. *Adv. Mater.* **1990,** *2* (5), 4.
25. Stupp, S. I.; LeBonheur, V.; Walker, K.; Li, L. S.; Huggins, K. E.; Keser, M.; Amstutz, A., Supramolecular Materials: Self-Organized Nanostructures. *Science* **1997,** *276* (5311), 384-389.
26. Sijbesma, R. P.; Beijer, F. H.; Brunsveld, L.; Folmer, B. J. B.; Hirschberg, J. H. K. K.; Lange, R. F. M.; Lowe, J. K. L.; Meijer, E. W., Reversible Polymers Formed from Self-Complementary Monomers Using Quadruple Hydrogen Bonding. *Science* **1997,** *278* (5343), 1601-1604.
27. Aida, T.; Meijer, E. W.; Stupp, S. I., Functional Supramolecular Polymers. *Science* **2012,** *335* (6070), 813-817.
28. Abbel, R.; Grenier, C.; Pouderoijen, M. J.; Stouwdam, J. W.; Leclère, P. E. L. G.; Sijbesma, R. P.; Meijer, E. W.; Schenning, A. P. H. J., White-Light Emitting Hydrogen-Bonded Supramolecular Copolymers Based on π-Conjugated Oligomers. *J. Am. Ceram. Soc.* **2009,** *131* (2), 833-843.
29. Schenning, A. P. H. J.; Jonkheijm, P.; Peeters, E.; Meijer, E. W., Hierarchical Order in Supramolecular Assemblies of Hydrogen-Bonded Oligo(p-phenylene vinylene)s. *J. Am. Ceram. Soc.* **2001,** *123* (3), 409-416.
30. Schmid, S. A.; Abbel, R.; Schenning, A. P. H.; Meijer, E. W.; Sijbesma, R. P.; Herz, L. M., Analyzing the Molecular Weight Distribution in Supramolecular Polymers. *J. Am. Ceram. Soc.* **2009,** *131* (48), 17696-17704.
31. Zhang, W.; Jin, W.; Fukushima, T.; Saeki, A.; Seki, S.; Aida, T., Supramolecular Linear Heterojunction Composed of Graphite-Like Semiconducting Nanotubular Segments. *Science* **2011,** *334* (6054), 340-343.
32. Pal, A.; Karthikeyan, S.; Sijbesma, R. P., Coexisting Hydrophobic Compartments through Self-Sorting in Rod-like Micelles of Bisurea Bolaamphiphiles. *J. Am. Ceram. Soc.* **2010,** *132* (23), 7842-7843.
33. Obert, E.; Bellot, M.; Bouteiller, L.; Andrioletti, F.; Lehen-Ferrenbach, C.; Boué, F., Both Water- and Organo-Soluble Supramolecular Polymer Stabilized by Hydrogen-Bonding and Hydrophobic Interactions. *J. Am. Ceram. Soc.* **2007,** *129* (50), 15601-15605.
34. Hartgerink, J. D.; Beniash, E.; Stupp, S. I., Self-Assembly and Mineralization of Peptide-Amphiphile Nanofibers. *Science* **2001,** *294* (5547), 1684-1688.
35. Hartgerink, J. D.; Beniash, E.; Stupp, S. I., Peptide-amphiphile nanofibers: A versatile scaffold for the preparation of self-assembling materials. *Proc. Nat. Acad. Sci.* **2002,** *99* (8), 5133-5138.
36. Mata, A.; Geng, Y.; Henrikson, K. J.; Aparicio, C.; Stock, S. R.; Satcher, R. L.; Stupp, S. I., Bone regeneration mediated by biomimetic mineralization of a nanofiber matrix. *Biomaterials* **2010,** *31* (23), 6004-6012.

37. Rajangam, K.; Behanna, H. A.; Hui, M. J.; Han, X.; Hulvat, J. F.; Lomasney, J. W.; Stupp, S. I., Heparin Binding Nanostructures to Promote Growth of Blood Vessels. *Nano Lett.* **2006,** *6* (9), 2086-2090.
38. Capito, R. M.; Azevedo, H. S.; Velichko, Y. S.; Mata, A.; Stupp, S. I., Self-Assembly of Large and Small Molecules into Hierarchically Ordered Sacs and Membranes. *Science* **2008,** *319* (5871), 1812-1816.
39. Rożkiewicz, D. I.; Myers, B. D.; Stupp, S. I., Interfacial Self-Assembly of Cell-like Filamentous Microcapsules. *Angew. Chem. Int. Ed.* **2011,** *50* (28), 6324-6327.
40. Shao, L.; Yang, J.; Hua, B., A dual-responsive cross-linked supramolecular polymer network gel: hierarchical supramolecular self-assembly driven by pillararene-based molecular recognition and metal–ligand interactions. *Polymer Chemistry* **2018,** *9* (11), 1293-1297.
41. Cook, T. R.; Zheng, Y.-R.; Stang, P. J., Metal–Organic Frameworks and Self-Assembled Supramolecular Coordination Complexes: Comparing and Contrasting the Design, Synthesis, and Functionality of Metal–Organic Materials. *Chem. Rev.* **2013,** *113* (1), 734-777.
42. Kobielska, P. A.; Howarth, A. J.; Farha, O. K.; Nayak, S., Metal–organic frameworks for heavy metal removal from water. *Coord. Chem. Rev.* **2018,** *358*, 92-107.
43. Kreno, L. E.; Leong, K.; Farha, O. K.; Allendorf, M.; Van Duyne, R. P.; Hupp, J. T., Metal–Organic Framework Materials as Chemical Sensors. *Chem. Rev.* **2012,** *112* (2), 1105-1125.
44. Yuan, S.; Feng, L.; Wang, K.; Pang, J.; Bosch, M.; Lollar, C.; Sun, Y.; Qin, J.; Yang, X.; Zhang, P.; Wang, Q.; Zou, L.; Zhang, Y.; Zhang, L.; Fang, Y.; Li, J.; Zhou, H.-C., Stable Metal–Organic Frameworks: Design, Synthesis, and Applications. *Adv. Mater.* **2018,** *30* (37), 1704303.
45. Farrusseng, D.; Aguado, S.; Pinel, C., Metal–Organic Frameworks: Opportunities for Catalysis. *Angew. Chem. Int. Ed.* **2009,** *48* (41), 7502-7513.
46. Martins, L.; Macreadie, L. K.; Sensharma, D.; Vaesen, S.; Zhang, X.; Gough, J. J.; O'Doherty, M.; Zhu, N.-Y.; Rüther, M.; O'Brien, J. E.; Bradley, A. L.; Schmitt, W., Light-harvesting, 3rd generation RuII/CoII MOF with a large, tubular channel aperture. *Chem. Commun.* **2019,** *55* (34), 5013-5016.
47. Cantekin, S.; de Greef, T. F. A.; Palmans, A. R. A., Benzene-1,3,5-tricarboxamide: a versatile ordering moiety for supramolecular chemistry. *Chem. Soc. Rev.* **2012,** *41* (18), 6125-6137.
48. Ried, W.; Königstein, F.-J., Über das 1.3.5-Triformyl-benzol (Benzol-trialdehyd-(1.3.5). *Chem. Ber.* **1959,** *92* (10), 2532-2542.
49. Nagarajan, V.; Pedireddi, V. R., Gelation and Structural Transformation Study of Some 1,3,5-Benzenetricarboxamide Derivatives. *Cryst. Growth Des.* **2014,** *14* (4), 1895-1901.
50. Invernizzi, C.; Dalvit, C.; Stoeckli-Evans, H.; Neier, R., Synthesis and NMR Spectroscopic Study of the Self-Aggregation of 2-Substituted Benzene-1,3,5-tricarboxamides. *Eur. J. Org. Chem.* **2015,** *2015* (23), 5115-5127.
51. Desmarchelier, A.; Alvarenga, B. G.; Caumes, X.; Dubreucq, L.; Troufflard, C.; Tessier, M.; Vanthuyne, N.; Idé, J.; Maistriaux, T.; Beljonne, D.; Brocorens, P.; Lazzaroni, R.; Raynal, M.; Bouteiller, L., Tuning the nature and stability of self-assemblies formed by ester benzene 1,3,5-tricarboxamides: the crucial role played by the substituents. *Soft Matter* **2016,** *12* (37), 7824-7838.
52. Lynes, A. D.; Hawes, C. S.; Ward, E. N.; Haffner, B.; Möbius, M. E.; Byrne, K.; Schmitt, W.; Pal, R.; Gunnlaugsson, T., Benzene-1,3,5-tricarboxamide n-alkyl ester and

carboxylic acid derivatives: tuneable structural, morphological and thermal properties. *CrystEngComm* **2017,** *19* (10), 1427-1438.
53. Bernet, A.; Albuquerque, R. Q.; Behr, M.; Hoffmann, S. T.; Schmidt, H.-W., Formation of a supramolecular chromophore: a spectroscopic and theoretical study. *Soft Matter* **2012,** *8* (1), 66-69.
54. Howe, R. C. T.; Smalley, A. P.; Guttenplan, A. P. M.; Doggett, M. W. R.; Eddleston, M. D.; Tan, J. C.; Lloyd, G. O., A family of simple benzene 1,3,5-tricarboxamide (BTA) aromatic carboxylic acid hydrogels. *Chem. Commun.* **2013,** *49* (39), 4268-4270.
55. VandenBerg, M. A.; Sahoo, J. K.; Zou, L.; McCarthy, W.; Webber, M. J., Divergent Self-Assembly Pathways to Hierarchically Organized Networks of Isopeptide-Modified Discotics under Kinetic Control. *ACS Nano* **2020**.
56. Shi, G.; Shao, C.; Pan, S.; Yu, J.; Zhang, Y., Silver-Catalyzed C–H Trifluoromethylation of Arenes Using Trifluoroacetic Acid as the Trifluoromethylating Reagent. *Organic Letters* **2015,** *17* (1), 38-41.
57. R. A. Palmans, A.; A. J. M. Vekemans, J.; W. Meijer, E.; R. A. Palmans, A.; Kooijman, H.; L. Spek, A., Hydrogen-bonded porous solid derived from trimesic amide. *Chem. Commun.* **1997,** (22), 2247-2248.
58. Bhattacharya, S.; Sengupta, S.; Bala, S.; Goswami, A.; Ganguly, S.; Mondal, R., Pyrazole-Based Metallogels Showing an Unprecedented Colorimetric Ammonia Gas Sensing through Gel-to-Gel Transformation with a Rare Event of Time-Dependent Morphology Transformation. *Cryst. Growth Des.* **2014,** *14* (5), 2366-2374.
59. Zhong, J.-L.; Jia, X.-J.; Liu, H.-J.; Luo, X.-Z.; Hong, S.-G.; Zhang, N.; Huang, J.-B., Self-assembled metallogels formed from N,N′,N″-tris(4-pyridyl)trimesic amide in aqueous solution induced by Fe(iii)/Fe(ii) ions. *Soft Matter* **2016,** *12* (1), 191-199.
60. Groombridge, A. S.; Palma, A.; Parker, R. M.; Abell, C.; Scherman, O. A., Aqueous interfacial gels assembled from small molecule supramolecular polymers. *Chem. Sci.* **2017,** *8* (2), 1350-1355.
61. Curtius, T., Hydrazide und Azide organischer Säuren. XXX. Abhandlung. Bildung von Hydrazihydraziden und Hydraziaziden dreibasischer Säuren. *Journal für Praktische Chemie* **1915,** *91* (1), 39-102.
62. Bose, P. P.; Drew, M. G. B.; Das, A. K.; Banerjee, A., Formation of triple helical nanofibers using self-assembling chiral benzene-1,3,5-tricarboxamides and reversal of the nanostructure's handedness using mirror image building blocks. *Chem. Commun.* **2006,** (30), 3196-3198.
63. L., B.; A.P.H.J., S.; M.A.C., B.; H.M., J.; J.A.J.M., V.; E.W., M., Chiral Amplification in Columns of Self-Assembled N,N′,N″-Tris((S)-3,7-dimethyloctyl)benzene-1,3,5-tricarboxamide in Dilute Solution. *Chem. Lett.* **2000,** *29* (3), 292-293.
64. Smulders, M. M. J.; Buffeteau, T.; Cavagnat, D.; Wolffs, M.; Schenning, A. P. H. J.; Meijer, E. W., C3-symmetrical self-assembled structures investigated by vibrational circular dichroism. *Chirality* **2008,** *20* (9), 1016-1022.
65. Cantekin, S.; Balkenende, D. W. R.; Smulders, M. M. J.; Palmans, A. R. A.; Meijer, E. W., The effect of isotopic substitution on the chirality of a self-assembled helix. *Nat. Chem.* **2011,** *3* (1), 42-46.
66. Smulders, M. M. J.; Schenning, A. P. H. J.; Meijer, E. W., Insight into the Mechanisms of Cooperative Self-Assembly: The "Sergeants-and-Soldiers" Principle of Chiral and Achiral C3-Symmetrical Discotic Triamides. *J. Am. Ceram. Soc.* **2008,** *130* (2), 606-611.

67. Veld, M. A. J.; Haveman, D.; Palmans, A. R. A.; Meijer*, E. W., Sterically demanding benzene-1,3,5-tricarboxamides: tuning the mechanisms of supramolecular polymerization and chiral amplification. *Soft Matter* **2011,** *7* (2), 524-531.
68. Filot, I. A. W.; Palmans, A. R. A.; Hilbers, P. A. J.; van Santen, R. A.; Pidko, E. A.; de Greef, T. F. A., Understanding Cooperativity in Hydrogen-Bond-Induced Supramolecular Polymerization: A Density Functional Theory Study. *J. Phys. Chem. B* **2010,** *114* (43), 13667-13674.
69. Leenders, C. M. A.; Albertazzi, L.; Mes, T.; Koenigs, M. M. E.; Palmans, A. R. A.; Meijer, E. W., Supramolecular polymerization in water harnessing both hydrophobic effects and hydrogen bond formation. *Chem. Commun.* **2013,** *49* (19), 1963-1965.
70. Lee, S.; Lee, J.-S.; Lee, C. H.; Jung, Y.-S.; Kim, J.-M., Nonpolymeric Thermosensitive Benzenetricarboxamides. *Langmuir* **2011,** *27* (5), 1560-1564.
71. Paikar, A.; Pramanik, A.; Haldar, D., Influence of side-chain interactions on the self-assembly of discotic tricarboxyamides: a crystallographic insight. *RSC Adv.* **2015,** *5* (40), 31845-31851.
72. Kumar, D. K.; Jose, D. A.; Dastidar, P.; Das, A., Nonpolymeric Hydrogelators Derived from Trimesic Amides. *Chem. Mater.* **2004,** *16* (12), 2332-2335.
73. Shen, Z.; Wang, T.; Liu, M., Macroscopic Chirality of Supramolecular Gels Formed from Achiral Tris(ethyl cinnamate) Benzene-1,3,5-tricarboxamides. *Angew. Chem. Int. Ed.* **2014,** *53* (49), 13424-13428.
74. Narayan, B.; Kulkarni, C.; George, S. J., Synthesis and self-assembly of a C3-symmetric benzene-1,3,5-tricarboxamide (BTA) anchored naphthalene diimide disc. *J. Mater. Chem. C* **2013,** *1* (4), 626-629.
75. Kumar, M.; Jonnalagadda, N.; George, S. J., Molecular recognition driven self-assembly and chiral induction in naphthalene diimide amphiphiles. *Chem. Commun.* **2012,** *48* (89), 10948-10950.
76. Zhang, Y.; Wang, Q.; Xiao, Y.-J.; Han, J.; Zhao, X.-L., Structure diversity of a series of new coordination polymers based on a C3-symmetric tridentate ligand with rosette architecture. *Polyhedron* **2012,** *33* (1), 127-136.
77. Gillissen, M. A. J.; Koenigs, M. M. E.; Spiering, J. J. H.; Vekemans, J. A. J. M.; Palmans, A. R. A.; Voets, I. K.; Meijer, E. W., Triple Helix Formation in Amphiphilic Discotics: Demystifying Solvent Effects in Supramolecular Self-Assembly. *J. Am. Ceram. Soc.* **2014,** *136* (1), 336-343.
78. Bünzli, J.-C. G., Benefiting from the Unique Properties of Lanthanide Ions. *Acc. Chem. Res.* **2006,** *39* (1), 53-61.
79. Bünzli, J.-C. G., Lanthanide Luminescence for Biomedical Analyses and Imaging. *Chem. Rev.* **2010,** *110* (5), 2729-2755.
80. Bradberry, S. J.; Savyasachi, A. J.; Martinez-Calvo, M.; Gunnlaugsson, T., Development of responsive visibly and NIR luminescent and supramolecular coordination self-assemblies using lanthanide ion directed synthesis. *Coord. Chem. Rev.* **2014,** *273-274*, 226-241.
81. Barry, D. E.; Caffrey, D. F.; Gunnlaugsson, T., Lanthanide-directed synthesis of luminescent self-assembly supramolecular structures and mechanically bonded systems from acyclic coordinating organic ligands. *Chem. Soc. Rev.* **2016,** *45* (11), 3244-3274.
82. Martínez-Calvo, M.; Kotova, O.; Möbius, M. E.; Bell, A. P.; McCabe, T.; Boland, J. J.; Gunnlaugsson, T., Healable Luminescent Self-Assembly Supramolecular Metallogels Possessing Lanthanide (Eu/Tb) Dependent Rheological and Morphological Properties. *J. Am. Ceram. Soc.* **2015,** *137* (5), 1983-1992.
83. Katkova, M. A.; Bochkarev, M. N., New trends in design of electroluminescent rare earth metallo-complexes for OLEDs. *Dalton Trans.* **2010,** *39* (29), 6599-6612.

84. McCoy, C. P.; Stomeo, F.; Plush, S. E.; Gunnlaugsson, T., Soft Matter pH Sensing: From Luminescent Lanthanide pH Switches in Solution to Sensing in Hydrogels. *Chem. Mater.* **2006,** *18* (18), 4336-4343.
85. Leonard, J. P.; dos Santos, C. M. G.; Plush, S. E.; McCabe, T.; Gunnlaugsson, T., pH driven self-assembly of a ternary lanthanide luminescence complex: the sensing of anions using a β-diketonate-Eu(iii) displacement assay. *Chem. Commun.* **2007,** (2), 129-131.
86. Aime, S.; Barge, A.; Botta, M.; Parker, D.; De Sousa, A. S., Prototropic vs Whole Water Exchange Contributions to the Solvent Relaxation Enhancement in the Aqueous Solution of a Cationic Gd3+ Macrocyclic Complex. *J. Am. Ceram. Soc.* **1997,** *119* (20), 4767-4768.
87. Dickins, R. S.; Howard, J. A. K.; Lehmann, C. W.; Moloney, J.; Parker, D.; Peacock, R. D., Structural Rigidity and Luminescence of Chiral Lanthanide Tetraamide Complexes Based on 1,4,7,10-Tetraazacyclododecane. *Angew. Chem. Int. Ed. Engl.* **1997,** *36* (5), 521-523.
88. Evans, W. J., The Importance of Questioning Scientific Assumptions: Some Lessons from f Element Chemistry. *Inorg. Chem.* **2007,** *46* (9), 3435-3449.
89. Bünzli, J.-C. G.; Piguet, C., Taking advantage of luminescent lanthanide ions. *Chem. Soc. Rev.* **2005,** *34* (12), 1048-1077.
90. Faulkner, S.; Pope, S. J. A.; Burton-Pye, B. P., Lanthanide Complexes for Luminescence Imaging Applications. *Appl. Spectrosc. Rev.* **2005,** *40* (1), 1-31.
91. Gunnlaugsson, T.; Stomeo, F., Recent advances in the formation of luminescent lanthanide architectures and self-assemblies from structurally defined ligands. *Org. Biomol. Chem.* **2007,** *5* (13), 1999-2009.
92. Bünzli, J.-C. G., Review: Lanthanide coordination chemistry: from old concepts to coordination polymers. *J. Coord. Chem.* **2014,** *67* (23-24), 3706-3733.
93. Eliseeva, S. V.; Bünzli, J.-C. G., Lanthanide luminescence for functional materials and bio-sciences. *Chem. Soc. Rev.* **2010,** *39* (1), 189-227.
94. Hänninen, P.; Härmä, H.; Ala-Kleme, T., Lanthanide luminescence : photophysical, analytical and biological aspects. **2011**.
95. Bünzli, J.-C. G.; de Bettencourt-Dias, A., Luminescence Bioimaging with Lanthanide Complexes. In *Luminescence of Lanthanide Ions in Coordination Compounds and Nanomaterials*, 2014; pp 125-196.
96. Hanaoka, K.; Kikuchi, K.; Kobayashi, S.; Nagano, T., Time-Resolved Long-Lived Luminescence Imaging Method Employing Luminescent Lanthanide Probes with a New Microscopy System. *J. Am. Ceram. Soc.* **2007,** *129* (44), 13502-13509.
97. Heffern, M. C.; Matosziuk, L. M.; Meade, T. J., Lanthanide Probes for Bioresponsive Imaging. *Chem. Rev.* **2014,** *114* (8), 4496-4539.
98. dos Santos, C. M. G.; Harte, A. J.; Quinn, S. J.; Gunnlaugsson, T., Recent developments in the field of supramolecular lanthanide luminescent sensors and self-assemblies. *Coord. Chem. Rev.* **2008,** *252* (23), 2512-2527.
99. Huang, C. H., Rare Earth Coordination Chemistry: Fundamentals and Application. In *Rare Earth Coordination Chemistry*, Wiley: 2011; pp 1-39.
100. Latva, M.; Takalo, H.; Mukkala, V.-M.; Matachescu, C.; Rodríguez-Ubis, J. C.; Kankare, J., Correlation between the lowest triplet state energy level of the ligand and lanthanide(III) luminescence quantum yield. *J. Lumin.* **1997,** *75* (2), 149-169.
101. Archer, R. D.; Chen, H.; Thompson, L. C., Synthesis, Characterization, and Luminescence of Europium(III) Schiff Base Complexes1a. *Inorg. Chem.* **1998,** *37* (8), 2089-2095.

102. Liu, G. K.; Jensen, M. P.; Almond, P. M., Systematic Behavior of Charge-Transfer Transitions and Energy Level Variation in Soft Donor Complexes of the Trivalent Lanthanides. *J. Phys. Chem. A* **2006,** *110* (6), 2081-2088.
103. Horrocks, W. D.; Sudnick, D. R., Lanthanide ion probes of structure in biology. Laser-induced luminescence decay constants provide a direct measure of the number of metal-coordinated water molecules. *J. Am. Ceram. Soc.* **1979,** *101* (2), 334-340.
104. Horrocks, W. D.; Sudnick, D. R., Lanthanide ion luminescence probes of the structure of biological macromolecules. *Acc. Chem. Res.* **1981,** *14* (12), 384-392.
105. Bünzli, J.-C. G., On the design of highly luminescent lanthanide complexes. *Coord. Chem. Rev.* **2015,** *293-294*, 19-47.
106. Beeby, A.; M. Clarkson, I.; S. Dickins, R.; Faulkner, S.; Parker, D.; Royle, L.; S. de Sousa, A.; A. Gareth Williams, J.; Woods, M., Non-radiative deactivation of the excited states of europium, terbium and ytterbium complexes by proximate energy-matched OH, NH and CH oscillators: an improved luminescence method for establishing solution hydration states. *J. Chem. Soc., Perkin. Trans. 2* **1999,** (3), 493-504.
107. Aime, S.; Botta, M.; Parker, D.; Williams, J. A. G., Extent of hydration of octadentate lanthanide complexes incorporating phosphinate donors: solution relaxometry and luminescence studies. *J. Chem. Soc., Dalton Trans.* **1996,** (1), 17-23.
108. Kotova, O.; Daly, R.; dos Santos, C. M. G.; Boese, M.; Kruger, P. E.; Boland, J. J.; Gunnlaugsson, T., Europium-Directed Self-Assembly of a Luminescent Supramolecular Gel from a Tripodal Terpyridine-Based Ligand. *Angew. Chem. Int. Ed.* **2012,** *51* (29), 7208-7212.
109. Whittell, G. R.; Hager, M. D.; Schubert, U. S.; Manners, I., Functional soft materials from metallopolymers and metallosupramolecular polymers. *Nature Materials* **2011,** *10* (3), 176-188.
110. Lohmeijer, B. G. G.; Schubert, U. S., Playing LEGO with macromolecules: Design, synthesis, and self-organization with metal complexes. *J. Polym. Sci., Part A: Polym. Chem.* **2003,** *41* (10), 1413-1427.
111. Daly, R.; Kotova, O.; Boese, M.; Gunnlaugsson, T.; Boland, J. J., Chemical Nano-Gardens: Growth of Salt Nanowires from Supramolecular Self-Assembly Gels. *ACS Nano* **2013,** *7* (6), 4838-4845.
112. Lynes, A. D. Supramolecular soft materials and structural studies of a series of BTA and pyridine-dicarboxamide derivatives with various *d*-metal ions. Doctoral Dissertation, Trinity College Dublin, Dublin, 2018.
113. El-Faham, A.; Albericio, F., Peptide Coupling Reagents, More than a Letter Soup. *Chem. Rev.* **2011,** *111* (11), 6557-6602.
114. Jaradat, D. s. M. M., Thirteen decades of peptide synthesis: key developments in solid phase peptide synthesis and amide bond formation utilized in peptide ligation. *Amino Acids* **2018,** *50* (1), 39-68.
115. Chichak, K. S.; Cantrill, S. J.; Pease, A. R.; Chiu, S.-H.; Cave, G. W. V.; Atwood, J. L.; Stoddart, J. F., Molecular Borromean Rings. *Science* **2004,** *304* (5675), 1308-1312.
116. Shunmugam, R.; Gabriel, G. J.; Aamer, K. A.; Tew, G. N., Metal–Ligand-Containing Polymers: Terpyridine as the Supramolecular Unit. *Macromol. Rapid Commun.* **2010,** *31* (9-10), 784-793.
117. Musumeci, C.; Zappalà, G.; Martsinovich, N.; Orgiu, E.; Schuster, S.; Quici, S.; Zharnikov, M.; Troisi, A.; Licciardello, A.; Samorì, P., Nanoscale Electrical Investigation of Layer-by-Layer Grown Molecular Wires. *Adv. Mater.* **2014,** *26* (11), 1688-1693.
118. Shanmugaraju, S.; Dabadie, C.; Byrne, K.; Savyasachi, A. J.; Umadevi, D.; Schmitt, W.; Kitchen, J. A.; Gunnlaugsson, T., A supramolecular Tröger's base derived

coordination zinc polymer for fluorescent sensing of phenolic-nitroaromatic explosives in water. *Chem. Sci.* **2017,** *8* (2), 1535-1546.
119. Bünzli, J.-C. G.; Piguet, C., Lanthanide-Containing Molecular and Supramolecular Polymetallic Functional Assemblies. *Chem. Rev.* **2002,** *102* (6), 1897-1928.
120. Binnemans, K., Interpretation of europium(III) spectra. *Coord. Chem. Rev.* **2015,** *295*, 1-45.
121. Gampp, H.; Maeder, M.; Meyer, C. J.; Zuberbühler, A. D., Calculation of equilibrium constants from multiwavelength spectroscopic data-IV Model-free least-squares refinement by use of evolving factor analysis. *Talanta* **1986,** *33* (12), 943-951.
122. Savyasachi, A. J. **Luminescent Self-assembled Supramolecular Polymers and Microspheres Based on Benzene-1,3,5-tricarboxamide (BTA) Derivatives**. **Trinity College Dublin**, Dublin, 2017.
123. Price, B., Electron Microscopy, Second Edition, John J. Bozzola and Lonnie D. Russell. Jones and Bartlett Publishers, Inc., Sudbury, MA, 1999, 670 pages (hardback, $56.25). ISBN 0-7637-0192-0. *Microsc. Microanal.* **2002,** *08*, 365.
124. Shaffner, T. J.; Veld, R. D. V., 'Charging' effects in the scanning electron microscope. *Journal of Physics E: Scientific Instruments* **1971,** *4* (9), 633-637.
125. Cazaux, J., Secondary electron emission and fundamentals of charging mechanisms in XPS. *J. Electron. Spectrosc. Relat. Phenom.* **2010,** *178-179*, 357-372.
126. Ji, Y.; Guo, H. S.; Zhong, T. X.; Zhang, H.; Quan, X. L.; Zhang, Y. Q.; Xu, X. D., Charge and charging compensation on oxides and hydroxides in oxygen environmental SEM. *Ultramicroscopy* **2005,** *103* (3), 191-198.
127. Djurić, N.; Lozano, J. A.; Smith, S. J.; Chutjian, A., Surface Charging and X-Ray Emission from Insulator Surfaces Induced by Collisions with Highly Charged Ions: Relevance to Cometary and Planetary Spectroscopy. *The Astrophysical Journal* **2005,** *635* (1), 718-722.
128. Folmer, B. J. B.; Sijbesma, R. P.; Versteegen, R. M.; van der Rijt, J. A. J.; Meijer, E. W., Supramolecular Polymer Materials: Chain Extension of Telechelic Polymers Using a Reactive Hydrogen-Bonding Synthon. *Adv. Mater.* **2000,** *12* (12), 874-878.
129. Canchi, D. R.; Paschek, D.; García, A. E., Equilibrium Study of Protein Denaturation by Urea. *J. Am. Ceram. Soc.* **2010,** *132* (7), 2338-2344.
130. O'Brien, E. P.; Dima, R. I.; Brooks, B.; Thirumalai, D., Interactions between Hydrophobic and Ionic Solutes in Aqueous Guanidinium Chloride and Urea Solutions: Lessons for Protein Denaturation Mechanism. *J. Am. Ceram. Soc.* **2007,** *129* (23), 7346-7353.
131. Rajdev, P.; Molla, M. R.; Ghosh, S., Understanding the Role of H-Bonding in Aqueous Self-Assembly of Two Naphthalene Diimide (NDI)-Conjugated Amphiphiles. *Langmuir* **2014,** *30* (8), 1969-1976.
132. Das, A.; Ghosh, S., H-bonding directed programmed supramolecular assembly of naphthalene-diimide (NDI) derivatives. *Chem. Commun.* **2016,** *52* (42), 6860-6872.
133. Aramballi J. Savyasachi, D. F. C., Kevin Byrne, Gerard Tobin, Bruno D'Agostino, Wolfgang Schmitt, Thorfinnur Gunnlaugsson, Self-assembled bright luminescent hierarchical materials from a tripodal benzoate antenna and heptadentate Eu(III) and Tb(III) cyclen complexes. *Front. Chem. Sci. Eng.* **2019,** *13* (1), 171-184.
134. Leonard, J. P.; Nolan, C. B.; Stomeo, F.; Gunnlaugsson, T., Photochemistry and Photophysics of Coordination Compounds: Lanthanides. In *Photochemistry and Photophysics of Coordination Compounds II*, Balzani, V.; Campagna, S., Eds. Springer Berlin Heidelberg: Berlin, Heidelberg, 2007; pp 1-43.

135. Surender, E. M.; Comby, S.; Martyn, S.; Cavanagh, B.; Lee, T. C.; Brougham, D. F.; Gunnlaugsson, T., Cyclen lanthanide-based micellar structures for application as luminescent [Eu(iii)] and magnetic [Gd(iii)] resonance imaging (MRI) contrast agents. *Chem. Commun.* **2016,** *52* (72), 10858-10861.
136. Nazarenko, M. A.; Oflidi, A. I.; Kolokolov, F. A.; Panyushkin, V. T., Electrochemical synthesis of anhydrous luminescent Tb3+ complexes with aromatic and heterocyclic carboxylic acids. *Russ. J. Gen. Chem.* **2017,** *87* (5), 1022-1025.
137. Consulting, J., ReactLab Equililbria. *Freemantle* **2016**.
138. Marchetti, L. A.; Kumawat, L. K.; Mao, N.; Stephens, J. C.; Elmes, R. B. P., The Versatility of Squaramides: From Supramolecular Chemistry to Chemical Biology. *Chem* **2019,** *5* (6), 1398-1485.
139. Ian Storer, R.; Aciro, C.; Jones, L. H., Squaramides: physical properties, synthesis and applications. *Chem. Soc. Rev.* **2011,** *40* (5), 2330-2346.
140. Cai, X.-J.; Li, Z.; Chen, W.-H., Synthesis, Anion Recognition and Transmembrane Anion-Transport Properties of Squaramides and Their Derivatives. *Mini-Reviews in Organic Chemistry* **2018,** *15* (2), 148-156.
141. Saez Talens, V.; Englebienne, P.; Trinh, T. T.; Noteborn, W. E. M.; Voets, I. K.; Kieltyka, R. E., Aromatic Gain in a Supramolecular Polymer. *Angew. Chem. Int. Ed.* **2015,** *54* (36), 10502-10506.
142. P. Davis, A.; M. Draper, S.; Dunne, G.; Ashton, P., The N-carbamoyl squaramide dimer: a compact, strongly associated H-bonding motif. *Chem. Commun.* **1999,** (22), 2265-2266.
143. Langdon-Jones, E. E.; Lloyd, D.; Hayes, A. J.; Wainwright, S. D.; Mottram, H. J.; Coles, S. J.; Horton, P. N.; Pope, S. J. A., Alkynyl-naphthalimide Fluorophores: Gold Coordination Chemistry and Cellular Imaging Applications. *Inorg. Chem.* **2015,** *54* (13), 6606-6615.
144. Carter, A. B.; Zhang, N.; Kühne, I. A.; Keene, T. D.; Powell, A. K.; Kitchen, J. A., Layered Ln(III) Complexes from a Sulfonate-Based 1,8-Naphthalimide: Structures, Magnetism and Photophysics. *ChemistrySelect* **2019,** *4* (6), 1850-1856.
145. Ni, Y.; Sun, Z.; Wang, Y.; Nour, H. F.; Sue, A. C. H.; Finney, N. S.; Baldridge, K. K.; Olson, M. A., Versatile hydrochromic fluorescent materials based on a 1,8-naphthalimide integrated fluorophore-receptor system. *J. Mater. Chem. C* **2019,** *7* (24), 7399-7410.
146. Mart, M.; #237; nez-Calvo, S. A. B., Emma B. Veale, Adam F. Henwood, D. Clive Williams, Thorfinnur Gunnlaugsson, 4-Amino-1,8-naphthalimide based fluorescent photoinduced electron transfer (PET) pH sensors as liposomal cellular imaging agents: The effect of substituent patterns on PET directional quenching. *Front. Chem. Sci. Eng.* **2020,** *14* (1), 61-75.
147. Calatrava-Pérez, E.; Acherman, S.; Stricker, L.; McManus, G.; Delente, J.; Lynes, A. D.; Henwood, A. F.; Lovitt, J. I.; Hawes, C. S.; Byrne, K.; Schmitt, W.; Kotova, O.; Gunnlaugsson, T.; Scanlan, E. M., Fluorescent supramolecular hierarchical self-assemblies from glycosylated 4-amino- and 4-bromo-1,8-naphthalimides. *Org. Biomol. Chem.* **2020,** *18* (18), 3475-3480.
148. Lovitt, J. I.; Hawes, C. S.; Lynes, A. D.; Haffner, B.; Möbius, M. E.; Gunnlaugsson, T., Coordination chemistry of N-picolyl-1,8-naphthalimides: colourful low molecular weight metallo-gelators and unique chelation behaviours. *Inorg. Chem. Frontiers* **2017,** *4* (2), 296-308.
149. Tang, Y.; Ma, Y.; Yin, J.; Lin, W., Strategies for designing organic fluorescent probes for biological imaging of reactive carbonyl species. *Chem. Soc. Rev.* **2019,** *48* (15), 4036-4048.

150. Delente, J. M.; Umadevi, D.; Shanmugaraju, S.; Kotova, O.; Watson, G. W.; Gunnlaugsson, T., Aggregation induced emission (AIE) active 4-amino-1,8-naphthalimide-Tröger's base for the selective sensing of chemical explosives in competitive aqueous media. *Chem. Commun.* **2020,** *56* (17), 2562-2565.
151. Banerjee, S.; Veale, E. B.; Phelan, C. M.; Murphy, S. A.; Tocci, G. M.; Gillespie, L. J.; Frimannsson, D. O.; Kelly, J. M.; Gunnlaugsson, T., Recent advances in the development of 1,8-naphthalimide based DNA targeting binders, anticancer and fluorescent cellular imaging agents. *Chem. Soc. Rev.* **2013,** *42* (4), 1601-1618.
152. Chen, X.; Wang, F.; Hyun, J. Y.; Wei, T.; Qiang, J.; Ren, X.; Shin, I.; Yoon, J., Recent progress in the development of fluorescent, luminescent and colorimetric probes for detection of reactive oxygen and nitrogen species. *Chem. Soc. Rev.* **2016,** *45* (10), 2976-3016.
153. Mei, J.; Hong, Y.; Lam, J. W. Y.; Qin, A.; Tang, Y.; Tang, B. Z., Aggregation-Induced Emission: The Whole Is More Brilliant than the Parts. *Adv. Mater.* **2014,** *26* (31), 5429-5479.
154. Luo, J.; Xie, Z.; Lam, J. W. Y.; Cheng, L.; Chen, H.; Qiu, C.; Kwok, H. S.; Zhan, X.; Liu, Y.; Zhu, D.; Tang, B. Z., Aggregation-induced emission of 1-methyl-1,2,3,4,5-pentaphenylsilole. *Chem. Commun.* **2001,** (18), 1740-1741.
155. Lin, H.-H.; Chan, Y.-C.; Chen, J.-W.; Chang, C.-C., Aggregation-induced emission enhancement characteristics of naphthalimide derivatives and their applications in cell imaging. *J. Mater. Chem.* **2011,** *21* (9), 3170-3177.
156. Prein, M.; Manley, P. J.; Padwa, A., Site selectivity in the rhodium(II)-catalyzed reaction of α-diazoimides. Ligand and substituent effects. *Tetrahedron* **1997,** *53* (23), 7777-7794.
157. Mahesh, M.; Panduranga, V.; Prabhu, G.; Kumar L, R.; Ramana, P. V.; Sureshbabu, V. V., Oxidative amidation of benzyl alcohols with amino acid esters mediated by N -hydroxysuccinimide/phenyliodine diacetate. *Synth. Commun.* **2017,** *47* (7), 716-721.
158. Benvenuti, S.; Severi, F.; Costantino, L.; Vampa, G.; Melegari, M., Synthesis and aldose reductase inhibitory activity of benzoyl-amino acid derivatives. *Il Farmaco* **1998,** *53* (6), 439-442.

Appendix

A.1 ^{1}H and ^{13}C NMR spectra

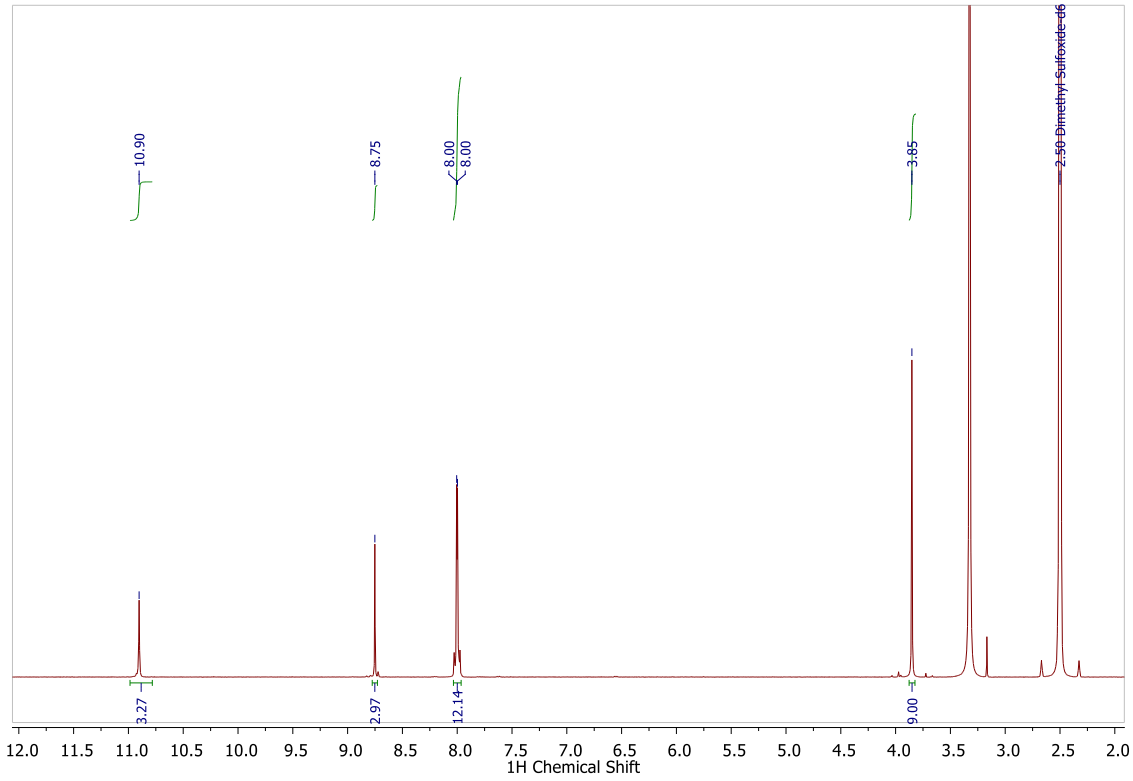

Figure A.1 *^{1}H NMR (400 MHz, DMSO-d_6) of **56**.*

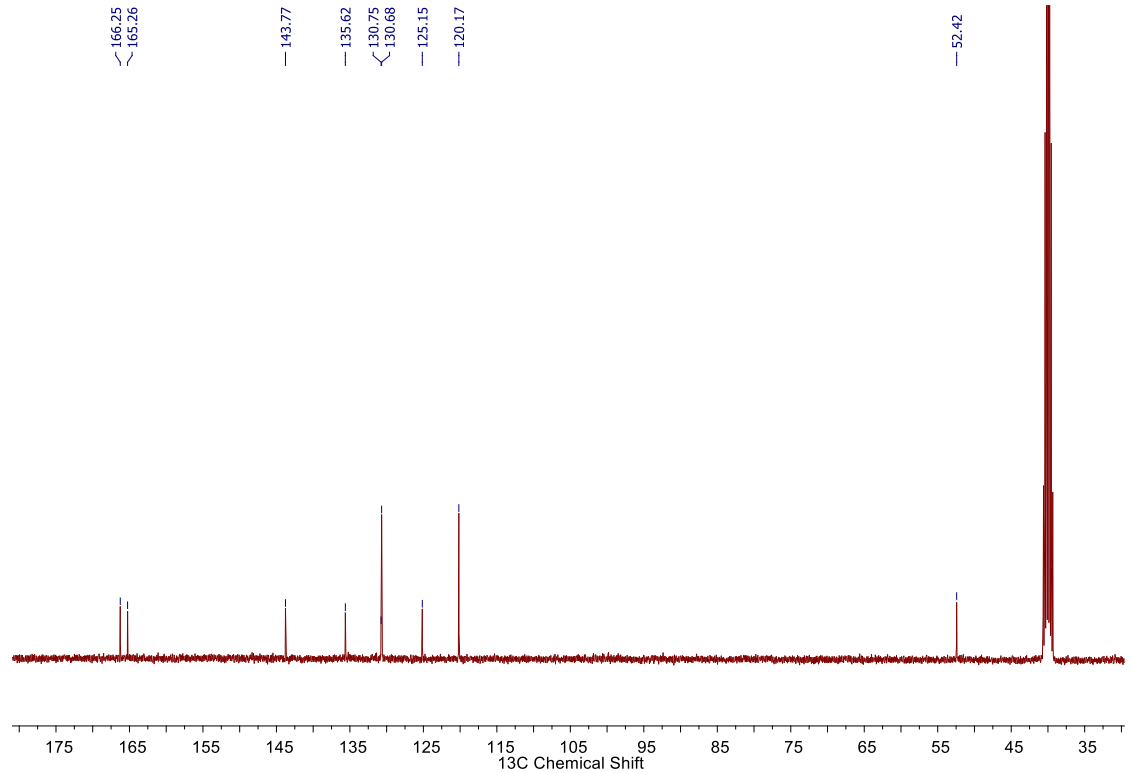

Figure A.2 *^{13}C NMR (100 MHz, DMSO-d_6) of **56**.*

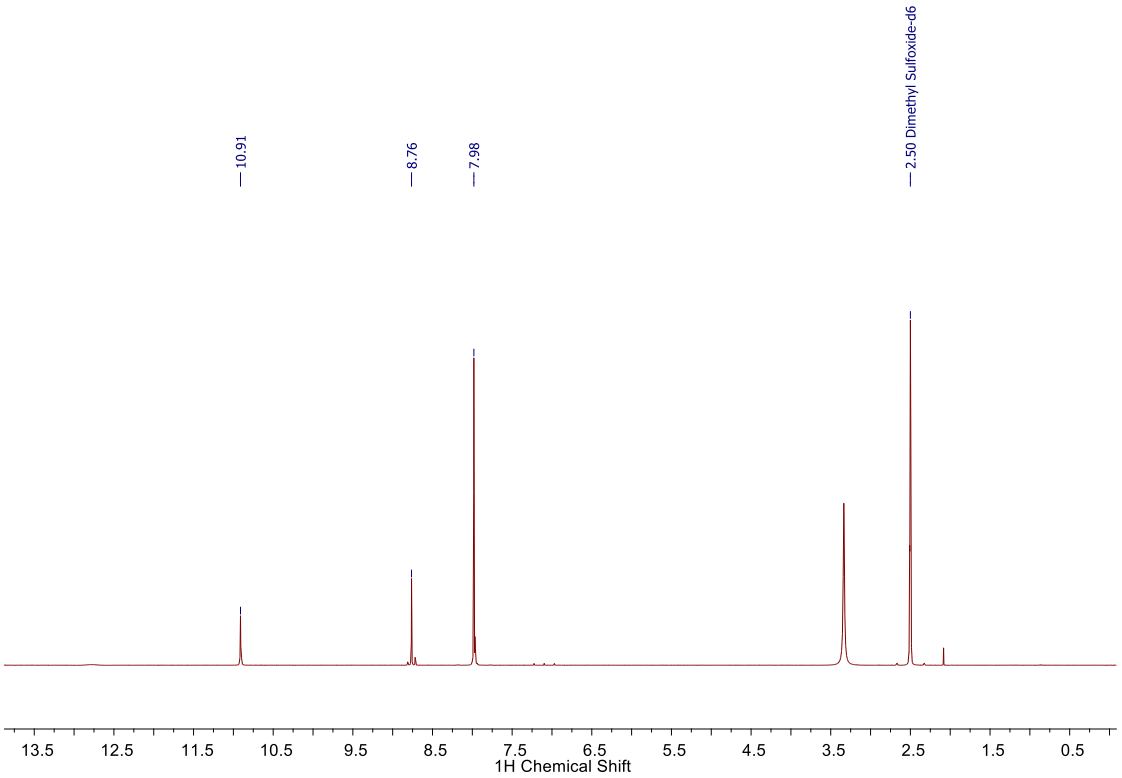

Figure A.3 *^{1}H NMR (400 MHz, DMSO-d_6) of **37**.*

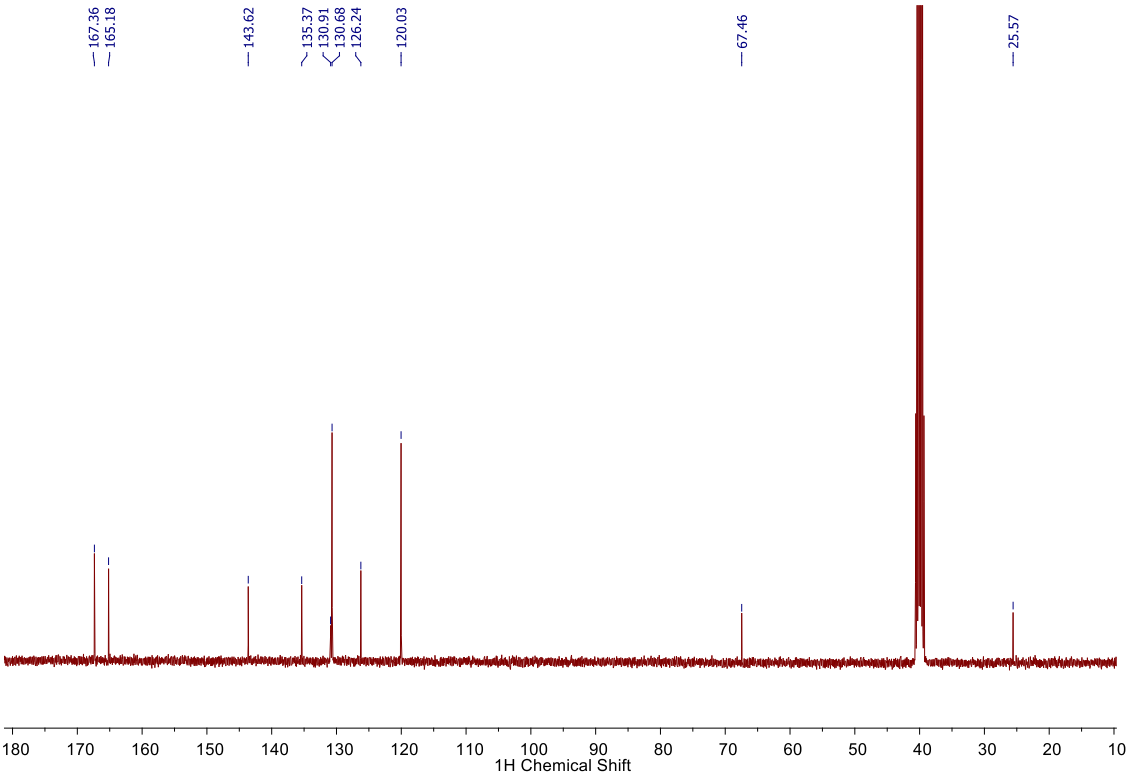

Figure A.4 *^{13}C NMR (100 MHz, DMSO-d_6) of **37**.*

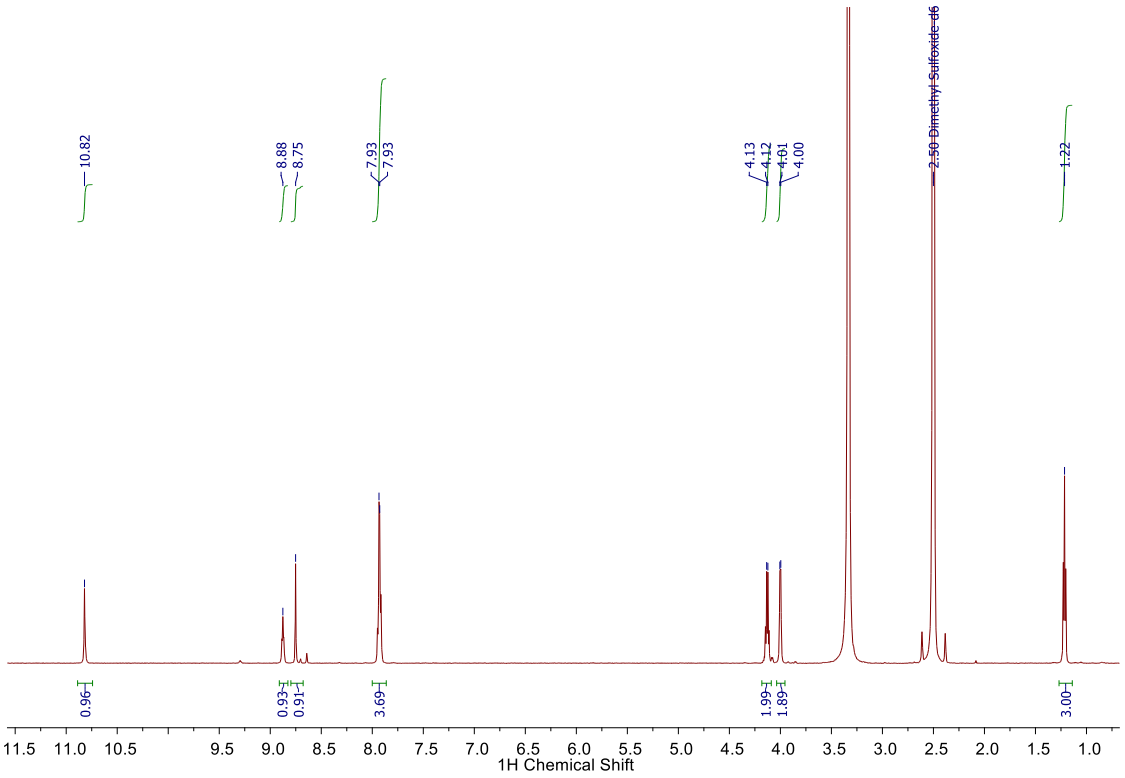

Figure A.5 *^{1}H NMR (400 MHz, DMSO-d_6) of **57**.*

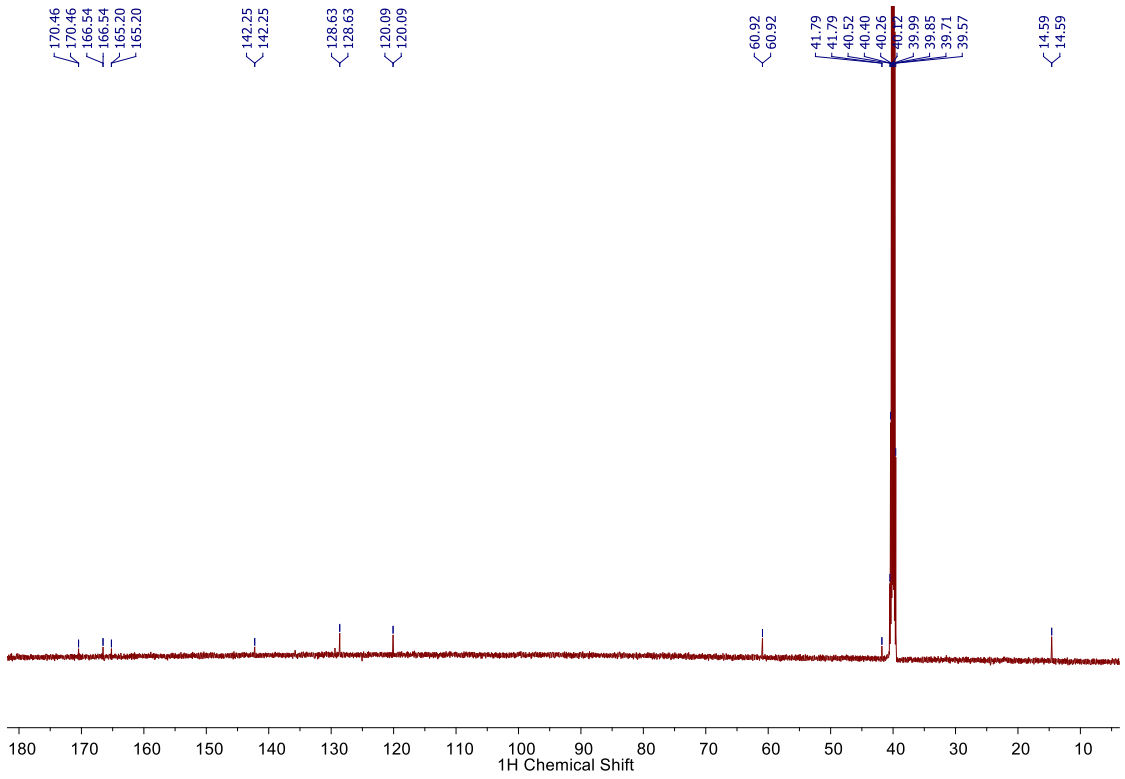

Figure A.6 *^{13}C NMR (100 MHz, DMSO-d_6) of **57**.*

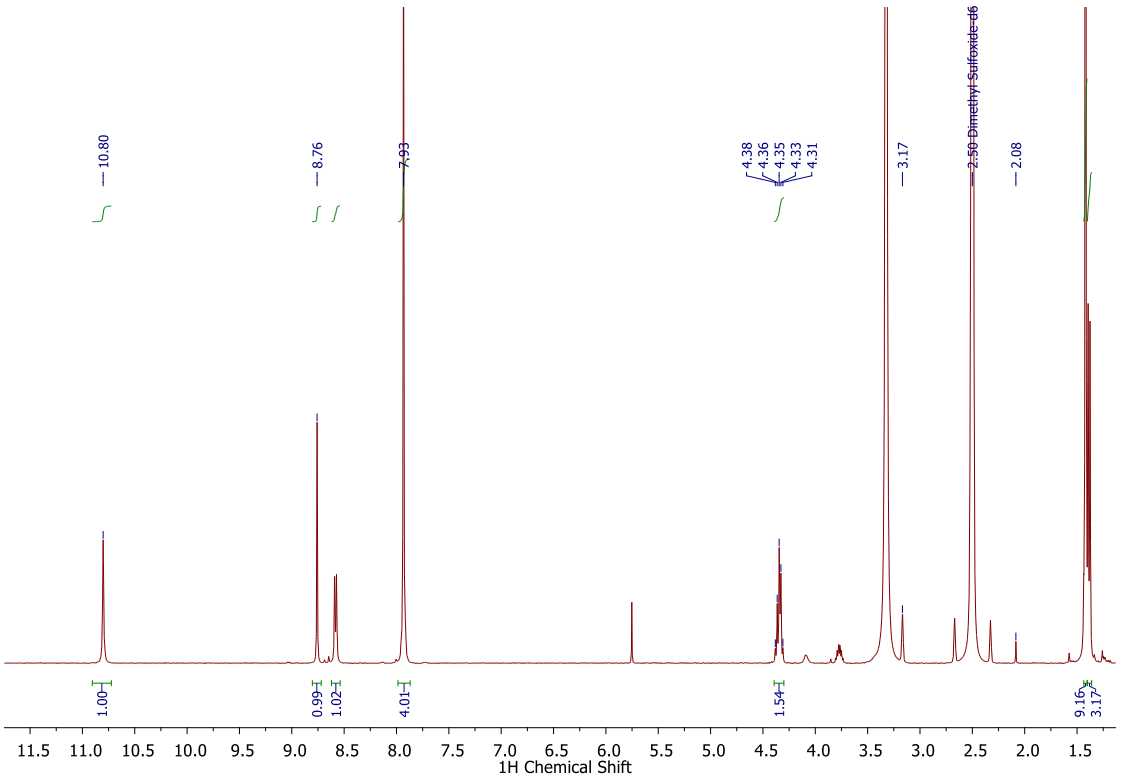

Figure A.7 *^{1}H NMR (400 MHz, DMSO-d_6) of* ***59****.*

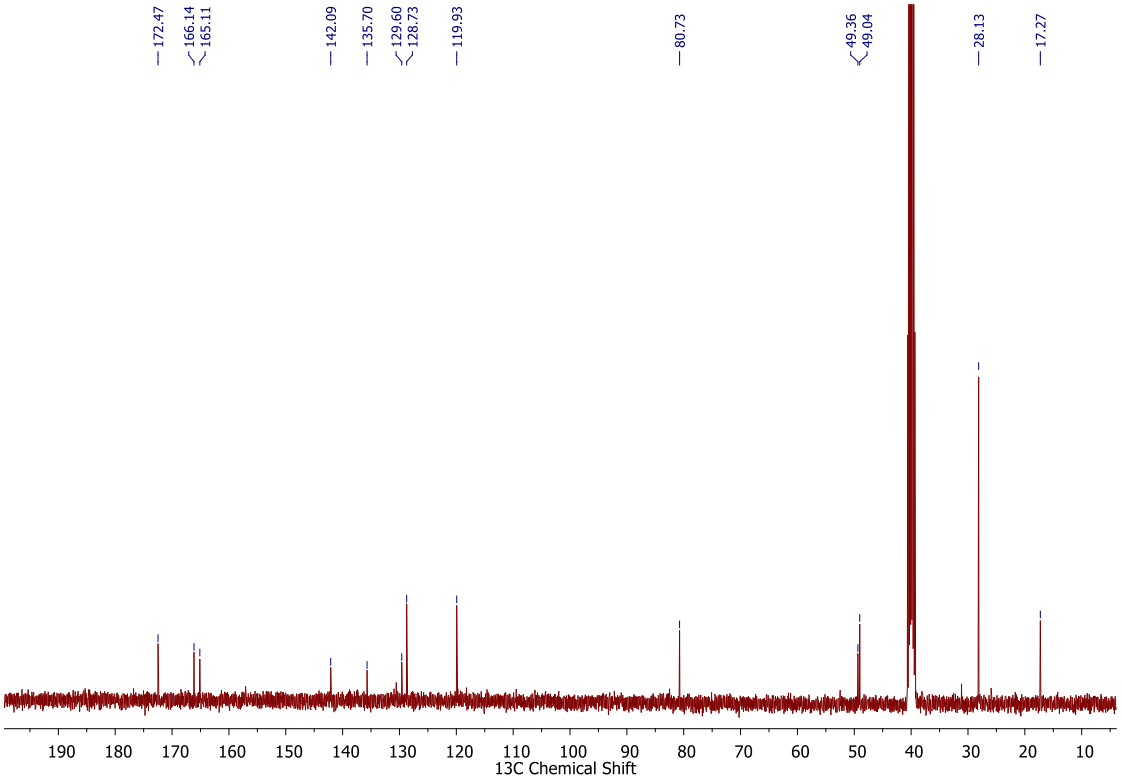

Figure A.8 *^{13}C NMR (100 MHz, DMSO-d_6) of* ***59****.*

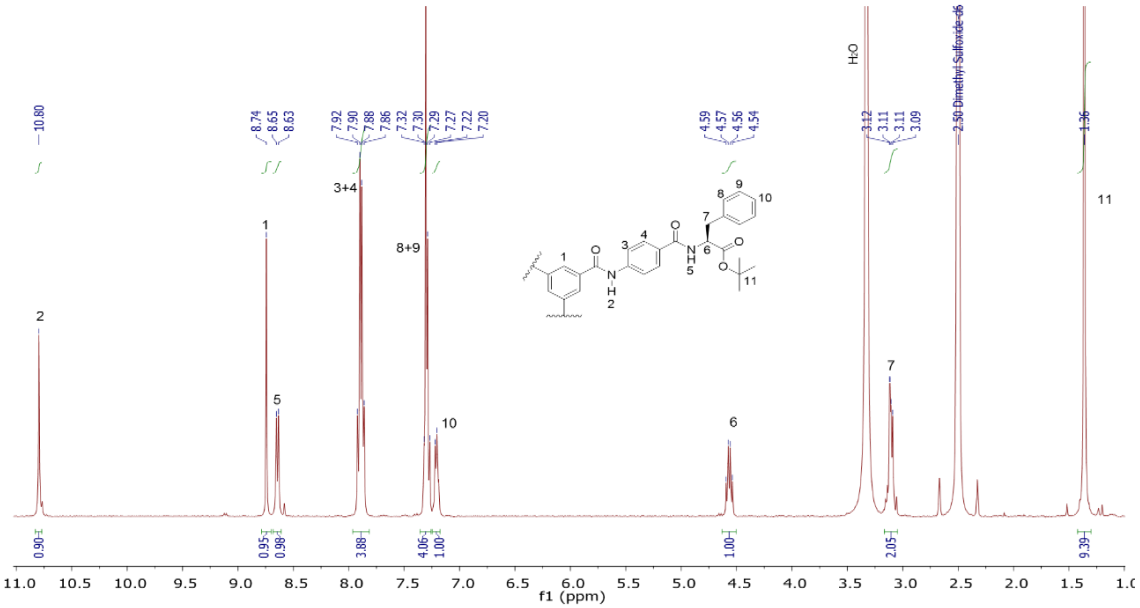

Figure A.9 *^{1}H NMR (400 MHz, DMSO-d_6) of* ***59****.*

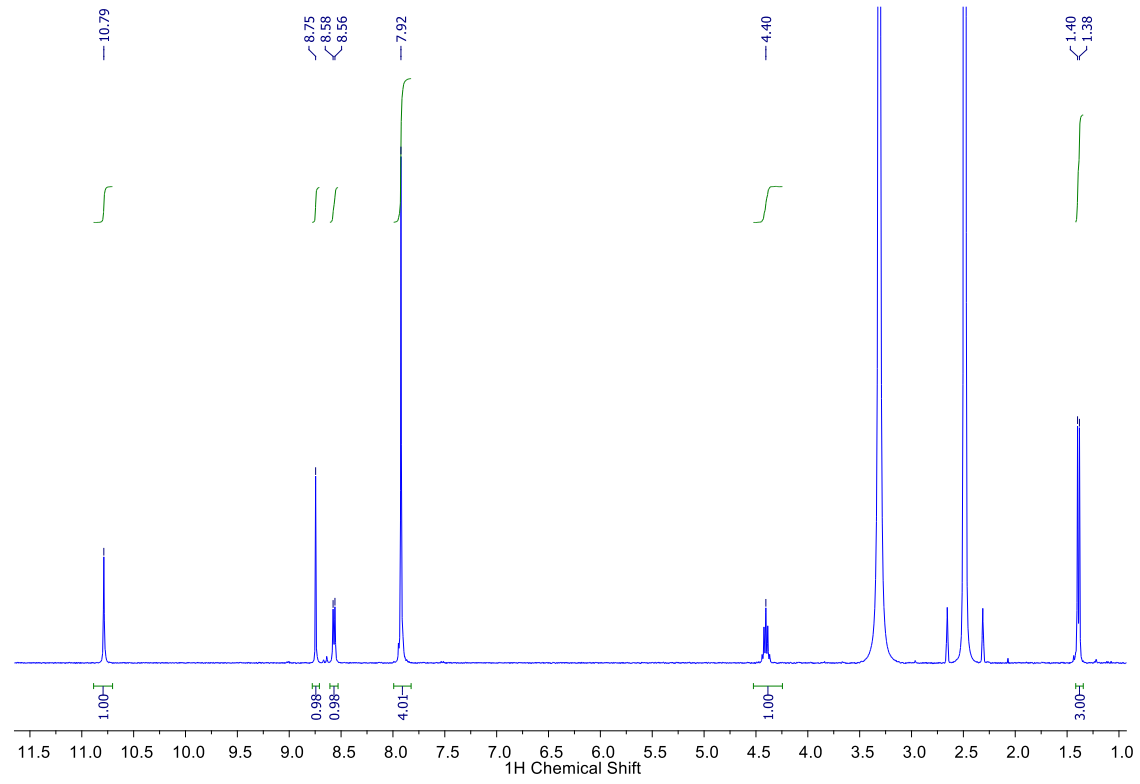

Figure A.10 *^{1}H NMR (400 MHz, DMSO-d_6) of* ***62****.*

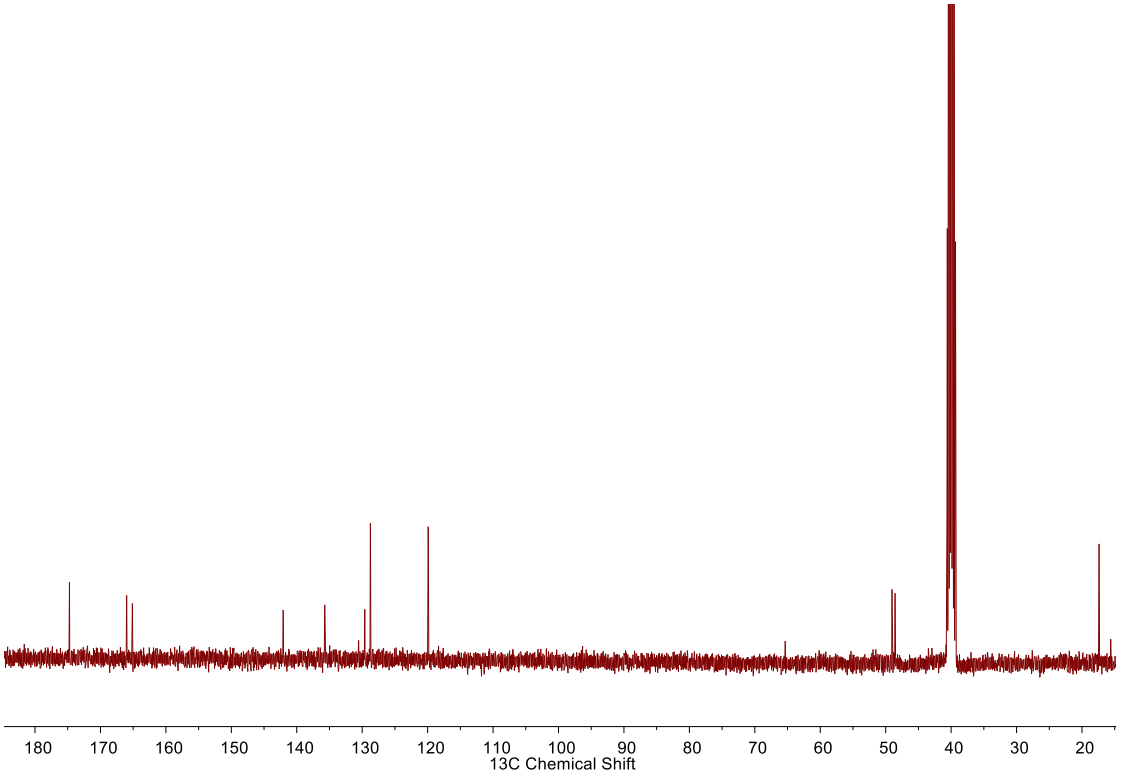

Figure A.11 *^{13}C NMR (100 MHz, DMSO-d_6) of* ***62****.*

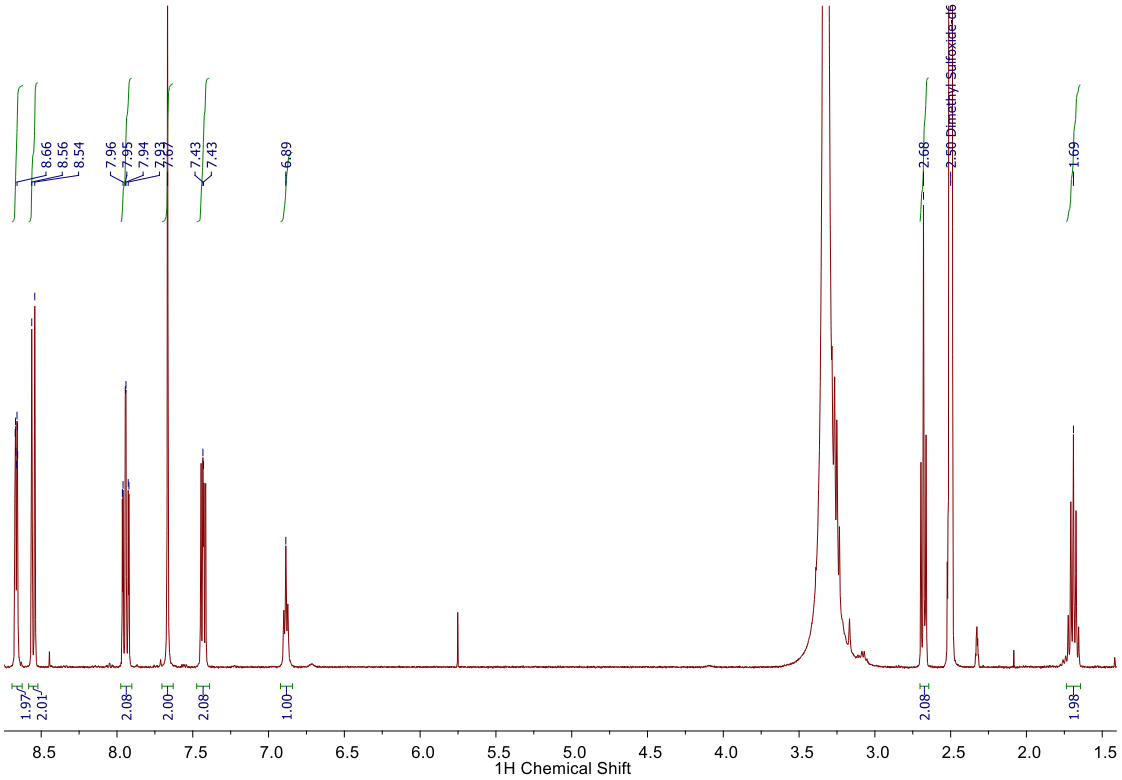

Figure A.12 *^{1}H NMR (400 MHz, DMSO-d_6) of* ***64****.*

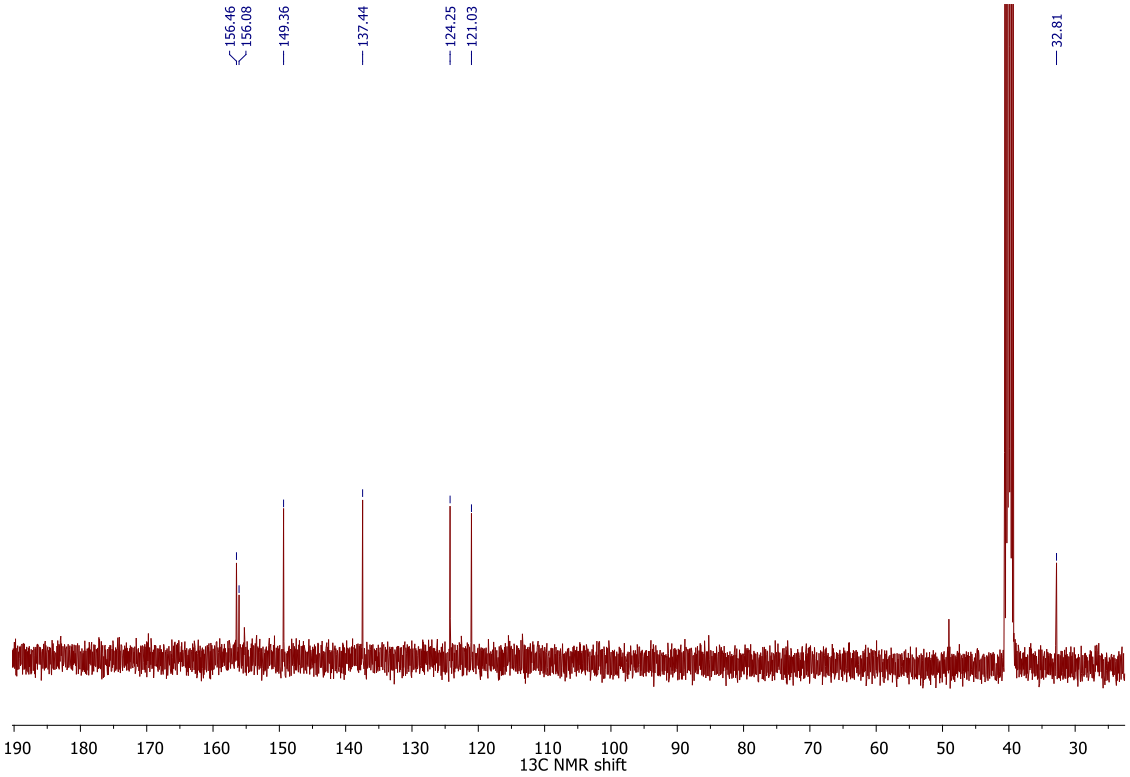

Figure A.13 *^{13}C NMR (400 MHz, DMSO-d_6) of* ***64****.*

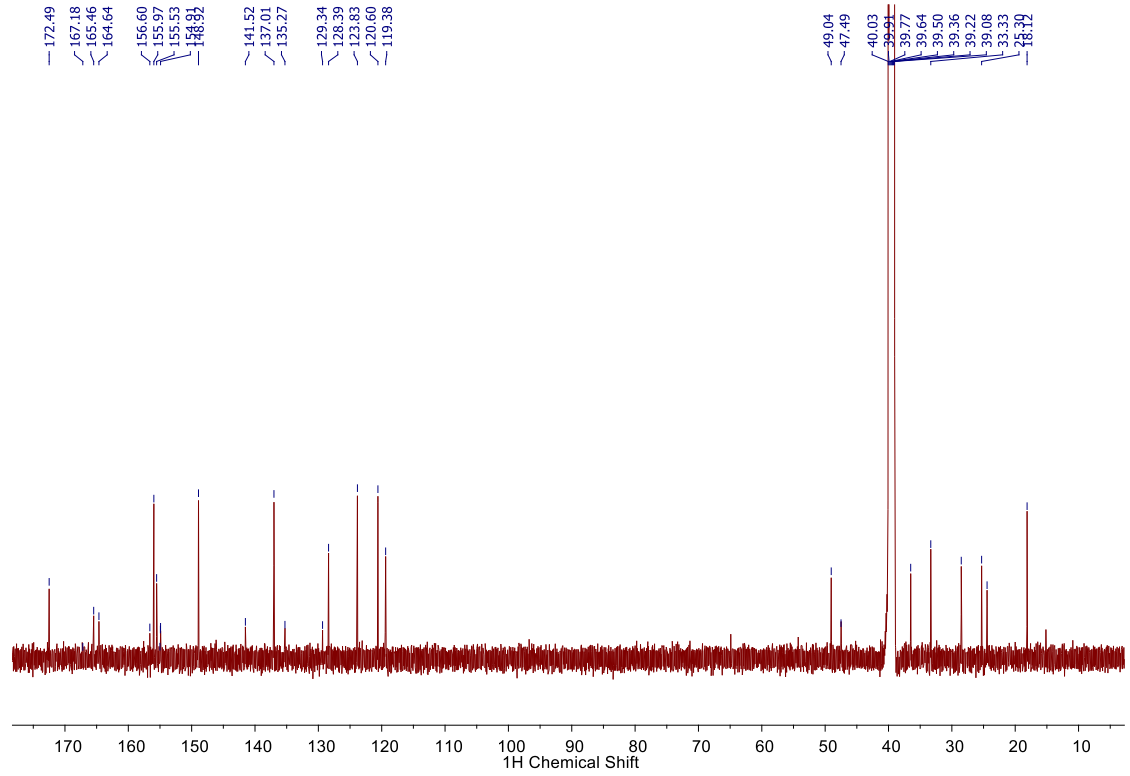

Figure A. 14 *^{13}C NMR (100 MHz, DMSO-d_6) of* ***54****.*

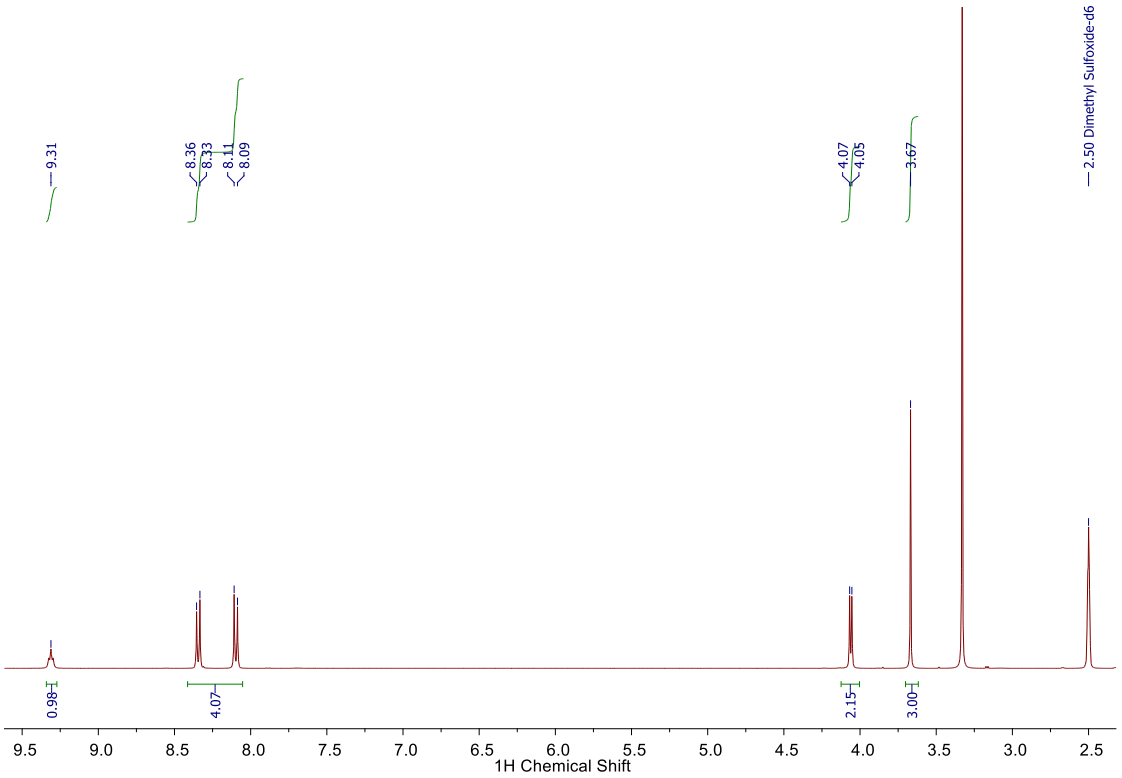

Figure A.15 *^{1}H NMR (400 MHz, DMSO-d_6) of* ***65****.*

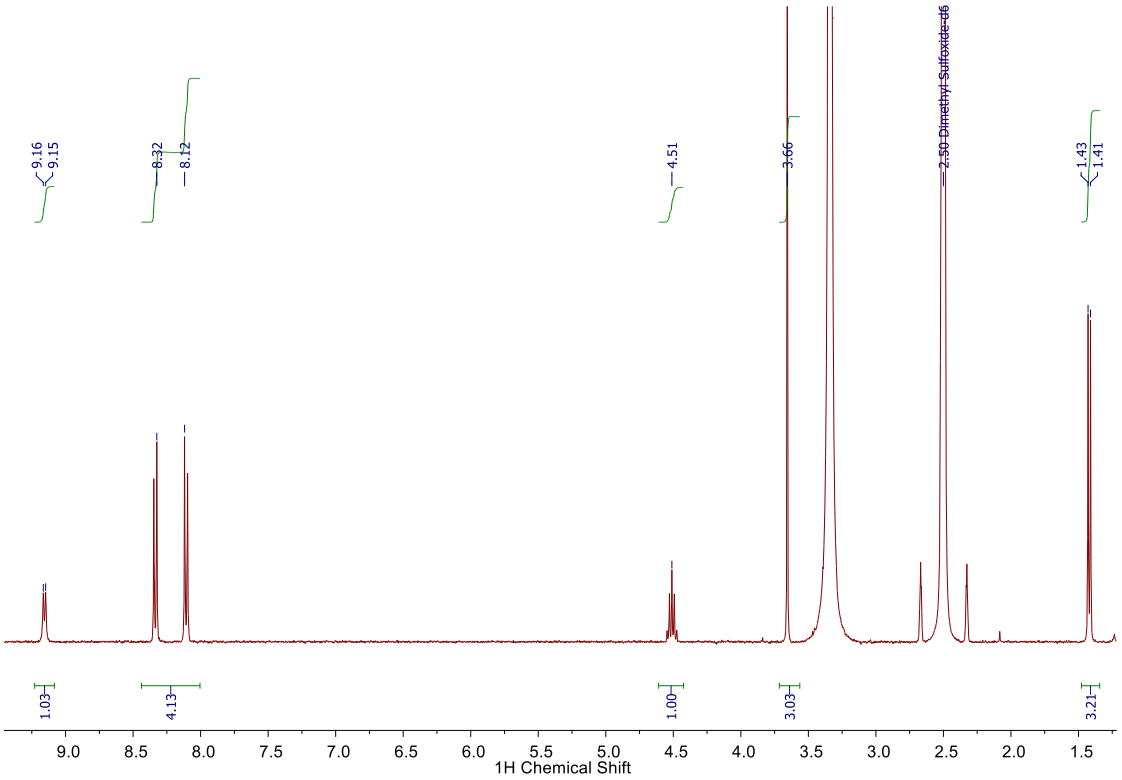

Figure A.16 *^{1}H NMR (400 MHz, DMSO-d_6) of* ***66****.*

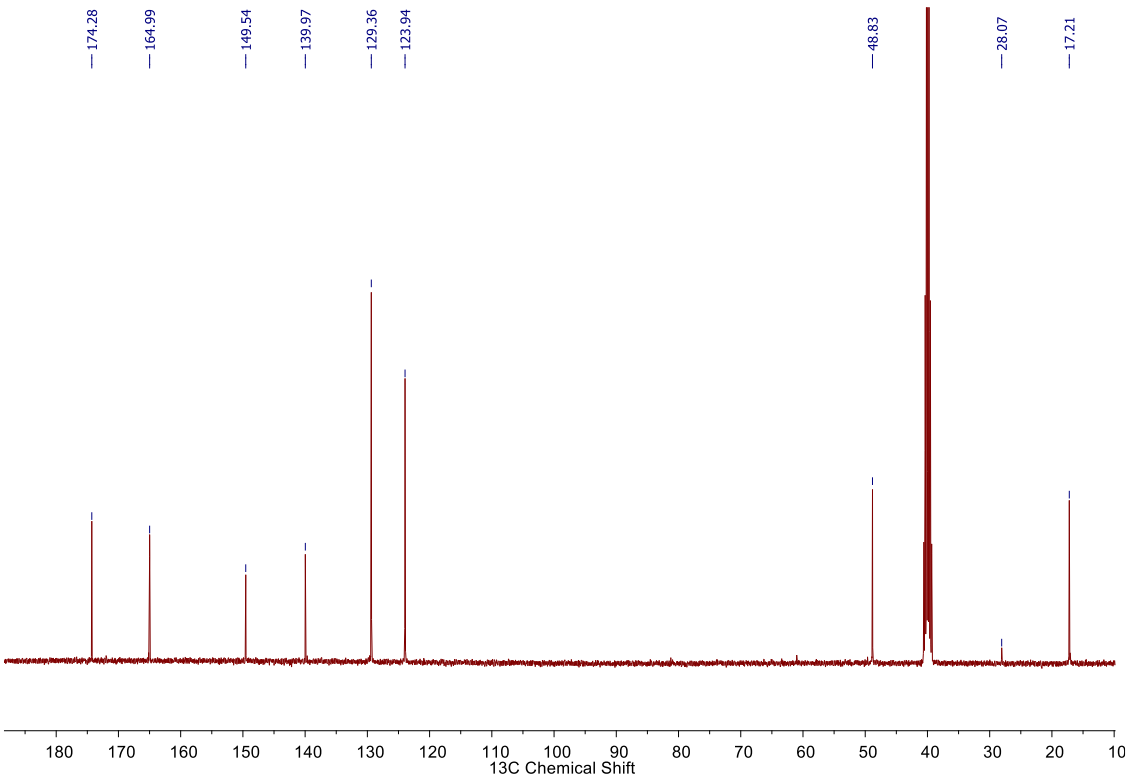

Figure A.17 *^{13}C NMR (100 MHz, DMSO-d_6) of* ***66****.*

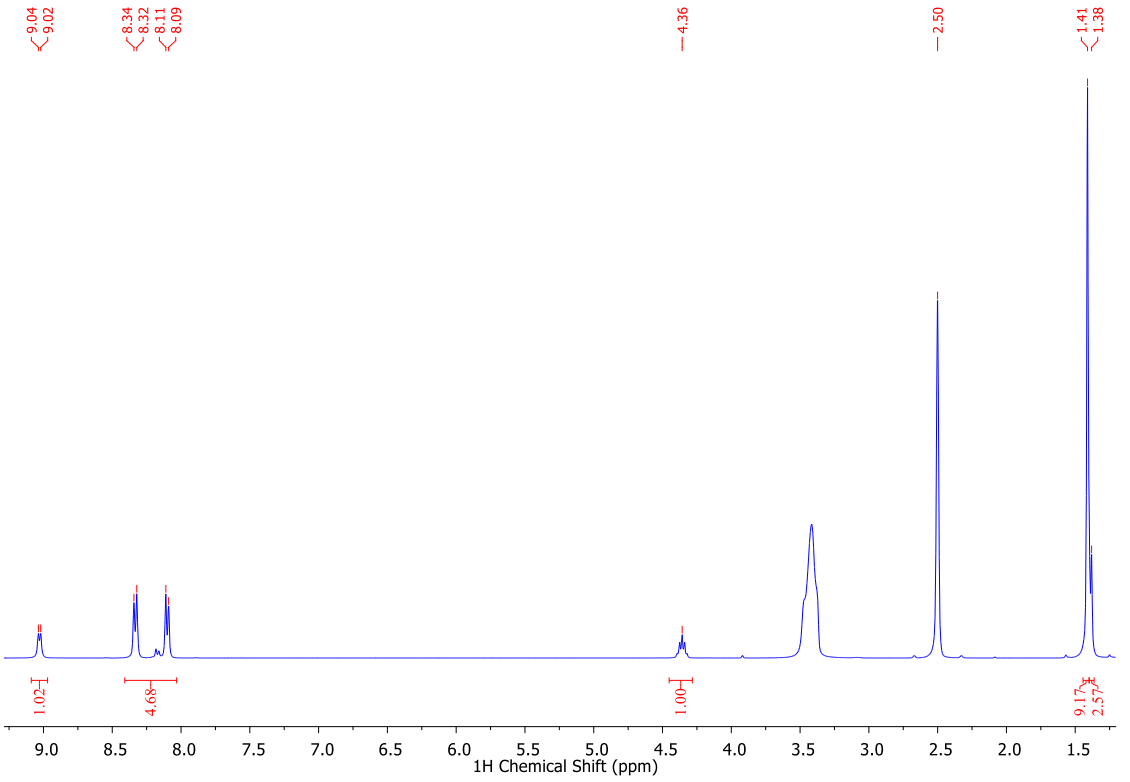

Figure A.18 *^{1}H NMR (400 MHz, DMSO-d_6) of* ***67****.*

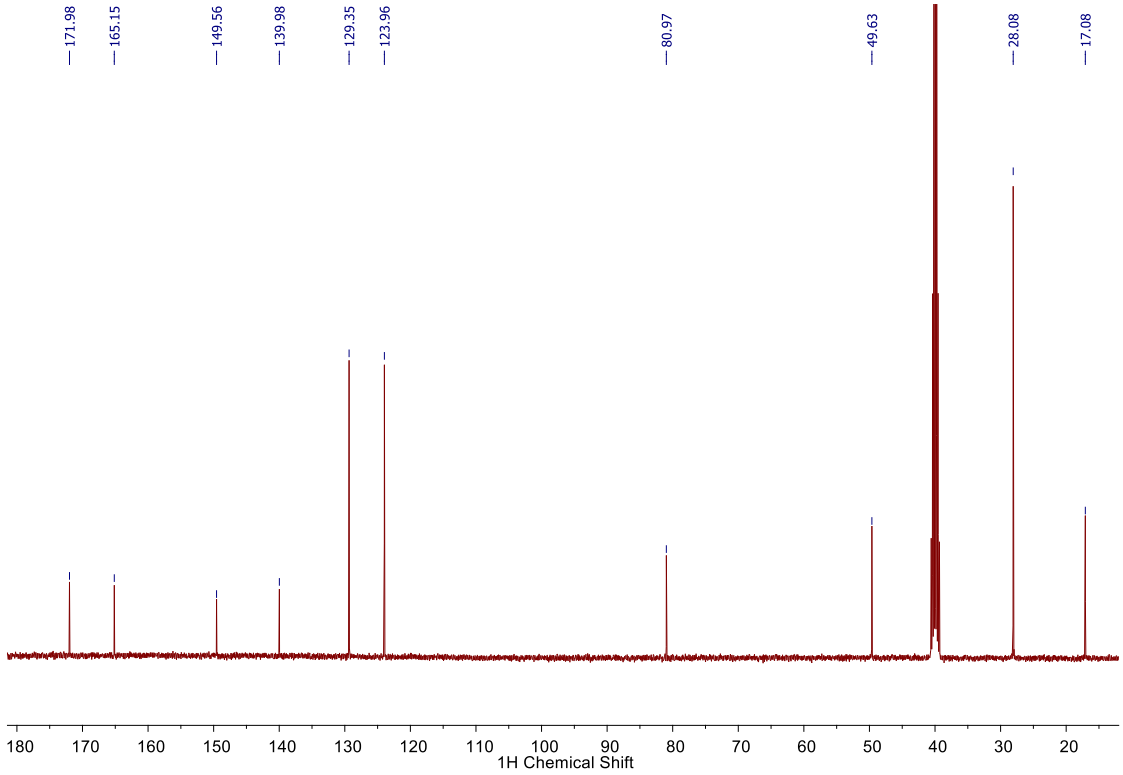

Figure A.19 *^{13}C NMR (100 MHz, DMSO-d_6) of* ***67****.*

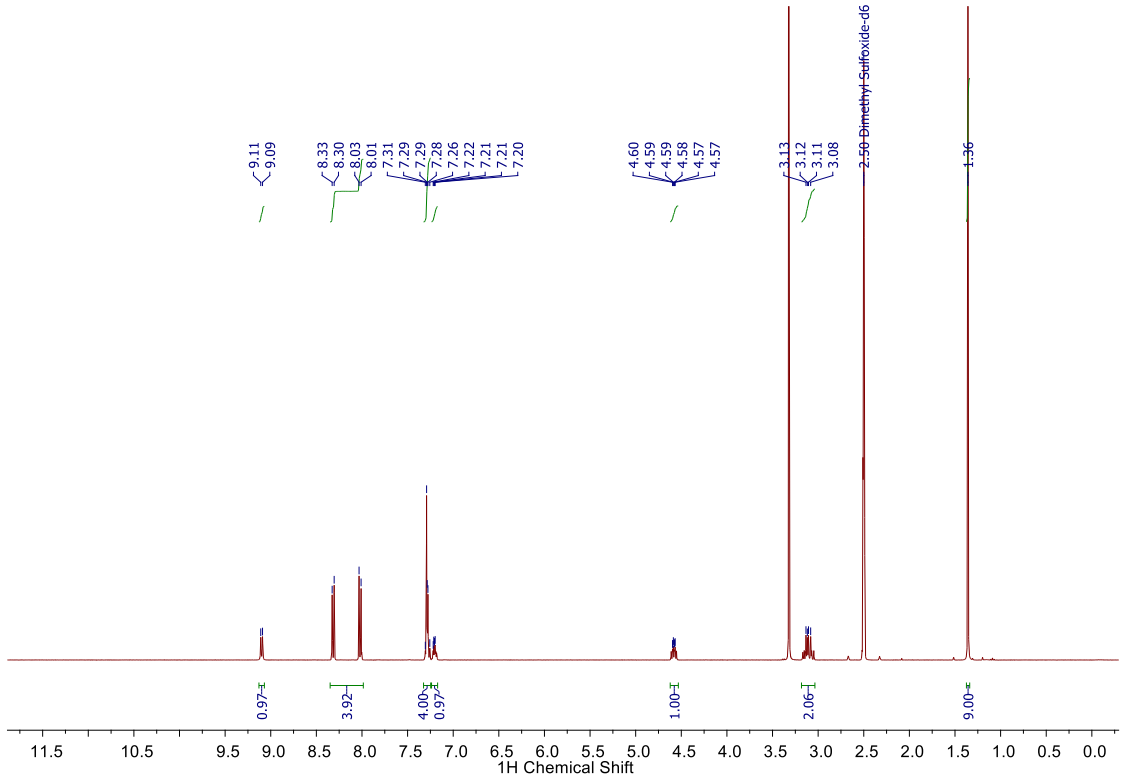

Figure A.20 *^{1}H NMR (400 MHz, DMSO-d_6) of* ***68****.*

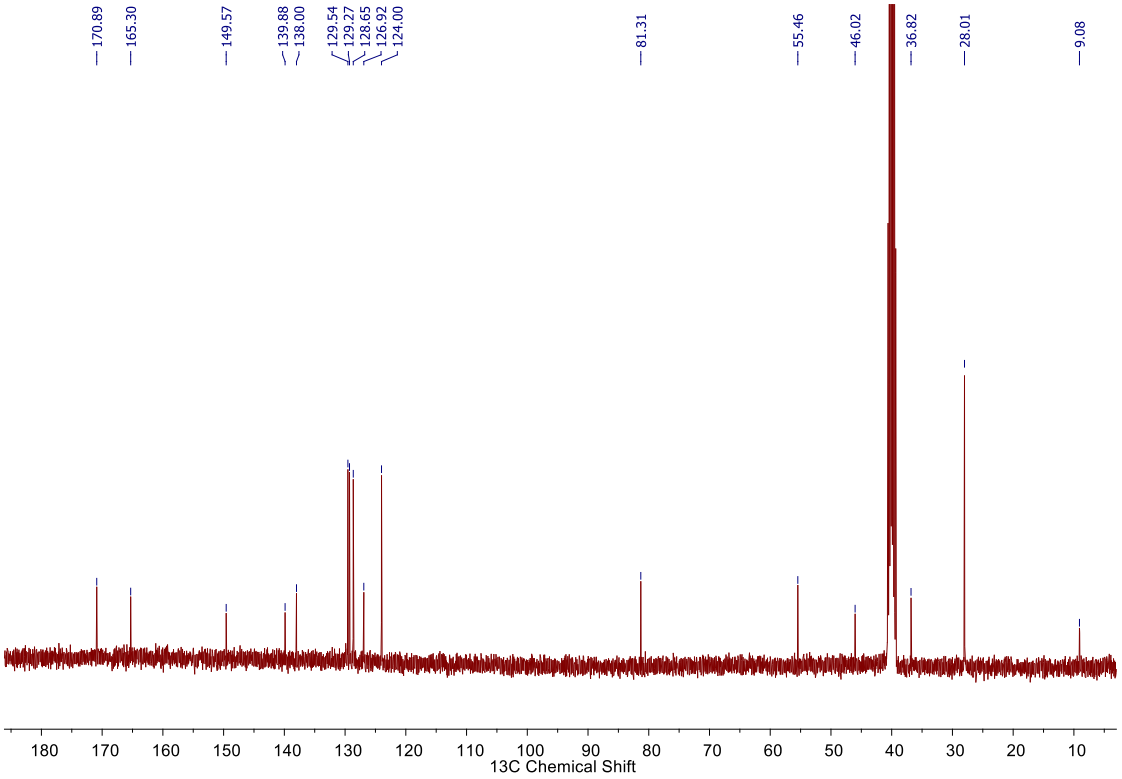

Figure A.21 *^{13}C NMR (100 MHz, DMSO-d_6) of* ***68***.

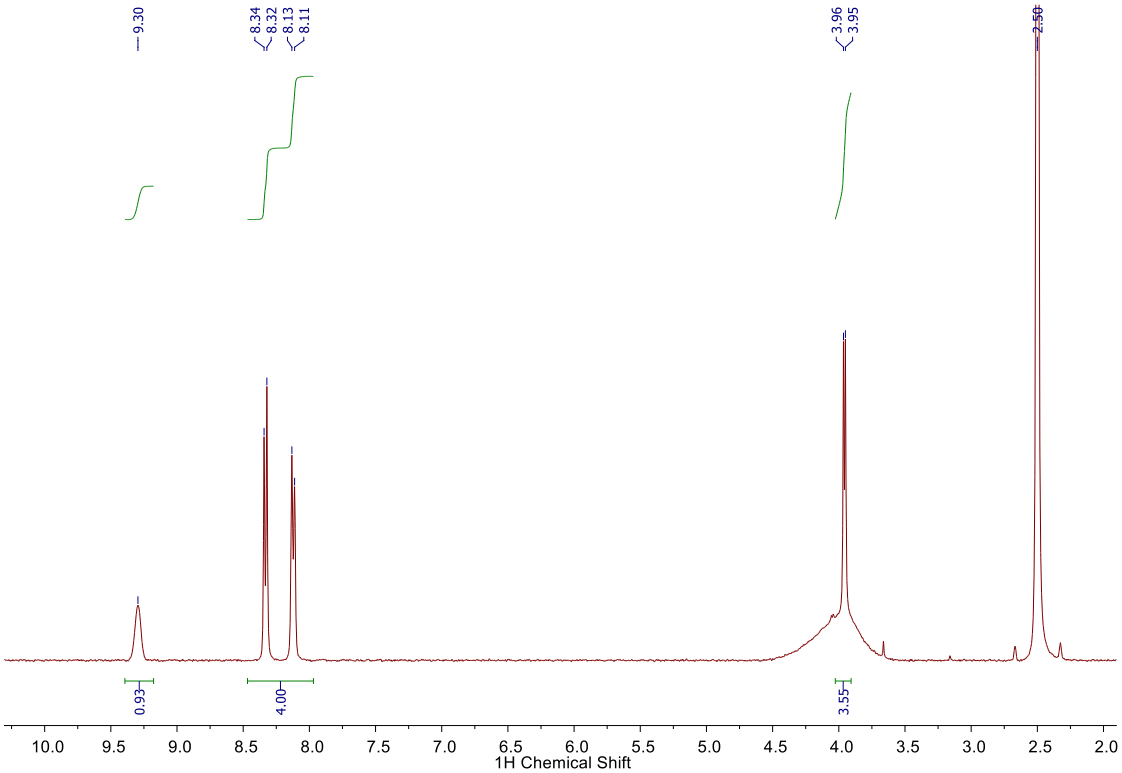

Figure A.22 *^{1}H NMR (400 MHz, DMSO-d_6) of* ***69***.

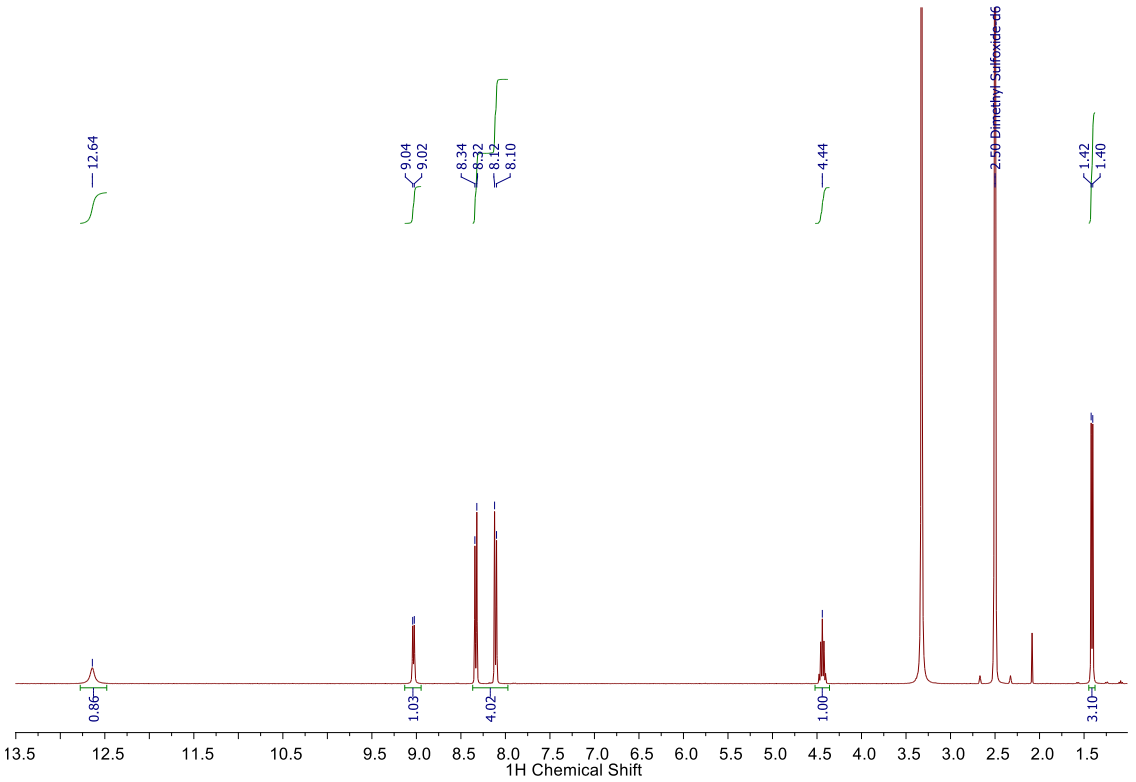

Figure A.23 *^{1}H NMR (400 MHz, DMSO-d_6) of* ***70****.*

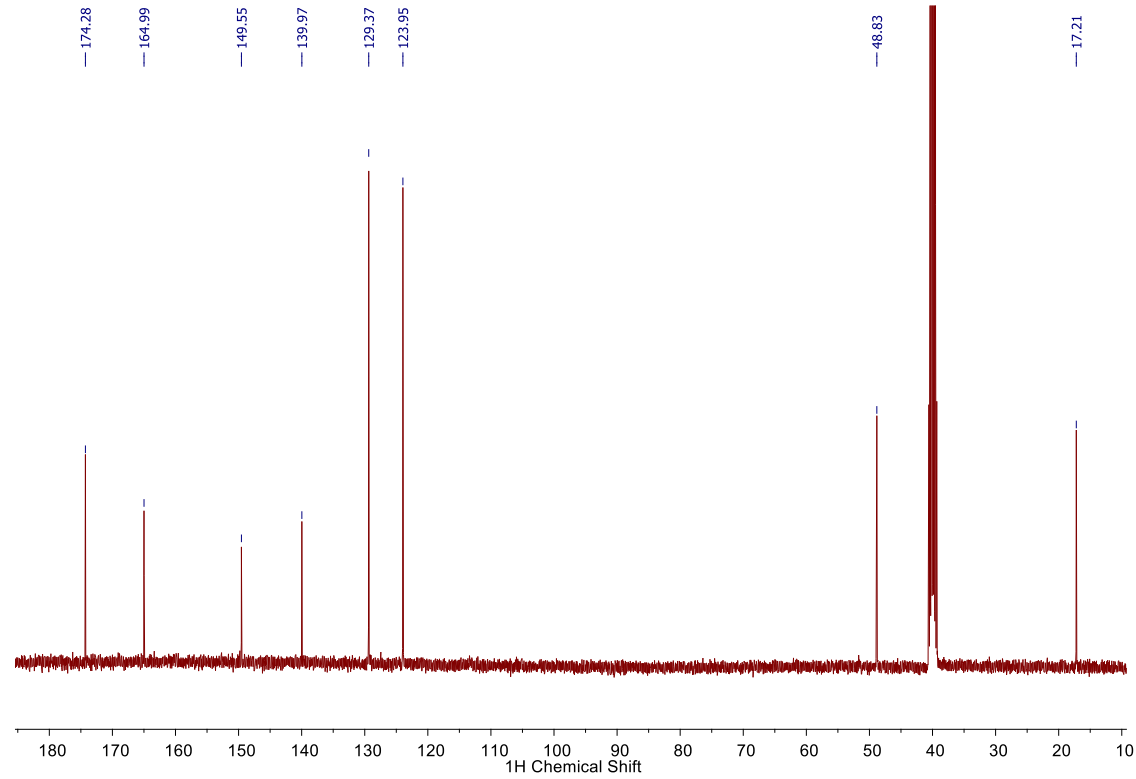

Figure A.24 *^{13}C NMR (100 MHz, DMSO-d_6) of* ***70****.*

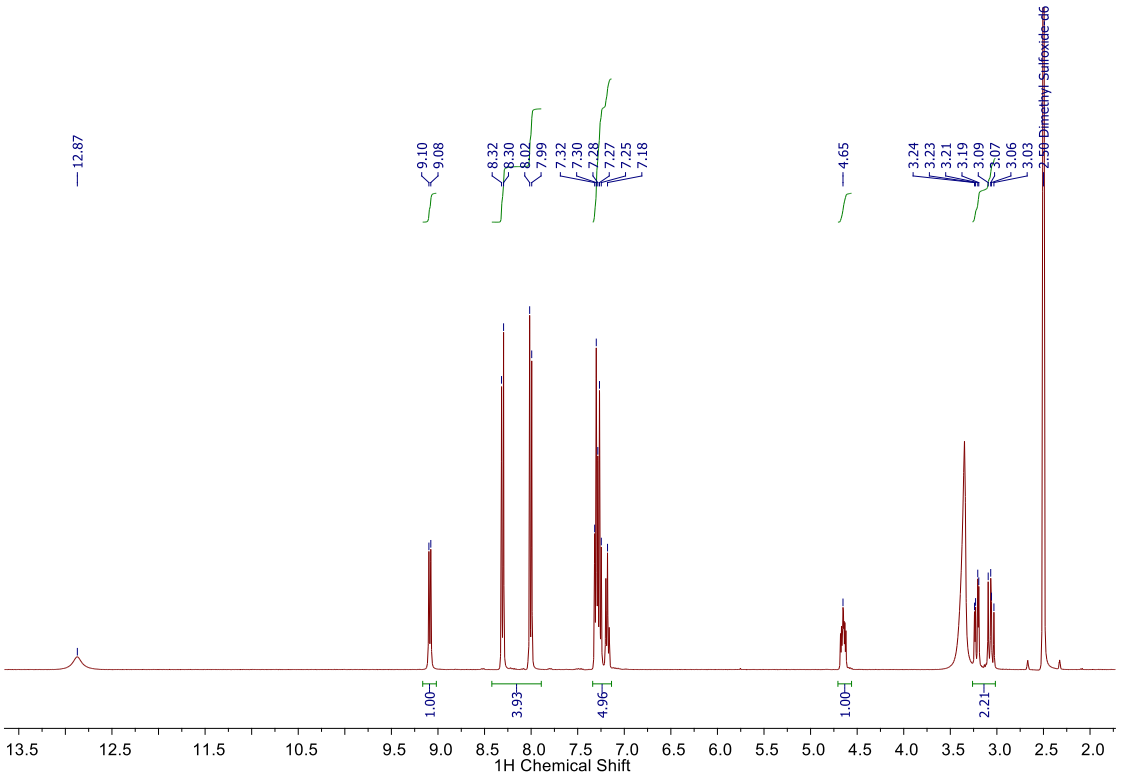

Figure A.25 *^{1}H NMR (400 MHz, DMSO-d_6) of* ***71****.*

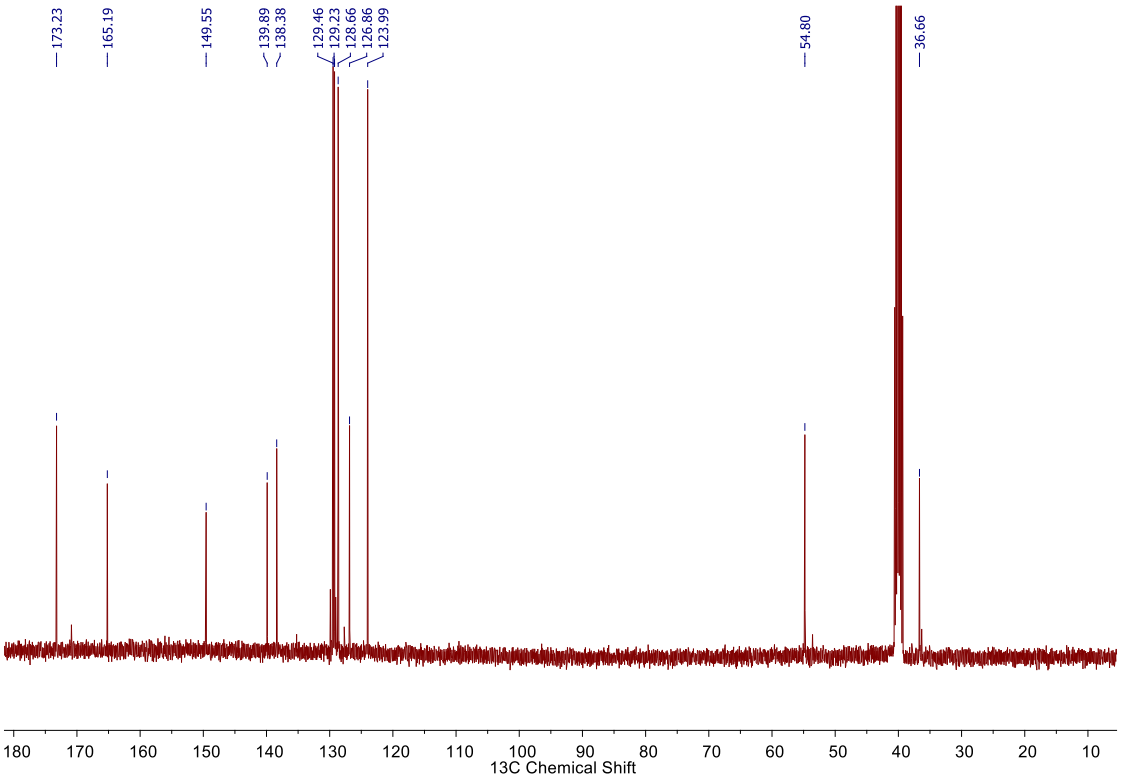

Figure A.26 *^{13}C NMR (100 MHz, DMSO-d_6) of* ***71****.*

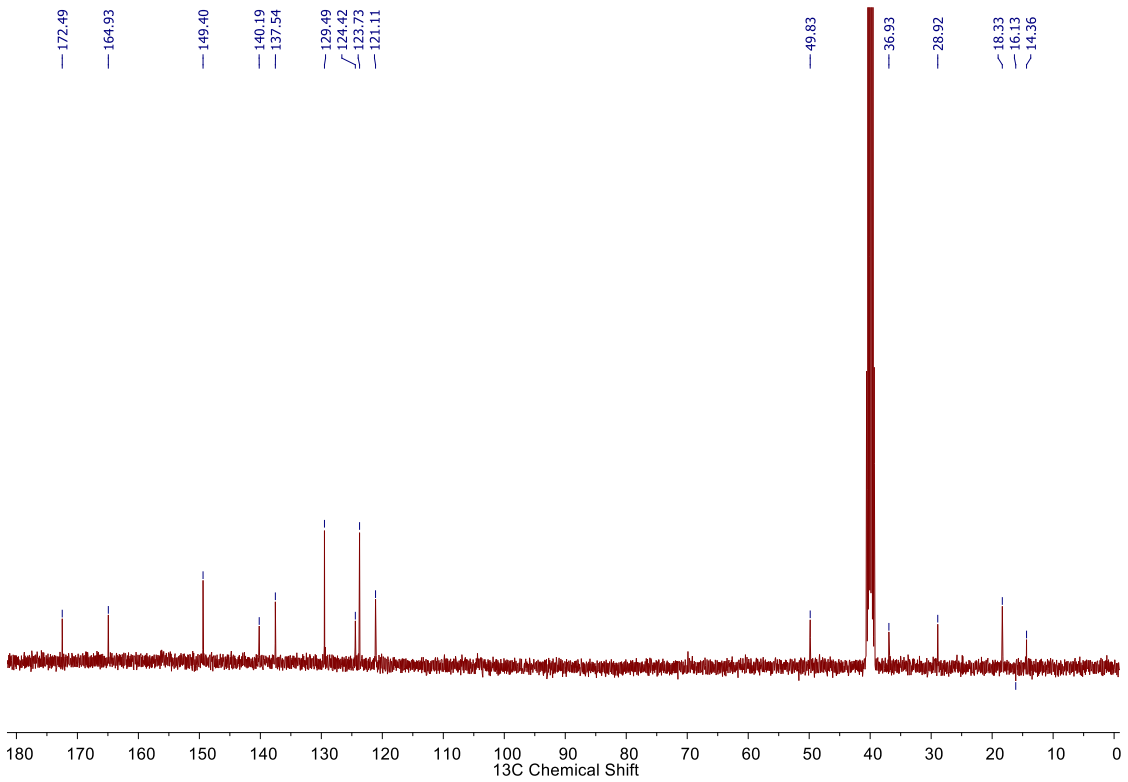

Figure A.27 *^{13}C NMR (100 MHz, DMSO-d_6) of **73**.*

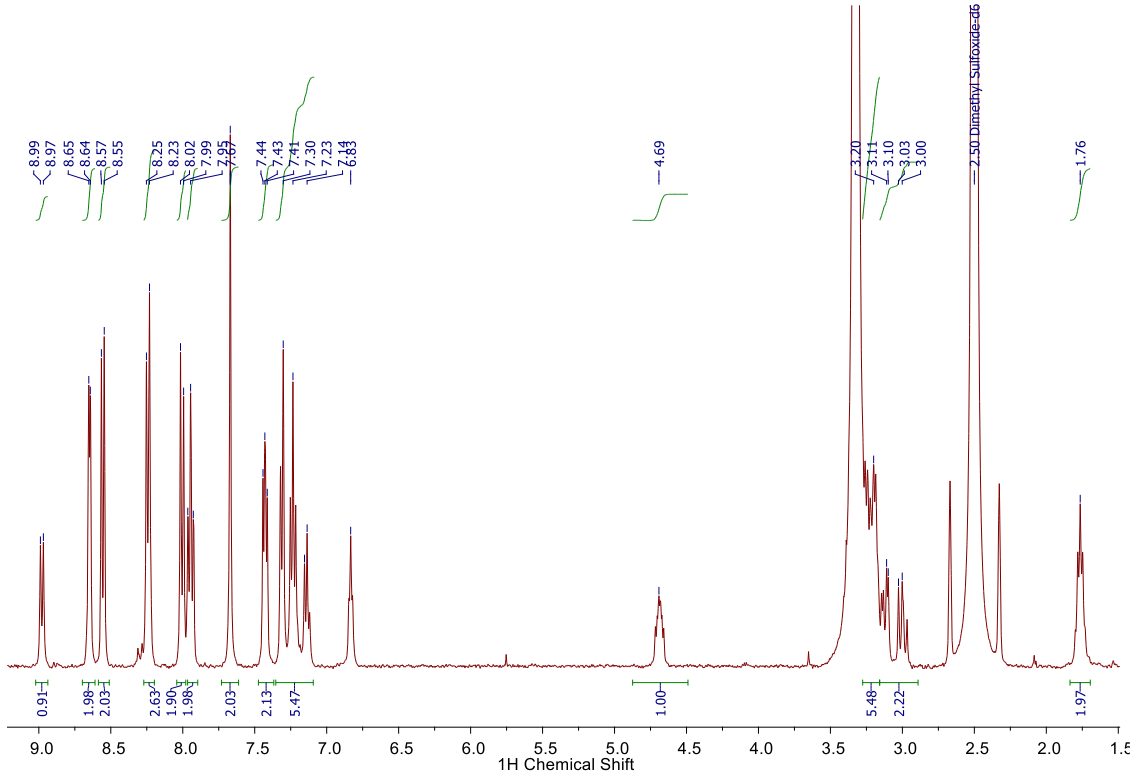

Figure A.28 *^{13}C NMR (100 MHz, DMSO-d_6) of **74**.*

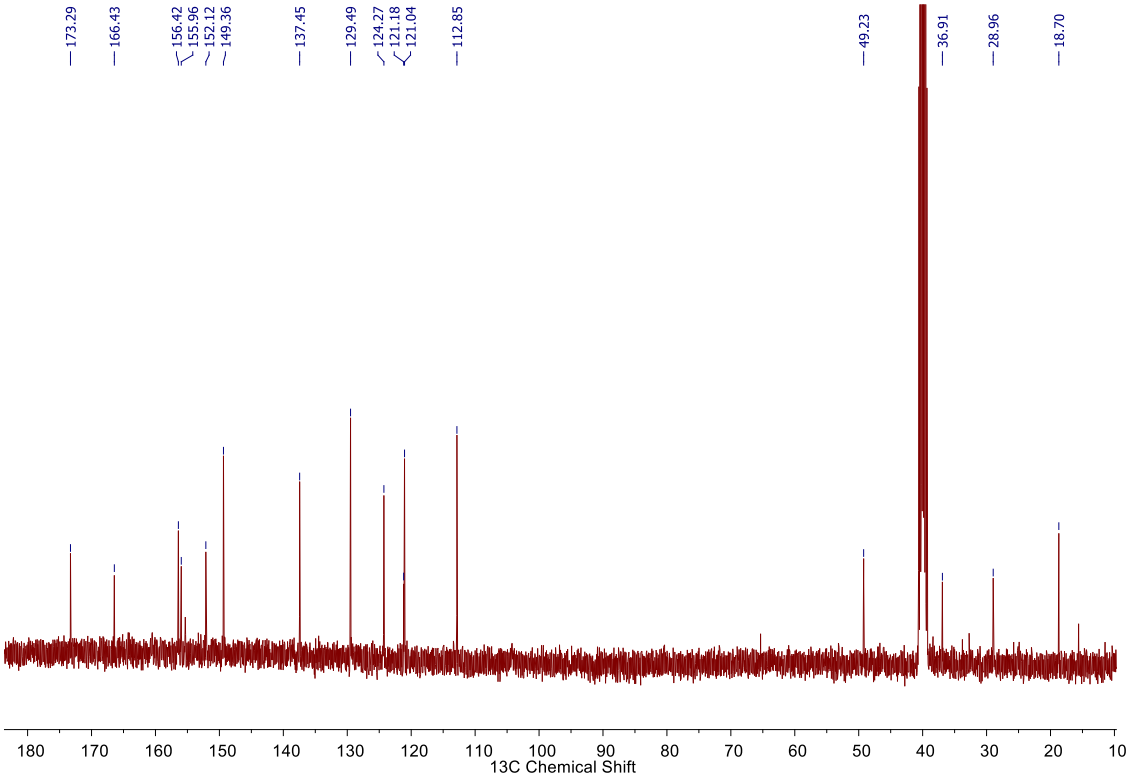

Figure A.29 *^{1}H NMR (100 MHz, DMSO-d_6) of **75**.*

A.2 Infrared Spectra

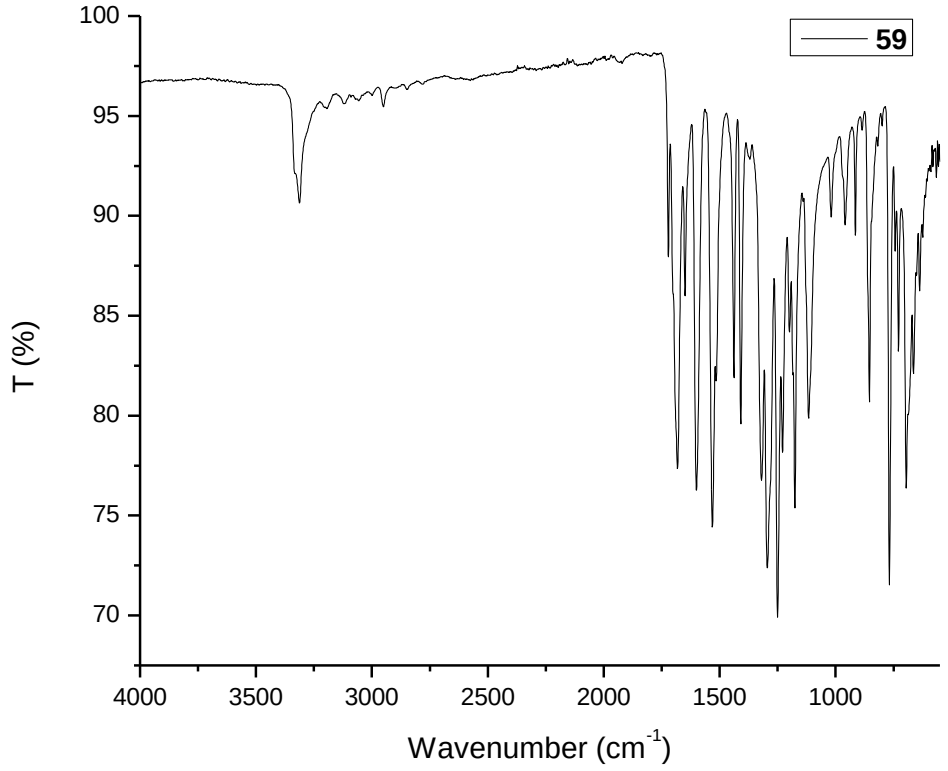

Figure A.30 *FTIR spectrum of* ***56****.*

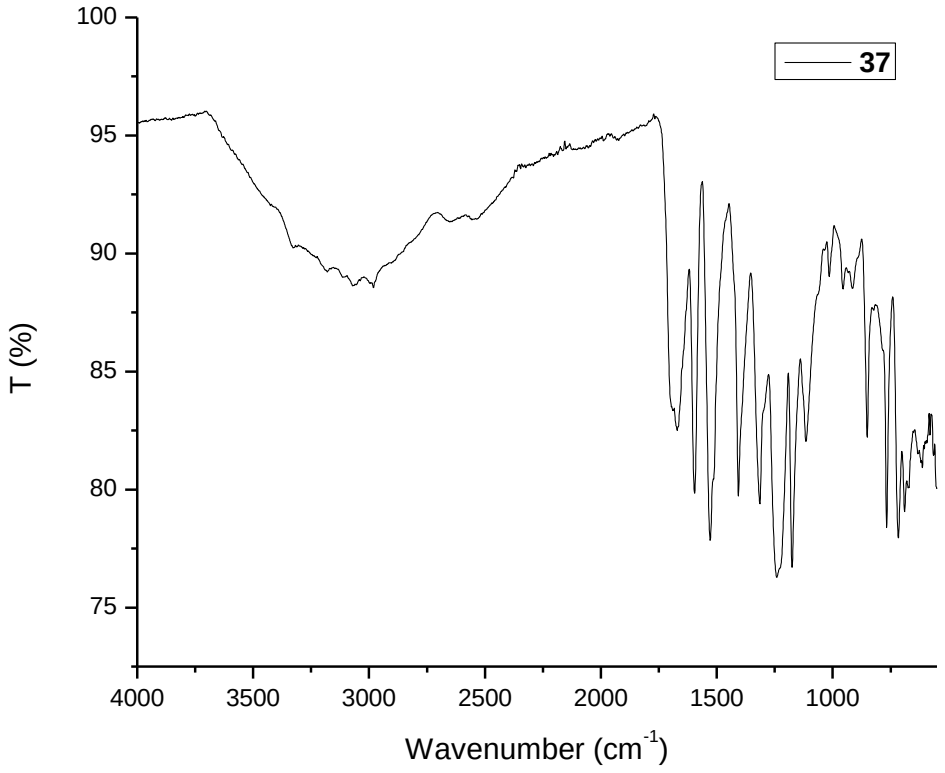

Figure A.31 *FTIR spectrum of* ***37****.*

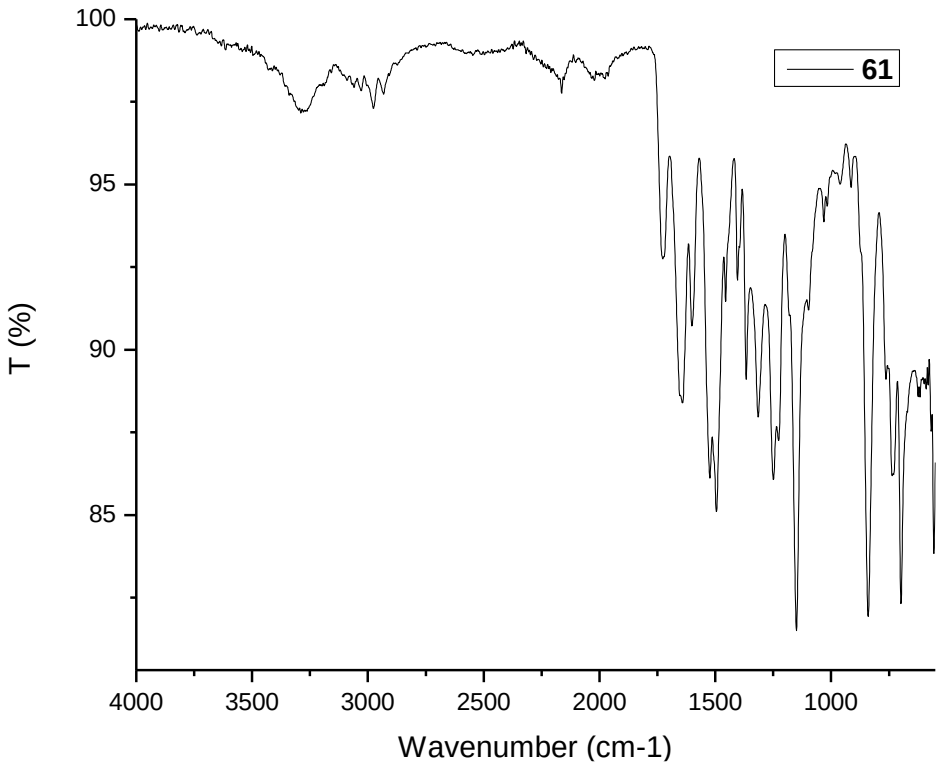

Figure A.32 *FTIR spectrum of* ***59****.*

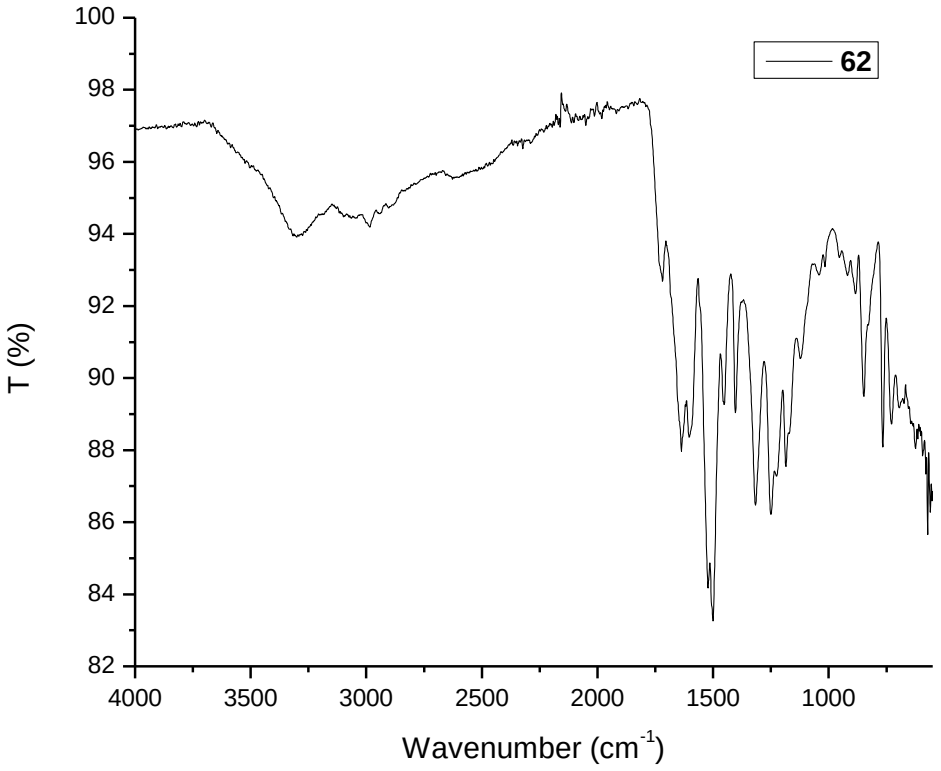

Figure A.33 *FTIR spectrum of* ***62****.*

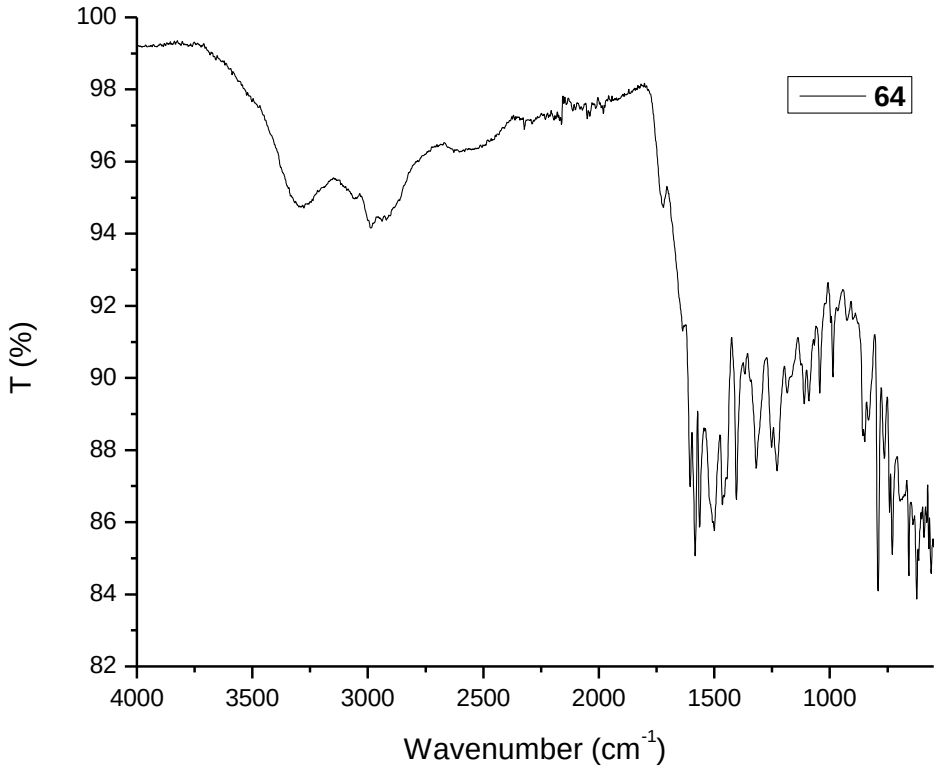

Figure A.34 *FTIR spectrum of* ***64****.*

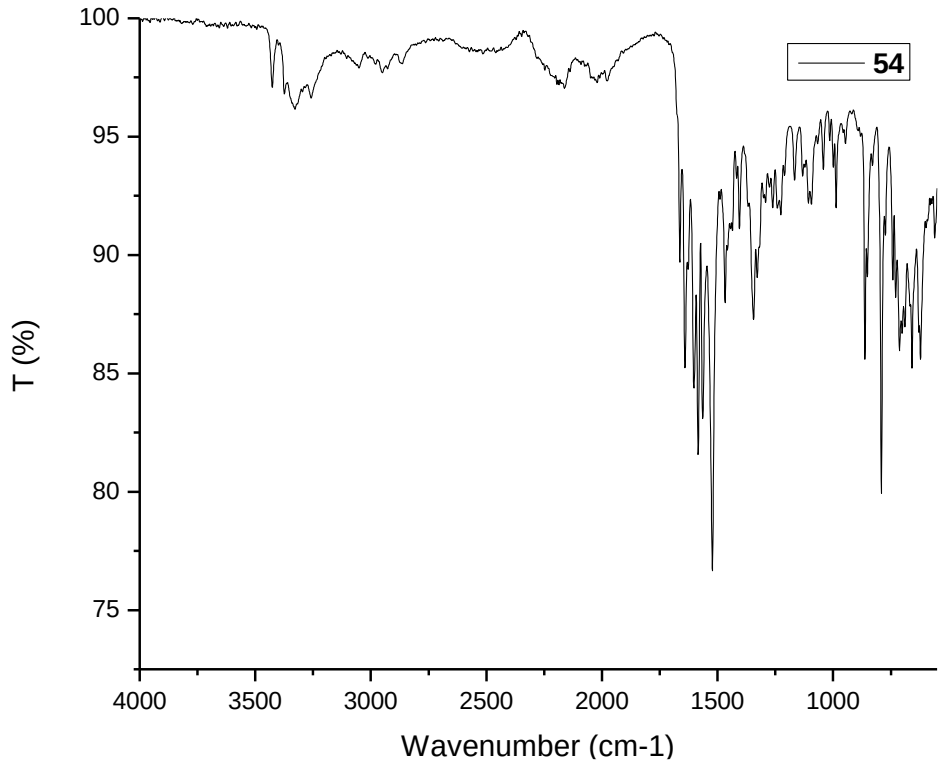

Figure A.35 *FTIR spectrum of* ***54.***

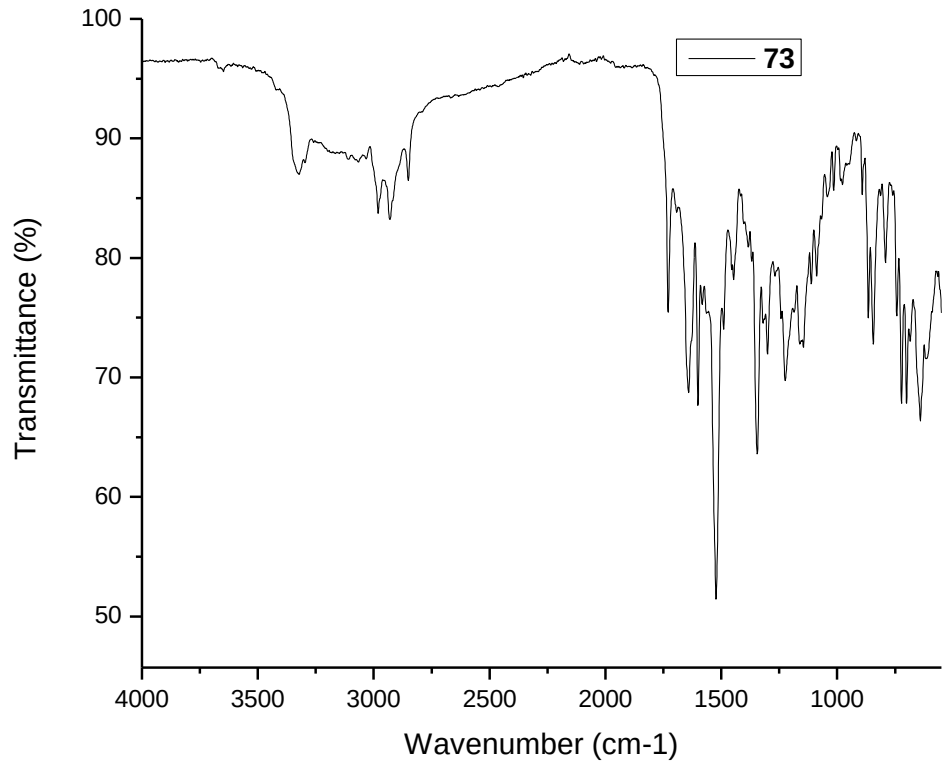

Figure A.36 *FTIR spectrum of* ***73.***

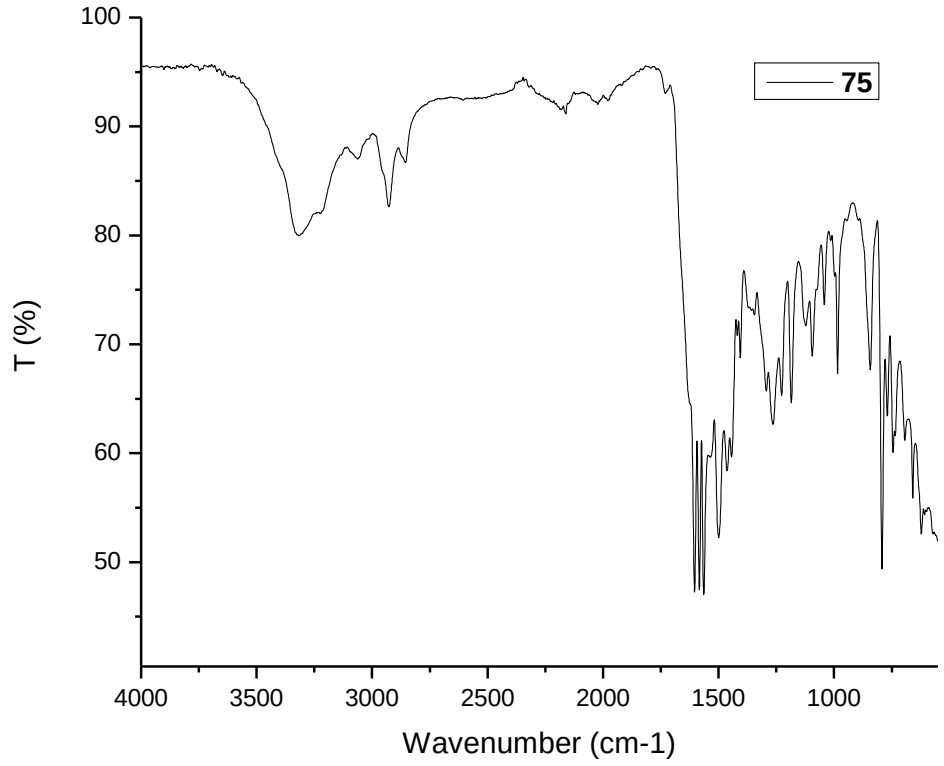

Figure A.37 *FTIR spectrum of* ***75.***

A.3 Mass Spectra

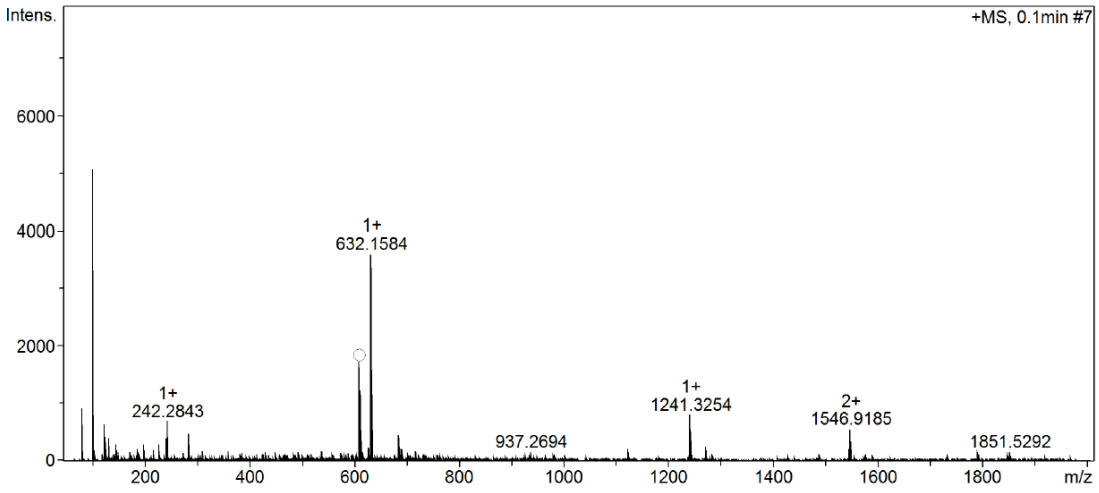

Meas. m/z	#	Ion Formula	m/z	err [mDa]	err [ppm]	rdb	N-Rule	e⁻ Conf	mSigma
610.180513	1	C33H28N3O9	610.182006	-1.5	-2.4	21.5	ok	even	268.6

Figure A.38 *Mass Spectrum (ESI+) for* ***56****.*

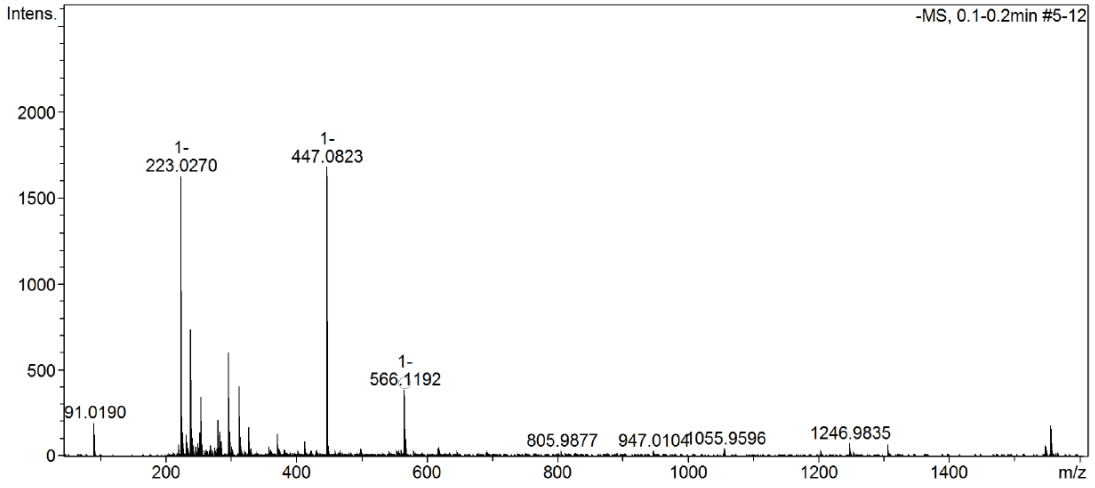

Meas. m/z	#	Ion Formula	m/z	err [mDa]	err [ppm]	rdb	N-Rule	e⁻ Conf	mSigma
566.119247	1	C30H20N3O9	566.120503	1.3	2.2	22.5	ok	even	31.5

Figure A.39 *Mass Spectrum (ESI-) for* ***37****.*

A.4 Additional Data

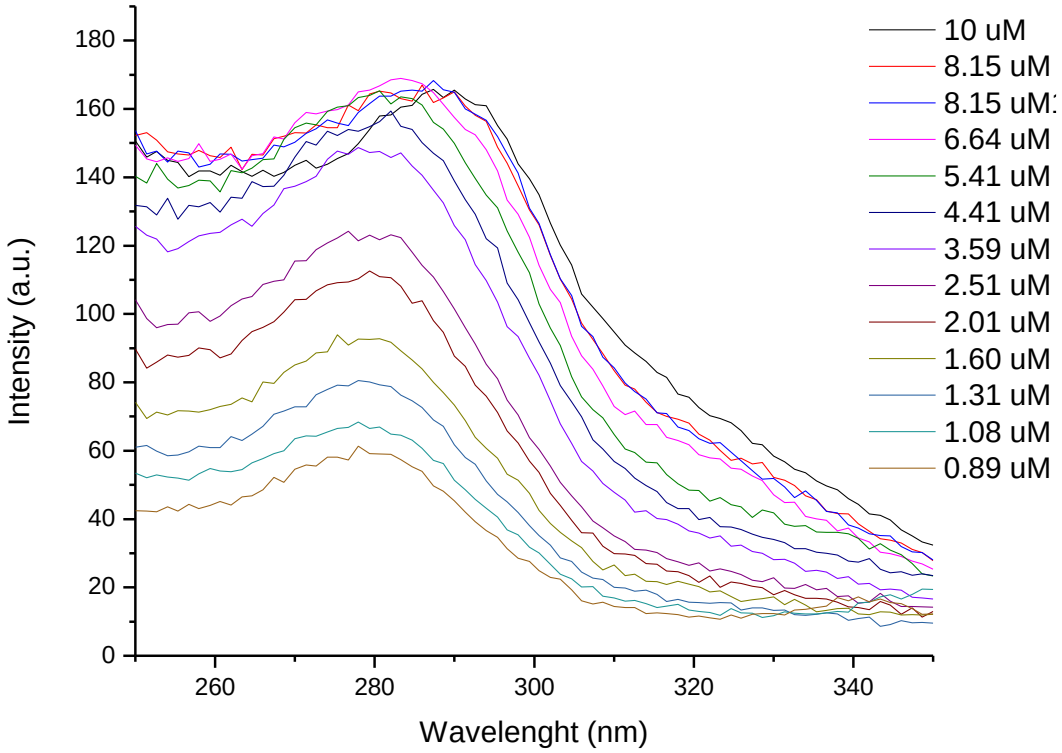

Figure A.40 *Excitation spectra (λ_{ex} = 408 nm) for the dilution of* ***54*** *performed in Chapter 3.*

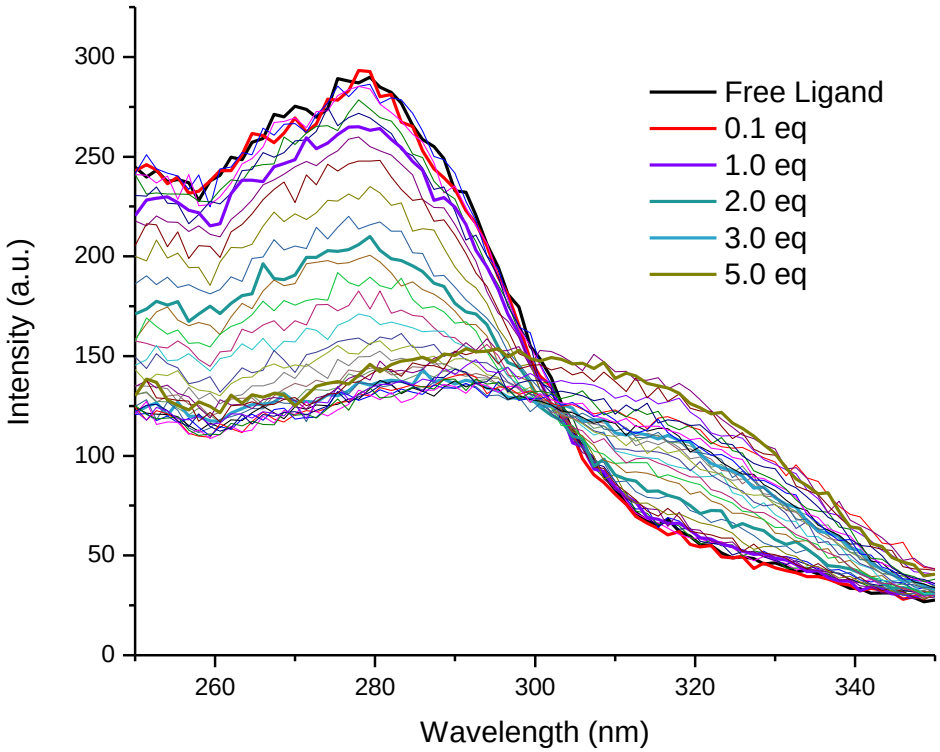

Figure A.41 *Excitation spectra (λ_{ex} = 408 nm) for the titration of* ***54*** *with Eu(III) ions performed in Chapter 3.*

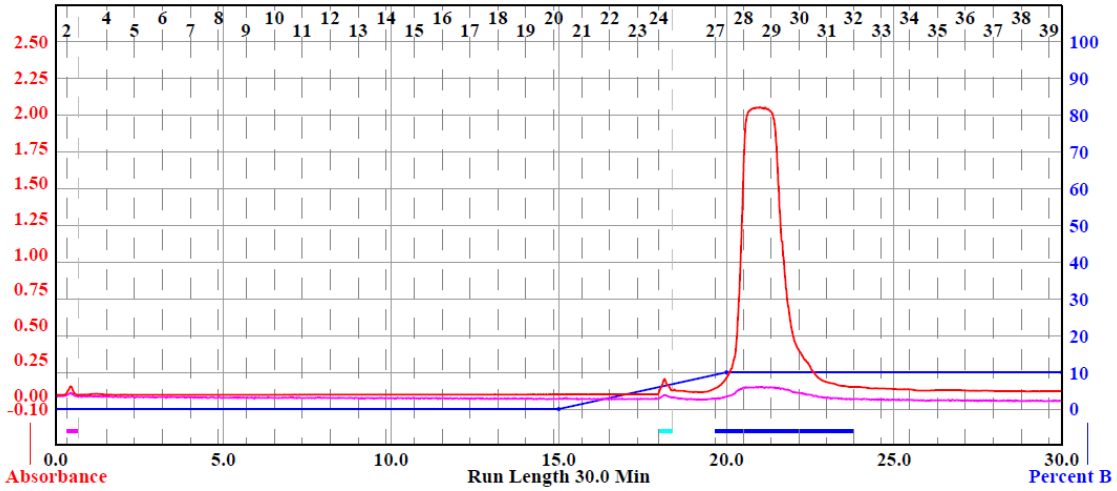

Figure A.42 *Chromatogram for the purification of* ***54*** *performed as described in Chapter 2.*